# Small influence of magnetic ordering on lattice dynamics in TaFe$_{1.25}$Te$_3$

M. Opačić,[1] N. Lazarević,[1] D. Tanasković,[2] M. M. Radonjić,[2] A. Milosavljević,[1] Yongchang Ma,[3,4]
C. Petrovic,[3] and Z. V. Popović[1,5]

[1]*Center for Solid State Physics and New Materials, Institute of Physics Belgrade, University of Belgrade, Pregrevica 118,
11080 Belgrade, Serbia*
[2]*Scientific Computing Laboratory, Center for the Study of Complex Systems, Institute of Physics Belgrade, University of Belgrade,
Pregrevica 118, 11080 Belgrade, Serbia*
[3]*Condensed Matter Physics and Materials Science Department, Brookhaven National Laboratory, Upton, New York 11973-5000, USA*
[4]*School of Materials Science and Engineering, Tianjin University of Technology, Tianjin 300384, People's Republic of China*
[5]*Serbian Academy of Sciences and Arts, Knez Mihailova 35, 11000 Belgrade, Serbia*

Raman scattering spectra of zigzag spin chain TaFe$_{1.25}$Te$_3$ single crystal are presented in a temperature range from 80 to 300 K. Nine Raman active modes of $A_g$ and $B_g$ symmetry are clearly observed and assigned by probing different scattering channels, which is confirmed by lattice dynamics calculations. Temperature dependence of the Raman modes linewidth is mainly governed by the lattice anharmonicity. The only deviation from the conventional behavior is observed for $A_g$ symmetry modes in a vicinity of the magnetic phase transition at $T_N \approx 200$ K. This implies that the electron-phonon interaction weakly changes with temperature and magnetic ordering, whereas small changes in the spectra near the critical temperature can be ascribed to spin fluctuations.

## I. INTRODUCTION

The discovery of superconductivity in La(O$_{1-x}$F$_x$)FeAs in 2008 [1] initiated an intensive search for new iron-based superconducting materials, in order to obtain better understanding of their physical properties and the mechanism of high-$T_c$ superconductivity [2–4]. Novel iron-based materials, however, are not only superconducting, but can also exhibit various types of magnetic ordering. In some cases the magnetic phase transition is continuous [5–8], whereas in others it is accompanied by structural changes [9–15], or even by a nanoscale coexistence of antiferromagnetic (AFM) and superconducting domains [16–18].

TaFe$_{1+y}$Te$_3$ was synthesized and characterized about 25 years ago [19,20]. It is a layered system consisting of FeTe chains, along the $b$ axis, separated by a Ta/Te network in between; see Fig. 1. These layers are parallel to the natural cleavage plane. There are also additional Fe ions, Fe2, randomly occupying interstitial sites [21–23]. TaFe$_{1+y}$Te$_3$ features anisotropic charge transport with metallic resistivity within the plane and insulating in the direction normal to the FeTe layers [23]. The first study of magnetic structure implies that TaFe$_{1+y}$Te$_3$ is composed of double zigzag spin chains with antiferromagnetic ordering of Fe1 spins [22]. The newest neutron diffraction measurements suggest that spin ordering within zigzag chains is ferromagnetic, whereas these zigzag chains couple antiferromagnetically [23], as shown in Fig. 1(b). However, the exact interaction mechanism is not clearly resolved.

There is a similarity between TaFe$_{1+y}$Te$_3$ and the extensively studied Fe$_{1+y}$Te compound since they are correlated bad metals which order antiferromagnetically below $T_N \approx$ 200 K and 70 K, respectively [10,23], both having rather large magnetic moments on Fe ions, $\approx 2$ $\mu_B$/Fe. TaFe$_{1+y}$Te$_3$, however, forms ferromagnetic (FM) zigzag spin chains which couple antiferromagnetically between the layers, whereas the Fe spins in Fe$_{1+y}$Te form a bicollinear AFM structure. The magnetic phase transition in Fe$_{1+y}$Te is accompanied by the

structural change from a tetragonal to a monoclinic, as opposed to TaFe$_{1+y}$Te$_3$ where a continuous transition to the AFM phase is observed in thermodynamic and transport measurements [22]. Just like in Fe$_{1+y}$Te, interest in spin chain and ladder materials [24] stems not only from their block-AFM states similar to parent compounds of iron-based superconductors [25], but also from superconductivity. It is worth noting that spin 1/2 copper oxide ladder structures host a spin gap and superconductivity upon doping [26–28]. In contrast to superconductivity in copper oxide ladder materials that was rather rare and with critical temperatures rather small when compared to highest achieved in copper square lattices [29,30], iron-ladder materials feature $T_c$'s similar to the highest found in Fe-based superconductors [31].

Raman spectra provide additional information on magnetic ordering and electron-phonon coupling. There exist several Raman studies of the phonon spectra of iron based materials near the superconducting or magnetic phase transition [32,33]. While no anomalies were observed in 1111 compounds [34,35], the Raman spectra show anomalous behavior near the spin density wave (SDW) transition in some of the 122 and 11 compounds [15,36–38], which was ascribed to the phonon renormalization due to the opening of the SDW or superconducting gap, or to the structural transition. Large anomalies were observed also in ferromagnetic K$_x$Co$_{2-y}$Se$_2$ [5], which was ascribed to the effect of electron-phonon coupling and spin fluctuations. Fe$_{1+y}$Te phonon spectra feature unusually large anomalies near the magnetic phase transition, as seen in sudden changes in the phonon frequencies and linewidths, due to the phonon modulation of magnetic interactions and structural phase transition [11–13]. Therefore, it is of interest to examine lattice dynamics in the normal state of iron-spin chain and ladder materials and compare it to materials like Fe$_{1+y}$Te. To the best of our knowledge, there are no published data on lattice dynamics of TaFe$_{1+y}$Te$_3$.

In this paper we present polarized Raman scattering spectra of TaFe$_{1.25}$Te$_3$ single crystal measured in a temperature range from 80 to 300 K. Nine out of 15 Raman active modes are
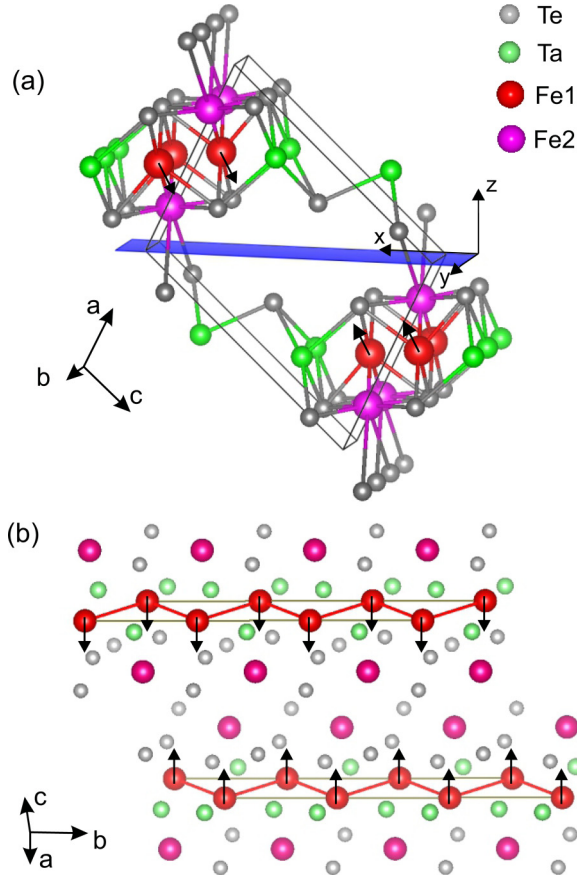
FIG. 1. (a) Structure of the TaFe$_{1.25}$Te$_3$ single crystal together with the natural cleavage plane [$\bar{1}$01]. $\mathbf{x} = 1/\sqrt{2}(\bar{1}0\bar{1})$ and $\mathbf{y} = (010)$ correspond to our laboratory system. (b) A view of the TaFe$_{1.25}$Te$_3$ structure along the $b$ axis. Two neighboring chains of Fe1 spins point in a parallel direction, forming a ferromagnetic zigzag chain, whereas spins of neighboring zigzag chains order antiferromagnetically. One should note that Fe2 is present with occupancy of 0.25.

observed and assigned using the selection rules for different polarization configurations and lattice dynamics calculations. In a sharp contrast to the related FeTe compound, TaFe$_{1.25}$Te$_3$ Raman spectra do not show significant changes near $T_N \approx$ 200 K, which clearly indicates that the phase transition is continuous. Temperature dependence of the frequency and linewidth is conventional, driven by the anharmonicity effects, except very near $T_N$ where some of phonon lines slightly broaden which should be the consequence of spin fluctuations near the critical temperature. These results indicate very small changes in the electron-phonon coupling and in the Fermi surface in the measured temperature range.

## II. EXPERIMENT AND NUMERICAL METHOD

Single crystals were grown using the self-flux method, as described elsewhere [19]. Raman scattering measurements were performed on freshly cleaved ($\bar{1}$01)-oriented samples, using Jobin Yvon T64000 Raman system, equipped with a nitrogen-cooled CCD detector, in the backscattering micro-Raman configuration. The 532 nm line of a solid state laser was used as an excitation source. A microscope objective with

50× magnification was used for focusing the laser beam. All measurements were performed at low laser power, to reduce local heating of the sample. For low temperature measurements KONTI CryoVac continuous flow cryostat with 0.5 mm thick window was used. All spectra were corrected for the Bose factor. For extracting the data from the Raman spectra, phonon modes were fitted with a Lorentzian profile.

The electronic structure is calculated for stoichiometric TaFeTe$_3$ in the paramagnetic phase within the density functional theory (DFT), and the phonon frequencies at the $\Gamma$-point are obtained within the density functional perturbation theory (DFPT) [39], using the QUANTUM ESPRESSO package [40]. We have used projector augmented wave (PAW) pseudopotentials with Perdew-Burke-Ernzerhof (PBE) exchange-correlation functional with nonlinear core correction and Gaussian smearing of 0.01 Ry. The electron wave function and the density energy cutoffs were 64 Ry and 782 Ry, respectively. The Brillouin zone is sampled with $8 \times 8 \times 8$ Monkhorst-Pack $k$-space mesh. The phonon frequencies were calculated with the unit cell size taken from the experiments and the relaxed positions of atoms within the unit cell. The forces acting on individual atoms in the relaxed configuration were smaller than $10^{-4}$ Ry/a.u.

## III. RESULTS AND DISCUSSION

TaFe$_{1+y}$Te$_3$ crystallizes in the monoclinic crystal structure, which is shown in Fig. 1. The space group is $P2_1/m$ (unique axis $b$), with two formula units per unit cell [19,20]. The experimental values of the unit cell parameters are $a = 7.436$ Å, $b = 3.638$ Å, $c = 10.008$ Å, and $\beta = 109.17°$. All atoms (including the excess Fe), are at $2e$ Wyckoff positions, with fractional coordinates given in Table I.

The factor group analysis (FGA) for $P2_1/m$ space group yields the following normal mode distribution at the $\Gamma$ point:

$$\Gamma_{\text{Raman}} = 10A_g + 5B_g,$$
$$\Gamma_{\text{IR}} = 4A_u + 8B_u,$$
$$\Gamma_{\text{acoustic}} = A_u + 2B_u.$$

The Raman spectra were measured from the ($\bar{1}$01) plane of the sample, which is the natural cleavage plane [23,42]. From the Raman tensors given in Table II, the $A_g$ phonon modes are expected to be observable in the $(xx)$ and $(yy)$ scattering configurations. The $B_g$ modes can be observed only in $(xy)$ polarization configuration.

TABLE I. Experimental fractional coordinates of TaFe$_{1.25}$Te$_3$ taken from Ref. [19]. In the parentheses are the calculated values for TaFeTe$_3$.

| Atom type | $x$ | $y$ | $z$ |
|---|---|---|---|
| Ta | 0.8340 (0.8331) | 0.25 | 0.3007 (0.2987) |
| Fe1 | 0.6147 (0.6223) | −0.25 | 0.0890 (0.0988) |
| Fe2 | 0.7686 | 0.25 | −0.0047 |
| Te1 | 0.4392 (0.4326) | 0.25 | 0.1860 (0.1637) |
| Te2 | 0.9835 (0.9842) | −0.25 | 0.1589 (0.1584) |
| Te3 | 0.2179 (0.2192) | 0.25 | 0.4970 (0.5028) |

TABLE II. Upper panel: atomic species (all of them are at $2e$ Wyckoff positions) and the contribution of each atom to the $\Gamma$-point phonons, the corresponding Raman tensors for the TaFeTe$_3$ single crystal ($P2_1/m$ space group) [41]. Lower panel: the calculated (for the stoichiometric TaFeTe$_3$) and experimental phonon energies at 100 K (for the TaFe$_{1.25}$Te$_3$ single crystal).

| Atoms | | | Irreducible representations | | |
|---|---|---|---|---|---|
| Ta, Fe1, Te1, Te2, Te3 | | | $2A_g + A_u + B_g + 2B_u$ | | |

Raman tensors

$$\hat{R}_{A_g} = \begin{pmatrix} a & 0 & d \\ 0 & b & 0 \\ d & 0 & c \end{pmatrix} \qquad \hat{R}_{B_g} = \begin{pmatrix} 0 & e & 0 \\ e & 0 & f \\ 0 & f & 0 \end{pmatrix}$$

| Raman active | | | Infrared active | | |
|---|---|---|---|---|---|
| Symmetry | Calc. (cm$^{-1}$) | Expt. (cm$^{-1}$) | Symmetry | Calc. (cm$^{-1}$) | Expt. (cm$^{-1}$) |
| $A_g^1$ | 36.2 | | $A_u^1$ | 42.8 | |
| $B_g^1$ | 43.8 | | $B_u^1$ | 54.9 | |
| $B_g^2$ | 57.9 | 61.6 | $B_u^2$ | 94.4 | |
| $A_g^2$ | 63.8 | 62.3 | $A_u^2$ | 101.4 | |
| $A_g^3$ | 75.3 | 68.5 | $B_u^3$ | 111.3 | |
| $A_g^4$ | 104.4 | 90 | $A_u^3$ | 131.1 | |
| $B_g^3$ | 105.1 | | $B_u^4$ | 143.2 | |
| $A_g^5$ | 124.6 | | $B_u^5$ | 160.4 | |
| $B_g^4$ | 127.2 | 130.4 | $B_u^6$ | 188.6 | |
| $A_g^6$ | 149.8 | 155 | $B_u^7$ | 227.9 | |
| $A_g^7$ | 164.9 | 165 | $A_u^4$ | 231.1 | |
| $A_g^8$ | 191 | | $B_u^8$ | 289.4 | |
| $B_g^5$ | 217.1 | 222.3 | | | |
| $A_g^9$ | 241.9 | 223.9 | | | |
| $A_g^{10}$ | 276.22 | | | | |

Raman scattering spectra of TaFe$_{1.25}$Te$_3$ single crystals, measured at 100 K in three different polarization configurations, are presented in Fig. 2. By using the selection rules, we assign the Raman peaks appearing in the ($xx$) and ($yy$) polarization configuration as the $A_g$ ones. This conclusion is supported by the lattice dynamics calculations, given in Table II. By comparing the calculated values of $A_g$ mode energies with those of the peaks appearing in the ($xx$) and ($yy$) spectra, we can unambiguously assign four Raman modes ($A_g^4$, $A_g^6$, $A_g^7$, and $A_g^9$). The broad structure around 65 cm$^{-1}$ probably originates from the $A_g^2$ and $A_g^3$ modes, although the contribution of the $A_g^1$ mode (with calculated energy of 42.7 cm$^{-1}$) cannot be excluded. The peaks at 57.9 cm$^{-1}$ and 130 cm$^{-1}$ that are clearly visible in ($xy$) but absent in ($yy$) configuration are assigned as $B_g^2$ and $B_g^4$ modes, respectively. The low intensity peak at $\approx 220$ cm$^{-1}$, that becomes clearly observable at low temperatures, is tentatively assigned as $B_g^5$ mode, although the contribution from the leakage of $A_g^9$ mode cannot be excluded. The origin of the two very broad structures at about 70 cm$^{-1}$ and 160 cm$^{-1}$, which are pronounced in the ($xy$) configuration, is not completely clear. Aside from providing additional charge, Fe2 atoms may contribute to momentum transfer scattering, in line with the pronounced quasielastic continuum, present in all the scattering configurations. Consequently, contribution from single-phonon scattering away from $\Gamma$ point becomes observable, which is theoretically predicted [43,44] and experimentally observed

[45,46]. Although we cannot exclude the possibility of two- and, in particular, double-phonon contributions, we believe it is less likely due to the nature of the processes and since they usually have more pronounced contribution to $A$ channel (for arbitrary irreducible symmetry $\mu$ of $C_{2h}$ holds $\mu \otimes \mu \ni A$).

The normal modes of the selected $A_g$ and $B_g$ vibrations, as obtained by the lattice dynamics calculations, are shown in Fig. 3. The low energy $B_g^2$ mode represents vibrations of Te and Ta atoms which tend to elongate the (Ta,Fe)Te tetrahedra in the $xy$ plane. $B_g^4$ phonon originates mainly from Ta and Te atom vibrations in directions opposite to each other, whereas $A_g^4$ mode represents dominantly vibrations of another Te atom in the $xy$ plane. $A_g^7$ and $A_g^9$ modes originate from the vibrations of Fe and Te atoms which tend to rotate the tetrahedra around the $x$ axis.

The DFT calculations are in very good agreement with the measured Raman spectra, specially having in mind the strength of electronic correlations in iron based compounds and the presence of additional Fe2 atoms in the measured sample. We restricted to the nonmagnetic DFT calculations. This is because small changes in the phonon energies due to the magnetic ordering cannot be reliably captured since the DFT does not treat strong correlation and spin-fluctuations effects. Our DFT calculations for the electronic band structure agree with the results from Ref. [42]. The calculated electronic dispersions are in rather good agreement with the ARPES measurements [42], which indicates that the main effect of the interstitial Fe2 ion is to provide additional charge and shift
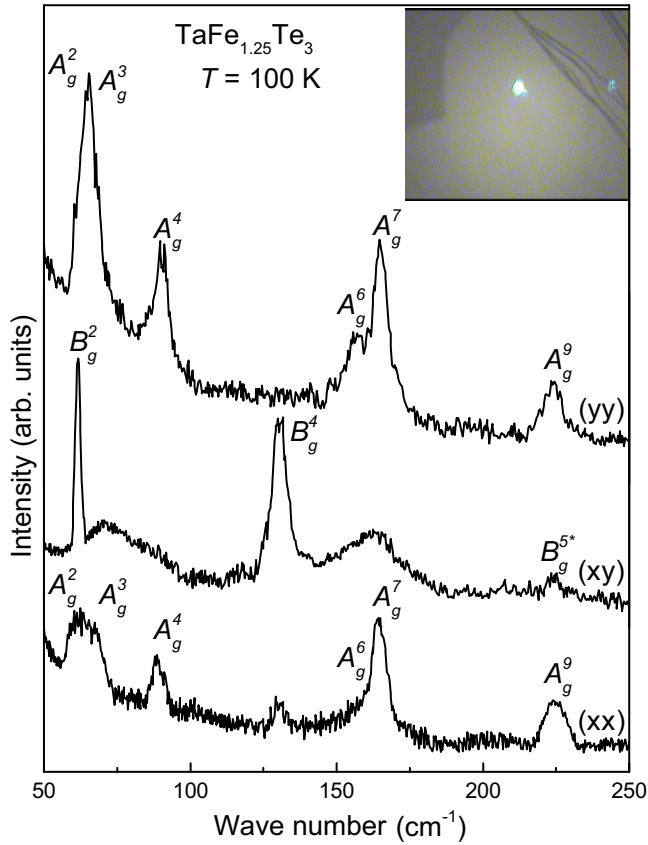
FIG. 2. Polarized Raman scattering spectra of TaFe$_{1.25}$Te$_3$ single crystal measured at 100 K in various polarizations. The notation in parentheses indicates the polarization directions of the incident and scattered light according to Fig. 1(a). Inset: surface of the probed TaFe$_{1.25}$Te$_3$ single crystal.

the Fermi level. This conclusion is supported with a small difference between the relaxed and experimental fractional coordinates; see Table I.
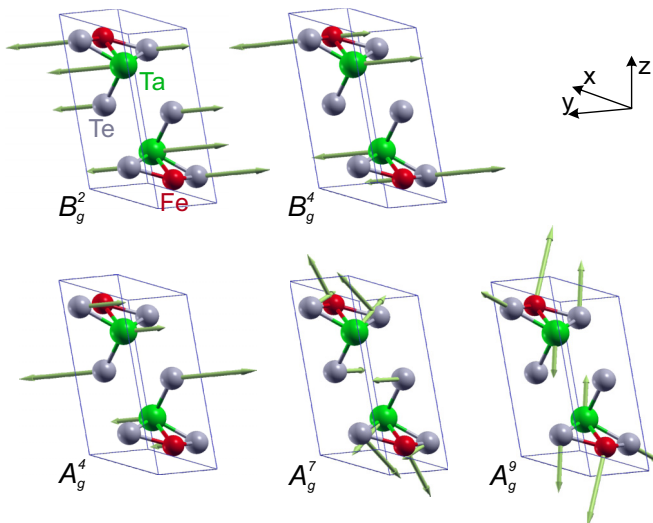


FIG. 3. Unit cell of TaFeTe$_3$ single crystal with the displacement patterns of several $A_g$ and $B_g$ Raman modes. Arrow lengths are proportional to the square root of the interatomic forces.
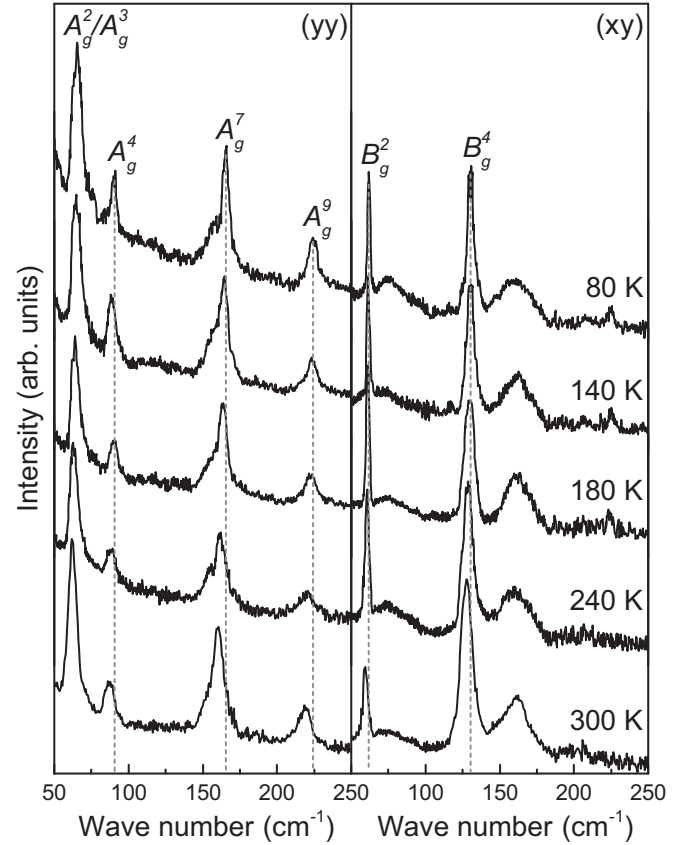


FIG. 4. Temperature dependent Raman scattering spectra of TaFe$_{1.25}$Te$_3$ single crystal in the $(yy)$ (left panel) and $(xy)$ (right panel) polarization.

In order to analyze the changes of the Raman spectra near the AFM transition at $T_N \approx 200$ K, we have performed measurements in a temperature range from 80 K up to 300 K. Raman spectra of TaFe$_{1.25}$Te$_3$ single crystal, measured at different temperatures in the $(yy)$ and $(xy)$ scattering configurations, are given in Fig. 4. In the following, we perform the temperature analysis of the energy and the linewidth for five most clearly observed modes.

The temperature dependence of the Raman mode energy is usually described with [47,48]

$$\omega_i(T) = \omega_{0,i} + \Delta_i^V(\gamma_i, \alpha_i(T)) + \Delta_i^A(C_i), \qquad (1)$$

where $\omega_{0,i}$ is a temperature independent contribution to the Raman mode energy. The second term represents a change of the phonon energy induced by the lattice thermal expansion and depends on the Grüneisen parameter $\gamma_i$ and the thermal expansion coefficient $\alpha_i(T)$. The term $\Delta_i^A$ describes the anharmonicity induced change of the Raman mode energy which is a function of the anharmonic constant $C_i$. Both $\Delta_i^V$ and $\Delta_i^A$ have qualitatively the same temperature dependence. Since there are no reported experimental data on the temperature dependence of the lattice parameters for TaFe$_{1+y}$Te$_3$, we didn't attempt to fit the data, and the black dotted lines in Figs. 5 and 6 are guides to the eye. The $\omega_i(T)$ curves follow the "standard" [5,15,37,49,50] continuous decrease in energy with temperature, with very small anomalies near $T_N$ except for the $A_g^4$ mode.
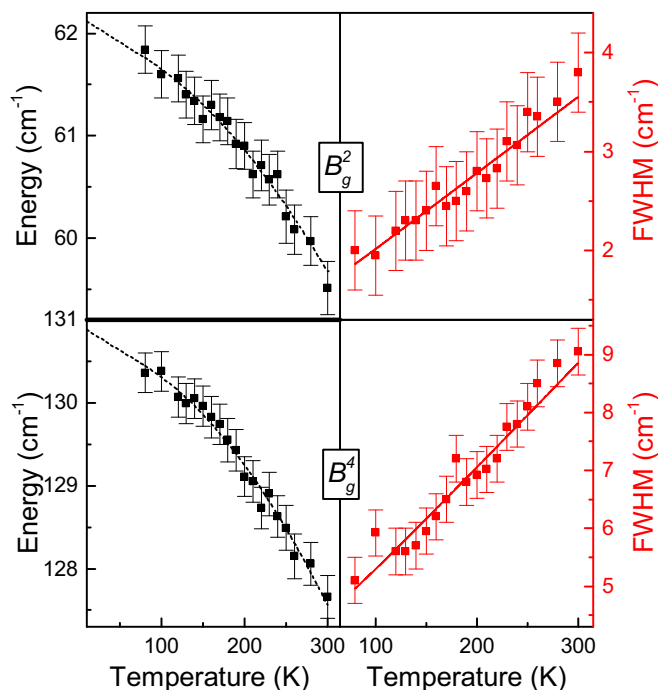
FIG. 5. Temperature dependence of the energy and linewidth for the $B_g^2$ and $B_g^4$ Raman modes of the $TaFe_{1.25}Te_3$ single crystal. The red lines are fitted according to Eq. (2), whereas black lines are guides to the eye.

The temperature dependences of the linewidth of selected $B_g$ and $A_g$ modes are given in the right panels of Figs. 5 and 6, respectively. While the $B_g^2$ and $B_g^4$ phonon modes do not show significant deviation from the usual behavior due to the anharmonicity effects, with gradual broadening with increasing temperature, the $A_g^4$, $A_g^7$, and $A_g^9$ modes exhibit moderate additional broadening above 200 K. The red lines present a fit to the standard formula for the temperature dependent linewidth due to the anharmonicity [11,47,51]:

$$\Gamma_i(T) = \Gamma_{0,i}\left(1 + \frac{2}{e^{\hbar\omega_{0,i}/2k_BT} - 1}\right) + A_i, \qquad (2)$$

where $\Gamma_{0,i}$ is the anharmonic constant and $A_i$ is the constant term due to the disorder and electron-phonon interaction [52]. The deviation from these anharmonicity curves is most pronounced around $T_N$ (see the insets of Fig. 6).

We can observe that all Raman modes have moderate linewidth and exhibit small anomalies near $T_N$. This shows that the phase transition is continuous, in agreement with the thermodynamic and transport measurements [22]. Small anomalies in the phonon spectra, which are restricted only to the vicinity of the phase transition, imply that the electron-phonon interaction of Raman active modes does not change with temperature. This is in agreement with the recent ARPES measurements which show negligible change of the Fermi surface across the AFM transition [42], indicating that the magnetic transition is not driven by the Fermi surface instability. The anomalies in the linewidth of some phonon modes near $T_N$ are likely the signature of the increased scattering by spin fluctuations near the phase transition [51,53].
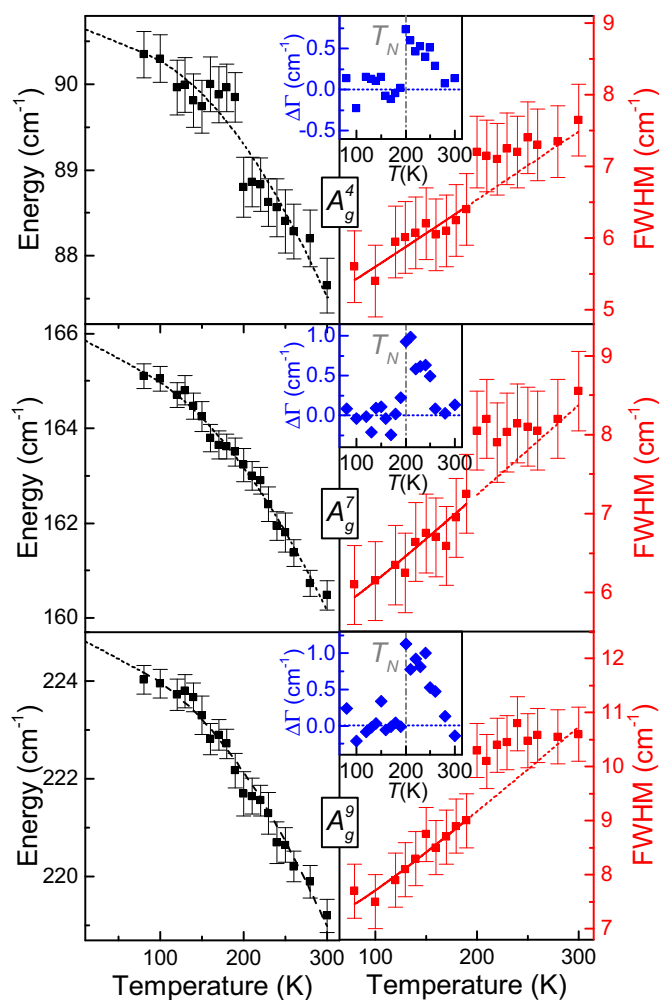


FIG. 6. Energy and linewidth of the $A_g^4$, $A_g^7$, and $A_g^9$ Raman modes of the $TaFe_{1.25}Te_3$ single crystal as a function of temperature. The red lines are plotted according to Eq. (2), and the black dotted lines are guides to the eye. The insets represent deviations of the Raman mode linewidth from the anharmonic form.

The density of states (DOS) at the Fermi level is not large. This can be concluded from the ARPES experiments [42] which have shown three bands crossing the Fermi level but with strong dispersion, while several relatively flat bands are found only well below the Fermi level. The DFT calculations also give moderate values for the DOS, $N(E_F) \approx 1\,\text{eV}^{-1}/\text{f.u.}$, after the Fermi level is shifted due to the additional charge provided by the Fe2 atoms. This value for the DOS also suggests that the electron-phonon coupling is not strong in $TaFe_{1.25}Te_3$, since it is proportional to $N(E_F)$.

$TaFe_{1.25}Te_3$ has a similar moment size as $Fe_{1+y}Te$, $\approx 2\mu_B/Fe$. However, the differences in the magnetic ordering and crystal structure cause different phonon properties of these two compounds. Namely, the phonon lines in the Raman spectra of $Fe_{1+y}Te$ have very large linewidth and pronounced anomalies both in the frequency and in the linewidth near the first order phase transition [11,13]. Small anomalies in the Raman spectra of $TaFe_{1.25}Te_3$ as compared to $Fe_{1+y}Te$ can be ascribed to the continuous, second order nature of the AFM transition and smaller electron-phonon coupling due to lower DOS at the

Fermi level. Also, the monoclinic angle $\beta$ in the TaFe$_{1.25}$Te$_3$ unit cell significantly differs from $90°$ and therefore the form of the vibrational modes is different.

## IV. CONCLUSION

In summary, we have performed the Raman scattering study of the zigzag spin chain TaFe$_{1.25}$Te$_3$ single crystal, together with the lattice dynamics calculations of TaFeTe$_3$. By analyzing the Raman spectra in different polarization configurations and using numerical calculations we have assigned nine Raman active modes predicted by the FGA. Very good agreement between the experimental frequencies and those calculated for the stoichiometric compound shows that the excess iron atoms weakly influence the phonon energies but provide momentum conservation for the phonon scattering away from $\Gamma$ point. The temperature dependence of the frequency and the linewidth of the $B_g$ Raman modes looks conventional, governed by the anharmonicity effects. While in a broad temperature range the behavior of the $A_g$ modes is also conventional, there are clear anomalies near the AFM transition. The anomalies in the frequency and the linewidth are in the form of small kinks near $T_N$. This implies that the electron-phonon interaction and the DOS at the Fermi level are approximately constant in the measured temperature range. The increase in the linewidth near $T_N$ is likely due to the coupling of spin fluctuations and vibration near the second order phase transition.

[1] Y. Kamihara, T. Watanabe, M. Hirano, and H. Hosono, J. Am. Chem. Soc. **130**, 3296 (2008).

[2] L. Ma, G. F. Ji, J. Dai, X. R. Lu, M. J. Eom, J. S. Kim, B. Normand, and W. Yu, Phys. Rev. Lett. **109**, 197002 (2012).

[3] B. Wei, H. Qing-Zhen, C. Gen-Fu, M. A. Green, W. Du-Ming, H. Jun-Bao, and Q. Yi-Ming, Chin. Phys. Lett. **28**, 086104 (2011).

[4] G. R. Stewart, Rev. Mod. Phys. **83**, 1589 (2011).

[5] M. Opačić, N. Lazarević, M. M. Radonjić, M. Šćepanović, H. Ryu, A. Wang, D. Tanasković, C. Petrovic, and Z. V. Popović, J. Phys.: Condens. Matter **28**, 485401 (2016).

[6] Z. S. Gönen, P. Fournier, V. Smolyaninova, R. Greene, F. M. Araujo-Moreira, and B. Eichhorn, Chem. Mater. **12**, 3331 (2000).

[7] H. Lei, H. Ryu, A. I. Frenkel, and C. Petrovic, Phys. Rev. B **84**, 214511 (2011).

[8] F. Han, X. Wan, B. Shen, and H.-H. Wen, Phys. Rev. B **86**, 014411 (2012).

[9] M. H. Fang, H. M. Pham, B. Qian, T. J. Liu, E. K. Vehstedt, Y. Liu, L. Spinu, and Z. Q. Mao, Phys. Rev. B **78**, 224503 (2008).

[10] S. Li, C. de la Cruz, Q. Huang, Y. Chen, J. W. Lynn, J. Hu, Y.-L. Huang, F.-C. Hsu, K.-W. Yeh, M.-K. Wu, and P. Dai, Phys. Rev. B **79**, 054503 (2009).

[11] V. Gnezdilov, Y. Pashkevich, P. Lemmens, A. Gusev, K. Lamonova, T. Shevtsova, I. Vitebskiy, O. Afanasiev, S. Gnatchenko, V. Tsurkan, J. Deisenhofer, and A. Loidl, Phys. Rev. B **83**, 245127 (2011).

[12] Y. J. Um, A. Subedi, P. Toulemonde, A. Y. Ganin, L. Boeri, M. Rahlenbeck, Y. Liu, C. T. Lin, S. J. E. Carlsson, A. Sulpice, M. J. Rosseinsky, B. Keimer, and M. Le Tacon, Phys. Rev. B **85**, 064519 (2012).

[13] Z. V. Popović, N. Lazarević, S. Bogdanović, M. M. Radonjić, D. Tanasković, R. Hu, H. Lei, and C. Petrovic, Solid State Commun. **193**, 51 (2014).

[14] K.-Y. Choi, D. Wulferding, P. Lemmens, N. Ni, S. L. Bud'ko, and P. C. Canfield, Phys. Rev. B **78**, 212503 (2008).

[15] M. Rahlenbeck, G. L. Sun, D. L. Sun, C. T. Lin, B. Keimer, and C. Ulrich, Phys. Rev. B **80**, 064509 (2009).

[16] F. Chen, M. Xu, Q. Q. Ge, Y. Zhang, Z. R. Ye, L. X. Yang, J. Jiang, B. P. Xie, R. C. Che, M. Zhang, A. F. Wang, X. H. Chen, D. W. Shen, J. P. Hu, and D. L. Feng, Phys. Rev. X **1**, 021020 (2011).

[17] W. Li, H. Ding, P. Deng, K. Chang, C. Song, K. He, L. Wang, X. Ma, J.-P. Hu, P. Chen, and Q.-K. Xue, Nat. Phys. **8**, 126 (2012).

[18] N. Lazarević, M. Abeykoon, P. W. Stephens, H. Lei, E. S. Bozin, C. Petrovic, and Z. V. Popović, Phys. Rev. B **86**, 054503 (2012).

[19] M. Badding, J. Li, F. DiSalvo, W. Zhou, and P. Edwards, J. Solid State Chem. **100**, 313 (1992).

[20] J. Neuhausen, E. Potthoff, W. Tremel, J. Ensling, P. Gütlich, and R. Kremer, Z. Naturforsch. B **48**, 797 (1993).

[21] C. Perez Vicente, M. Womes, J. C. Jumas, L. Sanchez, and J. L. Tirado, J. Phys. Chem. B **102**, 8712 (1998).

[22] R. H. Liu, M. Zhang, P. Cheng, Y. J. Yan, Z. J. Xiang, J. J. Ying, X. F. Wang, A. F. Wang, G. J. Ye, X. G. Luo, and X. H. Chen, Phys. Rev. B **84**, 184432 (2011).

[23] X. Ke, B. Qian, H. Cao, J. Hu, G. C. Wang, and Z. Q. Mao, Phys. Rev. B **85**, 214404 (2012).

[24] E. Dagotto, Rev. Mod. Phys. **85**, 849 (2013).

[25] W. Li, C. Setty, X. H. Chen, and J. Hu, Front. Phys. **9**, 465 (2014).

[26] E. Dagotto, J. Riera, and D. Scalapino, Phys. Rev. B **45**, 5744 (1992).

[27] E. Dagotto and T. M. Rice, Science **271**, 618 (1996).

[28] E. Dagotto, Rep. Prog. Phys. **62**, 1525 (1999).

[29] M. Uehara, T. Nagata, J. Akimitsu, H. Takahashi, N. Môri, and K. Kinoshita, J. Phys. Soc. Jpn. **65**, 2764 (1996).

[30] A. Hisada, K. Matsubayashi, Y. Uwatoko, N. Fujiwara, G. Deng, E. Pomjakushina, K. Conder, D. M. Radheep, R. Thiyagarajan, S. Esakkimuthu, and S. Arumugam, J. Phys. Soc. Jpn. **83**, 073703 (2014).

[31] H. Takahashi, A. Sugimoto, Y. Nambu, T. Yamauchi, Y. Hirata, T. Kawakami, M. Avdeev, K. Matsubayashi, F. Du, C. Kawashima, H. Soeda, S. Nakano, Y. Uwatoko, Y. Ueda, T. J. Sato, and K. Ohgushi, Nat. Mater. **14**, 1008 (2014).

[32] A.-M. Zhang and Q.-M. Zhang, Chin. Phys. B **22**, 087103 (2013).

[33] M. Opačić and N. Lazarević, J. Serb. Chem. Soc. **82**, 957 (2017).

[34] L. Zhang, T. Fujita, F. Chen, D. L. Feng, S. Maekawa, and M. W. Chen, Phys. Rev. B **79**, 052507 (2009).

[35] Y. Gallais, A. Sacuto, M. Cazayous, P. Cheng, L. Fang, and H. H. Wen, Phys. Rev. B **78**, 132509 (2008).

[36] V. Gnezdilov, Y. G. Pashkevich, P. Lemmens, D. Wulferding, T. Shevtsova, A. Gusev, D. Chareev, and A. Vasiliev, Phys. Rev. B **87**, 144508 (2013).

[37] A. P. Litvinchuk, B. Lv, and C. W. Chu, Phys. Rev. B **84**, 092504 (2011).

[38] K.-Y. Choi, P. Lemmens, I. Eremin, G. Zwicknagl, H. Berger, G. L. Sun, D. L. Sun, and C. T. Lin, J. Phys.: Condens. Matter **22**, 115802 (2010).

[39] S. Baroni, S. de Gironcoli, A. Dal Corso, and P. Giannozzi, Rev. Mod. Phys. **73**, 515 (2001).

[40] P. Gianozzi, S. Baroni, N. Bonini, M. Calandra, R. Car, C. Cavazzoni, D. Ceresoli, G. L. Chiarotti, M. Cococcioni, I. Dabo, A. D. Corso, S. de Gironcoli, S. Fabris, G. Fratesi, R. Gebauer, U. Gerstmann, C. Gougoussis, A. Kokalj, M. Lazzeri, L. Martin-Samos, N. Marzari, F. Mauri, R. Mazzarello, S. Paolini, A. Pasquarello, L. Paulatto, C. Sbraccia, S. Scandolo, G. Sclauzero, A. P. Seitsonen, A. Smogunov, P. Umari, and R. M. Wentzcovitch, J. Phys.: Condens. Matter **21**, 395502 (2009).

[41] D. L. Rousseau, R. P. Bauman, and S. P. S. Porto, J. Raman Spectrosc. **10**, 253 (1981).

[42] X. Min, W. Li-Min, P. Rui, G. Qing-Qin, C. Fei, Y. Zi-Rong, Z. Yan, C. Su-Di, X. Miao, L. Rong-Hua, M. Arita, K. Shimada, H. Namatame, M. Taniguchi, M. Matsunami, S. Kimura, S. Ming, C. Xian-Hui, Y. Wei-Guo, K. Wei, X. Bin-Ping, and F. Dong-Lai, Chin. Phys. Lett. **32**, 027401 (2015).

[43] R. Shuker and R. W. Gammon, Phys. Rev. Lett. **25**, 222 (1970).

[44] P. Benassi, O. Pilla, V. Mazzacurati, M. Montagna, G. Ruocco, and G. Signorelli, Phys. Rev. B **44**, 11734 (1991).

[45] H. Ryu, M. Abeykoon, K. Wang, H. Lei, N. Lazarevic, J. B. Warren, E. S. Bozin, Z. V. Popovic, and C. Petrovic, Phys. Rev. B **91**, 184503 (2015).

[46] B.-B. Zhang, N. Zhang, S.-T. Dong, Y. Lv, Y. B. Chen, S. Yao, S.-T. Zhang, Z.-B. Gu, J. Zhou, I. Guedes, D. Yu, and Y.-F. Chen, AIP Adv. **5**, 087111 (2015).

[47] J. Menéndez and M. Cardona, Phys. Rev. B **29**, 2051 (1984).

[48] H.-M. Eiter, P. Jaschke, R. Hackl, A. Bauer, M. Gangl, and C. Pfleiderer, Phys. Rev. B **90**, 024411 (2014).

[49] N. Lazarević, M. Radonjić, M. Šćepanović, H. Lei, D. Tanasković, C. Petrovic, and Z. V. Popović, Phys. Rev. B **87**, 144305 (2013).

[50] M. Opačić, N. Lazarević, M. Šćepanović, H. Ryu, H. Lei, C. Petrovic, and Z. V. Popović, J. Phys.: Condens. Matter **27**, 485701 (2015).

[51] M. N. Iliev, A. P. Litvinchuk, H.-G. Lee, C. W. Chu, A. Barry, and J. M. D. Coey, Phys. Rev. B **60**, 33 (1999).

[52] N. Lazarević, Z. V. Popović, R. Hu, and C. Petrovic, Phys. Rev. B **81**, 144302 (2010).

[53] M. N. Iliev, A. P. Litvinchuk, H.-G. Lee, C. L. Chen, M. L. Dezaneti, C. W. Chu, V. G. Ivanov, M. V. Abrashev, and V. N. Popov, Phys. Rev. B **59**, 364 (1999).

# Phonon anomalies in FeS

A. Baum,[1,2] A. Milosavljević,[3] N. Lazarević,[3] M. M. Radonjić,[4] B. Nikolić,[5] M. Mitschek,[1,2,*] Z. Inanloo Maranloo,[1,†]
M. Šćepanović,[3] M. Grujić-Brojčin,[3] N. Stojilović,[3,6] M. Opel,[1] Aifeng Wang (王爱峰),[7] C. Petrovic,[7]
Z. V. Popović,[3,8] and R. Hackl[1]

[1]*Walther Meissner Institut, Bayerische Akademie der Wissenschaften, 85748 Garching, Germany*
[2]*Fakultät für Physik E23, Technische Universität München, 85748 Garching, Germany*
[3]*Center for Solid State Physics and New Materials, Institute of Physics Belgrade, University of Belgrade,
Pregrevica 118, 11080 Belgrade, Serbia*
[4]*Scientific Computing Laboratory, Center for the Study of Complex Systems, Institute of Physics Belgrade, University of Belgrade,
Pregrevica 118, 11080 Belgrade, Serbia*
[5]*Faculty of Physics, University of Belgrade, Studentski trg 12, Belgrade, Serbia*
[6]*Department of Physics and Astronomy, University of Wisconsin Oshkosh, Oshkosh, Wisconsin 54901, USA*
[7]*Condensed Matter Physics and Materials Science Department, Brookhaven National Laboratory, Upton, New York 11973-5000, USA*
[8]*Serbian Academy of Sciences and Arts, Knez Mihailova 35, 11000 Belgrade, Serbia*

We present results from light scattering experiments on tetragonal FeS with the focus placed on lattice dynamics. We identify the Raman active $A_{1g}$ and $B_{1g}$ phonon modes, a second order scattering process involving two acoustic phonons, and contributions from potentially defect-induced scattering. The temperature dependence between 300 and 20 K of all observed phonon energies is governed by the lattice contraction. Below 20 K the phonon energies increase by 0.5–1 $cm^{-1}$, thus indicating putative short range magnetic order. Along with the experiments we performed lattice-dynamical simulations and a symmetry analysis for the phonons and potential overtones and find good agreement with the experiments. In particular, we argue that the two-phonon excitation observed in a gap between the optical branches becomes observable due to significant electron-phonon interaction.

## I. INTRODUCTION

In the iron based superconductors (IBS) magnetic order, structure, nematicity, and superconductivity are closely interrelated. Upon substituting atoms in the parent compounds the properties change in a way that the shape of the Fermi surface is generally believed to play a crucial role. Yet, the magnetic properties were found recently to be more complex and to depend also on the degree of correlation in the individual $d$ orbitals contributing to the density of states close to the Fermi surface [1–3].

The influence of correlation effects seems to increase from the 122 systems such as $BaFe_2As_2$ to the 11 chalcogenides FeTe, FeSe, and FeS [4,5]. Surprisingly, the properties of the 11 class members differ substantially although they are isostructural and isoelectronic [3,6]: FeSe undergoes a structural transition at $T_s \sim 90$ K and displays electronic nematicity [7]. While long-range magnetic order cannot be observed down to the lowest temperatures [7–10] the thermodynamic properties and the Raman spectra strongly support the presence of short-ranged magnetism [11,12]. Below $T_c \sim 9$ K superconductivity is observed [13] in pristine FeSe. In mono-layer FeSe $T_c$ can reach values close to 100 K [14,15].

The replacement of Se by Te leads to slightly off-stoichiometric $Fe_{1+y}Te$ which exhibits a simultaneous magnetostructural transition near 67 K [16] but is not superconducting [17,18]. Finally, FeS having a superconducting transition at $T_c \sim 5$ K [19] remains tetragonal down to the lowest temperatures [20]. It is still an open question whether tetragonal FeS hosts magnetic order. Obviously, the iron-chalcogenides are at the verge of various neighboring phases and very susceptible to small changes in the lattice and electronic structure. Yet direct access to the competing phases is still very difficult in FeTe and FeS because of the variation of the crystal quality across the families.

Here, we choose a slightly different approach and do not look directly at the electronic but rather at the lattice properties in FeS close to potential instabilities and use the Raman-active phonons as probes. We identify the $A_{1g}$ and $B_{1g}$ modes, a two-phonon scattering process, and a fourth mode from either defect-induced scattering or second-order scattering as well. These results are in good agreement with numerical calculations. Furthermore the temperature dependence of all phononic modes supports the results reported in Refs. [21,22], where emerging short range magnetic order at approximately 20 K was reported.

## II. EXPERIMENT

Single crystals of FeS were synthesized as described elsewhere [23]. Before the experiment the samples were cleaved in air.

---

*Present address: Physikalisches Institut, Goethe Universität, 60438 Frankfurt am Main, Germany.

†Present address: Fakultät für Physik E21, Technische Universität München, 85748 Garching, Germany.
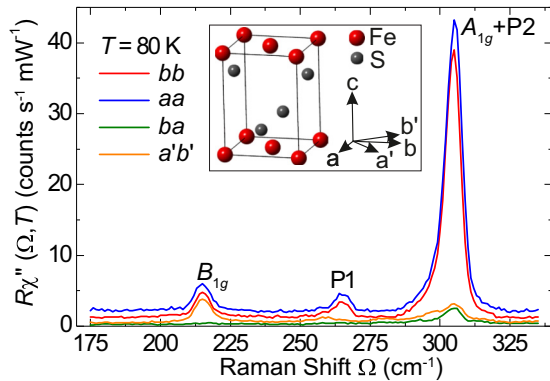
FIG. 1. Raman spectra of FeS at $T = 80$ K measured with light polarizations as indicated. The inset shows the crystal structure of FeS and the polarization directions with respect to the crystal orientation.

Calibrated customized Raman scattering equipment was used for the experiment. The samples were attached to the cold finger of a He-flow cryostat having a vacuum of approximately $5 \times 10^{-5}$ Pa. For excitation we used a diode-pumped solid state laser emitting at 575 nm (Coherent GENESIS). Polarization and power of the incoming light were adjusted in a way that the light inside the sample had the proper polarization state and, respectively, a power of typically $P_a = 3$ mW independent of polarization. The samples were mounted as shown in the inset of Fig. 1. The crystallographic axes are $a$ and $b$ with $|a| = |b|$. The $c$ axis is parallel to the optical axis. $a'$ and $b'$ are rotated by $45°$ with respect to $a$ and $b$. The laser beam reached the sample at an angle of incidence of $66°$ and was focused to a spot of approximately 50 $\mu$m diameter. The plane of incidence is the $bc$ plane. By choosing proper in-plane polarizations of the incident and scattered light the four symmetry channels $A_{1g}$, $A_{2g}$, $B_{1g}$, and $B_{2g}$ of the $D_{4h}$ space group can be accessed. Additionally, for the large angle of incidence, exciting photons being polarized along the $b$ axis have a finite $c$-axis projection and the $E_g$ symmetry can also be accessed. For the symmetry assignment we use the 2 Fe unit cell (crystallographic unit cell).

The observed phonon lines were analyzed quantitatively. Since the phonon lines are symmetric and $\Gamma_L(T) \ll \omega(T)$ the intrinsic line shape can be described by a Lorentz function with a central temperature dependent energy $\omega(T)$ and a width $\Gamma_L(T)$ (FWHM). The widths turn out to be comparable to the resolution $\sigma$ of the spectrometer. Therefore, the Lorentzian needs to be convoluted with a Gaussian having width $\Gamma_G \equiv \sigma$.

## III. THEORY

The electronic structure and the phonon dispersion were calculated using density functional theory (DFT) and density functional perturbation theory (DFPT), respectively, [24] within the QUANTUM ESPRESSO package [25]. The calculations were performed with the experimental unit cell parameters $a = 3.6735$ Å, $c = 5.0328$ Å, and $z = 0.2602$, where $z$ is the height of the sulfur atoms above the Fe plane in units of the $c$ axis [26]. We used the Vanderbilt ultrasoft pseudopotentials with the Becke-Lee-Yang-Parr (BLYP) exchange-correlation functional and $s$ and $p$ semicore states included in the valence for iron. The electron-wave-function and density energy cut-

offs were 70 Ry and 560 Ry, respectively, chosen to ensure stable convergence of the phonon modes. We used a Gaussian smearing of 0.01 Ry. The Brillouin zone was sampled with a $16 \times 16 \times 16$ Monkhorst-Pack $k$-space mesh. Our electronic structure and phonon calculations are in agreement with previously reported results [27,28].

The experimental positions of the S atoms entail a nonzero $z$ component of the force of $6 \times 10^{-2}$ Ry/$a_B$ acting on them with $a_B$ the Bohr radius. However, the relaxation of the $z$ positions of the S atoms would result in a large discrepancy between the calculated and experimental energies of the optical branches [28], whereas the phonon frequencies calculated from experimental structure parameters are in good agreement with the experiment (see Table II). When using the measured lattice parameters, including atomic positions, some of the acoustic phonons are unstable and do not have a linear dispersion at small **k**. Upon relaxing the atomic positions the acoustic dispersion becomes linear and the energies at the zone boundary decrease slightly. The energies of the optical branches, on the other hand, increase by some 10%. Having all this in mind, we choose to use the experimental lattice parameters stated above. In this sense our calculations should be understood as a compromise.

The phonon dispersion and the density of states were calculated on a $6 \times 6 \times 6$ Monkhorst-Pack $k$-point mesh, and the dispersion is interpolated along the chosen line. The calculated phonon dispersions of the experimental and relaxed structures qualitatively coincide and display similar shapes and a gap. Discrepancies only appear in the absolute energies.

The selection rules for two-phonon processes were calculated using the modified group projector technique (MGPT) [29], which avoids summing over an infinite set of space group elements.

## IV. RESULTS AND DISCUSSION

### A. Polarization dependence

Raman spectra of FeS for four linear polarization configurations at a sample temperature of $T = 80$ K are shown in Fig. 1. Three peaks can be identified at 215, 265, and 305 cm$^{-1}$. The symmetric peak at 215 cm$^{-1}$ shows up for $aa$, $bb$, and $a'b'$ polarizations, but vanishes for $ba$ polarization. Hence the excitation obeys $B_{1g}$ selection rules and can be identified as the out-of-phase vibration of iron atoms along the $c$ axis. The strongest slightly asymmetric peak at 305 cm$^{-1}$ obeys $A_{1g}$ selection rules with contributions of order 5% in $ba$ and $a'b'$ polarizations from either leakage or defect-induced scattering. An asymmetric Fano-type line shape can be acquired by coupling a phonon to an electronic continuum. However, as shown in Fig. 6 in the Appendixes, we find that the superposition of two symmetric, yet spectrally unresolved peaks gives a better agreement with the data than the description in terms of a Fano function. The stronger peak at 305 cm$^{-1}$ has $A_{1g}$ symmetry with some remaining leakage. We therefore identify this mode with the in-phase vibration of sulfur atoms along the $c$ axis. The second peak, labeled P2, appears in spectra with parallel light polarizations and vanishes in $ba$, but has some contribution in $a'b'$ polarizations, suggesting mixed $A_{1g}$ and $B_{1g}$ symmetry. The third peak, labeled P1, is symmetric and appears only in
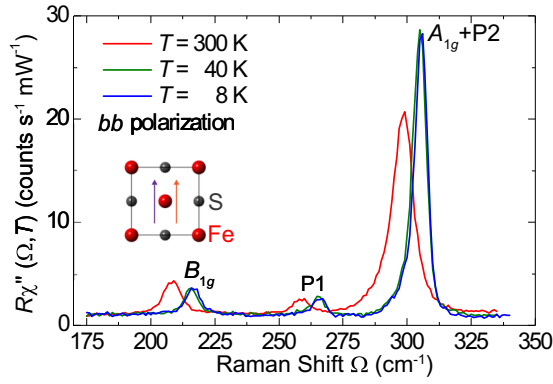
FIG. 2. Raman spectra of FeS in *bb* polarization projecting $A_{1g} + B_{1g} + E_g$ symmetries measured at temperatures given in the legend. The inset shows the light polarizations with respect to the crystal orientation.

spectra with parallel light polarizations and thus has pure $A_{1g}$ symmetry.

### B. Temperature dependence

For properly assigning all observed modes and for getting access to putative phase transitions we studied the temperature dependence. Figure 2 shows Raman spectra in *bb* polarization at 8, 40, and 300 K. The three peaks shift to higher energies upon cooling. The fourth peak P2 cannot be resolved in the raw data and can only be analyzed after a fitting procedure (see Appendix B). The peak energies $\omega(T)$ and the (intrinsic) linewidths $\Gamma_L(T)$ were determined as described at the end of Sec. II. All four modes show a monotonous increase in energy and decrease in linewidth upon cooling as shown in Fig. 3. Below 20 K the increase in the energies accelerates. We first address this overall behavior and disregard the anomaly around 50 K for the moment.

The shift and narrowing of all modes can be explained in terms of lattice contraction using a constant Grüneisen parameter $\gamma$ and anharmonic decay into other phonon modes, respectively. The change in the (Lorentzian) linewidth $\Gamma_L(T)$ is given by [30]

$$\Gamma_L(T) = \Gamma_{L,0}\left(1 + \frac{2\lambda_{ph\text{-}ph}}{\exp\left(\frac{\hbar\omega_0}{2k_BT}\right) - 1}\right). \quad (1)$$

The zero temperature limits $\Gamma_{L,0}$ and $\omega_0$ were obtained by extrapolating the respective experimental points of $\Gamma_L(T)$ and $\omega(T)$ in the range $20 \leqslant T \leqslant 50$ K to $T = 0$ (Fig. 3). With the phonon-phonon coupling $\lambda_{ph\text{-}ph}$ being the only free parameter the temperature dependence of $\Gamma_L(T)$ can be described as shown by red dashed lines in Fig. 3. The phonon energy $\omega(T)$ contains contributions from both the anharmonic decay and the lattice contraction, which depends essentially on the thermal occupation of the phonons, and can be written as [31]

$$\omega(T) = \omega_0\left[1 - \gamma\frac{V(T) - V_0}{V_0} - \left(\frac{\Gamma_{L,0}}{\sqrt{2}\omega_0}\right)^2\left(1 + \frac{4\lambda_{ph\text{-}ph}}{\exp\left(\frac{\hbar\omega_0}{2k_BT}\right) - 1}\right)\right]. \quad (2)$$
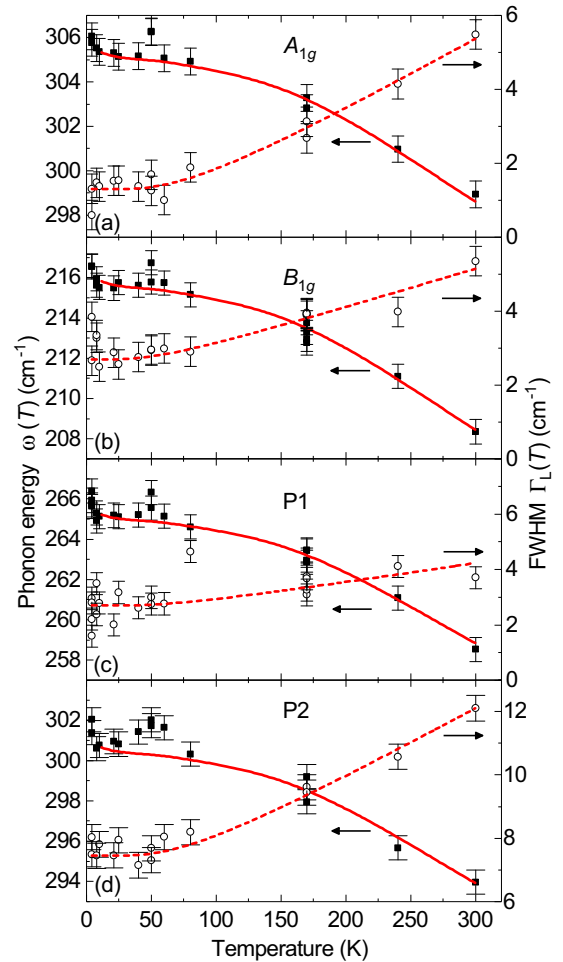


FIG. 3. Temperature dependence of energy and width of the four observed phonon modes in FeS. Black squares show the phonon energies $\omega$; open circles denote the phonon linewidths $\Gamma_L$. The red dashed and solid lines represent the temperature dependencies of the phonon linewidths and energies according to Eqs. (1) and (2), respectively. For better visualizing the low-temperature part, the data of this figure are plotted on a logarithmic temperature scale in Fig. 8 of Appendix D.

$V(T)$ and $V_0$ are the volumes of the unit cell at temperatures $T$ and $T \to 0$, respectively. The numbers for the calculations are taken from Ref. [20]. The second term describes the effect of phonon damping on the line position in the harmonic approximation. Using $\lambda_{ph\text{-}ph}$ from Eq. (1), the Grüneisen parameter $\gamma$ is the only free parameter and is assumed to be constant. The temperature dependencies $\omega(T)$ resulting from the fits are plotted in Fig. 3 as solid red lines. The numerical values for parameters $\gamma$ and $\lambda_{ph\text{-}ph}$ obtained from the $T$-dependent energy and linewidth are compiled in Table I.

Below 20 K and around 50 K anomalies are found in the experimental data as follows:

(i) At 50 K the peak energies of all four modes deviate significantly from the otherwise smooth temperature dependence. The nearly discontinuous increase in energy could be reproduced for the $A_{1g}$ phonon and peak P2 in multiple measurements. For the $B_{1g}$ phonon and mode P1 the anomaly is not as clearly reproducible. The energy anomalies do not

TABLE I. Symmetry, Grüneisen constant $\gamma$, and phonon-phonon coupling parameter $\lambda_{\text{ph-ph}}$ of the four experimentally observed modes.

| Mode | Symmetry | $\gamma$ | $\lambda_{\text{ph-ph}}$ |
|---|---|---|---|
| S | $A_{1g}$ | 2.2 | 1.68 |
| Fe | $B_{1g}$ | 3.4 | 0.31 |
| P1 | $A_{1g}$ | 2.4 | 0.25 |
| P2 | $A_{1g} + B_{1g}$ | 2.2 | 0.31 |

TABLE II. Raman active phonon modes in t-FeS. Shown are the symmetries, the theoretical predictions for the experimental lattice parameters at $T = 0$, and the atoms involved in the respective vibrations. The experimental energies in the third column are extrapolations to $T = 0$ of the points measured between 20 K and 50 K.

| Symmetry | Phonon energy (cm$^{-1}$) | | Atomic displacement |
|---|---|---|---|
| | Calculation | Experiment | |
| $A_{1g}$ | 316.1 | 305.3 | S |
| $B_{1g}$ | 220.4 | 215.8 | Fe |
| $E_g$ | 231.6 | | Fe, S |
| $E_g$ | 324.8 | | Fe, S |

have a correspondence in the linewidth. As there is neither an abrupt change in the lattice constants [20] nor any other known phase transition close to 50 K the origin of this anomaly remains unexplained although we consider it significant.

(ii) Upon cooling from 20 K to 4 K all four modes exhibit sudden, yet small, increases in energy. The changes in width are heterogeneous in that the $A_{1g}$ mode narrows and the $B_{1g}$ mode broadens. No clear tendencies can be derived for modes P1 and P2. Sudden changes in the temperature dependence typically indicate phase transitions. Yet, no phase transition has been identified so far. However, the anomaly at 20 K coincides with the emergence of short range magnetic order as inferred from two $\mu$SR studies [21,22]. Susceptibility measurements on a sample from the same batch were inconclusive. On the other hand, the XRD data show a small anomaly in the lattice parameters and the unit cell volume does not saturate at low temperature but rather decreases faster between 20 K and 10 K than above 20 K [20]. This volume contraction by and large reproduces the change in the phonon energies as can be seen by closely inspecting the low-temperature parts of Fig. 3 (see also Fig. 8). Hence the indications of short-range magnetism in FeS found by $\mu$SR have a correspondence in the temperature dependence of the volume and the phonon energies.

Clear phonon anomalies were observed at the onset of the spin density wave (SDW) phases in 122 systems [32–34] and of the more localized magnetic phase in FeTe [35], whereas continuous temperature dependence of the phonons was found in systems without long-range magnetism [36,37]. Upon entering the SDW state in the 122 systems the $A_{1g}$ (As) mode softens abruptly and narrows by a factor of 3, whereas the $B_{1g}$ (Fe) mode stays pinned and narrows only slightly [32]. The strong coupling of the As mode to magnetism was traced back to the interaction of the Fe magnetic moment with the Fe-As tetrahedra angle [38], which goes along with a change of the $c$-axis parameter. In Fe$_{1+y}$Te the roles of the $B_{1g}$ and $A_{1g}$ modes are interchanged [35,39,40]. In contrast, all four modes observed here in FeS harden below $T^* \approx 20$ K being indicative of a type of magnetic ordering apparently different from that in the other Fe-based systems.

Very recently, commensurate magnetic order with a wave vector of $\mathbf{q} = (0.25, 0.25, 0)$ was found in FeS below $T_\text{N} = 116$ K using neutron powder diffraction [41]. In the Raman spectra no anomalies can be seen around 120 K even if the range is studied with fine temperature increments of 10 K as shown in Appendix C. However, a small change in the temperature dependence of the $c$-axis parameter is observed around 100 K by XRD [20], which could be related to this type of magnetic order. Since the influence on the volume is small there is no detectable impact on the phonons.

## C. Analysis of the modes P1 and P2

Based on the energies, the selection rules, and the temperature dependence we first clarify the phononic nature of the two lines P1 and P2, which cannot as straightforwardly be identified as lattice vibrations as the in-phase sulfur and out-of-phase iron vibrations at 305.3 and 215.8 cm$^{-1}$. Second we derive their origin from the phonon density of states (PDOS) calculated for the zero-temperature limit.

All experimental energies for $T \rightarrow 0$ were derived from the points at low temperature as described in Sec. IV B (see also Fig. 3). The results for the modes at the $\Gamma$ point are summarized in Table II and can be directly compared to the results of the calculations. The discrepancies between the experimental and theoretical energies for the Raman-active phonons are smaller than 4%. The price for this accuracy in the optical energies is an instability and possibly too high energies in the acoustical branches at small and, respectively, large momentum (see Sec. III).

The unidentified peaks P1 and P2 appear in the spectra measured with $aa$ polarization, where none of the electric fields has a projection on the $c$ axis. Thus they cannot have $E_g$ symmetry obeying $ca$ and $cb$ selection rules. In addition, the observed energies would be relatively far off of the calculated energies (see Table II). Both peaks exhibit temperature dependencies similar to those of the two Raman-active phonons and the Grüneisen parameters are close to the typical value [42] of 2 and similar to those of the Raman-active phonons. The phonon-phonon coupling parameters $\lambda_{\text{ph-ph}}$ derived from the temperature dependence of the linewidths are close to 0.3 similar to that of the $B_{1g}$ phonon. $\lambda_{\text{ph-ph}}$ of the $A_{1g}$ phonon is roughly five times bigger for reasons we address later. Yet, because of the small prefactor $(\Gamma_{\text{L},0}/\sqrt{2}\omega_0)^2 = O(10^{-3})$, the contribution of phonon-phonon coupling to the temperature dependence of $\omega(T)$ remains negligible in all cases and the phonon energies are essentially governed by the lattice contraction. These considerations demonstrate the phononic origin of the peaks P1 and P2.

In the second step we try to identify the phonon branches to which P1 and P2 can be related. To this end the full phonon dispersion and density of states (PDOS) were derived as described in Sec. III and are plotted in Fig. 4.

Independent of using the relaxed or experimental structure, P1 is located in the gap of the (theoretical) PDOS and cannot result from first order defect-induced Raman scattering. What
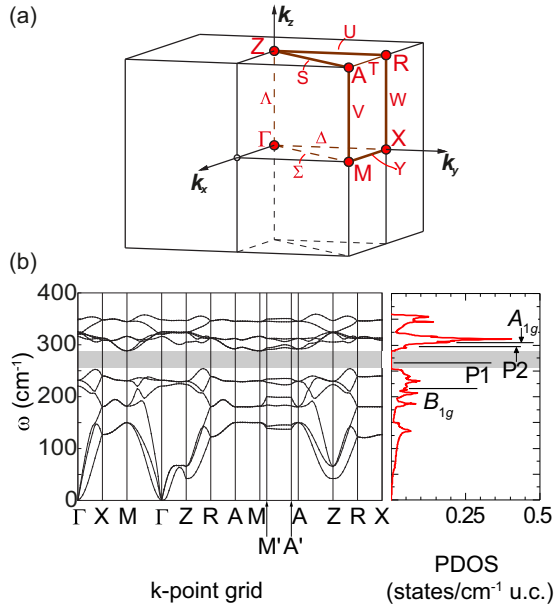
FIG. 4. Phonon dispersion of t-FeS. (a) Brillouin zone with high symmetry points and lines [43]. (b) Phonon dispersion along the directions as indicated and phonon density of states (PDOS). The gray-shaded area marks the gap in the phonon dispersion. The dispersion shown here is derived using experimental lattice parameters. For this reason some of the acoustic phonons are unstable and do not have a linear dispersion around the $\Gamma$ point. Upon relaxing the structure the acoustic dispersion becomes linear at $\Gamma$, and the energies at the zone boundary decrease slightly. The energies of the optical branches, on the other hand, increase by some 10%. $M' = (0.4, 0.4, 0.0)$ and $A' = (0.4, 0.4, 0.5)$. The experimental energies of the four observed modes are shown as black lines.

alternatives exist for explaining P1? If we exclude exotic explanations such as a collective mode for the reasons given above the energy of $\omega_{P1} = 265$ cm$^{-1}$ can only be obtained by the sum of two phonon modes having equal energy $\omega_{P1}/2$ and momenta **k** and $-$**k** (for maintaining the $q \approx 0$ selection rule). As shown for various transition metal compounds including TiN, ZrN, or NbC second-order phonon Raman scattering can occur in the presence of defects [44]. Then first-order scattering being proportional to the PDOS (modulo energy and symmetry dependent weighting factors) is expected to be also substantial if not stronger. Although our crystals are slightly disordered there is no indication of substantial intensity at energies with high PDOS as can be seen by directly comparing Figs. 1 and 4(b). Alternatively, second-order scattering can originate in enhanced electron-phonon coupling [45]. In either case the energies of two phonons add up as they get excited in a single scattering process. Generally, no selection rules apply for second order Raman scattering and the resulting peak would appear in all symmetry channels [46]. Exceptions exist if the phonon wave vectors coincide with high-symmetry points or lines of the Brillouin zone.

From the phonon dispersion alone several phonon branches having **k** and $-$**k** and energies in the range around $\omega_{P1}/2$ could add up to yield 265 cm$^{-1}$ (see Fig. 4). However, as explained in Appendix F and shown in Table III for the space group P4/nmm

of t-FeS, the $A_{1g}$ selection rules of P1 exclude all nonsymmetric combinations of branches (right column of Table III). On the other hand, all symmetric combinations include $A_{1g}$ selection rules for the two-phonon peak (left column of Table III) and one has to look essentially for a high PDOS in the range $\omega_{P1}/2$. As shown in Fig. 4(b) the PDOS has a maximum in the right energy range. Since the maximum results from momenta away from the high-symmetry points or lines (see Fig. 4) which alone lead to pure $A_{1g}$ symmetry one expects also intensity in $B_{1g}$ and $E_g$ symmetry as opposed to the experiment. For exclusive $A_{1g}$ selection rules only seven possibilities exist. Since phase space arguments favor modes having a flat dispersion in extended regions of the Brillouin zone the $\Gamma$, $M$, and/or $A$ points are unlikely to give rise to P1, and only the lines $S = A - Z$, $\Sigma = \Gamma - M$, and $V = A - M$ remain. The dispersion along the $S$ or $\Sigma$ branch contributes very little to the PDOS. On the high-symmetry line $V$ a doubly degenerate branch would have a flat dispersion [see Fig. 4(b)] and contributes substantially to the PDOS but the energy of 150 cm$^{-1}$ differs by 13% from the expected energy of 132.5 cm$^{-1}$. Instead of arguing about the accuracy of the theoretical phonon energies (see Sec. III) we looked at the dispersion close to but not strictly on $V$ where the contribution to $B_{1g}$ and $E_g$ symmetries is expected to be still very small, e.g., along $M' - A'$ [Fig. 4(b)]. A detailed inspection shows that the maximum of the PDOS between 130 and 140 cm$^{-1}$ comes from there. This explains both the selection rules and the energy of P1 to within a few percent.

Peak P2 cannot be explained in terms of one of the two $E_g$ phonons either. As opposed to P1 it is not inside the gap of the PDOS and thus can originate from either first or second order scattering. If P2 originates in second order scattering in the same fashion as P1 there are five possibilities yielding $A_{1g} + B_{1g}$ but not $E_g$ selection rules. As explained in the last paragraph only the branches $\Delta = \Gamma - X$ and $U = Z - R$ may contribute. For the low PDOS there we consider also first order defect-induced scattering for P2 to originate from. In fact, the PDOS possesses its strongest maximum 5 cm$^{-1}$ below the (theoretical) $A_{1g}$ phonon exactly where P2 is found. In spite of the very high PDOS here, the peak is weak explaining the negligible contributions from first order defect-induced scattering at lower energies. The high PDOS between 300 and 325 cm$^{-1}$ may also be an alternative yet less likely explanation for the weak contributions in crossed polarizations in the energy range of the $A_{1g}$ phonon (Fig. 1).

Finally, we wish to clarify whether the large phonon-phonon coupling $\lambda_{\text{ph-ph}}^{A1g}$ found for the $A_{1g}$ Raman-active mode (see Table I) is related to the appearance of P1. Due to the close proximity of the energies the $A_{1g}$ mode apparently decays into states close to those adding up to yield P1. The decay is less restricted by symmetry leaving more options. For both processes the phonon-phonon coupling has to be substantial with the order of magnitude given by $\lambda_{\text{ph-ph}}^{A1g} \approx 1.7$. Phonon-phonon coupling is present in any type of material because of the anharmonic potential. Defects enhance this effect [44]. Since FeS is a metal the phonon-phonon coupling goes at least partially through electronic states and may be indicative of enhanced electron-phonon coupling, $\lambda_{\text{el-ph}}$, as described, e.g., in Ref. [45]. The related contribution to $\lambda_{\text{ph-ph}}$ is then expected

TABLE III. Two-phonon processes in FeS. The symmetry group of the FeS system is the space group $P4/nmm$. For products of irreducible representations (IRs) in the left column Raman active modes (RM) in decomposition are given in the right one. Raman active modes of FeS are $\Gamma_1^+$ ($A_{1g}$), $\Gamma_2^+$ ($B_{1g}$), and two double degenerate $\Gamma_5^+$ ($E_g$). $\Gamma_1^+$ comes from vibrations of S atoms, $\Gamma_2^+$ from Fe ones, and both atom types contribute with one pair of $\Gamma_5^+$ modes. For complex representations ($V_{1,2,3,4}$ and all $W$) the double index indicates that the real representation is used, for example, $V_{13} = V_1 \oplus V_1^* = V_1 \oplus V_3$. Irreducible representations of the space group given in Ref. [53] are used.

| Overtones | | Combinations | |
|---|---|---|---|
| IR products (phonon states) | RM in decomposition | IR products (phonon states) | RM in decomposition |
| $[(\Gamma_i^\pm)^2]$ $(i=1,2,3,4)$ | $A_{1g}$ | $\Gamma_1^h \otimes \Gamma_2^h, \Gamma_3^h \otimes \Gamma_4^h$ $(h=\pm)$ | $B_{1g}$ |
| $[(\Gamma_5^\pm)^2]$ | $A_{1g}, B_{1g}$ | $\Gamma_i^h \otimes \Gamma_5^h$ $(i=1,2,3,4, h=\pm)$ | $E_g$ |
| $[(X_i)^2]$ $(i=1,2)$ | $A_{1g}, B_{1g}, E_g$ | $X_1 \otimes X_2$ | $E_g$ |
| $[(M_i)^2]$ $(i=1,2,3,4)$ | $A_{1g}$ | $M_1 \otimes M_2, M_3 \otimes M_4$ | $B_{1g}$ |
| $[(\Sigma_i)^2]$ $(i=1,2,3,4)$ | $A_{1g}$ | $M_1 \otimes M_3, M_1 \otimes M_4, M_2 \otimes M_3, M_2 \otimes M_4$ | $E_g$ |
| $[(\Delta_i)^2]$ $(i=1,2,3,4)$ | $A_{1g}, B_{1g}$ | $\Sigma_1 \otimes \Sigma_2, \Sigma_3 \otimes \Sigma_4$ | $B_{1g}$ |
| $[(V_{13})^2], [(V_{24})^2], [(V_5)^2]$ | $A_{1g}$ | $\Sigma_1 \otimes \Sigma_3, \Sigma_1 \otimes \Sigma_4, \Sigma_2 \otimes \Sigma_3, \Sigma_2 \otimes \Sigma_4$ | $E_g$ |
| $[(W_{13})^2], [(W_{24})^2]$ | $A_{1g}, B_{1g}, E_g$ | $\Delta_1 \otimes \Delta_2, \Delta_1 \otimes \Delta_3, \Delta_2 \otimes \Delta_4, \Delta_3 \otimes \Delta_4$ | $E_g$ |
| $[(Y_1)^2]$ | $A_{1g}, B_{1g}, E_g$ | $V_{13} \otimes V_{24}$ | $\Gamma_2^+$ |
| $[(Z_i^\pm)^2]$ $(i=1,2,3,4)$ | $A_{1g}$ | $V_{13} \otimes V_5, V_{24} \otimes V_5$ | $\Gamma_5^+$ |
| $[(Z_5^\pm)^2]$ | $A_{1g}, B_{1g}$ | $W_{13} \otimes W_{24}$ | $\Gamma_5^+$ |
| $[(A_i)^2]$ $(i=1,2,3,4)$ | $A_{1g}$ | $Z_1^h \otimes Z_2^h, Z_3^h \otimes Z_4^h$ $(h=\pm)$ | $B_{1g}$ |
| $[(R_i)^2]$ $(i=1,2)$ | $A_{1g}, B_{1g}, E_g$ | $Z_i^h \otimes Z_5^h$ $(i=1,2,3,4, h=\pm)$ | $E_g$ |
| $[(S_i)^2]$ $(i=1,2,3,4)$ | $A_{1g}$ | $A_1 \otimes A_2, A_3 \otimes A_4$ | $B_{1g}$ |
| $[(U_i)^2]$ $(i=1,2,3,4)$ | $A_{1g}, B_{1g}$ | $A_1 \otimes A_3, A_1 \otimes A_4, A_2 \otimes A_3, A_2 \otimes A_4$ | $E_g$ |
| $[(\Lambda_i)^2]$ $(i=1,2,3,4)$ | $A_{1g}$ | $R_1 \otimes R_2$ | $E_g$ |
| $[(\Lambda_5)^2]$ | $A_{1g}, B_{1g}$ | $S_1 \otimes S_2, S_3 \otimes S_4$ | $B_{1g}$ |
| $[(T_1)^2]$ | $A_{1g}, B_{1g}, E_g$ | $S_1 \otimes S_3, S_1 \otimes S_4, S_2 \otimes S_3, S_2 \otimes S_4$ | $E_g$ |
| | | $U_1 \otimes U_2, U_1 \otimes U_3, U_2 \otimes U_4, U_3 \otimes U_4$ | $E_g$ |
| | | $\Lambda_1 \otimes \Lambda_2, \Lambda_3 \otimes \Lambda_4$ | $B_{1g}$ |
| | | $\Lambda_i \otimes \Lambda_5$ $(i=1,2,3,4)$ | $E_g$ |

to be proportional to $\lambda_{\text{el-ph}}^2$. This conclusion is compatible with early results on the branch-dependent electron-phonon coupling in LaFeAsOF, where the strongest effects are reported for some $\Gamma$-point modes and the acoustic branches with intermediate to large momenta [47]. $\lambda_{\text{ph-ph}}^{A1g} > 1$ and the two-phonon peak P1 indicate that the electron-phonon coupling is possibly larger than in the other Fe-based systems and reaches values up to unity. In BaFe$_2$As$_2$, as an example from the pnictide family, $\lambda_{\text{el-ph}}^2 \approx (1\text{–}4) \times 10^{-2} < \lambda_{\text{ph-ph}} \approx 0.1$ is reported [32,48,49]. On the other hand, one finds $\lambda_{\text{el-ph}}^2 \approx 0.4 < \lambda_{\text{ph-ph}} \approx 0.9$ for the $E_g$ phonon in MgB$_2$, being generally believed to be a conventional superconductor [50,51]. Thus one may speculate whether $\lambda_{\text{el-ph}}$ might be even large enough in FeS to account for a $T_c$ in the 5 K range.

## V. CONCLUSION

We have studied and identified phonons in tetragonal FeS by Raman scattering. For the $A_{1g}$ sulfur and $B_{1g}$ iron mode the DFT and DFPT calculations agree to within a few percent with the experiment. A third observed peak within a gap in the theoretical phonon density of states can be identified as a second order scattering process involving two phonons. Both the selection rules, based on the modified group projector technique, and the energy are in agreement with the experiment. A fourth mode identified close to the $A_{1g}$ sulfur phonon can be traced back to the biggest maximum of the PDOS and is most likely activated by a small amount of defects.

The temperature dependence of all four modes is governed by the contraction of the lattice, but shows anomalies at 50 K and below 20 K. The anomaly observed at 20 K has a correspondence in the thermal expansion [20] and $\mu$SR experiments [21,22], which indicate short-range magnetic order. The long-range magnetic order observed recently by neutron diffraction experiments [41] below $T_N = 116$ K has no correspondence in the Raman spectra.

The appearance of two-phonon scattering indicates strong phonon-phonon scattering, which is likely to originate from an electron-phonon interaction being enhanced in comparison to other pnictides and chalcogenides. We argue that in FeS the $T_c$ can in principle entirely result from electron-phonon interaction.
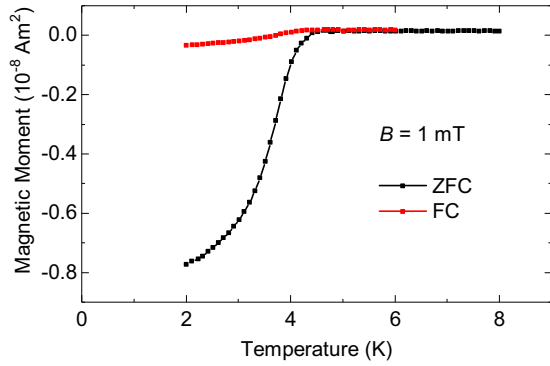
FIG. 5. Magnetization measurements of t-FeS at an applied field of $B = 1$ mT cooled to 2 K with (red curve) and without applied field (black curve).

## APPENDIX A: MAGNETIZATION MEASUREMENTS

Figure 5 shows magnetization measurements on a t-FeS sample from the batch studied in small applied fields. Measurements were done on a Quantum Design MPMS XL-7 SQUID magnetometer by cooling the sample to 2 K and sweeping
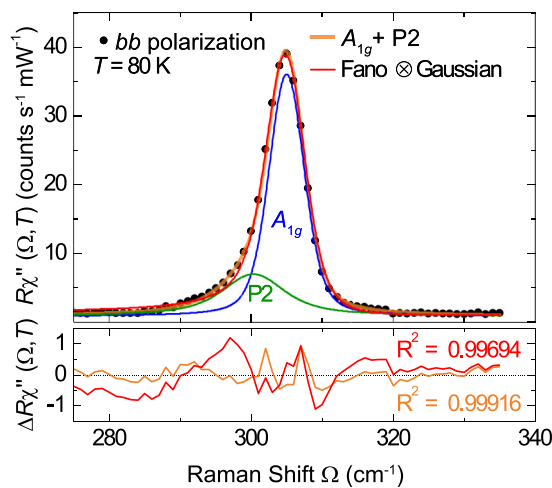


FIG. 6. Decomposition of the asymmetric phonon peak at 305 cm$^{-1}$. Measured data are shown as black dots. The orange line shows the sum of two Voigt profiles shown as blue and green lines, respectively. The convolution of Fano and Gaussian (red line) deviates in the peak flanks and the nearby continuum.
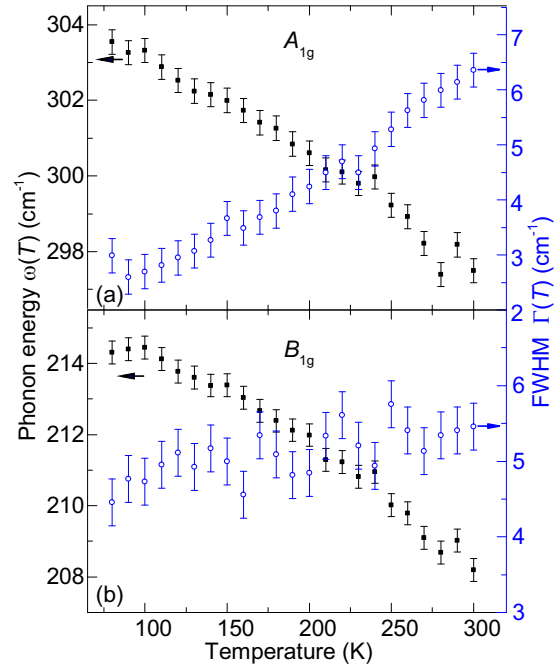


FIG. 7. Temperature dependence of $A_{1g}$ and $B_{1g}$ phonon modes in the temperature range between 80 K and 300 K. Black squares denote the phonon energies; open circles denote the phonon linewidths.

the temperature at 0.1 K/min. When cooled without applied field (ZFC, black curve) the sample shows a superconducting transition with onset at 4.5 K and a center of the transition at 3.6 K. When cooled in an applied field the magnetization decreases only weakly in the superconducting state indicating strong pinning.

## APPENDIX B: DECOMPOSITION
## OF THE LINE AT 305 cm$^{-1}$

The peak at 305 cm$^{-1}$ at low temperatures shows a significant asymmetry towards lower energies (see also Fig. 1). Coupling of the $A_{1g}$ phonon mode to an electronic continuum by strong electron-phonon coupling would result in a line shape given by the convolution of a Fano function and a Gaussian, the latter representing the resolution of the spectrometer. We find, however, that this does not yield a satisfactory description of the measured line shape as can be seen from the red curve in Fig. 6, and thus conclude that the asymmetry of the peak stems from the overlap of two peaks which cannot be resolved separately. The corresponding line shape is the sum of two Lorentzians convoluted with a Gaussian which governs the resolution of the setup. Due to the distributivity of the convolution this is identical to the sum of two Voigt functions sharing the same width $\Gamma_G$ of the Gaussian part. The overall spectral shape is shown in Fig. 6 as an orange line and agrees excellently with the data. The two contributing lines are shown in blue and green. From the selection rules (see Fig. 1) we identify the blue curve as the in-phase vibration of sulfur atoms in $A_{1g}$ symmetry. The green line denotes a second mode P2, the origin of which is discussed in the main text.
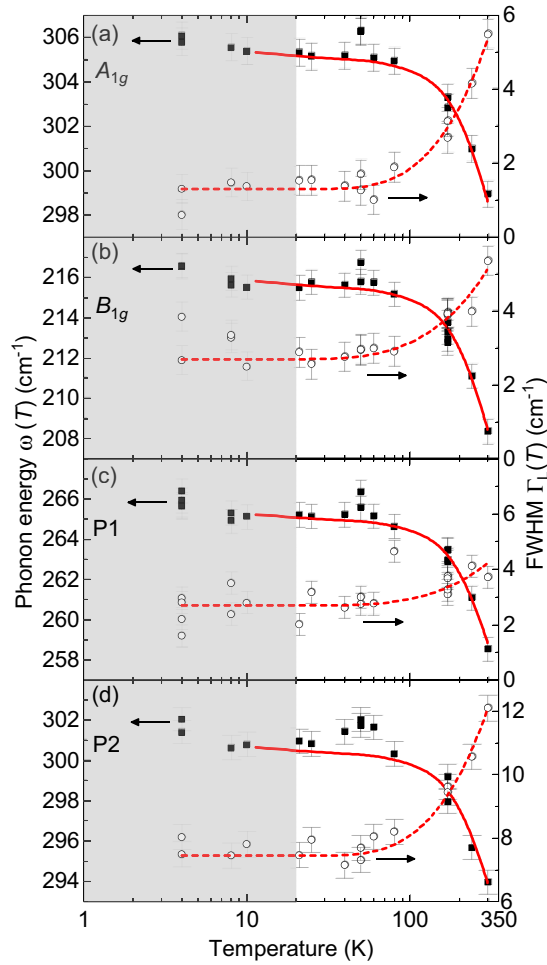
FIG. 8. Temperature dependence of energy and width of the four observed phonon modes in FeS on a logarithmic scale. The data is identical to Fig. 3 of the main text. Black squares show the phonon energies $\omega$; open circles denote the phonon linewidths $\Gamma_L$. The red dashed and full lines represent the temperature dependence of the phonon linewidths and energies according to Eqs. (1) and (2), respectively. The region below 20 K is shaded light gray. Since the data for the volume are limited to the range above 10 K the theoretical curves for the phonon energies (full red lines) end at 10 K.

## APPENDIX C: DETAILED TEMPERATURE DEPENDENCE FOR $80 \leqslant T \leqslant 300$ K

Figure 7 shows the temperature dependence of the energies $\omega$ and linewidths $\Gamma(T)$ (FWHM) from 80 K to 300 K measured in temperature increments of 10 K. Raman scattering measurements were performed using a Jobin Yvon T64000 Raman system in micro-Raman configuration. A solid state laser with 532 nm line was used as an excitation source. Measurements were performed in high vacuum ($10^{-6}$ mbar) using a KONTI CryoVac continuous helium flow cryostat with 0.5 mm thick window. Laser beam focusing was accomplished using a microscope objective with $\times 50$ magnification. The samples were cleaved right before being placed in the vacuum. As can be seen from Fig. 7, there is no deviation from the standard temperature behavior around 120 K.

## APPENDIX D: TEMPERATURE DEPENDENCE ON A LOGARITHMIC SCALE

To better illustrate the behavior of the phonons at low temperatures Fig. 8 shows the experimental data and the theoretical curves from Fig. 3 of the main text on a logarithmic temperature scale. The region below 20 K is shaded light gray. As explained in Sec. IV B all four modes show an increase in energy below 20 K instead of the expected saturation, indicative of the putative onset of short range magnetic order. This effect manifests itself also in an incipient decrease of the unit cell volume [20] and is visible in the theoretical results for the phonon energies (full red lines). No clear tendency can be seen for the linewidths. The energy anomaly found around 50 K is discussed in the same section.

## APPENDIX E: SECOND SAMPLE BATCH

Figure 9 shows Raman spectra on a t-FeS sample from a different batch (E256) taken at $T = 310$ K. The sample was oriented the same way as described in the main text. All three modes are visible for parallel light polarizations ($bb$), but vanish for crossed polarizations ($ba$), confirming the selection rules observed in the sample described in the main text. The inset shows magnetization measurements on a sample from batch E256 similar to the ones described in Appendix A. The superconducting transition sets in at 4.1 K.

## APPENDIX F: SELECTION RULES FOR TWO-PHONON PROCESSES AND MGPT

In the multiphonon scattering process the system goes from an initial vibrational state (ground vibrational state) $|0,0,\ldots\rangle$ to a final multiphonon state $|n_\mu, n_{\mu'}, \ldots\rangle$, where $n_\mu$ is the number of phonons in the same state $\mu$ and $\mu$ stands for the entire set of quantum numbers (quasimomentum $k$, angular momentum quantum number $m$, etc.). For two-phonon processes the final vibrational state is the state with two phonons in the same quantum state (double-phonon or the first overtone state) or with two phonons in different states (combination state). The corresponding matrix element for
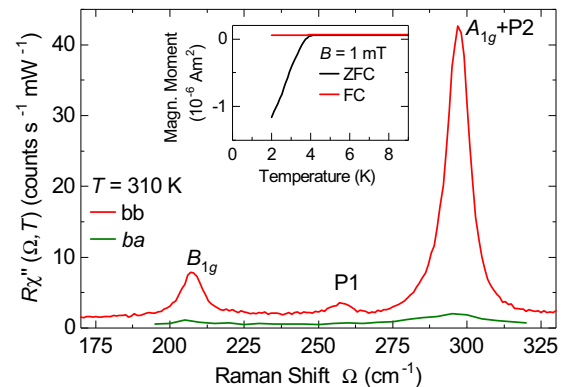


FIG. 9. Raman spectra of a t-FeS sample from a different batch taken at $T = 310$ K in polarizations as given in the legend. The inset shows magnetization measurements on a sample from this batch similar to Appendix A.

two-phonon Raman scattering is

$$\langle 0,\ldots,n_\mu,0,\ldots|\mathcal{R}|0,0,\ldots\rangle, n_\mu = 2, \text{overtones},$$

$$\langle 0,\ldots,n_\mu,0,\ldots,n_{\mu'},\ldots|\mathcal{R}|0,0,\ldots\rangle,$$

$$n_\mu = n_{\mu'} = 1, \text{combinations}, \tag{F1}$$

where $\mathcal{R}$ is the Raman tensor. This matrix element should be a scalar or should transform as unit representation of the system space group $\mathcal{S}$. The standard approximation for the Raman tensor in infinite wavelength-light approximation for the non-resonant case is the polarizability tensor, which transforms as the (symmetrized) square of the vector representation, $D^{\mathcal{R}}(\mathcal{S})$. Decomposition of $D^{\mathcal{R}}(\mathcal{S})$ gives irreducible representations of the Raman active modes. The ground vibrational state transforms as unit representation, whereas the final two-phonon state transforms as symmetrized square, $[(D^\mu(\mathcal{S}))^2]$, of the corresponding irreducible representation $D^\mu(\mathcal{S})$ (overtones) or the direct product of two irreducible representations $D^\mu(\mathcal{S}) \otimes D^{\mu'}(\mathcal{S})$ (combinations). Symmetrization in the case of overtones comes from the bosonic nature of phonons. The matrix element [Eq. (F1)] transforms as reducible representation

$$[(D^\mu(\mathcal{S}))^2] \otimes D^{\mathcal{R}}(\mathcal{S}), \quad \text{for overtones, or}$$
$$D^\mu(\mathcal{S}) \otimes D^{\mu'}(\mathcal{S}) \otimes D^{\mathcal{R}}(\mathcal{S}), \quad \text{for combinations.} \tag{F2}$$

It is a scalar if the decomposition of the representations shown above contains the unit representation or, equivalently, if the intersection of decompositions of $[(D^\mu(\mathcal{S}))^2]$ or $D^\mu(\mathcal{S}) \otimes D^{\mu'}(\mathcal{S})$ and $D^{\mathcal{R}}(\mathcal{S})$ is a nonempty set. To obtain selection rules for two-phonon processes, following Birman's original method [52], it is enough to find the decomposition of $[(D^\mu(\mathcal{S}))^2]$ (for overtones) and $D^\mu(\mathcal{S}) \otimes D^{\mu'}(\mathcal{S})$ (for combinations) for all irreducible representations. If there is any representation

of the Raman active mode in those decompositions then that overtone or two-phonon combination is symmetrically allowed in the Raman scattering process. The decomposition of the (symmetrized) square of the vector representation is straightforward and is actually a finite dimensional point group problem. On the other hand, decomposition of $[(D^\mu(\mathcal{S}))^2]$ or $D^\mu(\mathcal{S}) \otimes D^{\mu'}(\mathcal{S})$ for any irreducible representation could be a difficult task because space groups are infinite. In the standard method based on character theory summation over all group elements is used and it is a problem in the infinite case. Therefore, it is necessary to apply a method which avoids summation over group elements. As is proven in Ref. [29] the modified group projector technique (MGPT) uses only group generators and finite dimensional matrices. Actually, the decomposition $D(\mathcal{S}) = \oplus_\mu f_D^\mu D^{(\mu)}(\mathcal{S})$ of the arbitrary reducible representation $D(\mathcal{S})$ into irreducible representations is effectively a determination of the frequency numbers $f_D^\mu$. The MGPT expression for frequency numbers involves group generators $s_i$ only:

$$f_D^\mu = \text{Tr}\, F\left(\prod_{i=1}^{S} F(D(s_i) \otimes D^{(\mu)^*}(s_i))\right). \tag{F3}$$

Here $S$ is the number of group generators, $F(X)$ is the projector on the subspace of the fixed points of the operator $X$, and Tr is the matrix trace (sum of the diagonal matrix elements). Consequently, the problem is reduced to calculation of the $S + 1$ projector to the fixed points. Technically, one looks for the eigenspaces for the eigenvalue 1 of each of the operators $D(s_i) \otimes D^{(\mu)^*}(s_i)$, finding projectors on them, then multiplies the corresponding projectors, and repeats the procedure for the whole product from Eq. (F3). The trace of the final projector gives the corresponding frequency number.

---

[1] Z. P. Yin, K. Haule, and G. Kotliar, Magnetism and charge dynamics in iron pnictides, Nat. Phys. **7**, 294 (2011).

[2] Q. Si, R. Yu, and E. Abrahams, High-temperature superconductivity in iron pnictides and chalcogenides, Nat. Rev. Mater. **1**, 16017 (2016).

[3] I. Leonov, S. L. Skornyakov, V. I. Anisimov, and D. Vollhardt, Correlation-Driven Topological Fermi Surface Transition in FeSe, Phys. Rev. Lett. **115**, 106402 (2015).

[4] C. Tresca, G. Giovannetti, M. Capone, and G. Profeta, Electronic properties of superconducting FeS, Phys. Rev. B **95**, 205117 (2017).

[5] J. Miao, X. H. Niu, D. F. Xu, Q. Yao, Q. Y. Chen, T. P. Ying, S. Y. Li, Y. F. Fang, J. C. Zhang, S. Ideta, K. Tanaka, B. P. Xie, D. L. Feng, and F. Chen, Electronic structure of FeS, Phys. Rev. B **95**, 205127 (2017).

[6] S. L. Skornyakov, V. I. Anisimov, D. Vollhardt, and I. Leonov, Effect of electron correlations on the electronic structure and phase stability of FeSe upon lattice expansion, Phys. Rev. B **96**, 035137 (2017).

[7] T. M. McQueen, A. J. Williams, P. W. Stephens, J. Tao, Y. Zhu, V. Ksenofontov, F. Casper, C. Felser, and R. J. Cava, Tetragonal-to-Orthorhombic Structural Phase Transition at 90 K in the Superconductor $Fe_{1.01}Se$, Phys. Rev. Lett. **103**, 057002 (2009).

[8] Y. Mizuguchi, T. Furubayashi, K. Deguchi, S. Tsuda, T. Yamaguchi, and Y. Takano, Mössbauer studies on FeSe and FeTe, Physica C (Amsterdam) **470**, S338 (2010).

[9] M. Bendele, A. Amato, K. Conder, M. Elender, H. Keller, H.-H. Klauss, H. Luetkens, E. Pomjakushina, A. Raselli, and R. Khasanov, Pressure Induced Static Magnetic Order in Superconducting $FeSe_{1-x}$, Phys. Rev. Lett. **104**, 087003 (2010).

[10] S.-H. Baek, D. V. Efremov, J. M. Ok, J. S. Kim, J. van den Brink, and B. Büchner, Orbital-driven nematicity in FeSe, Nat. Mater. **14**, 210 (2015).

[11] M. He, L. Wang, F. Hardy, L. Xu, T. Wolf, P. Adelmann, and C. Meingast, Evidence for short-range magnetic order in the nematic phase of FeSe from anisotropic in-plane magnetostriction and susceptibility measurements, arXiv:1709.03861 [cond-mat.supr-con].

[12] A. Baum, H. N. Ruiz, N. Lazarević, Y. Wang, T. Böhm, R. Hosseinian Ahangharnejhad, P. Adelmann, T. Wolf, Z. V. Popović, B. Moritz, T. P. Devereaux, and R. Hackl, Frustrated spin order and stripe fluctuations in FeSe, arXiv:1709.08998 [cond-mat.str-el].

[13] F.-C. Hsu, J.-Y. Luo, K.-W. Yeh, T.-K. Chen, T.-W. Huang, P. M. Wu, Y.-C. Lee, Y.-L. Huang, Y.-Y. Chu, D.-C. Yan, and M.-K.

Wu, Superconductivity in the PbO-type structure α-FeSe, Proc. Natl. Acad. Sci. U.S.A. **105**, 14262 (2008).

[14] S. He, J. He, W. Zhang, L. Zhao, D. Liu, X. Liu, D. Mou, Y.-B. Ou, Q.-Y. Wang, Z. Li, L. Wang, Y. Peng, Y. Liu, C. Chen, L. Yu, G. Liu, X. Dong, J. Zhang, C. Chen, Z. Xu, X. Chen, X. Ma, Q. Xue, and X. J. Zhou, Phase diagram and electronic indication of high-temperature superconductivity at 65 K in single-layer FeSe films, Nat. Mater. **12**, 605 (2013).

[15] J.-F. Ge, Z.-L. Liu, C. Liu, C.-L. Gao, D. Qian, Q.-K. Xue, Y. Liu, and J.-F. Jia, Superconductivity above 100 K in single-layer FeSe films on doped SrTiO₃, Nat. Mater. **14**, 285 (2014).

[16] S. Li, C. de la Cruz, Q. Huang, Y. Chen, J. W. Lynn, J. Hu, Y.-L. Huang, F.-C. Hsu, K.-W. Yeh, M.-K. Wu, and P. Dai, First-order magnetic and structural phase transitions in $Fe_{1+y}Se_xTe_{1-x}$, Phys. Rev. B **79**, 054503 (2009).

[17] M. H. Fang, H. M. Pham, B. Qian, T. J. Liu, E. K. Vehstedt, Y. Liu, L. Spinu, and Z. Q. Mao, Superconductivity close to magnetic instability in $Fe(Se_{1-x}Te_x)_{0.82}$, Phys. Rev. B **78**, 224503 (2008).

[18] K.-W. Yeh, T.-W. Huang, Y.-l. Huang, T.-K. Chen, F.-C. Hsu, P. M. Wu, Y.-C. Lee, Y.-Y. Chu, C.-L. Chen, J.-Y. Luo, D.-C. Yan, and M.-K. Wu, Tellurium substitution effect on superconductivity of the α-phase iron selenide, Europhys. lett. **84**, 37002 (2008).

[19] X. Lai, H. Zhang, Y. Wang, X. Wang, X. Zhang, J. Lin, and F. Huang, Observation of superconductivity in tetragonal FeS, J. Am. Chem. Soc. **137**, 10148 (2015).

[20] U. Pachmayr, N. Fehn, and D. Johrendt, Structural transition and superconductivity in hydrothermally synthesized FeX (X = S, Se), Chem. Commun. **52**, 194 (2016).

[21] S. Holenstein, U. Pachmayr, Z. Guguchia, S. Kamusella, R. Khasanov, A. Amato, C. Baines, H.-H. Klauss, E. Morenzoni, D. Johrendt, and H. Luetkens, Coexistence of low-moment magnetism and superconductivity in tetragonal FeS and suppression of T_c under pressure, Phys. Rev. B **93**, 140506 (2016).

[22] F. K. K. Kirschner, F. Lang, C. V. Topping, P. J. Baker, F. L. Pratt, S. E. Wright, D. N. Woodruff, S. J. Clarke, and S. J. Blundell, Robustness of superconductivity to competing magnetic phases in tetragonal FeS, Phys. Rev. B **94**, 134509 (2016).

[23] A. Wang, L. Wu, V. N. Ivanovski, J. B. Warren, J. Tian, Y. Zhu, and C. Petrovic, Critical current density and vortex pinning in tetragonal $FeS_{1-x}Se_x$ ($x = 0, 0.06$), Phys. Rev. B **94**, 094506 (2016).

[24] S. Baroni, S. de Gironcoli, A. Dal Corso, and P. Giannozzi, Phonons and related crystal properties from density-functional perturbation theory, Rev. Mod. Phys. **73**, 515 (2001).

[25] P. Giannozzi, S. Baroni, N. Bonini, M. Calandra, R. Car, C. Cavazzoni, D. Ceresoli, G. L. Chiarotti, M. Cococcioni, I. Dabo, A. D. Corso, S. de Gironcoli, S. Fabris, G. Fratesi, R. Gebauer, U. Gerstmann, C. Gougoussis, A. Kokalj, M. Lazzeri, L. Martin-Samos, N. Marzari, F. Mauri, R. Mazzarello, S. Paolini, A. Pasquarello, L. Paulatto, C. Sbraccia, S. Scandolo, G. Sclauzero, A. P. Seitsonen, A. Smogunov, P. Umari, and R. M. Wentzcovitch, QUANTUM ESPRESSO: a modular and open-source software project for quantum simulations of materials, J. Phys.: Condens. Matter **21**, 395502 (2009).

[26] A. R. Lennie, S. A. T. Redfern, P. F. Schofield, and D. J. Vaughan, Synthesis and Rietveld crystal structure refinement of mackinawite, tetragonal FeS, Mineral. Mag. **59**, 677 (1995).

[27] A. Subedi, L. Zhang, D. J. Singh, and M. H. Du, Density functional study of FeS, FeSe, and FeTe: Electronic structure,

[28] Y. El Mendili, B. Minisini, A. Abdelouas, and J.-F. Bardeau, Assignment of Raman-active vibrational modes of tetragonal mackinawite: Raman investigations and *ab initio* calculations, RSC Adv. **4**, 25827 (2014).

[29] M. Damnjanović and I. Milošević, Full symmetry implementation in condensed matter and molecular physics–Modified group projector technique, Phys. Rep. **581**, 1 (2015).

[30] P. G. Klemens, Anharmonic decay of optical phonons, Phys. Rev. **148**, 845 (1966).

[31] H.-M. Eiter, P. Jaschke, R. Hackl, A. Bauer, M. Gangl, and C. Pfleiderer, Raman study of the temperature and magnetic-field dependence of the electronic and lattice properties of MnSi, Phys. Rev. B **90**, 024411 (2014).

[32] M. Rahlenbeck, G. L. Sun, D. L. Sun, C. T. Lin, B. Keimer, and C. Ulrich, Phonon anomalies in pure and underdoped $R_{1-x}K_xFe_2As_2$ (R = Ba, Sr) investigated by Raman light scattering, Phys. Rev. B **80**, 064509 (2009).

[33] L. Chauvière, Y. Gallais, M. Cazayous, A. Sacuto, M. A. Measson, D. Colson, and A. Forget, Doping dependence of the lattice dynamics in $Ba(Fe_{1-x}Co_x)_2As_2$ studied by Raman spectroscopy, Phys. Rev. B **80**, 094504 (2009).

[34] L. Chauvière, Y. Gallais, M. Cazayous, M. A. Méasson, A. Sacuto, D. Colson, and A. Forget, Raman scattering study of spin-density-wave order and electron-phonon coupling in $Ba(Fe_{1-x}Co_x)_2As_2$, Phys. Rev. B **84**, 104508 (2011).

[35] Y. J. Um, A. Subedi, P. Toulemonde, A. Y. Ganin, L. Boeri, M. Rahlenbeck, Y. Liu, C. T. Lin, S. J. E. Carlsson, A. Sulpice, M. J. Rosseinsky, B. Keimer, and M. Le Tacon, Anomalous dependence of c-axis polarized Fe $B_{1g}$ phonon mode with Fe and Se concentrations in $Fe_{1+y}Te_{1-x}Se_x$, Phys. Rev. B **85**, 064519 (2012).

[36] Y. J. Um, J. T. Park, B. H. Min, Y. J. Song, Y. S. Kwon, B. Keimer, and M. Le Tacon, Raman scattering study of the lattice dynamics of superconducting LiFeAs, Phys. Rev. B **85**, 012501 (2012).

[37] V. Gnezdilov, Y. G. Pashkevich, P. Lemmens, D. Wulferding, T. Shevtsova, A. Gusev, D. Chareev, and A. Vasiliev, Interplay between lattice and spin states degree of freedom in the FeSe superconductor: Dynamic spin state instabilities, Phys. Rev. B **87**, 144508 (2013).

[38] T. Yildirim, Strong Coupling of the Fe-Spin State and the As-As Hybridization in Iron-Pnictide Superconductors from First-Principle Calculations, Phys. Rev. Lett. **102**, 037003 (2009).

[39] V. Gnezdilov, Yu. Pashkevich, P. Lemmens, A. Gusev, K. Lamonova, T. Shevtsova, I. Vitebskiy, O. Afanasiev, S. Gnatchenko, V. Tsurkan, J. Deisenhofer, and A. Loidl, Anomalous optical phonons in FeTe chalcogenides: Spin state, magnetic order, and lattice anharmonicity, Phys. Rev. B **83**, 245127 (2011).

[40] Z. V. Popović, N. Lazarević, S. Bogdanović, M. M. Radonjić, D. Tanasković, R. Hu, H. Lei, and C. Petrovic, Signatures of the spin-phonon coupling in $Fe_{1+y}Te_{1-x}Se_x$ alloys, Solid State Commun. **193**, 51 (2014).

[41] S. J. Kuhn, M. K. Kidder, D. S. Parker, C. dela Cruz, M. A. McGuire, W. M. Chance, L. Li, L. Debeer-Schmitt, J. Ermentrout, K. C. Littrell, M. R. Eskildsen, and A. S. Sefat, Structure and property correlations in FeS, Physica C (Amsterdam) **534**, 29 (2017).

[42] R. A. MacDonald and W. M. MacDonald, Thermodynamic properties of fcc metals at high temperatures, Phys. Rev. B **24**, 1715 (1981).

[43] M. I. Aroyo, D. Orobengoa, G. de la Flor, E. S. Tasci, J. M. Perez-Mato, and H. Wondratschek, Brillouin-zone database on the *Bilbao Crystallographic Server*, Acta Crystallogr. A **70**, 126 (2014).

[44] W. Spengler and R. Kaiser, First and second order Raman scattering in transition metal compounds, Solid State Commun. **18**, 881 (1976).

[45] W. Spengler, R. Kaiser, A. N. Christensen, and G. Müller-Vogt, Raman scattering, superconductivity, and phonon density of states of stoichiometric and nonstoichiometric TiN, Phys. Rev. B **17**, 1095 (1978).

[46] W. Hayes and R. Loudon, *Scattering of Light by Crystals* (John Wiley and Sons, New York, 1978).

[47] L. Boeri, O. V. Dolgov, and A. A. Golubov, Is $LaFeAsO_{1-x}F_x$ an Electron-Phonon Superconductor? Phys. Rev. Lett. **101**, 026403 (2008).

[48] B. Mansart, D. Boschetto, A. Savoia, F. Rullier-Albenque, F. Bouquet, E. Papalazarou, A. Forget, D. Colson, A. Rousse, and M. Marsi, Ultrafast transient response and electron-phonon cou-pling in the iron-pnictide superconductor $Ba(Fe_{1-x}Co_x)_2As_2$, Phys. Rev. B **82**, 024513 (2010).

[49] L. Rettig, R. Cortés, H. S. Jeevan, P. Gegenwart, T. Wolf, J. Fink, and U. Bovensiepen, Electron-phonon coupling in 122 Fe pnictides analyzed by femtosecond time-resolved photoemis-sion, New J. Phys. **15**, 083023 (2013).

[50] H. Martinho, C. Rettori, P. G. Pagliuso, A. A. Martin, N. O. Moreno, and J. L. Sarrao, Role of the $E_{2g}$ phonon in the superconductivity of $MgB_2$: a Raman scattering study, Solid State Commun. **125**, 499 (2003).

[51] Y. Wang, T. Plackowski, and A. Junod, Specific heat in the superconducting and normal state (2–300 K, 0–16 T), and magnetic susceptibility of the 38 K superconductor $MgB_2$: evidence for a multicomponent gap, Physica C (Amsterdam) **355**, 179 (2001).

[52] J. L. Birman, Theory of infrared and Raman processes in crystals: Selection rules in diamond and zincblende, Phys. Rev. **131**, 1489 (1963).

[53] M. I. Aroyo, A. Kirov, C. Capillas, J. M. Perez-Mato, and H. Wondratschek, Bilbao Crystallographic Server. II. Representa-tions of crystallographic point groups and space groups, Acta Crystallogr. A **62**, 115 (2006).

# Evidence of spin-phonon coupling in CrSiTe₃

A. Milosavljević,[1] A. Šolajić,[1] J. Pešić,[1] Yu Liu (刘育),[2] C. Petrovic,[2] N. Lazarević,[1,*] and Z. V. Popović[1,3]

[1]*Center for Solid State Physics and New Materials, Institute of Physics Belgrade,*
*University of Belgrade, Pregrevica 118, 11080 Belgrade, Serbia*
[2]*Condensed Matter Physics and Materials Science Department, Brookhaven National Laboratory, Upton, New York 11973-5000, USA*
[3]*Serbian Academy of Sciences and Arts, Knez Mihailova 35, 11000 Belgrade, Serbia*

We present Raman scattering results on the layered semiconducting ferromagnetic compound CrSiTe₃. Four Raman-active modes, predicted by symmetry, are observed and assigned. The experimental results are supported by density functional theory calculations. The self-energies of the $A_g^3$ and the $E_g^3$ symmetry modes exhibit unconventional temperature evolution around 180 K. In addition, the doubly degenerate $E_g^3$ mode shows a clear change of asymmetry in the same temperature region. The observed behavior is consistent with the presence of the previously reported short-range magnetic order and strong spin-phonon coupling.

## I. INTRODUCTION

Trichalcogenides Cr$X$Te₃ ($X =$ Si, Ge) belong to a rare class of quasi-two-dimensional semiconducting materials with a ferromagnetic order, band gaps of 0.4 eV for Si and 0.7 eV for Ge compounds, and Curie temperatures ($T_C$) of 32 and 61 K, respectively [1–6]. Because of their layered structure, due to van der Waals bonding, they can be exfoliated to mono- and few-layer nanosheets, which, together with their semiconducting and magnetic properties, make an ideal combination for applications in optoelectronics and nanospintronics [7–11]. This was further supported by the observation of giant resistivity modulation of CrGeTe₃-based devices [12].

From an x-ray diffraction study [1], it was revealed that CrSiTe₃ crystals are twined along $c$ axes, the thermal expansion is negative at low temperatures, and the thermal conductivity shows strong magnon-phonon scattering effects. A very small single-ion anisotropy favoring magnetic order along $c$ axes and spin waves was found in CrSiTe₃ by elastic and inelastic neutron scattering [13]. Spin-wave measurements suggest the absence of three-dimensional correlations above $T_C$, whereas in-plane dynamic correlations are present up to 300 K. First-principles calculations suggested the possibility of graphenelike mechanical exfoliation for Cr$X$Te₃ ($X =$ Si, Ge) single crystals with conserved semiconducting and ferromagnetic properties [14]. The exfoliation of CrSiTe₃ bulk to mono- and few-layer two-dimensional crystals onto a Si/SiO₂ substrate has been achieved [15] with a resistivity between 80 and 120 K, depending on the number of layers. Critical exponents for CrSiTe₃ were also determined from theoretical analysis [16].

Spin-phonon coupling in CrGeTe₃ was investigated in Raman scattering experiments [17]. Splitting of the two lowest-energy $E_g$ modes in the ferromagnetic phase has been observed and ascribed to time-reversal symmetry breaking by the spin ordering. Furthermore, the significant renormalization of the three higher-energy modes' self-energies below $T_C$ provided additional evidence of spin-phonon coupling [17]. The external pressure-induced effect on lattice dynamics and magnetization in CrGeTe₃ has also been studied [18].

The Raman spectrum of CrSiTe₃ single crystals was reported in Ref. [1], where three Raman-active modes have been observed. Similar results have also been presented in Ref. [15] for ultrathin nanosheets of CrSiTe₃. Here, we report a Raman scattering study of CrSiTe₃ single crystals, with the main focus on phonon properties in the temperature range between 100 and 300 K. Our experimental results are qualitatively different from those previously reported [1,15] but consistent with the results obtained for CrGeTe₃ [17,18]. Furthermore, our data reveal the asymmetry of the $E_g^3$ mode, which is suppressed at higher temperatures. The $A_g^3$ and $E_g^3$ symmetry modes exhibit nonanharmonic self-energy temperature dependence in the region around 180 K, related to the strong spin-lattice interaction due to short-range magnetic order [1]. Energies and symmetries of the observed Raman-active modes are in good agreement with theoretical calculations.

## II. EXPERIMENT AND NUMERICAL METHOD

Single crystals of CrSiTe₃ and CrGeTe₃ were grown as described previously [19]. For a Raman scattering experiment, a Tri Vista 557 spectrometer was used in the backscattering micro-Raman configuration with a 1800/1800/2400 grooves/mm diffraction grating combination. A coherent Verdi G solid-state laser with a 532-nm line was used as the excitation source. The direction of the incident (scattered) light coincides with a crystallographic $c$ axis. Right before being placed in the vacuum, the samples were cleaved in the air. All measurements were performed in a high vacuum ($10^{-6}$ mbar) using a KONTI CryoVac continuous-helium-flow cryostat with a 0.5-mm-thick window. Laser-beam focusing was achieved through a microscope objective with $\times 50$ magnification, a spot size of approximately 8 $\mu$m, and a power

*nenadl@ipb.ac.rs

TABLE I. Calculated and experimental crystallographic lattice parameters for CrSiTe$_3$ ($|a| = |b|$), bond lengths, interlayer distance ($d$), and van der Waals (vdW) gap.

| CrSiTe$_3$ | Calculation (Å) | Experiment (Å) [20] |
|---|---|---|
| $a$ | 6.87 | 6.76 |
| $c$ | 19.81 | 20.67 |
| Si-Si | 2.27 | 2.27 |
| Si-Te | 2.52 | 2.51 |
| Cr-Te | 2.77 | 2.78 |
| $d$ | 6.86 | 6.91 |
| vdW gap | 3.42 | 3.42 |

<2 mW on the surface of a sample. All spectra were corrected for the Bose factor.

Density functional theory calculations were performed in the Quantum Espresso software package [21], using the PBE exchange-correlation functional [22], PAW pseudopotentials [23,24], and energy cutoffs for wave functions and the charge density of 85 and 425 Ry, respectively. For $k$-point sampling, the Monkhorst-Pack scheme was used, with a $\Gamma$-centered $8 \times 8 \times 8$ grid. Optimization of the atomic positions in the unit cell was performed until the interatomic forces were minimized down to $10^{-6}$ Ry/Å. In order to obtain the parameters accurately, treatment of the van der Waals interactions was included using the Grimme-D2 correction [25]. Phonon frequencies were calculated at the $\Gamma$ point

within the linear response method implemented in Quantum Espresso. Calculated crystallographic properties obtained by relaxing the structures are in good agreement with x-ray diffraction measurements [20]. A comparison between our, calculated, and experimental results is presented in Table I.

## III. RESULTS AND DISCUSSION

### A. Polarization dependence

CrSiTe$_3$ crystallizes in the rhombohedral crystal structure, described by $R\overline{3}$ ($C_{3i}^2$) [26]. Wyckoff positions of atoms, together with each site's contribution to phonons at the $\Gamma$ point and corresponding Raman tensors, are listed in Table II. The phonon mode distribution obtained by factor-group analysis for the $R\overline{3}$ space group is as follows:

$$\Gamma_{\text{Raman}} = 5A_g + 5E_g,$$
$$\Gamma_{\text{IR}} = 4A_u + 4E_u,$$
$$\Gamma_{\text{Acoustic}} = A_u + E_u.$$

Since the plane of incidence is $ab$, where $|a| = |b|$ [$\angle(a,b) = 120°$], and the direction of light propagation is along $c$ axes, from the selection rules, it is possible to observe all Raman-active modes, i.e., five $A_g$ modes and five doubly degenerate $E_g$ modes. According to the Raman tensors presented in Table II, $A_g$ symmetry modes are observable only in the parallel polarization configuration, whereas $E_g$ symmetry

TABLE II. (a) Type of atoms, Wyckoff positions, each site's contribution to the phonons at the $\Gamma$ point, and corresponding Raman tensors for the $R\overline{3}$ space group of CrSiTe$_3$. (b) Phonon symmetry, calculated optical phonon frequencies at 0 K, and experimental values for Raman-active (at 100 K) and infrared (IR)-active (at 110 K) [1] CrSiTe$_3$ phonons.

| (a) Space group $R\overline{3}$ (No. 148) | | |
|---|---|---|
| Atom(s) (Wyckoff positions) | | Irreducible representations |
| Cr, Si (6$c$) | | $A_g + E_g + A_u + E_u$ |
| Te (18$f$) | | $3A_g + 3E_g + 3A_u + 3E_u$ |

(b) Raman tensors

$$A_g = \begin{pmatrix} a & 0 & 0 \\ 0 & b & 0 \\ 0 & 0 & c \end{pmatrix} \quad E_g^1 = \begin{pmatrix} c & d & e \\ d & -c & f \\ e & f & 0 \end{pmatrix} \quad E_g^2 = \begin{pmatrix} d & -c & -f \\ -c & -d & e \\ -f & e & 0 \end{pmatrix}$$

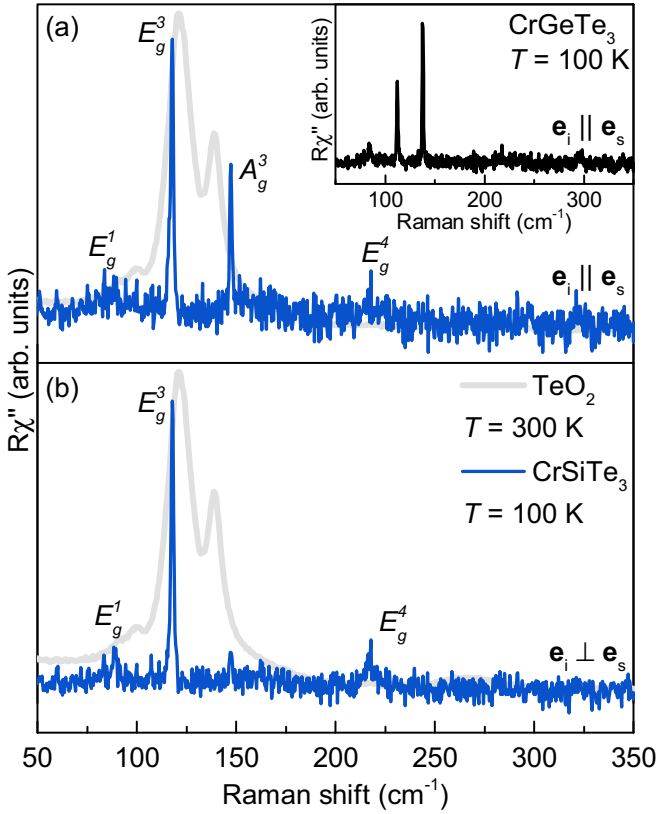| | Raman active | | | IR active [1] | | |
|---|---|---|---|---|---|---|
| Symmetry | Calc. (cm$^{-1}$) | Expt. (cm$^{-1}$) | Symmetry | Calc. (cm$^{-1}$) | Expt. (cm$^{-1}$) |
| $A_g^1$ | 88.2 | – | $A_u^1$ | 91.8 | 91.0 |
| $E_g^1$ | 93.5 | 88.9 | $E_u^1$ | 93.7 | – |
| $E_g^2$ | 96.9 | – | $A_u^2$ | 116.8 | – |
| $E_g^3$ | 118.3 | 118.2 | $E_u^2$ | 117.1 | – |
| $A_g^2$ | 122.0 | – | $A_u^3$ | 202.4 | – |
| $A_g^3$ | 148.0 | 147.4 | $E_u^3$ | 206.2 | 207.9 |
| $A_g^4$ | 208.7 | – | $A_u^4$ | 243.7 | – |
| $E_g^4$ | 219.5 | 217.2 | $E_u^4$ | 365.8 | 370.4 |
| $E_g^5$ | 357.4 | – | | | |
| $A_g^5$ | 508.8 | – | | | |

FIG. 1. Raman spectra of CrSiTe$_3$ single crystals measured at 100 K in (a) parallel and (b) cross polarization configurations. The gray line represents the TeO$_2$ spectrum measured at 300 K. Inset: Raman spectrum of CrGeTe$_3$ in the parallel polarization configuration measured at 100 K.



FIG. 2. (a) The $E_g^3$ mode Raman spectra of CrSiTe$_3$ at four temperatures measured in the cross polarization configuration. Blue lines represent line shapes obtained as a convolution of the Fano line shape and Gaussian, calculated to fit the experimetal data. Temperature dependence of (b) the energy, (c) the line width, and (d) the Fano parameter $q$ of the $E_g^3$ mode. The dashed red line represents standard anharmonic behavior [28,29]. All the parameters show a change in tendency around 180 K.

modes can be expected to appear for both in-parallel and cross polarization configurations.

The Raman spectra of CrSiTe$_3$ for two main linear polarization configurations, at 100 K, are shown in Fig. 1. Four peaks can be observed in the spectra, at energies of 88.9, 118.2, 147.4, and 217.2 cm$^{-1}$. Since only the peak at 147.4 cm$^{-1}$ vanishes in the cross polarization configuration, it corresponds to the $A_g$ symmetry mode. The other three modes appear in both parallel and cross polarization configurations and, thereby, can be assigned as $E_g$ symmetry modes (Fig. 1).

In order to exclude the possibility that any of the observed features originate from the TeO$_2$ [17,27], its Raman spectrum is also presented in Fig. 1. It can be noted that no TeO$_2$ contribution is present in our CrSiTe$_3$ data. Furthermore, the observed CrSiTe$_3$ Raman spectra are also consistent with the CrGeTe$_3$ Raman spectra (see inset in Fig. 1), isostructural to CrSiTe$_3$. Five Raman-active modes have been observed for CrGeTe$_3$, two $A_g$ modes, at 137.9 and 296.6 cm$^{-1}$, and three $E_g$ modes, at 83.5, 112.2, and 217.5 cm$^{-1}$, in agreement with the previously published data [17,18]. The main difference in the spectra of CrSiTe$_3$ and CrGeTe$_3$ arises from the change in mass and lattice parameter effects that cause the peaks to shift.

Calculated and observed Raman-active phonon energies are compiled in Table II, together with the experimental energies of the infrared (IR)-active phonons [1], and are found to be in good agreement. Displacement patterns of the $A_g$
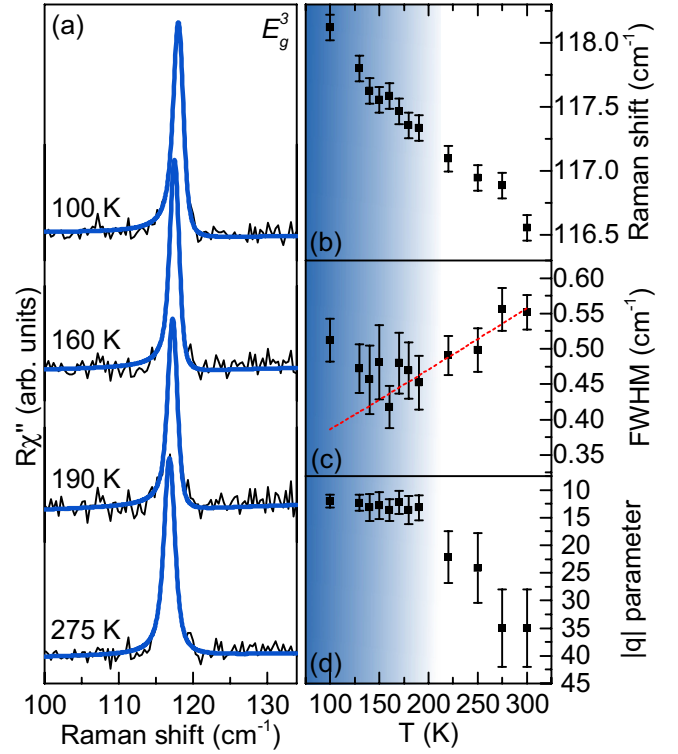
and $E_g$ symmetry modes are presented in Fig. 4, in the Appendix.

### B. Temperature dependence

After proper assignment of all the observed CrSiTe$_3$ Raman-active modes we proceeded with temperature evolution of their properties, focusing on the most prominent ones, $E_g^3$ and $A_g^3$. Figure 2(a) shows the spectral region of the doubly degenerate $E_g^3$ mode at an energy of 118.2 cm$^{-1}$, at four temperatures. Closer inspection of the 100 K spectra revealed clear asymmetry of the peak on the low-energy side. The presence of defects may result in the appearance of the mode asymmetry [30], however, they would also contribute to the mode line width and, possibly, the appearance of phonons from the edge of the Brillouin zone in the Raman spectra [29]. The very narrow lines and absence of additional features in the Raman spectra of CrSiTe$_3$ do not support this scenario. The asymmetry may also arise when the phonon is coupled to a continuum [31]. Such a coupling of the $E_g^3$ phonon mode would result in a line shape given by the convolution of a Fano function and a Gaussian, the latter representing the resolution of the spectrometer [29]. Comparison between the Fano line shape convoluted with a Gaussian, the Voigt line shape, and the experimental data at 100 K is presented in Fig. 5, in the
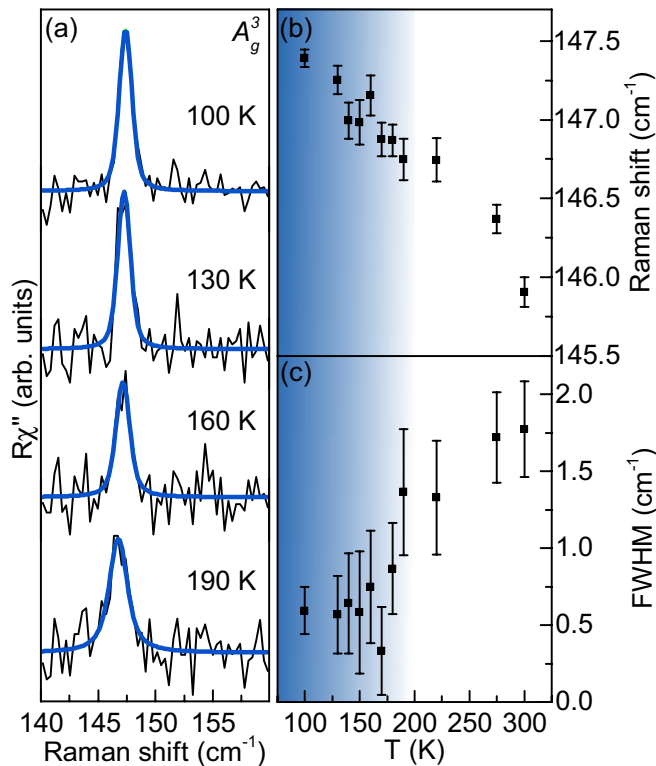
FIG. 3. (a) $A_g^3$ mode Raman spectra of CrSiTe$_3$ at four temperatures measured in the parallel polarization configuration. Blue lines represent Voigt line shapes. (b) Energy and (c) line-width temperature dependence of the $A_g^3$ mode.



FIG. 4. Unit cell of a CrSiTe$_3$ single crystal (solid lines) with the displacement patterns of the $A_g$ and $E_g$ symmetry modes. Arrow lengths are proportional to the square root of the interatomic forces.

Appendix, with the former yielding better agreement with the experimental data. Furthermore, it fully captures the $E_g^3$ mode line shape at all temperatures under investigation [Figs. 2(a) and 6].

Upon cooling of the sample, the $E_g^3$ mode energy hardens [Fig. 2(b)] with a very small discontinuity in the temperature range around 180 K. Down to the same temperature, the line width monotonically narrows in line with the standard anharmonic behavior [dashed red line in Fig. 2(c)]. Upon further cooling, the line width increased, deviating from the expected anharmonic tendency. This indicates activation of an additional scattering mechanism, e.g., spin-phonon interaction. Figure 2(d) shows the evolution of the Fano parameter, $|q|$. Whereas in the region below 180 K, it increases slightly but continuously, at higher temperatures it promptly goes to lower values and the mode recovers a symmetric line shape. We believe that the observed behavior of the $E_g^3$ mode can be traced back to the short-range magnetic correlations, which, according to Ref. [1], persist up to 150 K, and the strong spin-phonon coupling in CrSiTe$_3$. Similar behavior of the energy and line width, which differs from the conventional anharmonic, as well as the $E_g$ mode Fano-type line shape, was recently reported in $\alpha$-RuCl$_3$ and was interpreted as a consequence of the spin-phonon interaction [32].

Unlike the $E_g^3$ mode, no pronounced asymmetry was observed for the $A_g^3$ mode. As can be seen from Figs. 3(b) and 3(c) both the energy and the line width of the $A_g^3$ mode showed
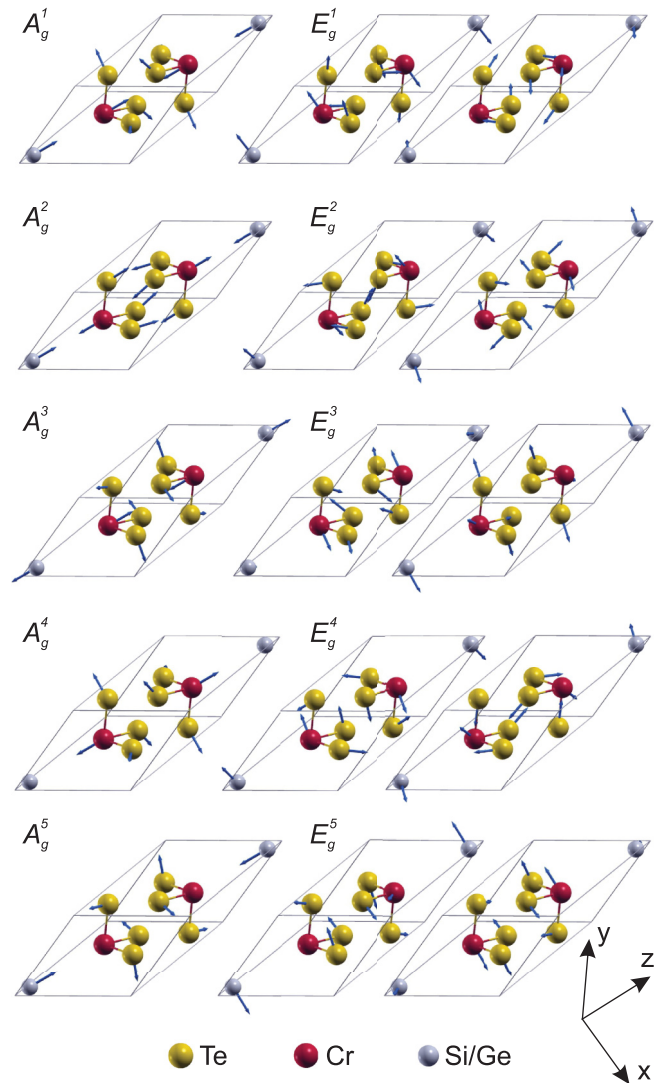
a similar change in tendency in the same temperature region as the $E_g^3$ mode, most likely due to the spin-phonon coupling.

## IV. CONCLUSION

The lattice dynamics of CrSiTe$_3$, a compound isostructural to CrGeTe$_3$, is presented. An $A_g$ and three $E_g$ modes were observed and assigned. The experimental results are well supported by theoretical calculations. The temperature dependences of the energies and line widths of the $A_g^3$ and $E_g^3$ modes deviate from the conventional anharmonic model in the temperature range around 180 K. In addition, the $E_g^3$ mode shows clear Fano resonance at lower temperatures. This can be related to the previously reported short-range magnetic correlations at temperatures up to 150 K [1] and the strong spin-phonon coupling.
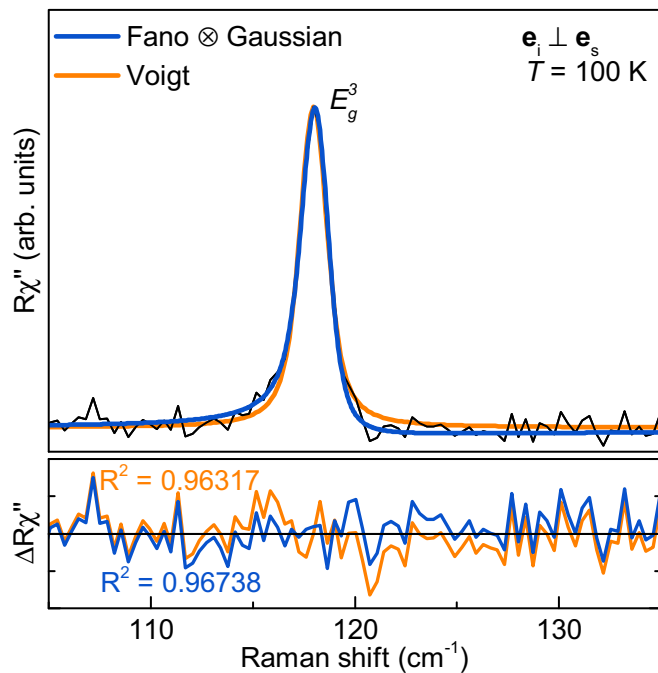
FIG. 5. Analysis of the $E_g^3$ asymmetry. Measured data are shown as the black line. The solid blue line represents the line shape obtained as a convolution of the Fano line shape and a Gaussian, whereas the orange line represents a Voigt line shape, both calculated to fit the experimental data. The Voigt profile deviates from the experimental data at the peak flanks.

## APPENDIX

### 1. Eigenvectors of Raman-active modes

Figure 4 summarizes the $A_g$ and $E_g$ symmetry mode displacement patterns of a CrSiTe₃ single crystal ($R\bar{3}$ space group). Arrow lengths are proportional to the square root of the interatomic forces.

### 2. Asymmetry of the $E_g^3$ line

The peak at 118.2 cm⁻¹, which we assigned as the $E_g^3$ symmetry mode, at low temperatures shows a significant asymmetry towards lower energies. The possibility of additional defect-induced features in Raman spectra can be excluded, since the modes are very narrow, suggesting high crystallinity
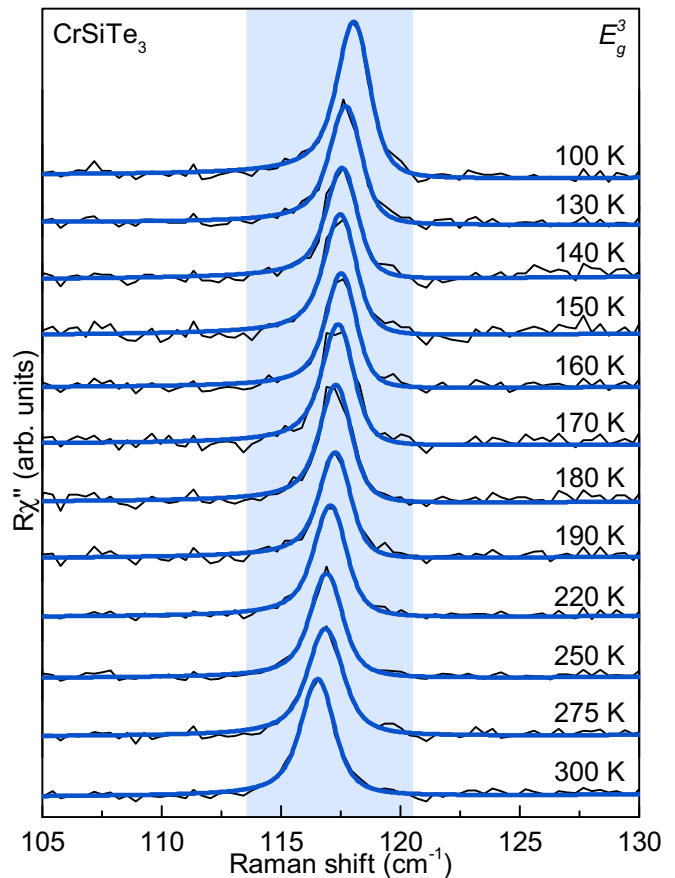


FIG. 6. The $E_g^3$ mode Raman spectra of CrSiTe₃ at all temperatures measured in the cross polarization configuration. Blue lines represent calculated spectra obtained as the convolution of the Fano line shape and Gaussian.

of the sample. Also, the theoretical calculations do not predict additional Raman-active modes in this energy region. On the other hand, coupling of the phonon mode to a continuum may result in an asymmetric line shape described with the Fano function. Due to the finite resolution of the spectrometer it has to be convoluted with a Gaussian ($\Gamma_G = 1\,\text{cm}^{-1}$). In Fig. 5 we present a comparison of the line obtained as a convolution of the Fano line shape and a Gaussian (blue line) and a Voigt line shape (orange line) fitted to the experimental data. Whereas the Voigt line shape deviates at the peak flanks, excellent agreement has been achieved for convolution of the Fano line shape and a Gaussian.

### 3. $E_g^3$ mode temperature dependence

Figure 6 shows Raman spectra of CrSiTe₃ in the region of the $E_g^3$ mode in the cross polarization configuration at various temperatures. Solid blue lines represent the convolution of the Fano line shape and Gaussian fitted to the experimental data. The asymmetry is the most pronounced below 190 K. Above this temperature, the asymmetry is decreasing, and at high temperatures the peak recovers the fully symmetric line shape.

[1] L. D. Casto, A. J. Clune, M. O. Yokosuk, J. L. Musfeldt, T. J. Williams, H. L. Zhuang, M.-W. Lin, K. Xiao, R. G. Hennig, B. C. Sales, J.-Q. Yan, and D. Mandrus, Strong spin-lattice coupling in CrSiTe$_3$, APL Mater. **3**, 041515 (2015).

[2] X. Zhang, Y. Zhao, Q. Song, S. Jia, J. Shi, and W. Han, Magnetic anisotropy of the single-crystalline ferromagnetic insulator Cr$_2$Ge$_2$Te$_6$, Jpn. J. Appl. Phys. **55**, 033001 (2016).

[3] T. Leineweber and H. Kronmuller, Micromagnetic examination of exchange coupled ferromagnetic nanolayers, J. Magn. Magn. Mater. **176**, 145 (1997).

[4] G. Ouvrard, E. Sandre, and R. Brec, Synthesis and crystal structure of a new layered phase: The chromium hexatellurosilicate Cr$_2$Si$_2$Te$_6$, J. Solid State Chem. **73**, 27 (1988).

[5] B. Siberchicot, S. Jobic, V. Carteaux, P. Gressier, and G. Ouvrard, Band structure calculations of ferromagnetic chromium tellurides CrSiTe$_3$ and CrGeTe$_3$, J. Phys. Chem. **100**, 5863 (1996).

[6] V. Carteaux, F. Moussa, and M. Spiesser, 2D Ising-like ferromagnetic behaviour for the lamellar Cr$_2$Si$_2$Te$_6$ compound: A neutron scattering investigation, Europhys. Lett. **29**, 251 (1995).

[7] N. Sivadas, M. W. Daniels, R. H. Swendsen, S. Okamoto, and D. Xiao, Magnetic ground state of semiconducting transition-metal trichalcogenide monolayers, Phys. Rev. B **91**, 235425 (2015).

[8] K. S. Novoselov, A. K. Geim, S. V. Morozov, D. Jiang, Y. Zhang, S. V. Dubonos, I. V. Grigorieva, and A. A. Firsov, Electric field effect in atomically thin carbon films, Science **306**, 666 (2004).

[9] Q. H. Wang, K. Kalantar-Zadeh, A. Kis, J. N. Coleman, and M. S. Strano, Electronics and optoelectronics of two-dimensional transition metal dichalcogenides, Nat. Nanotechnol. **7**, 699 (2012), review Article.

[10] C. Gong, L. Li, Z. Li, H. Ji, A. Stern, Y. Xia, T. Cao, W. Bao, C. Wang, Y. Wang, Z. Q. Qiu, R. J. Cava, S. G. Louie, J. Xia, and X. Zhang, Discovery of intrinsic ferromagnetism in two-dimensional van der Waals crystals, Nature **546**, 265 (2017).

[11] B. Huang, G. Clark, E. Navarro-Moratalla, D. R. Klein, R. Cheng, K. L. Seyler, D. Zhong, E. Schmidgall, M. A. McGuire, D. H. Cobden, W. Yao, D. Xiao, P. Jarillo-Herrero, and X. Xu, Layer-dependent ferromagnetism in a van der Waals crystal down to the monolayer limit, Nature **546**, 270 (2017).

[12] W. Xing, Y. Chen, P. M. Odenthal, X. Zhang, W. Yuan, T. Su, Q. Song, T. Wang, J. Zhong, S. Jia, X. C. Xie, Y. Li, and W. Han, Electric field effect in multilayer Cr$_2$Ge$_2$Te$_6$: A ferromagnetic 2D material, 2D Mater. **4**, 024009 (2017).

[13] T. J. Williams, A. A. Aczel, M. D. Lumsden, S. E. Nagler, M. B. Stone, J.-Q. Yan, and D. Mandrus, Magnetic correlations in the quasi-two-dimensional semiconducting ferromagnet CrSiTe$_3$, Phys. Rev. B **92**, 144404 (2015).

[14] X. Li and J. Yang, CrXTe$_3$ (X = Si, Ge) nanosheets: Two dimensional intrinsic ferromagnetic semiconductors, J. Mater. Chem. C **2**, 7071 (2014).

[15] M.-W. Lin, H. L. Zhuang, J. Yan, T. Z. Ward, A. A. Puretzky, C. M. Rouleau, Z. Gai, L. Liang, V. Meunier, B. G. Sumpter, P. Ganesh, P. R. C. Kent, D. B. Geohegan, D. G. Mandrus, and K. Xiao, Ultrathin nanosheets of CrSiTe$_3$: A semiconducting two-dimensional ferromagnetic material, J. Mater. Chem. C **4**, 315 (2016).

[16] B. Liu, Y. Zou, S. Zhou, L. Zhang, Z. Wang, H. Li, Z. Qu, and Y. Zhang, Critical behavior of the van der Waals bonded high T$_C$ ferromagnet Fe$_3$GeTe$_2$, Sci. Rep. **7**, 6184 (2017).

[17] Y. Tian, M. J. Gray, H. Ji, R. J. Cava, and K. S. Burch, Magneto-elastic coupling in a potential ferromagnetic 2D atomic crystal, 2D Mater. **3**, 025035 (2016).

[18] Y. Sun, R. C. Xiao, G. T. Lin, R. R. Zhang, L. S. Ling, Z. W. Ma, X. Luo, W. J. Lu, Y. P. Sun, and Z. G. Sheng, Effects of hydrostatic pressure on spin-lattice coupling in two-dimensional ferromagnetic Cr$_2$Ge$_2$Te$_6$, Appl. Phys. Lett. **112**, 072409 (2018).

[19] Y. Liu and C. Petrovic, Critical behavior of quasi-two-dimensional semiconducting ferromagnet Cr$_2$Ge$_2$Te$_6$, Phys. Rev. B **96**, 054406 (2017).

[20] G. T. Lin, H. L. Zhuang, X. Luo, B. J. Liu, F. C. Chen, J. Yan, Y. Sun, J. Zhou, W. J. Lu, P. Tong, Z. G. Sheng, Z. Qu, W. H. Song, X. B. Zhu, and Y. P. Sun, Tricritical behavior of the two-dimensional intrinsically ferromagnetic semiconductor CrGeTe$_3$, Phys. Rev. B **95**, 245212 (2017).

[21] P. Giannozzi, S. Baroni, N. Bonini, M. Calandra, R. Car, C. Cavazzoni, D. Ceresoli, G. L. Chiarotti, M. Cococcioni, I. Dabo, A. D. Corso, S. de Gironcoli, S. Fabris, G. Fratesi, R. Gebauer, U. Gerstmann, C. Gougoussis, A. Kokalj, M. Lazzeri, L. Martin-Samos, N. Marzari, F. Mauri, R. Mazzarello, S. Paolini, A. Pasquarello, L. Paulatto, C. Sbraccia, S. Scandolo, G. Sclauzero, A. P. Seitsonen, A. Smogunov, P. Umari, and R. M. Wentzcovitch, Quantum espresso: A modular and open-source software project for quantum simulations of materials, J. Phys.: Condens. Matter **21**, 395502 (2009).

[22] J. P. Perdew, K. Burke, and M. Ernzerhof, Generalized Gradient Approximation Made Simple, Phys. Rev. Lett. **77**, 3865 (1996).

[23] P. E. Blöchl, Projector augmented-wave method, Phys. Rev. B **50**, 17953 (1994).

[24] G. Kresse and D. Joubert, From ultrasoft pseudopotentials to the projector augmented-wave method, Phys. Rev. B **59**, 1758 (1999).

[25] G. Stefan, Semiempirical GGA-type density functional constructed with a long-range dispersion correction, J. Comput. Chem. **27**, 1787 (2006).

[26] R. E. Marsh, The crystal structure of Cr$_2$Si$_2$Te$_6$: Corrigendum, J. Solid State Chem. **77**, 190 (1988).

[27] N. Lazarević, E. S. Bozin, M. Šćepanović, M. Opačić, Hechang Lei, C. Petrovic, and Z. V. Popović, Probing IrTe$_2$ crystal symmetry by polarized Raman scattering, Phys. Rev. B **89**, 224301 (2014).

[28] M. Opačić, N. Lazarević, M. Šćepanović, H. Ryu, H. Lei, C. Petrovic, and Z. V. Popović, Evidence of superconductivity-induced phonon spectra renormalization in alkali-doped iron selenides, J. Phys.: Condens. Matter **27**, 485701 (2015).

[29] A. Baum, A. Milosavljević, N. Lazarević, M. M. Radonjić, B. Nikolić, M. Mitschek, Z. Inanloo Maranloo, M. Šćepanović, M. Grujić-Brojčin, N. Stojilović, M. Opel, Aifeng Wang, C. Petrovic, Z. V. Popović, and R. Hackl, Phonon anomalies in FeS, Phys. Rev. B **97**, 054306 (2018).

[30] N. Lazarević, M. Radonjić, M. Šćepanović, Hechang Lei, D. Tanasković, C. Petrovic, and Z. V. Popović, Lattice dynamics of KNi$_2$Se$_2$, Phys. Rev. B **87**, 144305 (2013).

[31] N. Lazarević, Z. V. Popović, Rongwei Hu, and C. Petrovic, Evidence for electron-phonon interaction in Fe$_{1-x}$$M_x$Sb$_2$ ($M =$ Co and Cr; $0 \leqslant x \leqslant 0.5$) single crystals, Phys. Rev. B **81**, 144302 (2010).

[32] L. J. Sandilands, Y. Tian, K. W. Plumb, Y.-J. Kim, and K. S. Burch, Scattering Continuum and Possible Fractionalized Excitations in $\alpha$-RuCl$_3$, Phys. Rev. Lett. **114**, 147201 (2015).

# Lattice dynamics and phase transitions in Fe$_{3-x}$GeTe$_2$

A. Milosavljević,[1] A. Šolajić,[1] S. Djurdjić-Mijin,[1] J. Pešić,[1] B. Višić,[1] Yu Liu (刘育),[2] C. Petrovic,[2]
N. Lazarević,[1] and Z. V. Popović[1,3]

[1]*Center for Solid State Physics and New Materials, Institute of Physics Belgrade,*
*University of Belgrade, Pregrevica 118, 11080 Belgrade, Serbia*
[2]*Condensed Matter Physics and Materials Science Department, Brookhaven National Laboratory, Upton, New York 11973-5000, USA*
[3]*Serbian Academy of Sciences and Arts, Knez Mihailova 35, 11000 Belgrade, Serbia*

We present Raman spectroscopy measurements of the van der Waals bonded ferromagnet Fe$_{3-x}$GeTe$_2$, together with lattice dynamics. Four out of eight Raman active modes are observed and assigned, in agreement with numerical calculations. The energies and linewidths of the observed modes display an unconventional temperature dependence at about 150 and 220 K, followed by the nonmonotonic evolution of the Raman continuum. Whereas the former can be related to the magnetic phase transition, the origin of the latter anomaly remains an open question.

## I. INTRODUCTION

A novel class of magnetism hosting van der Waals bonded materials has recently become of great interest, since the materials are suitable candidates for numbers of technical applications [1–5]. Whereas Cr$X$Te$_3$ ($X$ = Si, Ge, Sn) and Cr$X_3$ ($X$ = Cl, Br, I) classes maintain low phase transition temperatures [1,6–9] even in a monolayer regime [10], Fe$_{3-x}$GeTe$_2$ has a high bulk transition temperature, between 220 and 230 K [11,12], making it a promising applicant.

The Fe$_{3-x}$GeTe$_2$ crystal structure consists of Fe$_{3-x}$Ge sublayers stacked between two sheets of Te atoms, and a van der Waals gap between neighboring Te layers [13,14]. Although the structure contains two different types of Fe atoms, it is revealed that vacancies take place only in the Fe2 sites [13,15].

Neutron diffraction, thermodynamic and transport measurements, and Mössbauer spectroscopy were used to analyze the magnetic and functional properties of Fe$_{3-x}$GeTe$_2$, with an Fe atom deficiency of $x \approx 0.1$ and $T_C = 225$ K. It is revealed that at a temperature of 1.5 K, magnetic moments of $1.95(5)\mu_B$ and $1.56(4)\mu_B$ are directed along the easy magnetic $c$ axes [16]. In chemical vapor transport (CVT) grown Fe$_3$GeTe$_2$ single crystals, besides the ferromagnetic (FM)-paramagnetic (PM) transition at a temperature of 214 K, FM layers order antiferromagnetically at 152 K [17]. Close to a ferromagnetic transition temperature of 230 K, a possible Kondo lattice behavior, i.e., coupling of traveling electrons and periodically localized spins, is indicated at $T_K = 190 \pm 20$ K, which is in good agreement with theoretical predictions of 222 K [18].

Lattice parameters, as well as the magnetic transition temperature, vary with Fe ion concentration. Lattice parameters $a$ and $c$ follow the opposite trend, whereas the Curie temperature $T_C$ decreases with an increase of Fe ion concentration [15]. For flux-grown crystals, the critical behavior was investigated by bulk dc magnetization around the ferromagnetic phase transition temperature of 152 K [13]. The anomalous Hall effect was also studied, where a significant amount of defects produces bad metallic behavior [19].

Theoretical calculations predict a dynamical stability of Fe$_3$GeTe$_2$ single-layer, uniaxial magnetocrystalline anisotropy that originates from spin-orbit coupling [20]. Recently, anomalous Hall effect measurements on single-crystalline metallic Fe$_3$GeTe$_2$ nanoflakes with different thicknesses are reported, with a $T_C$ near 200 K and strong perpendicular magnetic anisotropy [21].

We report Fe$_{3-x}$GeTe$_2$ single-crystal lattice dynamic calculations, together with Raman spectroscopy measurements. Four out of eight Raman active modes were observed and assigned. Phonon energies are in a good agreement with theoretical predictions. Analyzed phonon energies and linewidths reveal fingerprint of a ferromagnetic phase transition at a temperature around 150 K. Moreover, discontinuities in the phonon properties are found at temperatures around 220 K. Consistently, in the same temperature range, the Raman continuum displays nonmonotonic behavior.

## II. EXPERIMENT AND NUMERICAL METHOD

Fe$_{3-x}$GeTe$_2$ single crystals were grown by the self-flux method as previously described [13]. Samples for scanning electron microscopy (SEM) were cleaved and deposited on graphite tape. Energy dispersive spectroscopy (EDS) maps were collected using a FEI Helios NanoLab 650 instrument equipped with an Oxford Instruments EDS system, equipped with an X-max SSD detector operating at 20 kV. The surface of the as-cleaved Fe$_{3-x}$GeTe$_2$ crystal appears to be uniform for several tens of microns in both directions, as shown in Fig. 4 of Appendix A. Additionally, the elemental composition maps of Fe, Ge, and Te show a distinctive homogeneity of all the three elements (Fig. 5 of Appendix A).

For Raman scattering experiments, a Tri Vista 557 spectrometer was used in the backscattering micro-Raman configuration. As an excitation source, a solid state laser with a 532 nm line was used. In our scattering configuration, the plane of incidence is the $ab$ plane, where $|a| = |b|$ ($\angle(a, b) = 120°$), with the incident (scattered) light propagation direction

TABLE I. Top panel: The type of atoms, Wyckoff positions, each site's contribution to the phonons in the $\Gamma$ point, and corresponding Raman tensors for the $P6_3/mmc$ space group of $Fe_{3-x}GeTe_2$. Bottom panel: Phonon symmetry, calculated optical Raman active phonon frequencies (in $cm^{-1}$) for the magnetic (M) phase, and experimental values for Raman active phonons at 80 K.

| Space group $P6_3/mmc$ (No. 194) | |
|---|---|
| Fe1 (4e) | $A_{1g} + E_{1g} + E_{2g} + A_{2u} + E_{1u}$ |
| Fe2 (2c) | $E_{2g} + A_{2u} + E_{1u}$ |
| Ge (2d) | $E_{2g} + A_{2u} + E_{1u}$ |
| Te (2c) | $A_{1g} + E_{1g} + E_{2g} + A_{2u} + E_{1u}$ |

Raman tensors

$$A_{1g} = \begin{pmatrix} a & 0 & 0 \\ 0 & a & 0 \\ 0 & 0 & b \end{pmatrix} \qquad E_{1g} = \begin{pmatrix} 0 & 0 & -c \\ 0 & 0 & c \\ -c & c & 0 \end{pmatrix} \qquad E_{2g} = \begin{pmatrix} d & -d & 0 \\ -d & -d & 0 \\ 0 & 0 & 0 \end{pmatrix}$$

Raman active modes

| Symmetry | Calculations (M) | Experiment (M) |
|---|---|---|
| $E_{2g}^1$ | 50.2 | |
| $E_{1g}^1$ | 70.3 | |
| $E_{2g}^2$ | 122.2 | 89.2 |
| $A_{1g}^1$ | 137.2 | 121.1 |
| $E_{1g}^2$ | 209.5 | |
| $E_{2g}^3$ | 228.6 | 214.8 |
| $A_{1g}^2$ | 233.4 | 239.6 |
| $E_{2g}^4$ | 334.3 | |

along the $c$ axes. Samples were cleaved in the air, right before being placed in the vacuum. All the measurements were performed in the high vacuum ($10^{-6}$ mbar) using a KONTI CryoVac continuous helium flow cryostat with a 0.5 mm thick window. To achieve laser beam focusing, a microscope objective with $\times 50$ magnification was used. A Bose factor correction of all spectra was performed. More details can be found in Appendix C.

Density functional theory (DFT) calculations were performed with the QUANTUM ESPRESSO (QE) software package [22]. We used the projector augmented-wave (PAW) pseudopotentials [23,24] with the Perdew-Burke-Ernzerhof (PBE) exchange-correlation functional [25]. The electron wave function and charge density cutoffs of 64 and 782 Ry were chosen, respectively. The $k$ points were sampled using the Monkhorst-Pack scheme, with an $8 \times 8 \times 4$ $\Gamma$-centered grid. Both magnetic and nonmagnetic calculations were performed, using the experimentally obtained lattice parameters and the calculated values obtained by relaxing the theoretically proposed structure. In order to obtain the lattice parameters accurately, a treatment of the van der Waals interactions is introduced. The van der Waals interaction was included in all calculations using the Grimme-D2 correction [26]. Phonon frequencies in the $\Gamma$ point are calculated within the linear response method implemented in QE.

### III. RESULTS AND DISCUSSION

$Fe_{3-x}GeTe_2$ crystallizes in a hexagonal crystal structure, described with the $P6_3/mmc$ ($D_{6h}^4$) space group. The atom type, site symmetry, each site's contribution to the phonons

in the $\Gamma$ point, and corresponding Raman tensors for the $P6_3/mmc$ space group are presented in Table I.

Calculated displacement patterns of Raman active modes, which can be observed in our scattering configuration, are presented in Fig. 1(a). Since the Raman tensor of the $E_{1g}$ mode contains only the $z$ component (Table I), by selection rules, it cannot be detected when measuring from the $ab$ plane in the backscattering configuration. Whereas $A_{1g}$ modes include vibrations of Fe and Te ions along the $c$ axis, $E_{2g}$ modes include in-plane vibrations of all four atoms. The Raman spectra of $Fe_{3-x}GeTe_2$ in the magnetic phase (M), at 80 K, and nonmagnetic phase (NM), at 280 K, in a parallel scattering configuration ($\mathbf{e}_i \parallel \mathbf{e}_s$), are presented in Fig. 1 (b). As it can be seen, four peaks at 89.2, 121.1, 214.8, and 239.6 $cm^{-1}$ can be clearly observed at 80 K. According to numerical calculations (see Table I), peaks at 89.2 and 239.6 $cm^{-1}$ correspond to two out of four $E_{2g}$ modes, whereas peaks at 121.1 and 239.6 $cm^{-1}$ can be assigned as two $A_{1g}$ symmetry modes. One should note that numerical calculations performed by using experimentally obtained lattice parameters in the magnetic phase yield a better agreement with experimental values. This is not surprising since the calculations are performed for the stoichiometric compound as opposed to the nonstoichiometry of the sample. Furthermore, it is known that lattice parameters strongly depend on the Fe atom deficiency [15]. All calculated Raman and infrared phonon frequencies, for the magnetic and nonmagnetic phase of $Fe_{3-x}GeTe_2$, using relaxed and experimental lattice parameters, together with experimentally observed Raman active modes, are summarized in Table II of Appendix D.

After assigning all observed modes we focused on their temperature evolution. Having in mind finite instrumental
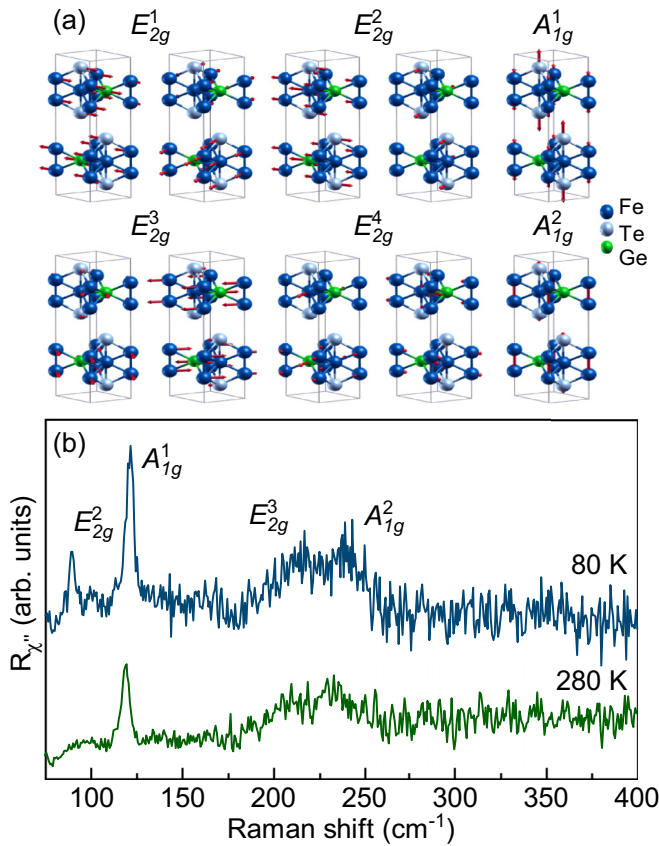
FIG. 1. (a) Displacement patterns of $A_{1g}$ and $E_{2g}$ symmetry modes. (b) Raman spectra of Fe$_{3-x}$GeTe$_2$ single crystal measured at different temperatures in a parallel polarization configuration.



FIG. 2. Energy and linewidth temperature dependence of $A_{1g}^1$ [(a) and (b)], $E_{2g}^3$ [(c) and (d)], and $A_{1g}^2$ [(e) and (f)] phonon modes in Fe$_{3-x}$GeTe$_2$.

broadening, the Voigt line shape was used for the data analysis [27,28]. The modeling procedure is described in detail in Appendix B and presented in Fig. 6. Figure 2 shows the temperature evolution of the energy and linewidth of the $A_{1g}^1$, $E_{2g}^3$, and $A_{1g}^2$ modes between 80 and 300 K. Upon heating the sample, both the energy and linewidth of $A_{1g}^1$ and $A_{1g}^2$ symmetry modes exhibit a small but sudden discontinuity at about 150 K [Figs. 2(a) and 2(e)]. An apparent discontinuity in energy of all analyzed Raman modes is again present at temperatures around 220 K. In the same temperature range the linewidths of these Raman modes show a clear deviation from the standard anharmonic behavior [27–31].

Apart from the anomalies in the phonon spectra, a closer inspection of the temperature-dependent Raman spectra measured in the parallel polarization configuration reveals a pronounced evolution of the Raman continuum [Fig. 3(a)]. For the analysis we have used a simple model including a damped Lorentzian and linear term, $\chi''_{cont} \propto a\Gamma\omega/(\omega^2 + \Gamma^2) + b\omega$ [32], where $a$, $b$, and $\Gamma$ are temperature-dependent parameters. Figure 3(b) summarizes the results of the analysis with the linear term omitted (most likely originating from a luminescence). At approximately the same temperatures, where phonon properties exhibit discontinuities, the continuum temperature dependence manifests nonmonotonic behavior. The maximum positions of the curve were obtained by integrating
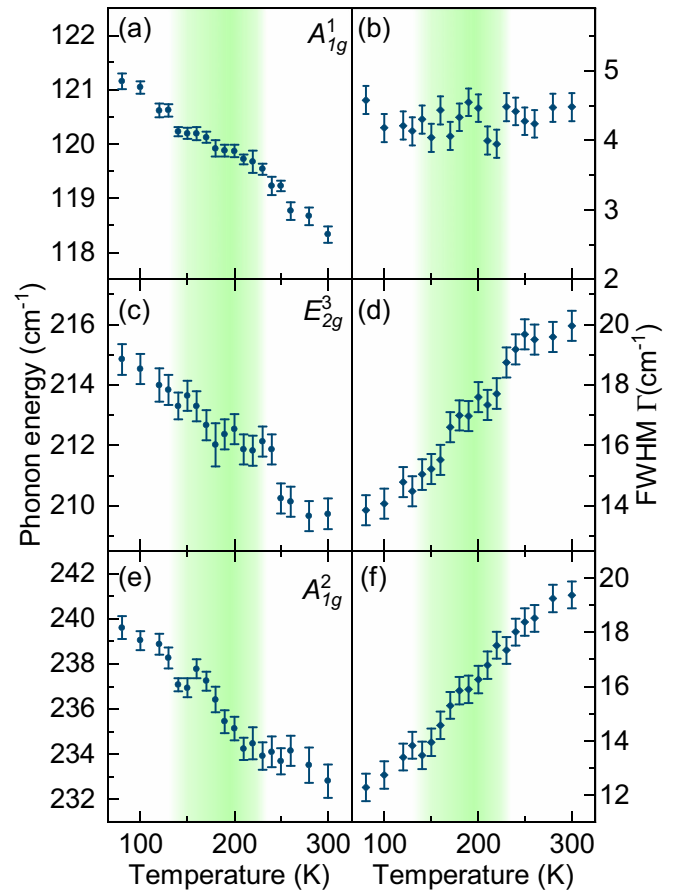
those shown in Fig. 3(b). The inset of Fig. 3(b) shows the temperature evolution of their displacements. This analysis confirms the presence of discontinuities in the electronic continuum at temperatures around 150 and 220 K, which leaves a trace in the phonon behavior around these temperatures (Fig. 2). While we do not have evidence for the Kondo effect in the Fe$_{3-x}$GeTe$_2$ crystals we measured, a modification of the electronic background at FM ordering due to localization or the Kondo effect cannot be excluded.

The temperature evolutions of the phonon self-energies and the continuum observed in the Raman spectra of Fe$_{3-x}$GeTe$_2$ suggest the presence of phase transition(s). Magnetization measurements of the samples were performed as described in Ref. [13], revealing a FM-PM transition at 150 K. Thus, the discontinuity in the observed phonon properties around this temperature can be traced back to the weak to moderate spin-phonon coupling. The question remains open regarding the anomaly observed at about 220 K. As previously reported, the Curie temperature of the Fe$_{3-x}$GeTe$_2$ single crystals grown by the CVT method is between 220 and 230 K [11,12,14], varying with the vacancy concentration, i.e., a decrease in the vacancy content will result an increment of $T_C$ [15]. On the other hand, the Fe$_{3-x}$GeTe$_2$ crystals grown by the self-flux method usually have a lower Curie temperature, since the
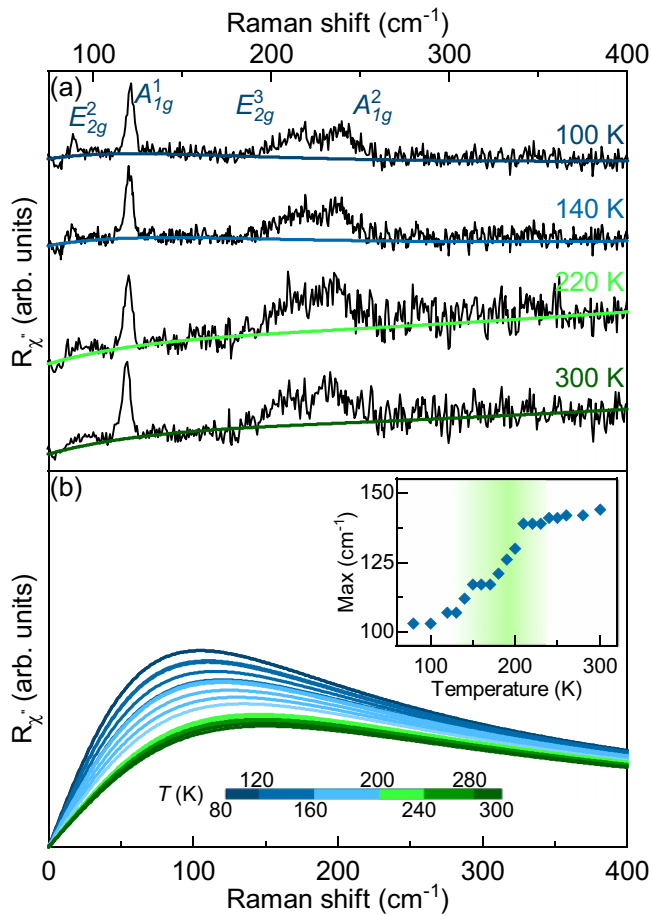
FIG. 3. (a) Raman spectra of Fe$_{3-x}$GeTe$_2$ at four temperatures measured in a parallel polarization configuration. Solid lines represent the theoretical fit to the experimental data. (b) Temperature evolution of the electronic continuum after omitting the linear term. Inset: Displacement of the maximum of fitted curves.

vacancy content is higher [13,15]. Crystals used in the Raman scattering experiment presented here were grown by the self-flux method with a Fe vacancy content of $x \approx 0.36$ [13]. This is in good agreement with our EDS results of $x = 0.4 \pm 0.1$, giving rise to the FM-PM transition at 150 K. Nevertheless,
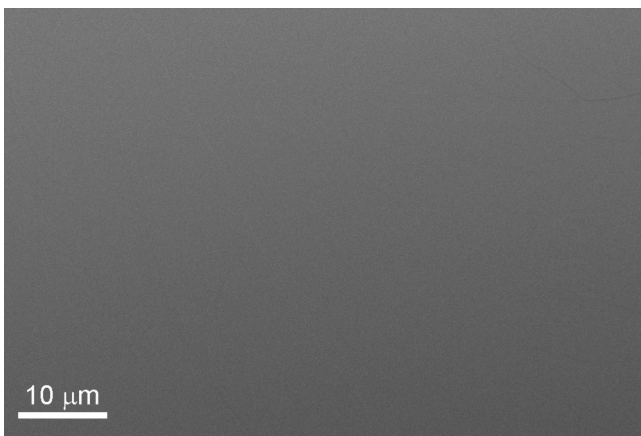


FIG. 4. SEM image of a Fe$_{3-x}$GeTe$_2$ single crystal.



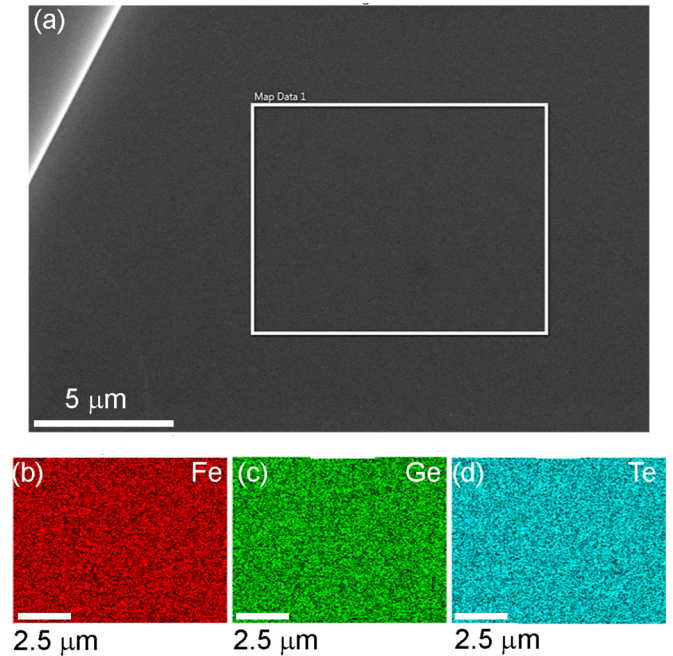FIG. 5. EDS mapping on a Fe$_{3-x}$GeTe$_2$ single crystal. (a) Secondary electron image of the crystal with the mapping performed within the rectangle. (b)–(d) Associated EDS maps for Fe, Ge, and Te, respectively.

an inhomogeneous distribution of vacancies may result the formation of vacancy depleted "islands" which in turn would result in an anomaly at 220 K similar to the one observed in our Raman data. However, the EDS data (see Fig. 5) do not support this possibility. At this point we can only speculate that while the long-range order temperature is shifted to a lower temperature by the introduction of vacancies, short-range correlations may develop at 220 K.

## IV. CONCLUSION

We have studied the lattice dynamics of flux-grown Fe$_{3-x}$GeTe$_2$ single crystals by means of Raman spectroscopy and DFT. Four out of eight Raman active modes, two $A_{1g}$ and two $E_{2g}$, have been observed and assigned. DFT calculations are in good agreement with experimental results. The temperature dependence of the $A_{1g}^1$, $E_{2g}^3$, and $A_{1g}^2$ mode properties reveals a clear fingerprint of spin-phonon coupling, at a temperature of around 150 K. Furthermore, the anomalous behavior in the energies and linewidths of the observed phonon modes is present in the Raman spectra at temperatures around 220 K with the discontinuity also present in the electronic continuum. Its origin still remains an open question, and requires further analysis.
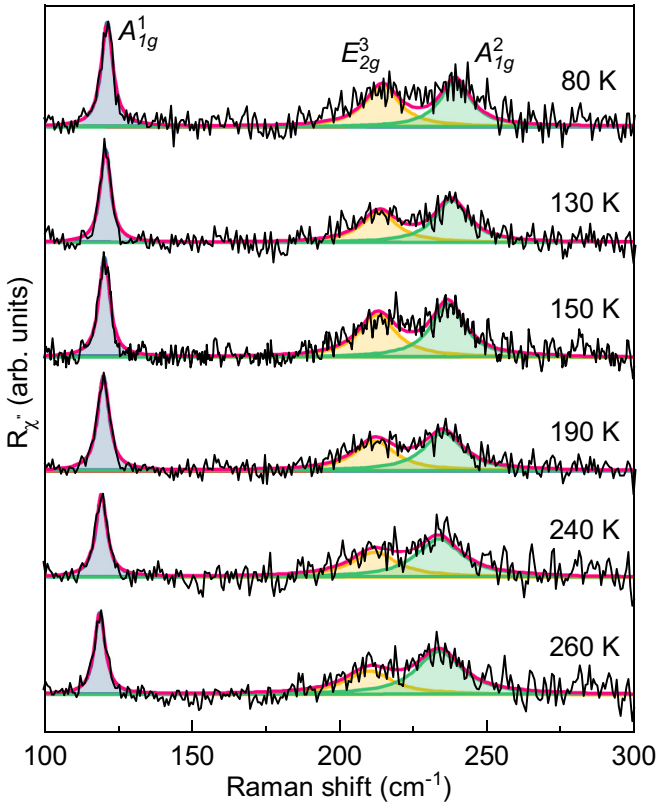
FIG. 6. Modeled Raman spectra of $Fe_{3-x}GeTe_2$ single crystal, after subtracting continuum contributions, obtained at various temperatures. For experimental data modeling, the Voigt line shape was used.

TABLE II. Top panel: Comparison of calculated energies of Raman active phonons using relaxed (R) and experimental [nonrelaxed (NR)] lattice parameters for the magnetic (M) and nonmagnetic phase (NM), given in $cm^{-1}$. Obtained experimental values in the magnetic phase at a temperature of 80 K are given in the last column. Bottom panel: Comparison of calculated energies of infrared optical phonons of $Fe_{3-x}GeTe_2$.

| Raman active modes | | | | | |
|---|---|---|---|---|---|
| | Calculations | | | | |
| Sym. | NM-R | M-R | NM-NR | M-NR | Experiment (M) |
| $E_{2g}^1$ | 28.4 | 49.6 | 33.9 | 50.2 | |
| $E_{1g}^1$ | 79.2 | 70.2 | 71.7 | 70.3 | |
| $E_{2g}^2$ | 115.5 | 121.0 | 100.0 | 122.2 | 89.2 |
| $A_{1g}^1$ | 151.7 | 139.2 | 131.7 | 137.2 | 121.1 |
| $E_{1g}^2$ | 225.5 | 206.0 | 194.3 | 209.5 | |
| $E_{2g}^3$ | 238.0 | 232.6 | 204.9 | 228.6 | 214.8 |
| $A_{1g}^2$ | 272.0 | 262.6 | 235.7 | 233.4 | 239.6 |
| $E_{2g}^4$ | 362.0 | 337.6 | 315.4 | 334.7 | |
| Infrared active modes | | | | | |
| $A_{2u}^1$ | 70.7 | 96.6 | 73.5 | 92.7 | |
| $E_{1u}^1$ | 112.5 | 121.2 | 89.4 | 121.6 | |
| $A_{2u}^2$ | 206.0 | 162.5 | 183.1 | 153.7 | |
| $E_{1u}^2$ | 226.4 | 233.6 | 192.1 | 231.3 | |
| $A_{2u}^3$ | 271.8 | 248.6 | 240.8 | 241.0 | |
| $E_{1u}^3$ | 361.1 | 336.6 | 314.7 | 334.7 | |

## APPENDIX A: ELECTRON MICROSCOPY

In order to examine the uniformity of $Fe_{3-x}GeTe_2$, Scanning electron microscopy (SEM) was performed on as-cleaved crystals. It can be seen from Fig. 4 that the crystals maintain uniformity for several tens of microns. Furthermore, the elemental composition was obtained using EDS mapping, as shown in Fig. 5. The atomic percentage, averaged over ten measurements, is 47%, 17%, and 36% ($\pm 2\%$) for Fe, Ge, and Te, respectively, with the vacancy content $x = 0.4 \pm 0.1$. The maps associated with the selected elements appear homogeneous, as they are all present uniformly with no apparent islands or vacancies.

## APPENDIX B: DATA MODELING

In order to obtain the temperature dependence of the energies and linewidths of the observed $Fe_{3-x}GeTe_2$ phonon modes, the Raman continuum, shown in colored lines in

Fig. 3(a), was subtracted for simplicity from the raw Raman susceptibility data (black line). The spectra obtained after the subtraction procedure are presented in Fig. 6 (black line) for various temperatures. Because of the finite resolution of the spectrometer and the fact that line shapes of all the observed phonons are symmetric, the Voigt line shape ($\Gamma_G = 0.8$ $cm^{-1}$) was used for data modeling. Blue, yellow, and green lines in Fig. 6 represent fitting curves for $A_{1g}^1$, $E_{2g}^3$, and $A_{1g}^2$ phonon modes, respectively, whereas the overall spectral shape is shown in the red line.

## APPENDIX C: EXPERIMENTAL DETAILS

Before being placed in a vacuum and being cleaved, the sample was glued to a copper plate with GE varnish in order to achieve good thermal conductivity and prevent strain effects. Silver paste, as a material with high thermal conductivity, was used to attach the copper plate with the sample to the cryostat. The laser beam spot, focused through an Olympus long-range objective of $\times$ 50 magnification, was approximately 6 $\mu m$ in size, with a power less than 1 mW at the sample surface. A TriVista 557 triple spectrometer was used in the subtractive mode, with a diffraction grating combination of 1800/1800/2400 grooves/mm and the entrance and second intermediate slit set to 80 $\mu m$, in order to enhance stray light rejection and attain good resolution.

## APPENDIX D: CALCULATIONS

In Table II the results of DFT calculations are presented for magnetic (M) and nonmagnetic (NM) relaxed and experimental lattice parameters. For comparison, the experimental results are shown in the last column. Since the lattice parameters strongly depend on the Fe atom deficiency, the best agreement with experimental results gives the magnetic nonrelaxed solution.

[1] N. Sivadas, M. W. Daniels, R. H. Swendsen, S. Okamoto, and D. Xiao, Magnetic ground state of semiconducting transition-metal trichalcogenide monolayers, Phys. Rev. B **91**, 235425 (2015).

[2] K. S. Novoselov, A. K. Geim, S. V. Morozov, D. Jiang, Y. Zhang, S. V. Dubonos, I. V. Grigorieva, and A. A. Firsov, Electric field rffect in atomically thin carbon films, Science **306**, 666 (2004).

[3] Q. H. Wang, K. Kalantar-Zadeh, A. Kis, J. N. Coleman, and M. S. Strano, Electronics and optoelectronics of two-dimensional transition metal dichalcogenides, Nat. Nanotechnol. **7**, 699 (2012).

[4] C. Gong, L. Li, Z. Li, H. Ji, A. Stern, Y. Xia, T. Cao, W. Bao, C. Wang, Y. Wang, Z. Q. Qiu, R. J. Cava, S. G. Louie, J. Xia, and X. Zhang, Discovery of intrinsic ferromagnetism in two-dimensional van der Waals crystals, Nature (London) **546**, 265 (2017).

[5] B. Huang, G. Clark, E. Navarro-Moratalla, D. R. Klein, R. Cheng, K. L. Seyler, D. Zhong, E. Schmidgall, M. A. McGuire, D. H. Cobden, W. Yao, D. Xiao, P. Jarillo-Herrero, and X. Xu, Layer-dependent ferromagnetism in a van der Waals crystal down to the monolayer limit, Nature (London) **546**, 270 (2017).

[6] M. A. McGuire, H. Dixit, V. R. Cooper, and B. C. Sales, Coupling of crystal structure and magnetism in the layered, ferromagnetic insulator CrI₃, Chem. Mater. **27**, 612 (2015).

[7] H. L. Zhuang, Y. Xie, P. R. C. Kent, and P. Ganesh, Computational discovery of ferromagnetic semiconducting single-layer CrSnTe₃, Phys. Rev. B **92**, 035407 (2015).

[8] G. T. Lin, H. L. Zhuang, X. Luo, B. J. Liu, F. C. Chen, J. Yan, Y. Sun, J. Zhou, W. J. Lu, P. Tong, Z. G. Sheng, Z. Qu, W. H. Song, X. B. Zhu, and Y. P. Sun, Tricritical behavior of the two-dimensional intrinsically ferromagnetic semiconductor CrGeTe₃, Phys. Rev. B **95**, 245212 (2017).

[9] L. D. Casto, A. J. Clune, M. O. Yokosuk, J. L. Musfeldt, T. J. Williams, H. L. Zhuang, M.-W. Lin, K. Xiao, R. G. Hennig, B. C. Sales, J.-Q. Yan, and D. Mandrus, Strong spin-lattice coupling in CrSiTe₃, APL Mater. **3**, 041515 (2015).

[10] M.-W. Lin, H. L. Zhuang, J. Yan, T. Z. Ward, A. A. Puretzky, C. M. Rouleau, Z. Gai, L. Liang, V. Meunier, B. G. Sumpter, P. Ganesh, P. R. C. Kent, D. B. Geohegan, D. G. Mandrus, and K. Xiao, Ultrathin nanosheets of CrSiTe₃: A semiconducting two-dimensional ferromagnetic material, J. Mater. Chem. C **4**, 315 (2016).

[11] J.-X. Zhu, M. Janoschek, D. S. Chaves, J. C. Cezar, T. Durakiewicz, F. Ronning, Y. Sassa, M. Mansson, B. L. Scott, N. Wakeham, E. D. Bauer, and J. D. Thompson, Electronic correlation and magnetism in the ferromagnetic metal Fe₃GeTe₂, Phys. Rev. B **93**, 144404 (2016).

[12] B. Chen, J. H. Yang, H. D. Wang, M. Imai, H. Ohta, C. Michioka, K. Yoshimura, and M. H. Fang, Magnetic properties of layered itinerant electron ferromagnet Fe₃GeTe₂, J. Phys. Soc. Jpn. **82**, 124711 (2013).

[13] Y. Liu, V. N. Ivanovski, and C. Petrovic, Critical behavior of the van der Waals bonded ferromagnet Fe₃₋ₓGeTe₂, Phys. Rev. B **96**, 144429 (2017).

[14] H.-J. Deiseroth, K. Aleksandrov, C. Reiner, L. Kienle, and R. K. Kremer, Fe₃GeTe₂ and Ni₃GeTe₂ - Two new layered transition-metal compounds: Crystal structures, HRTEM investigations, and magnetic and electrical properties, Eur. J. Inorg. Chem. **2006**, 1561 (2006).

[15] A. F. May, S. Calder, C. Cantoni, H. Cao, and M. A. McGuire, Magnetic structure and phase stability of the van der Waals bonded ferromagnet Fe₃₋ₓGeTe₂, Phys. Rev. B **93**, 014411 (2016).

[16] V. Yu. Verchenko, A. A. Tsirlin, A. V. Sobolev, I. A. Presniakov, and A. V. Shevelkov, Ferromagnetic order, strong magnetocrystalline anisotropy, and magnetocaloric effect in the layered telluride Fe₃₋δGeTe₂, Inorg. Chem. **54**, 8598 (2015).

[17] J. Yi, H. Zhuang, Q. Zou, Z. Wu, G. Cao, S. Tang, S. A. Calder, P. R. C. Kent, D. Mandrus, and Z. Gai, Competing antiferromagnetism in a quasi-2D itinerant ferromagnet: Fe₃GeTe₂, 2D Mater. **4**, 011005 (2016).

[18] Y. Zhang, H. Lu, X. Zhu, S. Tan, W. Feng, Q. Liu, W. Zhang, Q. Chen, Y. Liu, X. Luo, D. Xie, L. Luo, Z. Zhang, and X. Lai, Emergence of Kondo lattice behavior in a van der Waals itinerant ferromagnet, Fe₃GeTe₂, Sci. Adv. **4**, eaao6791 (2018).

[19] Y. Liu, E. Stavitski, K. Attenkofer, and C. Petrovic, Anomalous Hall effect in the van der Waals bonded ferromagnet Fe₃₋ₓGeTe₂, Phys. Rev. B **97**, 165415 (2018).

[20] H. L. Zhuang, P. R. C. Kent, and R. G. Hennig, Strong anisotropy and magnetostriction in the two-dimensional Stoner ferromagnet Fe₃GeTe₂, Phys. Rev. B **93**, 134407 (2016).

[21] C. Tan, J. Lee, S.-G. Jung, T. Park, S. Albarakati, J. Partridge, M. R. Field, D. G. McCulloch, L. Wang, and C. Lee, Hard magnetic properties in nanoflake van der Waals Fe₃GeTe₂, Nat. Commun. **9**, 1554 (2018).

[22] P. Giannozzi *et al.*, QUANTUM ESPRESSO: A modular and open-source software project for quantum simulations of materials, J. Phys.: Condens. Matter **21**, 395502 (2009).

[23] P. E. Blöchl, Projector augmented-wave method, Phys. Rev. B **50**, 17953 (1994).

[24] G. Kresse and D. Joubert, From ultrasoft pseudopotentials to the projector augmented-wave method, Phys. Rev. B **59**, 1758 (1999).

[25] J. P. Perdew, K. Burke, and M. Ernzerhof, Generalized Gradient Approximation Made Simple, Phys. Rev. Lett. **77**, 3865 (1996).

[26] S. Grimme, Semiempirical GGA-type density functional constructed with a long-range dispersion correction, J. Comput. Chem. **27**, 1787 (2006).

[27] A. Milosavljević, A. Šolajić, J. Pešić, Y. Liu, C. Petrovic, N. Lazarević, and Z. V. Popović, Evidence of spin-phonon coupling in CrSiTe₃, Phys. Rev. B **98**, 104306 (2018).

[28] A. Baum, A. Milosavljević, N. Lazarević, M. M. Radonjić, B. Nikolić, M. Mitschek, Z. I. Maranloo, M. Šćepanović, M. Grujić-Brojčin, N. Stojilović, M. Opel, A. Wang,

C. Petrovic, Z. V. Popović, and R. Hackl, Phonon anomalies in FeS, Phys. Rev. B **97**, 054306 (2018).

[29] M. Opačić, N. Lazarević, M. M. Radonjić, M. Šćepanović, H. Ryu, A. Wang, D. Tanasković, C. Petrovic, and Z. V. Popović, Raman spectroscopy of $K_x K_{2-y} Se_2$ single crystals near the ferromagnet–paramagnet transition, J. Phys.: Condens. Matter **28**, 485401 (2016).

[30] Z. V. Popović, N. Lazarević, S. Bogdanović, M. M. Radonjić, D. Tanasković, R. Hu, H. Lei, and C. Petrovic, Signatures of

the spin-phonon coupling in $Fe_{1+y} Te_{1-x} Se_x$ alloys, Solid State Commun. **193**, 51 (2014).

[31] Z. V. Popović, M. Šćepanović, N. Lazarević, M. Opačić, M. M. Radonjić, D. Tanasković, H. Lei, and C. Petrovic, Lattice dynamics of $BaFe_2 X_3$ ($X =$ S, Se) compounds, Phys. Rev. B **91**, 064303 (2015).

[32] T. P. Devereaux and R. Hackl, Inelastic light scattering from correlated electrons, Rev. Mod. Phys. **79**, 175 (2007).

**RESEARCH ARTICLE**

Journal of
**RAMAN SPECTROSCOPY** WILEY

# Vacancies and spin–phonon coupling in $CrSi_{0.8}Ge_{0.1}Te_3$

**Ana Milosavljević[1]** | **Andrijana Šolajić[1]** | **Bojana Višić[1]** | **Marko Opačić[1]** |
**Jelena Pešić[1]** | **Yu Liu[2]** | **Cedomir Petrovic[2]** | **Zoran V. Popović[1,3]** |
**Nenad Lazarević[1]**

[1]Institute of Physics Belgrade, University of Belgrade, Pregrevica 118, Belgrade, 11080, Serbia

[2]Condensed Matter Physics and Materials Science Department, Brookhaven National Laboratory, Upton, New York, 11973-5000, USA

[3]Serbian Academy of Sciences and Arts, Knez Mihailova 35, Belgrade, 11000, Serbia

**Correspondence**
Ana Milosavljević, Institute of Physics Belgrade, University of Belgrade, Pregrevica 118, 11080 Belgrade, Serbia.
Email: ana.milosavljevic@ipb.ac.rs

**Funding information**
Serbian Academy of Sciences and Arts, Grant/Award Number: F-134; Slovenian Research Agency, Grant/Award Number: P1-0099; Ministry of Education, Science and Technological Development of the Republic of Serbia U.S. DOE-BES, Division of Materials Science and Engineering, Grant/Award Number: DE-SC0012704

**Abstract**

We report temperature-dependent Raman scattering and magnetization studies of van der Waals ferromagnetic compound $CrSi_{0.8}Ge_{0.1}Te_3$. Magnetic susceptibility measurements revealed dominant ferromagnetic interactions below $T_C$ which shift to the lower values due to the presence of vacancies. A Raman active mode, additional to the ones predicted by symmetry in the parent compounds, has been observed. This $A_g$ symmetry mode most likely emerges as a consequence of the atomic vacancies on Si/Ge site. Presence of the strong spin–phonon coupling at temperature around 210 K is indicated by deviations from conventional phonon self-energy temperature dependence of all analysed modes.

**KEYWORDS**
magnetism, phonons, raman spectroscopy, van der Waals materials

## 1 | INTRODUCTION

Considerable progress has been made in the field of material science through developing new materials and revealing their properties in the last decade. Namely, in the recent years, large family of van der Waals materials with inherent magnetism became the focus of experimental and theoretical research, because they seem suitable for numerous technical applications.[1-7] The family includes $Fe_{3-x}GeTe_2$ metallic materials with high magnetic transition temperature,[8-10] semiconductors $CrXTe_3$ (X = Si, Ge, Sn) and $CrX_3$ (X = Cl, Br, I) monolayers[2,11-13] and heterostructures.[14]

$CrSiTe_3$ and $CrGeTe_3$ are ferromagnetic (FM) semiconductors with band gap of 0.4 and 0.7 eV and Curie temperatures ($T_C$) of 32 and 61 K, respectively.[15-18] Twining of $CrSiTe_3$ single crystals along $c$-axes was revealed by X-ray diffraction experiment as well as $Cr^{3+}$ ions magnetic order.[15] Recently, through high-resolution angle-resolved photoemission spectroscopy (ARPES), it was possible to identify full electronic structure near the Fermi level. Due to spin–orbit coupling, $CrSiTe_3$ is a Mott-type FM insulator.[19] Electronic structure of $CrGeTe_3$ single crystals was also investigated by ARPES.[20] It was shown that the low-lying valence bands are centred around the Γ point and are mainly formed from Te $5p$ orbitals.

Raman scattering studies of $CrSiTe_3$ reveal strong spin–lattice coupling in the paramagnetic phase[15,21] as a consequence of a short-range magnetic order in this compound. In addition to renormalization of energies and linewidths of observed Raman active modes, coupling of doubly degenerate $E_g$ mode with magnetic continuum was found.[21] The coupling results in an asymmetric phonon line shape up to 180 K. Besides the splitting of two low-energy $E_g$ modes in the magnetic phase of $CrGeTe_3$ and unconventional behaviour of phonon properties around transition temperature, experimental results indicate spin–phonon coupling effect with magnetic quasi-elastic scattering.[22] Pressure-dependent Raman scattering study of $CrGeTe_3$ showed a decrease in bond length, the deviation of Cr–Te–Cr angle, and reduction of phase transition temperature.[23]

Change of the carrier concentration plays an important role in the physics of semiconducting materials as it can lead to surprising physical properties. Very small variations in dopant concentrations can lead to structural modifications and considerable changes in magnetic transition temperature. Here, we report a Raman scattering and magnetization studies of $CrSi_{0.8}Ge_{0.1}Te_3$. Our scanning electron microscopy (SEM) measurements reveal 10% of Ge atoms concentration and 10% of vacancies. Vacancies induced a decrease in $T_C$ was detected within magnetic susceptibility measurements. In the Raman scattering results, we identified three $A_g$ and four $E_g$ symmetry modes. Additional peak of the $A_g$ symmetry is also observed in our spectra. This mode may be traced to vacancies and possible inhomogeneous distribution of Ge atoms substitution on Si atomic site at nano-scale. Energies of modes predicted by symmetry analysis are found between the experimental values of parent compounds $CrSiTe_3$ and $CrGeTe_3$, reported previously in Milosavljevi et al..[21] The presence of the strong spin–phonon interaction at temperature around 210 K is indicated in small deviations from conventional temperature-dependent behaviour of the observed modes energies and linewidths, including additional one.

## 2 | EXPERIMENT AND NUMERICAL METHOD

$CrSi_{0.8}Ge_{0.1}Te_3$ single crystals were grown as described previously.[24] Magnetic properties were measured in a Quantum Design MPMS-XL5 system.

SEM measurements were performed using FEI HeliosNanolab 650. This microscope is equipped with an Oxford Instruments energy dispersive spectroscopy (EDS) system with an X-max SSD detector operating at 20 kV. Measurements were performed on as-cleaved samples

deposited on a graphite tape. The elemental composition EDS mapping was obtained on crystals that appeared to be uniform for several tens of microns. The maps show the presence of Cr, Ge, Te and Si.

For Raman scattering experiment, Tri Vista 557 spectrometer was used in the subtractive backscattering micro-Raman configuration. The combination of gratings was 1800/1800/2400 grooves/mm and the entrance slit of 80 $\mu$m. Solid state laser with 532-nm line was used as an excitation source. In our scattering configuration, plane of incidence is $ab$-plane, where $|a| = |b|$ ($\measuredangle(a,b) = 120°$), with incident (scattered) light propagation direction along $c$-axes. Samples were cleaved in the air before being placed in vacuum. All measurements were performed in high vacuum ($10^{-6}$ mbar) using a KONTI CryoVac continuous Helium flow cryostat with 0.5-mm thick window. Laser beam focusing was achieved using microscope objective with ×50 magnification. All spectra were corrected for Bose factor.

Spin-polarized density functional theory calculations were performed in Quantum Espresso software package,[25] based on plane waves and pseudopotentials, using Perdew–Burke–Ernzerhof (PBE) exchange-correlation functional[26] and projector augmented wave (PAW) pseudopotentials.[27,28] The cutoff for wavefunctions and the charge density of 85 and 425 Ry were chosen, respectively. The $k$-point were sampled using the Monkhorst-Pack scheme, on $8 \times 8 \times 8$ Γ centred grid used for both structures. Optimization of the lattice parameters and atomic positions in unit cell was performed until the interatomic forces were minimized down to $10^{-6}$ Ry/Å. Treatment of the van der Waals interactions is included using the Grimme-D2 correction, in order to obtain the lattice parameters more accurately. Phonon wave numbers were calculated within the linear response method, as implemented in PHonon part of Quantum Espresso.
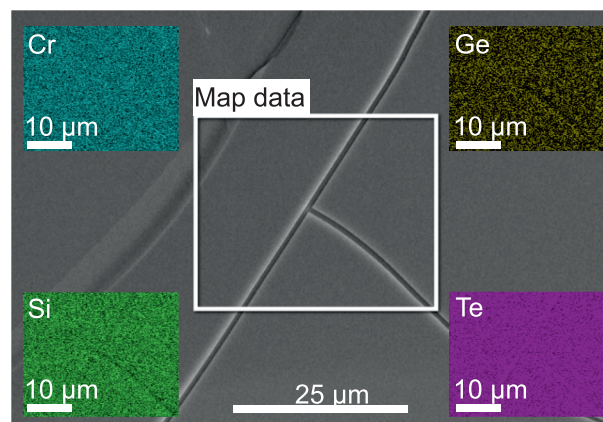


**FIGURE 1** Energy dispersive spectroscopy (EDS) mapping on a $CrSi_{0.8}Ge_{0.1}Te_3$ single crystal [Colour figure can be viewed at wileyonlinelibrary.com]

## 3 | RESULTS AND DISCUSSION

In order to investigate uniformity and elemental composition of $CrSi_{0.8}Ge_{0.1}Te_3$ sample, SEM measurements were performed on as-cleaved crystals. EDS mapping presented in Figure 1 shows that the ratio of Cr:Si:Ge:Te (averaged over 10 measurements) is 1:0.8:0.1:3. This result reveals the presence of 10% Ge atomic vacancies in the sample.

Figure 2a,b presents the temperature dependence of zero-field cooling (ZFC) magnetic susceptibility $\chi(T) = M(T)/H$ measured in 1-kOe magnetic field applied parallel to $a$ (a) and $c$ (b) crystallographic axes. Curie–Weiss law $\chi = \frac{C}{T-\theta}$ fit at high temperatures yields Weiss temperatures $\theta_a = 61(2)$ K, $\theta_c = 70(2)$ K and high temperature paramagnetic moments $\mu_{eff,a} = 4.14(2)\mu_B$ and $\mu_{eff,c} = 3.91(2)\mu_B$ for $CrSi_{0.8}Ge_{0.1}Te_3$, consistent with dominant FM interactions below $T_c$ and in line with the observed FM $T_c$ and magnetic hysteresis loops.[13,24] The approximate $T_c$ value can be determined from the minima of the $d\chi/dT$ curves insets in Figure 2(a,b). It should be noted
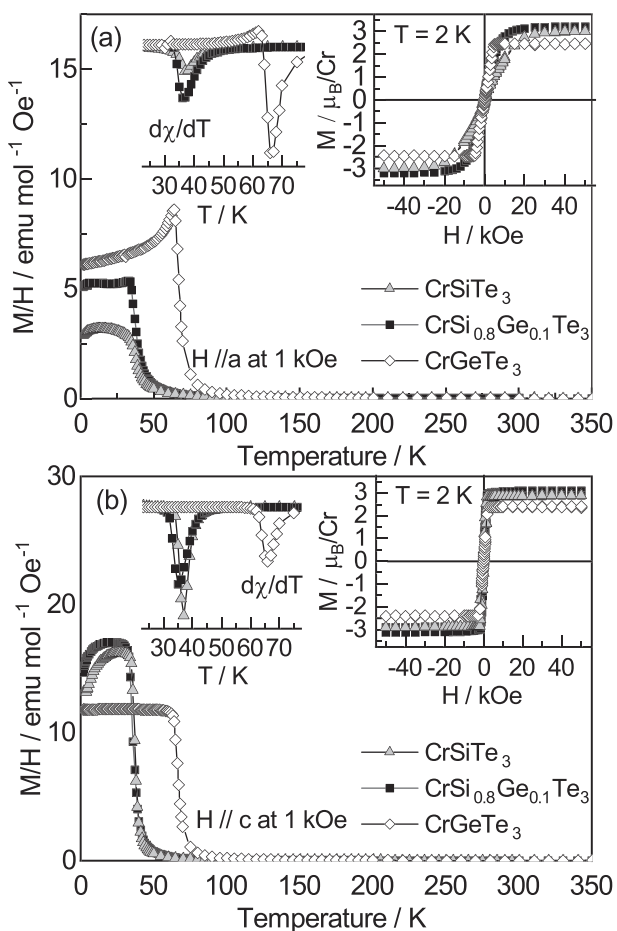
that, instead of monotonous rise, there is a weak but discernible shift to lower temperature in $d\chi/dT$ in $CrSi_{0.8}Ge_{0.1}Te_3$ when compared with $CrSiTe_3$. This small reduction in FM transition temperature is likely induced by the presence of vacancies, as suggested by the EDS data. The presence of vacancies in this class of materials usually disarrange magnetic exchange due to disorder increment, which leads to the reduction of $T_C$.[29]

Isostructural parent compounds $CrSiTe_3$ and $CrGeTe_3$ crystallize in the rhombohedral crystal structure, described with space group $R\overline{3}$ ($C_{3i}^2$).[30] According to factor group analysis, five $A_g$ and five double degenerate $E_g$ symmetry modes are to be observed in the light scattering experiment. Detailed symmetry analysis, phonon mode distribution and selection rules for parent compounds ($CrSiTe_3$ and $CrGeTe_3$) can be found in Milosavljević et al.[21] In our scattering configuration, the plane of incidence is $ab$ plane, where $|a| = |b|$ ($\measuredangle(a,b) = 120°$) (inset in Figure 3), and the direction of incident (scattered) light propagation is along $c$-axes. According to the selection rules for this scattering configuration,[21] all Raman active modes may be observed, having in mind that $A_g$ symmetry modes can be detected only in parallel polarization configuration. The $E_g$ symmetry modes are expected to appear in both the parallel and cross polarization configurations. Raman spectra of $CrSi_{0.8}Ge_{0.1}Te_3$, obtained by continuous change of the angle between polarization vectors of incident and



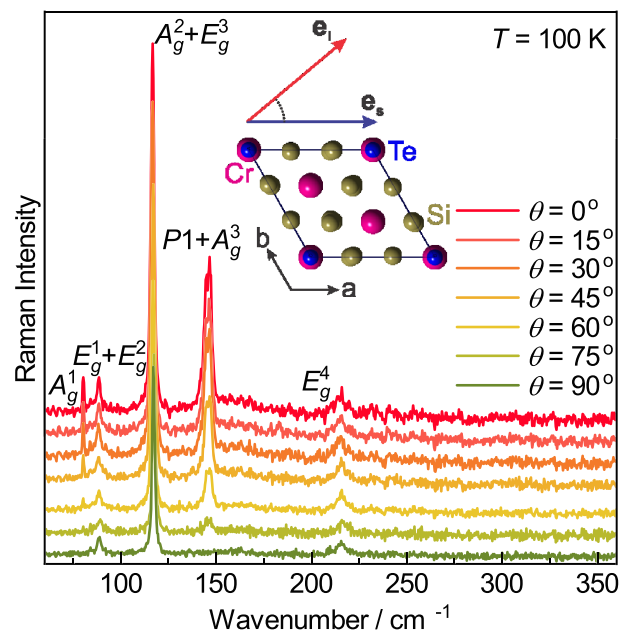**FIGURE 2** Temperature dependence of zero-field cooling (ZFC) $\chi = M/H$ for $CrSiTe_3$, $CrSi_{0.8}Ge_{0.1}Te_3$ and $CrGeTe_3$ in 1-kOe magnetic field applied in-plane (a) and along the $c$-axis (b). Insets show transition temperatures of ferromagnetic orders ($d\chi/dT$) and magnetic hysteresis loops taken at 2 K



**FIGURE 3** Raman spectra of $CrSi_{0.8}Ge_{0.1}Te_3$ single crystal, measured at 100 K, as a function of angle $\theta$, between incident and scattered light polarization. Inset: schematic representation of the incident and scattered light polarization with respect to the crystal orientation [Colour figure can be viewed at wileyonlinelibrary.com]

scattered light, $\theta = \measuredangle(\mathbf{e}_i, \mathbf{e}_s)$, $(0° \leqslant \theta \leqslant 90°)$ at 100 K, are shown in Figure 3. It can be seen that by changing this angle, starting from $\theta = 0°$, the intensities of the peaks at energies 80.2, 116.4 and 145.5 $cm^{-1}$ continuously decrease and completely vanish for polarization angle of 90°. Therefore, these excitations obey pure $A_g$ symmetry. On the other hand, the peaks at energies of 84.5, 88.3, 117.2 and 215.0 $cm^{-1}$ are not influenced by change of polarization angle, so they can be identified as $E_g$ symmetry modes.

Here, one should note that the feature observed at around 117 $cm^{-1}$ in both scattering configurations is actually a two-peak structure comprising of 116.4-$cm^{-1}$ $A_g$ and 117.2-$cm^{-1}$ $E_g$ symmetry modes. Detailed analysis of the structure for two scattering configurations is presented in Figure A1 of Appendix. Furthermore, closer inspection of the data revealed that peak at energy of 145.5 $cm^{-1}$, which obeys pure $A_g$ symmetry, is also composed of two modes, $P1$ (144.6 $cm^{-1}$) and $A_g^3$ (146.7 $cm^{-1}$), as shown in Figure A2 of Appendix.

Calculated optical phonon wavenumbers of the parent compounds, $CrSiTe_3$ and $CrGeTe_3$, together with their experimental Raman active values as well as Raman mode energies of $CrSi_{0.8}Ge_{0.1}Te_3$, are compiled in Table 1. As expected, experimental values of $CrSi_{0.8}Ge_{0.1}Te_3$ Raman active modes are found between the values of the observed modes in parent compounds.[21] Figure 4a shows compositional evolution of the peaks with highest
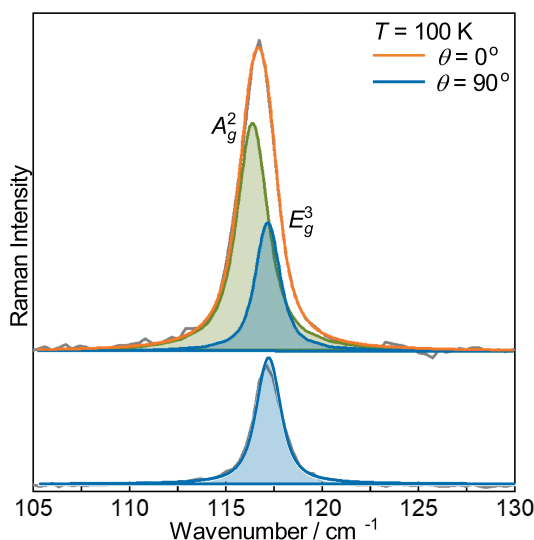


**FIGURE A2** Decomposition of phonon mode in parallel scattering configuration on two $A_g$ symmetry modes. Open circles represent the measured data and the blue one sum of two Voigt profile line shapes. Data modelled with one Voigt profile line shape (orange line) deviates significantly from measured data [Colour figure can be viewed at wileyonlinelibrary.com]

intensity, assigned as $E_g^3$ and $A_g^3$ symmetry modes in parent compounds. The $E_g^3$ mode energy changes almost linearly (Figure 4b), as a consequence of change in lattice parameters and "change of mass" effect. The observed energy shift is followed by doubling of the linewidth, dominantly induced by the significant crystalline disorder. The similar type of behaviour, with somewhat larger increase in the linewidth, was also observed for the $A_g^3$ symmetry mode. The most striking feature was the additional $A_g$ symmetry mode (denoted as $P1$, see Figure A2 of the Appendix), observed in the doped sample. Generally, both the substitutional defects and vacancies may have similar impact on the Raman modes energy and linewidth. Here, the appearance of $P1$ peak can be understood as a consequence of the presence of vacancies on Si/Ge atomic site and their inharmonious distribution at nano-scale. The mode "splitting" is detected only for the $A_g^3$ but not for other observed modes, due to the fact that different nature of these vibrations results in different values of energy shifts. In the case of other modes, the difference between the shifts for corresponding domains is smaller than the spectral resolution of the instrument ($\sim$1.8 $cm^{-1}$), and therefore, the separate modes can not be resolved.

Figure 5 shows $CrSi_{0.8}Ge_{0.1}Te_3$ Raman scattering spectra measured at various temperatures. For clarity, spectra obtained for cross polarization configuration are



**FIGURE A1** Decomposition of unresolved $A_g^2$ and $E_g^3$ symmetry modes obtained by simultaneous modelling in parallel and cross polarization configuration. Grey line represents the measured data, Voigt line of $A_g^2$ mode is shown by green, and blue lines represent the $E_g^3$ symmetry mode in parallel (upper panel) and cross (lower panel) polarization. The orange line is the superposition of these two lines [Colour figure can be viewed at wileyonlinelibrary.com]
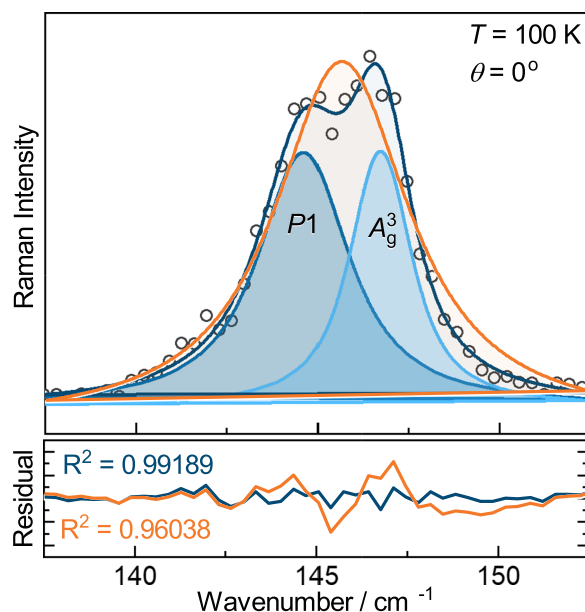
**TABLE 1** Phonon symmetry, calculated ($T = 0$ K) and experimental ($T = 100$ K) Raman active phonon wavenumbers of parent compounds $CrSiTe_3$ and $CrGeTe_3$.[21] Experimental values for Raman active phonons of $CrSi_{0.8}Ge_{0.1}Te_3$ at 100 K are shown in the last column

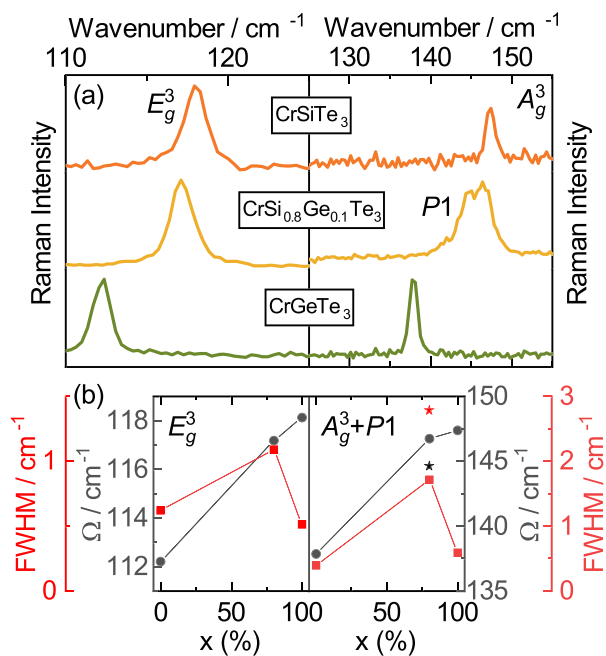| Raman active modes | | | | | |
|---|---|---|---|---|---|
| | Calculations | | Experiment | | |
| Symmetry | $CrSiTe_3$ | $CrGeTe_3$ | $CrSiTe_3$ | $CrGeTe_3$ | $CrSi_{0.8}Ge_{0.1}Te_3$ |
| $A_g^1$ | 88.2 | 84.2 | — | — | 80.2 |
| $E_g^1$ | 93.5 | 82.0 | 88.9 | 83.5 | 84.5 |
| $E_g^2$ | 96.9 | 90.8 | — | — | 88.3 |
| $E_g^3$ | 118.3 | 114.2 | 118.2 | 112.2 | 117.2 |
| $A_g^2$ | 122.0 | 105.9 | — | — | 116.4 |
| $A_g^3$ | 148.0 | 134.8 | 147.4 | 137.9 | 146.7 |
| $A_g^4$ | 208.7 | 200.3 | — | — | — |
| $E_g^4$ | 219.5 | 209.6 | 217.2 | 217.5 | 215.0 |
| $E_g^5$ | 357.4 | 229.8 | — | — | — |
| $A_g^5$ | 508.9 | 290.7 | — | 296.6 | — |

*Note:* All values are given in $cm^{-1}$.



**FIGURE 4** (a) Raman scattering spectra of $E_g^3$ and $A_g^3$ phonon modes of $CrSiTe_3$ (orange line), $CrSi_{0.8}Ge_{0.1}Te_3$ (yellow line) and $CrGeTe_3$ (green line) at $T = 100$ K measured in cross (left panel) and parallel (right panel) scattering configuration, respectively. (b) Energy (grey line) and linewidth (red line) of these two modes with respect to the percentage of Si atoms concentration. Energy and linewidth of $P1$ mode are marked with black and red star, respectively [Colour figure can be viewed at wileyonlinelibrary.com]
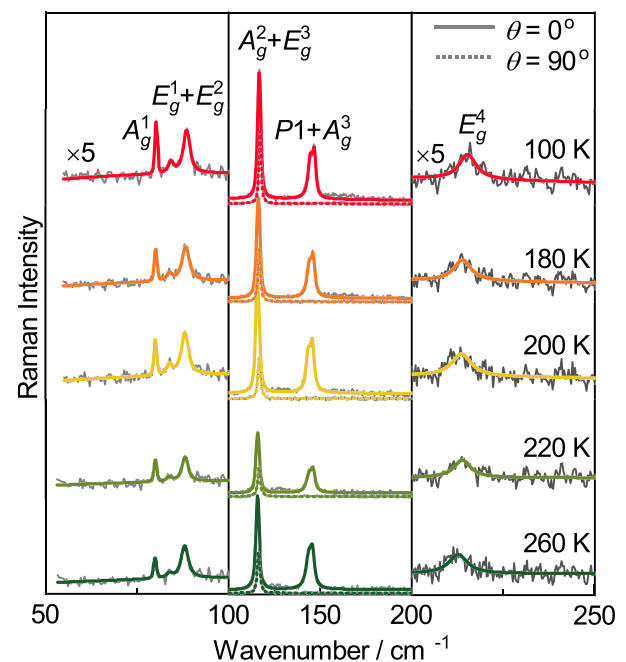


**FIGURE 5** Raman spectra of $CrSi_{0.8}Ge_{0.1}Te_3$ single crystal measured at various temperatures. The spectra were analysed by using multiple Voigt peak functions and a single $\chi''_{cont} = a\Gamma\omega/(\Gamma^2 + \omega^2) + b\omega$ function, for parallel ($\theta = 0°$, solid coloured lines) and cross ($\theta = 90°$, dashed coloured lines) scattering configuration. For clarity, higher and lower energy ranges (left and right panel) are multiplied by the factor of five [Colour figure can be viewed at wileyonlinelibrary.com]
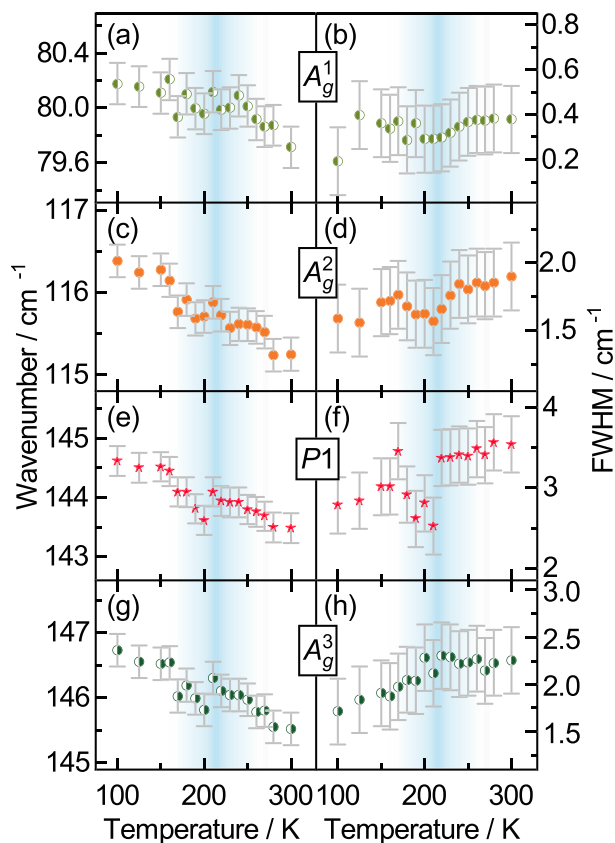
**FIGURE 6** Energy and linewidth temperature dependence of $A_g^1$ (a,b), $A_g^2$ (c,d), $P1$ (e,f) and $A_g^3$ (g,h) Raman modes [Colour figure can be viewed at wileyonlinelibrary.com]
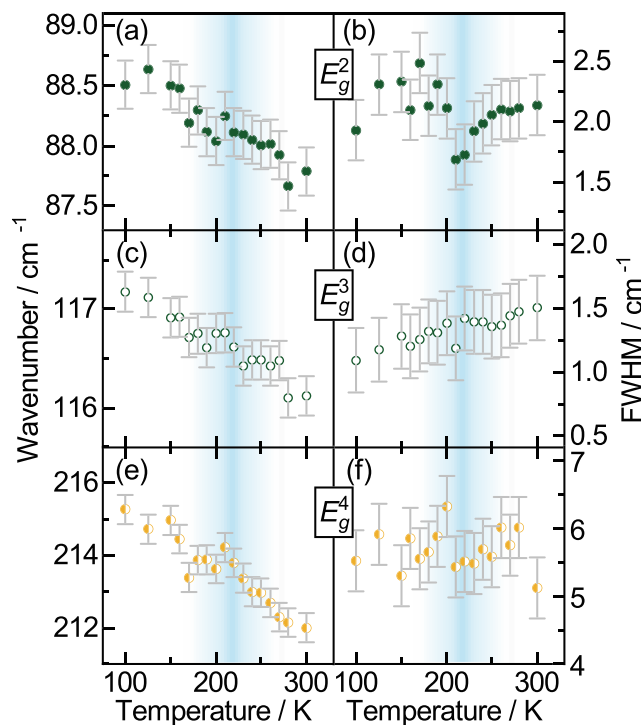


**FIGURE 7** Energy and linewidth temperature dependence of $E_g^2$ (a,b), $E_g^3$ (c,d) and $E_g^4$ (e,f) symmetry modes [Colour figure can be viewed at wileyonlinelibrary.com]

only shown for the mid-energy range. Temperature dependence of energies and linewidths of all the observed $A_g$ symmetry modes, including $P1$, are presented in Figure 6. By heating the sample from 100 K to approximately 210 K, monotonous decrease in energy of all the $A_g$ symmetry modes is present, dominantly driven by thermal expansion.[31] In the temperature region around 210 K, these modes' energy exhibit small deviation, followed by a continuous decrease up to room temperature. In the same temperature region, deviation from expected anharmonic type of behaviour is observed for all the $A_g$ symmetry modes linewidth. This effect is more pronounced for higher energy modes where the anharmonicity is expected to be higher. Similar response of analysed $E_g$ symmetry modes is present and shown in Figure 7.

Concerning previously reported strong spin–phonon coupling in $CrSiTe_3$,[15,21] which persists up to 180 K, we believe that this unconventional behaviour of energies and linewidths can be attributed to the coupling of the phonon modes to the spin system.[32] Due to the doping and presence of vacancies, strong magnetic correlations in $CrSi_{0.8}Ge_{0.1}Te_3$ are sustained up to 210 K.

## 4 | CONCLUSIONS

In summary, we presented temperature-dependent Raman scattering and magnetization studies of doped van der Waals ferromagnet $CrSi_{0.8}Ge_{0.1}Te_3$. SEM measurements revealed the presence of 10% vacancies on Si/Ge atomic site. As a consequence, magnetization measurements detected small but clear decrease in $T_C$. Seven out of 10 Raman active modes have been assigned in our Raman spectra. Temperature dependence of all the observed modes shows the persistence of magnetic correlations up to 210 K. In addition, the results revealed the appearance of the peak that obey pure $A_g$ symmetry, which is attributed to the possible inhomogeneous distribution of Ge atoms and vacancies at nano-scale. This study provides an insight into the impact of doping and presence of vacancies on magnetic and lattice properties in this class of materials.

**ORCID**

*Ana Milosavljević* https://orcid.org/0000-0002-8654-0475

**REFERENCES**

[1] F. Hellman, A. Hoffmann, Y. Tserkovnyak, G. S. Beach, E. E. Fullerton, C. Leighton, A. H. MacDonald, D. C. Ralph, D. A. Arena, H. A. Dürr, P. Fischer, *Rev. Mod. Phys.* **2017**, *89*, 025006.

[2] N. Sivadas, M. W. Daniels, R. H. Swendsen, S. Okamoto, D. Xiao, *Phys. Rev. B.* **2015**, *91*, 235425.

[3] K. S. Novoselov, A. K. Geim, S. V. Morozov, D. Jiang, Y. Zhang, S. V. Dubonos, I. V. Grigorieva, A. A. Firsov, *Science* **2004**, *306*(5696), 666.

[4] Q. H. Wang, K. Kalantar-Zadeh, A. Kis, J. N. Coleman, M. S. Strano, *Nat. Nanotechnol.* **2012**, *7*, 699.

[5] G. Cheng, L. Lin, L. Zhenglu, S. Huiwen, S. Alex, X. Yang, C. Ting, B. Wei, W. Chenzhe, W. Yuan, Z. Q. Qiu, R. J. Cava, G. L. Steven, X. Jing, Z. Xiang, *Nature* **2017**, *546*, 265.

[6] B. Huang Bevin, G. Clark, E. Navarro-Moratalla, D. R. Klein, R. Cheng, K. L. Seyler, D. Zhong, E. Schmidgall, M. A. McGuire, D. H. Cobden, W. Yao, *Nature* **2017**, *546*, 270.

[7] K. S. Burch, D. Mandrus, J.-G. Park, *Nature* **2018**, *563* (7729), 47.

[8] J.-X. Zhu, M. Janoschek, D. Chaves, S. J. C. Cezar, T. Durakiewicz, F. Ronning, Y. Sassa, M. Mansson, B. L. Scott, N. Wakeham, E. D. Bauer, J. D. Thompson, *Phys. Rev. B.* **2016**, *93*, 144404.

[9] B. Chen, J. H. Yang, H. D. Wang, M. Imai, H. Ohta, C. Michioka, K. Yoshimura, M. H. Fang, *J. Phys. Soc. Japan* **2013**, *82*(12), 124711.

[10] A. Milosavljević, A. Šolajić, S. Djurdjić-Mijin, J. Pešć, B. Višić, Y. Liu, C. Petrovic, N. Lazarević, Z. V. Popović, *Phys. Rev. B.* **2019**, *99*, 214304.

[11] M. A. McGuire, H. Dixit, V. R. Cooper, B. C. Sales, *Chem. Mat.* **2015**, *27*(2), 612.

[12] H. L. Zhuang, Y. Xie, P. R. C. Kent, P. Ganesh, *Phys. Rev. B.* **2015**, *92*, 035407.

[13] G. T. Lin, H. L. Zhuang, X. Luo, B. J. Liu, F. C. Chen, J. Yan, Y. Sun, J. Zhou, W. J. Lu, P. Tong, Z. G. Sheng, *Phys. Rev. B.* **2017**, *95*, 245212.

[14] M. Gibertini, M. Koperski, A. F. Morpurgo, K. S. Novoselov, *Nat. Nanotech.* **2019**, *14*(5), 408.

[15] L. D. Casto, A. J. Clune, M. O. Yokosuk, J. L. Musfeldt, T. J. Williams, H. L. Zhuang, M.-W. Lin, K. Xiao, R. G. Hennig, B. C. Sales, J.-Q. Yan, D. Mandrus, *APL Mat.* **2015**, *3*(4), 041515.

[16] X. Zhang, Y. Zhao, Q. Song, S. Jia, J. Shi, W. Han, *JJpn. J. Appl. Phys.* **2016**, *55*(3), 033001.

[17] B. Siberchicot, S. Jobic, V. Carteaux, P. Gressier, G. Ouvrard, *Phys. J. Chem.* **1996**, *100*(14), 5863.

[18] V. Carteaux, F. Moussa, M. Spiesser, *EPL.* **1995**, *29*(3), 251.

[19] J. Zhang, X. Cai, W. Xia, A. Liang, J. Huang, C. Wang, L. Yang, H. Yuan, Y. Chen, S. Zhang, Y. Guo, *Phys. Rev. Lett.* **2019**, *123*, 047203.

[20] Y. F. Li, W. Wang, W. Guo, C. Y. Gu, H. Y. Sun, L. He, J. Zhou, Z. B. Gu, Y. F. Nie, X. Q. Pan, *Phys. Rev. B.* **2018**, *98*, 125127.

[21] A. Milosavljević, A. Šolajić, J. Pešć, Y. Liu, C. Petrovic, N. Lazarević, Z. V. Popović, *Phys. Rev. B.* **2018**, *98*, 104306.

[22] Y. Tian, M. J. Gray, H. Ji, R. J. Cava, K. S. Burch, *2D Mater.* **2016**, *3*(2), 025035.

[23] Y. Sun, R. C. Xiao, G. T. Lin., R. R. Zhang, L. S. Ling, Z. W. Ma, X. Luo, W. J. Lu, Y. P. Sun, Z. G. Sheng, *Appl. Phys. Lett.* **2018**, *112*(7), 072409.

[24] Y. Liu, C. Petrovic, *Phys. Rev. Mater.* **2019**, *3*, 014001.

[25] P. Giannozzi, S. Baroni, N. Bonini, M. Calandra, R. Car, C. Cavazzoni, D. Ceresoli, G. L. Chiarotti, M. Cococcioni, I. Dabo, A. Dal Corso, *J. Phys. Condens. Matter.* **2009**, *21*(39), 395502.

[26] J. P. Perdew, K. Burke, M. Ernzerhof, *Phys. Rev. Lett.* **1996**, *77*, 3865.

[27] P. E. Blöchl, *Phys. Rev. B.* **1994**, *50*, 17953.

[28] G. Kresse, D Joubert, *Phys. Rev. B.* **1999**, *59*, 1758.

[29] F. A. May, S. Calder, C. Cantoni, H. Cao, M. A. McGuire, *Phys. Rev. B* **2016**, *93*, 014411.

[30] R. E. Marsh, *J. Solid State Chem.* **1988**, *77*(1), 190.

[31] M. Opačić, N. Lazarević, M. Šćepanović, H. Ryu, H. Lei, C. Petrovic, Z. V. Popović, *J. Phys. Condens. Matter.*, *48*(27), 485701.

[32] F. Feng, N. Lazarević, C. Liu, J. Ji, Y. Wang, S. He, H. Lei, C. Petrovic, R. Yu, Z. V. Popović, Q. Zhang, *Phys. Rev. B.* **2019**, *99*, 144419.

**APPENDIX: A DECOMPOSITION OF UNRESOLVED MODES**

Analysing the spectra of $CrSi_{0.8}Ge_{0.1}Te_3$ single crystal, in different polarization configurations (Figure 3), in the energy range around $117\,cm^{-1}$, becomes clear that lower energy part completely disappears in cross polarization configuration, whereas higher energy part persists. Enlarged part of this energy region is shown in Figure A1, in parallel and cross polarization configuration at temperature of $100\,K$. After simultaneous modelling of these spectra becomes clear that they consist of the $A_g^2$ and $E_g^3$ modes, at energies 116.4 and $117.2\,cm^{-1}$, respectively. This is completely supported with theoretical calculations presented in Table 1.

On the other hand, existence of $P1$ is not predicted by theoretical calculations, as Raman active peak. Only closer inspection and detailed analysis, presented in Figure A2, shows that much better agreement with experimental results gives modelling as a superposition of two Voigt lines.

# Short-Range Order in VI$_3$

Sanja Djurdjić Mijin, A. M. Milinda Abeykoon, Andrijana Šolajić, Ana Milosavljević, Jelena Pešić, Yu Liu, Cedomir Petrovic, Zoran V. Popović, and Nenad Lazarević*

Cite This: https://dx.doi.org/10.1021/acs.inorgchem.0c02060

Read Online

ACCESS | Metrics & More | Article Recommendations

**ABSTRACT:** We present a detailed investigation of the crystal structure of VI$_3$, a two-dimensional van der Waals material of interest for studies of low-dimensional magnetism. As opposed to the average crystal structure that features $R\bar{3}$ symmetry of the unit cell, our Raman scattering and X-ray atomic pair distribution function analysis supported by density functional theory calculations point to the coexistence of short-range ordered $P\bar{3}1c$ and long-range ordered $R\bar{3}$ phases. The highest-intensity peak, $A_{1g}^3$, exhibits a moderate asymmetry that might be traced back to the spin−phonon interactions, as in the case of CrI$_3$.
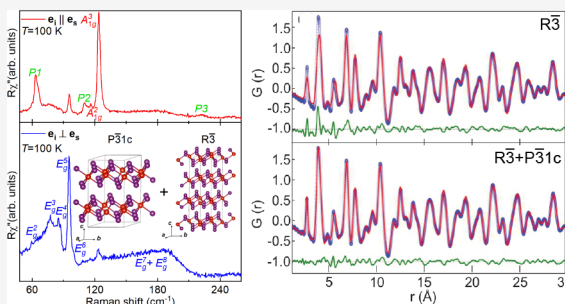
## INTRODUCTION

A well-known family of transition metal trihalides (TMTs) MX$_3$ (X = Cr, B, or I) have received a great deal of attention due to potential existence of two-dimensional (2D) ferromagnetism,[1−6] which has been confirmed in CrI$_3$.[7,8] The similar crystal structure and magnetic properties of CrI$_3$ and VI$_3$ fostered a belief that the same might be found in the latter. In fact, magnetization measurements revealed the 2D ferromagnetic nature of VI$_3$ with a Currie temperature ($T_c$) of around 50 K.[9,10] Contrary to a layer-dependent ferromagnetism in CrI$_3$,[11] the first-principles calculations predict that ferromagnetism in VI$_3$ persists down to a single layer,[9] making it a suitable candidate for engineering 2D spintronic devices. Resistivity measurements showed VI$_3$ is an insulator with an optical band gap of ∼0.6 eV.[9,12]

Whereas laboratory X-ray diffraction studies reported three possible high-temperature VI$_3$ unit cell symmetries,[9,12−14] high-resolution synchrotron X-ray diffraction confirmed a rhombohedral $R\bar{3}$ space group.[10] A very recently published Raman spectroscopy study indicated that the VI$_3$ crystal structure can be described within the $C_{2h}$ point group.[15] All results agree on the existence of a phase transition at a temperature of 79 K. However, the subtle[12] structural changes below 79 K are still under debate.

The long-range magnetic order in ultrathin 2D van der Waals (vdW) crystals stems from strong uniaxial anisotropy, in contrast to materials with isotropic exchange interactions where order parameters are forbidden.[16−18] 2D vdW magnetic materials are of interest both as examples of exotic magnetic order[19] and for potential applications in spintronic technology.[2,4,20,21]

Atomically thin flakes of CrCl$_3$ have a magnetic transition temperature that is different from that of bulk crystals possibly due to the different crystal structure of the monolayer and ultrathin crystals when compared to bulk.[22,23] Similar observations were made on CrI$_3$ monolayers.[22,24,25] It has been proposed[23] that the second anomaly in heat capacity in bulk CrCl$_3$ arises due to regions close to the surface that host a different crystal structure when compared to bulk;[26,27] however, due to the substantial mass fraction detected in heat capacity measurements, this could also reflect differences between the short-range order and long-range crystallographic order of Bragg planes. The short-range order is determined by the space group that is energetically favorable for a monolayer or a few layers, whereas the long-range crystallographic order is established over large packing lengths.

In this paper, we present an experimental Raman scattering study of the bulk VI$_3$ high-temperature structure, supported by density functional theory (DFT) calculations and the X-ray atomic pair distribution function (PDF) analysis. The comparison between the Raman experiment and DFT calculations for each of the previously reported space groups suggested that the high-temperature lattice vibrations of bulk VI$_3$ are consistent with a $P\bar{3}1c$ trigonal structure. Nine ($2A_{1g}$ + $7E_g$) of 12 observed peaks were assigned on the basis of factor group analysis (FGA) and DFT calculations. The PDF analysis indicated the coexistence of two crystallographic phases at two different interatomic distances, short-range ordered $P\bar{3}1c$ and

long-range ordered $R\bar{3}$, as two segregated phases and/or as randomly distributed short-range ordered $P\bar{3}1c$ domains in the long-range ordered $R\bar{3}$ lattice. Raman data displayed a moderate asymmetry of the $A_{1g}^3$ phonon line. This behavior was attributed to the spin−phonon interaction, similar to the case for $CrI_3$. The additional peaks in our spectra obey $A_g$ selection rules and can be described in terms of overtones, as well as the $A_{2g}$ silent modes "activated" by the symmetry breaking.

## EXPERIMENTAL AND COMPUTATIONAL DETAILS

The preparation of single-crystal $VI_3$ samples used in this study is presented elsewhere.[10] For the Raman scattering experiment, a Tri Vista 557 spectrometer was used in the backscattering micro-Raman configuration with a 1800/1800/2400 grooves/mm diffraction grating combination. A Coherent $Ar^+/Kr^+$ ion laser with a 514 nm line was used as an excitation source. Laser beam focusing was achieved through the microscope objective with 50× magnification. The direction of the incident (scattered) light coincides with the crystallographic c axis. The sample, cleaved in open air, was held inside a KONTI CryoVac continuous helium flow cryostat with a 0.5 mm thick window. Raman scattering measurements were performed under high vacuum ($10^{-6}$ mbar). All of the obtained Raman spectra were corrected by the Bose factor. The spectrometer resolution is comparable to the Gaussian width of 1 $cm^{-1}$.

PDF and wide-angle X-ray scattering measurements were carried out in capillary transmission geometry using a PerkinElmer amorphous silicon area detector placed 206 and 983 mm downstream from the sample, respectively, at beamline 28-ID-1 (PDF) of National Synchrotron Light Source II at Brookhaven National Laboratory. The setup utilized a 74.3 keV ($\lambda$ = 0.1668 Å) X-ray beam.

Two-dimensional diffraction data were integrated using the Fit2D software package.[28] Data reduction was performed to obtain experimental PDFs ($Q_{max}$ = 26$A^{-1}$) using the xPDFsuite software package.[29] The Rietveld and PDF analyses were carried out using GSAS-II[30] and PDFgui[31] software packages, respectively.

Density functional theory calculations were performed using the Quantum Espresso software package,[32] employing the PBE exchange-correlation functional[33] and PAW pseudopotentials.[34,35] All calculations are spin-polarized. The cutoff for wave functions and the charge density were set to 48 and 650 Ry, respectively. The k-points were sampled using the Monkhorst−Pack scheme, on a 6 × 6 × 6 Γ-centered grid for $R\bar{3}$ and $C2/m$ structures and a 12 × 12 × 8 grid for the $P\bar{3}1c$ structure. Optimization of the lattice parameters and atomic positions in the unit cell was performed until the interatomic forces were <$10^{-6}$ Ry/Å. To obtain more accurate lattice parameters, treatment of the van der Waals interactions is included using the Grimme-D2 correction. The correlation effects are treated with the Hubbard U correction (LDA+U), using a rotationally invariant formulation implemented in QE,[36] where U = 3.68 eV. Band structure plots are calculated at 800 k-points on the chosen path over high-symmetry points. Phonon frequencies were calculated with the linear response method, as implemented in the -honon part of Quantum Espresso.

## RESULTS AND DISCUSSION

The first reported results for $VI_3$, dating from the 1950s,[37−39] indicated that $VI_3$ adopts a honeycomb layer-type $BiI_3$ structure described with space group $R\bar{3}$, which is a structure common in TMTs, also found in the low-temperature phase of $CrI_3$.[6,40]

There have been several proposed unit cell symmetries for $VI_3$ in the literature: $R\bar{3}$,[12,13] $C2/m$,[14] and $P\bar{3}1c$.[9] Schematic representations of the $P\bar{3}1c$, $R\bar{3}$, and $C2/m$ crystal structures are depicted in Figure 1. The corresponding crystallographic unit cell parameters, previously reported, are listed in Table 1.
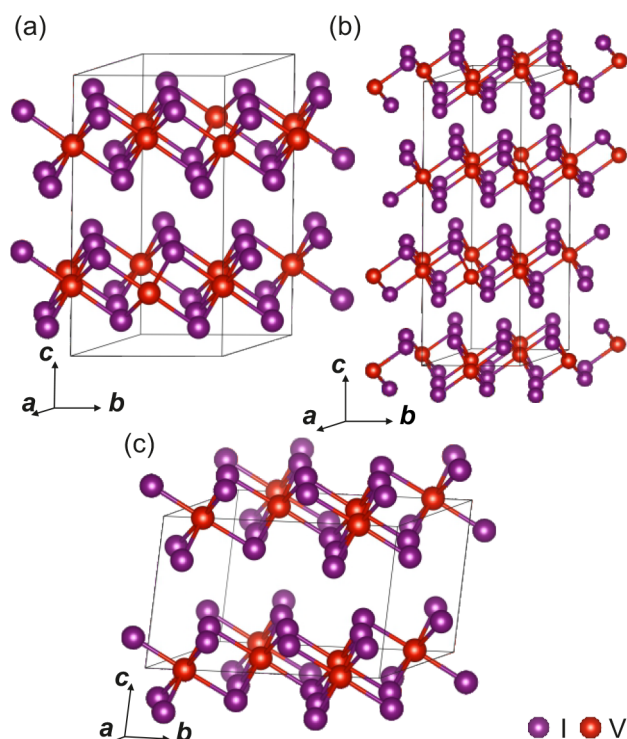


**Figure 1.** Schematic representation of the high-temperature (a) $P\bar{3}1c$, (b) $R\bar{3}$, and (c) $C2/m$ structures of $VI_3$. Black solid lines represent unit cells.

Each of the suggested symmetries implies a different distribution of Raman active modes.

According to FGA, eight ($4A_g$ + $4E_g$), 11 ($3A_{1g}$ + $8E_g$), and 12 ($6A_g$ + $6B_g$) Raman active modes are expected to be observed in the light scattering experiment for $R\bar{3}$, $P\bar{3}1c$, and $C2/m$ crystal structures, respectively. Wyckoff positions, irreducible representations, and corresponding tensors of Raman active modes for each space group are listed in Table 2.

The first step in determining the crystal symmetry from the light scattering experiment is to compare the expected and observed Raman active modes, shown in Figure 2. The red solid line represents the spectrum measured in the parallel polarization configuration, whereas the blue line corresponds to the cross polarization configuration. Five of 12 observed peaks emerge only in parallel, whereas five peaks and a broad peak-like structure can be observed for both polarization configurations. The emergence of the 123.4 $cm^{-1}$ peak in the cross polarization can be understood as a "leakage" of the $A_{1g}^3$ mode due to a possible finite c axis projection and/or the presence of defects.

Now the peaks that appear only for the parallel polarization configuration can be assigned as either $A_{1g}$ or $A_g$ symmetry modes, assuming the light polarization direction along the main crystal axis of the $C2/m$ structure for the later. On the basis of the FGA for possible symmetry group candidates, the remaining Raman active modes can be either of $E_g$ or $B_g$ symmetry. The selection rules (Table 2) do not allow observation of the $B_g$ symmetry modes for the parallel polarization configuration. Consequently, the peaks that can be observed in both scattering channels were recognized as $E_g$ modes. The absence of $B_g$ modes in the Raman spectra rules out the possibility of the $AlCl_3$ type of structure (space group $C2/m$). Two possible remaining crystal symmetries ($R\bar{3}$ and

**Table 1. Previously Reported Experimental and Calculated Unit Cell Parameters for $P\bar{3}1c$, $R\bar{3}$, and $C2/m$ Structures of VI$_3$**

| | $P\bar{3}1c$ | | $R\bar{3}$ | | $C2/m$ | |
| --- | --- | --- | --- | --- | --- | --- |
| | calcd | exp.[9] | calcd | exp.[12] | calcd | exp.[14] |
| $a$ (Å) | 6.87 | 6.89(10) | 6.69 | 6.89(3) | 7.01 | 6.84(3) |
| $b$ (Å) | 6.87 | 6.89(10) | 6.69 | 6.89(3) | 12.14 | 11.83(6) |
| $c$ (Å) | 13.224 | 13.289(1) | 19.81 | 19.81(9) | 7.01 | 6.95(4) |
| $\alpha$ (deg) | 90 | 90 | 90 | 90 | 90 | 90 |
| $\beta$ (deg) | 90 | 90 | 90 | 90 | 109.05 | 108.68 |
| $\gamma$ (deg) | 120 | 120 | 120 | 120 | 90 | 90 |
| cell volume (Å$^3$) | 559.62 | 547.74(10) | 767.71 | 814.09(8) | 563.33 | 533.66(36) |

**Table 2. Wyckoff Positions of Atoms and Their Contributions to the $\Gamma$-Point Phonons for the $R\bar{3}$, $C2/m$, and $P\bar{3}1c$ Structures and the Raman Tensors for the Corresponding Space Groups**

| space group $P\bar{3}1c$ | | space group $R\bar{3}$ | | space group $C2/m$ | |
| --- | --- | --- | --- | --- | --- |
| atom | irreducible representation | atom | irreducible representation | atom | irreducible representation |
| V (2a) | $A_{2g} + A_{2u} + E_g + E_u$ | V (3a) | | V (4g) | $A_g + A_u + 2B_g + 2B_u$ |
| V (2c) | $A_{2g} + A_{2u} + E_g + E_u$ | V (6c) | $A_g + A_u + E_g + E_u$ | I (4i) | $2A_g + A_u + B_g + 2B_u$ |
| I (12i) | $3A_{1g} + 3A_{1u} + 3A_{2g} + 3A_{2u} + 6E_g + 6E_u$ | I (18f) | $3A_g + 3A_u + 3E_g + 3E_u$ | I (8j) | $3A_g + 3A_u + 3B_g + 3B_u$ |

$$A_{1g} = \begin{pmatrix} a & & \\ & a & \\ & & b \end{pmatrix}$$

$$A_g = \begin{pmatrix} a & & \\ & a & \\ & & b \end{pmatrix}$$

$$A_g = \begin{pmatrix} a & & d \\ & c & \\ d & & b \end{pmatrix}$$

$$^{1}E_g = \begin{pmatrix} c & & \\ & -c & d \\ & d & \end{pmatrix} \quad ^{2}E_g = \begin{pmatrix} & -c & -d \\ -c & & \\ d & & \end{pmatrix}$$

$$^{1}E_g = \begin{pmatrix} c & d & e \\ d & -c & f \\ e & f & \end{pmatrix} \quad ^{2}E_g = \begin{pmatrix} d & -c & -f \\ -c & -d & e \\ -f & e & \end{pmatrix}$$

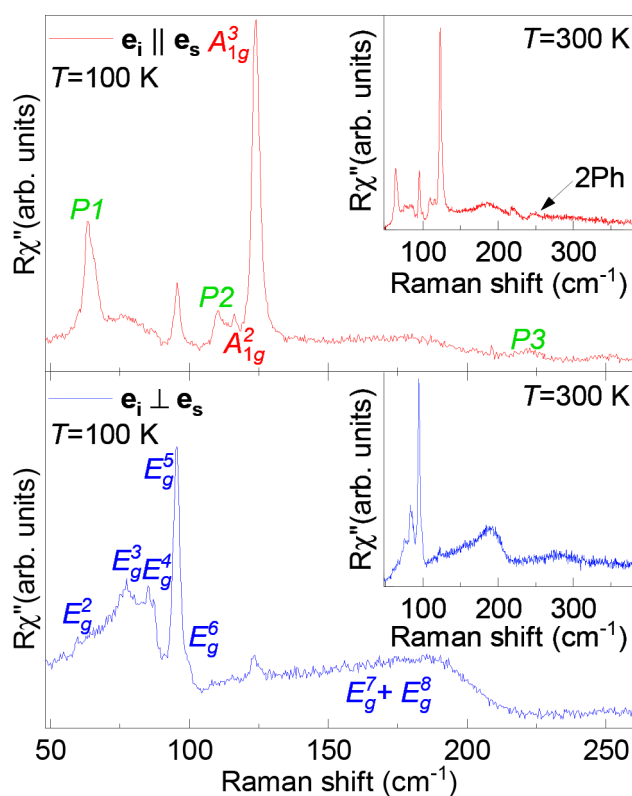$$B_g = \begin{pmatrix} & & e \\ & & f \\ e & f & \end{pmatrix}$$



**Figure 2.** Raman spectra of the high-temperature VI$_3$ single-crystal structure measured in parallel (red solid line) and cross (blue solid line) polarization configurations at 100 K. Peaks observed in both spectra were identified as $E_g$ modes, whereas peaks observed only in the red spectrum were assigned as $A_{1g}$ modes. Additional peaks that obey pure $A_{1g}$ symmetry are marked as P1–P3.

$P\bar{3}1c$) are difficult to single out on the basis of the Raman data symmetry analysis alone. To overcome this obstacle, the DFT method was applied for each of the suggested structures.

It was reported in the literature that $P\bar{3}1c$ VI$_3$ can have two possible electronic states[9,14,41−43] that both can be obtained using DFT+U calculations by varying the smearing and mixing parameters. This approach resulted in a Mott-insulator state having a lower energy making it the electronic ground state of VI$_3$. However, the total energy difference of these two states is small and will not be mentioned further because it is outside of the scope of our analysis. For the sake of completeness, both sets of phonon energies obtained through DFT calculations for these electronic states of the $P\bar{3}1c$ structure are listed in Table 3 together with the results for the $R\bar{3}$ and $C2/m$ space groups as well as the experimental results measured at 100 K.

Now one can see that, even though the Raman mode symmetries for the case of the $R\bar{3}$ crystal structure can describe our Raman spectra, there is a stronger mismatch in calculated and experimentally determined phonon energies when compared to the results obtained for the $P\bar{3}1c$ structure. The deviation is largest for the calculated $A_g^1$ mode. The closest mode in energy, which obeys the same symmetry rules as the calculated $A_g^1$, is a peak at ~64.1 cm$^{-1}$, yielding a deviation of ~30%. Also, the calculated energy of the $A_g^4$ mode could not be identified within our spectrum, with the closest experimental $A_g$ peaks being within 20%. Such deviation in theory and experiment, >20%, indicates that the room-temperature phonon vibrations in VI$_3$ do not originate predominantly from the BiI$_3$ structure type either, leaving $P\bar{3}1c$ as the only candidate. This indication is further reinforced by the inability to connect the experimentally observed $E_g$ modes at ~77 and ~86 cm$^{-1}$ with the $R\bar{3}$-calculated modes.

Our experimental data (Table 3) are mostly supported by the phonon energies obtained for possible electronic states of

**Table 3. Comparison between Calculated Values of Raman Active Phonon Energies for Insulating and Half-Metallic States of the $P\bar{3}1c$ Structure and Experimentally Obtained Values (left)[a] and Phonon Symmetries and Calculated Phonon Energies for the $R\bar{3}$ and $C2/m$ Structures of VI$_3$[b]**

| space group $P\bar{3}1c$ | | | | space group $R\bar{3}$ | | space group $C2/m$ | |
|---|---|---|---|---|---|---|---|
| symmetry | calcd (cm$^{-1}$) | calcd (cm$^{-1}$) | exp. (cm$^{-1}$) | symmetry | calcd (cm$^{-1}$) | symmetry | calcd (cm$^{-1}$) |
| $E_g^1$ | 17.2 | 15.2 | – | $E_g^1$ | 45.2 | $A_g^1$ | 58.1 |
| $A_{2g}^1$ (silent) | 35.0 | 56.8 | | $E_g^2$ | 69.9 | $B_g^1$ | 60.0 |
| $E_g^2$ | 62.2 | 61.6 | 59.8 | $A_g^1$ | 99.3 | $A_g^2$ | 82.7 |
| $A_{2g}^2$ (silent) | 69.4 | 72.3 | | $E_g^3$ | 99.8 | $B_g^2$ | 82.9 |
| $E_g^3$ | 74.1 | 75.9 | 77.2 | $A_g^2$ | 105.1 | $A_g^3$ | 85.7 |
| $A_{1g}^1$ | 83.3 | 84.2 | – | $A_g^3$ | 135.5 | $B_g^3$ | 88.9 |
| $E_g^4$ | 84.9 | 86.6 | 86.7 | $A_g^4$ | 167.9 | $A_g^4$ | 99.3 |
| $E_g^5$ | 91.5 | 98.4 | 95.2 | $E_g^4$ | 176.8 | $B_g^4$ | 99.3 |
| $A_{2g}^3$ (silent) | 92.2 | 96.3 | | | | $A_g^5$ | 122.3 |
| $E_g^6$ | 97.4 | 108.3 | 100.4 | | | $B_g^5$ | 149.9 |
| $A_{1g}^2$ | 113.2 | 119.3 | 116.8 | | | $B_g^6$ | 161.0 |
| $A_{1g}^3$ | 117.1 | 123.9 | 123.4 | | | $A_g^6$ | 164.0 |
| $A_{2g}^4$ (silent) | 121.3 | 147.8 | | | | | |
| $E_g^7$ | 132.2 | 151.9 | c | | | | |
| $E_g^8$ | 149.4 | 166.9 | c | | | | |
| $A_{2g}^5$ (silent) | 185.9 | 212.1 | | | | | |

[a]The experimental values were determined at 100 K. The experimental uncertainty is 0.3 cm$^{-1}$. [b]All calculations were performed at 0 K. [c]See the text for an explanation.

the $P\bar{3}1c$ trigonal structure with deviations of around 10% and 15%. Nine of 11 Raman modes were singled out and identified, with $E_g^1$ being not observable in our experimental setup due to its low energy. The $A_{1g}^1$ mode might be missing due to its low intensity and/or the finite spectrometer resolution. The most striking was the observation of the broad feature at ∼180 cm$^{-1}$, persisting up to 300 K in both scattering channels. Whereas its line shape resembles those of the two-magnon type of excitation, we believe that scenario is unlikely for a ferromagnetic material. The energy region where the feature was observed may also suggest the possibility of a two-phonon type of excitation. However, their scattering cross sections are usually small and dominated by overtones, thus mostly observed for the parallel scattering configuration.[45] For example, such an excitation was observed at ∼250 cm$^{-1}$ (Figure 2). Finally, the observed feature also falls into the energy region where, as suggested by the numerical calculations, observation of the $E_g^7$ and $E_g^8$ modes is expected. We believe that it is actually a complex structure comprising $E_g^7$ and $E_g^8$ Raman modes, significantly broadened by the spin−phonon interaction, that is particularly strong on these phonon branches. The proximity of the two very broad, presumably asymmetric peaks hampers their precise assignment.

Closer inspection of other Raman peaks revealed that some of them also exhibit an asymmetric line shape. To further demonstrate this virtue, we have quantitatively analyzed the highest-intensity peak, $A_{1g}^3$, using the symmetric Voigt line shape and convolution of a Fano profile and a Gausian.[44−46] The asymmetric line shape (with a Fano parameter of $|q|$ = 12.3) gives a slightly better agreement with the experimental data, as depicted in Figure 3. Considering that the observed asymmetry in similar materials was shown to reflect the spin−phonon interaction,[46,47] we propose it as a possible scenario in VI$_3$, as well.

Our findings, based on the inelastic light scattering experiments, at first glance differ from those presented in ref 10. To resolve this discrepancy, we used synchrotron X-ray Rietveld and PDF analysis. Typically, the short-range order
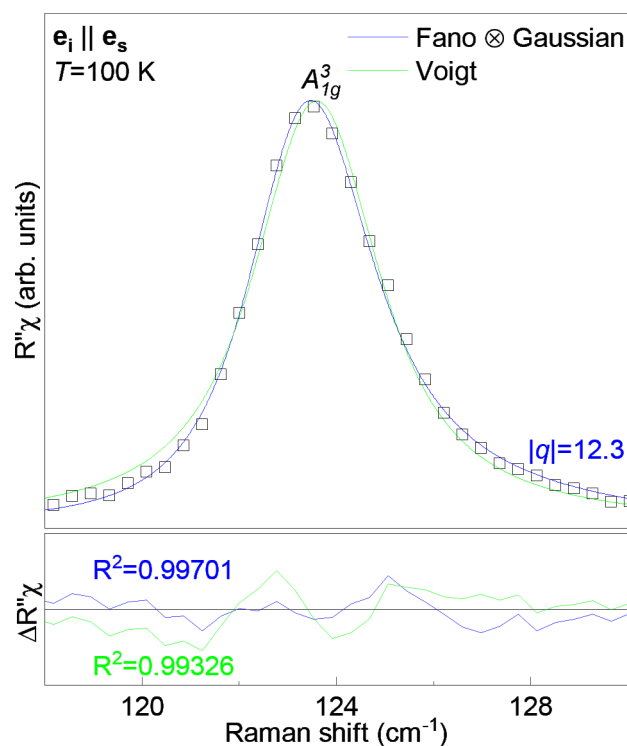


**Figure 3.** Quantitative analysis of the $A_{1g}^3$ mode. The blue solid line represents the line shape obtained as a convolution of the Fano line shape and the Gaussian, whereas the green one represents a Voigt profile fitted to experimental data (□). For details, see refs 44 and 45.

(SRO) contributes to diffuse scattering under the long-range order (LRO) Bragg peaks when they coexist. Because the diffuse scattering is subtracted as part of the background in the Rietveld refinement, this method is more sensitive to the average structure of materials. In contrast, PDF analysis is performed on the sine Fourier transform of the properly corrected diffraction patten, including both Bragg and diffuse

components. PDF is a real space function that provides a histogram of interatomic distances, which contain information regarding all length scales.[48−51] The 1−10 and 11−30 Å PDF length scales are more sensitive to SRO and LRO, respectively. For the $VI_3$ system, the best Rietveld fit was obtained using the $R\bar{3}$ space group (Figure 4a), in agreement with that previously
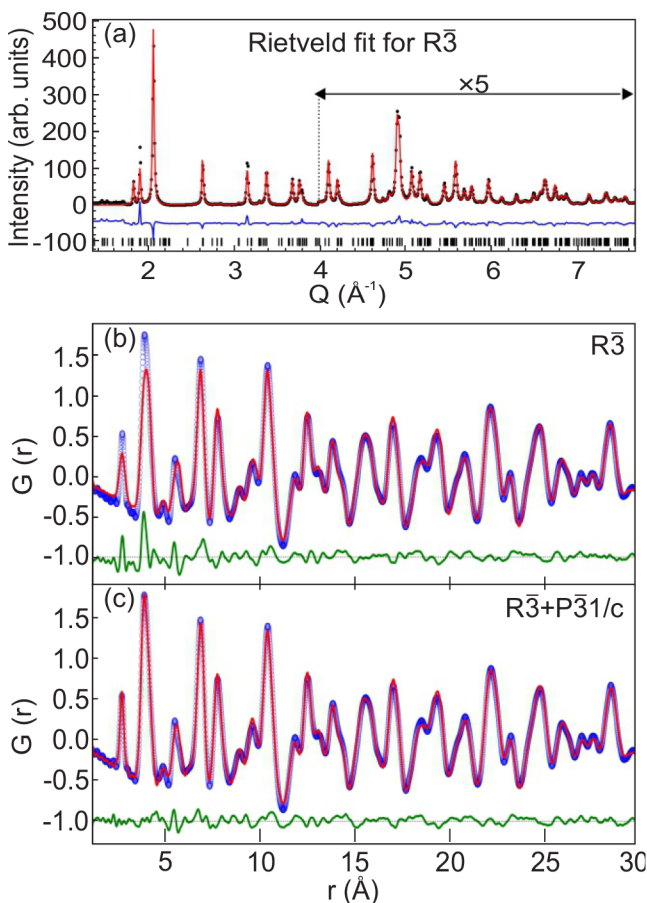


**Figure 4.** Best structural model fits to diffraction data. (a) Rietveld fit using the $R\bar{3}$ space group with black vertical bars indicating calculated peak positions. (b) PDF fit using the $R\bar{3}$ space group. (c) Two-phase PDF fit using $R\bar{3}$ and $P\bar{3}1c$ space groups to fit LRO and SRO, respectively. Black dots (XRD) and blue dots (PDF) represent experimental data, and red solid lines represent the model-based fits. The fit residues are shown at the bottom of each plot.

observed.[10] Not surprisngly, LRO obtained from the Rietveld refinement showed a good agreement on the PDF length scale of 10−30 Å. However, the $R\bar{3}$ space group gave a poor fit on the length scale of 1.5−15 Å with refined $\delta 1$ to account for correlated motion (Figure 4b). In contrast, $P\bar{3}1c$ gave a better fit to SRO, but a poor fit to LRO. The best PDF fits were obtained by refining a weighted two-phase structural model containing ~25 wt % SRO $P\bar{3}1c$ and ~75 wt % LRO $R\bar{3}$ phases. The refined correlation length of the SRO is ~15−20 Å (Figure 4c). These results suggest two possible seanarios: (1) coexistence of two segregated phases, LRO $R\bar{3}$ and SRO $P\bar{3}1c$, and (2) randomly distributed short-range ordered $P\bar{3}1c$ domains in the long-range ordered $R\bar{3}$ lattice. A detailed structural analysis is required to pinpoint scenario 1 and/or 2, which is beyond the scope of this work.

In addition to the peaks already assigned to $\Gamma$-point Raman active phonons of the $P\bar{3}1c$ crystal structure (Table 2), three

additional peaks at 64.2 cm$^{-1}$ ($P1$), 110.1 cm$^{-1}$ ($P2$), and 220.6 cm$^{-1}$ ($P3$) are observed (see Figure 2). According to the results of DFT, energies of these modes correspond well to those calculated for silent $A_{2g}^2$, $A_{2g}^3$, and $A_{2g}^5$ modes. Their observability in Raman data may come from the release of the symmetry selection rules by breaking of the (translation) symmetry as suggested by the PDF in both scenarios.[52−55] However, as previously discussed, these peaks obey $A_{1g}$ selection rules, indicating the possibility for them to be overtones in nature. In this less likely scenario, the phonon−phonon coupling is enhanced by the spin−phonon interaction and/or by the structural imperfections, thus enhancing the Raman scattering rate for the two-phonon processes.[45] Hence, the observed Raman modes reflect the symmetry of phonon vibrations related to the SRO.[56,57] It is interesting to note that, besides a possible short-range crystallography that is different from the average, $VI_3$ might also feature short-range magnetic order above 79 K.[14]

## CONCLUSION

In summary, room-temperature phonon vibrations of $VI_3$ stem from the $P\bar{3}1c$ symmetry of the unit cell. The PDF analysis suggested the coexistence of two phases, short-range ordered $P\bar{3}1c$ and long-range ordered $R\bar{3}$, as two segregated phases and/or as randomly distributed short-range ordered $P\bar{3}1c$ domains in the long-range ordered $R\bar{3}$ lattice. Nine of 12 observed peaks in the Raman spectra were assigned in agreement with $P\bar{3}1c$ symmetry calculations. Three additional peaks, which obey $A_{1g}$ symmetry rules, could be explained as either overtones or as activated $A_{2g}$ silent modes caused by a symmetry breaking. The asymmetry of one of the $A_{1g}$ phonon modes, together with the anomalous behavior of $E_g^7$ and $E_g^8$, indicates strong spin−phonon coupling, which has already been reported in similar 2D materials.[46,58]

## AUTHOR INFORMATION

### Corresponding Author

**Nenad Lazarević** − *Institute of Physics Belgrade, University of Belgrade, 11080 Belgrade, Serbia;* orcid.org/0000-0001-6310-9511; Email: nenadl@ipb.ac.rs

### Authors

**Sanja Djurdjić Mijin** − *Institute of Physics Belgrade, University of Belgrade, 11080 Belgrade, Serbia*

**A. M. Milinda Abeykoon** − *National Synchrotron Light Source II, Brookhaven National Laboratory, Upton, New York 11973, United States*

**Andrijana Šolajić** − *Institute of Physics Belgrade, University of Belgrade, 11080 Belgrade, Serbia*

**Ana Milosavljević** − *Institute of Physics Belgrade, University of Belgrade, 11080 Belgrade, Serbia*

**Jelena Pešić** − *Institute of Physics Belgrade, University of Belgrade, 11080 Belgrade, Serbia*

**Yu Liu** − *Condensed Matter Physics and Materials Science Department, Brookhaven National Laboratory, Upton, New York 11973-5000, United States;* orcid.org/0000-0001-8886-2876

**Cedomir Petrovic** − *Condensed Matter Physics and Materials Science Department, Brookhaven National Laboratory, Upton, New York 11973-5000, United States;* orcid.org/0000-0001-6063-1881

**Zoran V. Popović** − *Institute of Physics Belgrade, University of Belgrade, 11080 Belgrade, Serbia; Serbian Academy of Sciences and Arts, 11000 Belgrade, Serbia*

Complete contact information is available at:
https://pubs.acs.org/10.1021/acs.inorgchem.0c02060

**Notes**
The authors declare no competing financial interest.

## ACKNOWLEDGMENTS

## REFERENCES

(1) Seyler, K. L.; Zhong, D.; Klein, D. R.; et al. Ligand-field helical luminescence in a 2D ferromagnetic insulator. *Nat. Phys.* **2018**, *14*, 277−281.

(2) Klein, D. R.; MacNeill, D.; Lado, J. L.; Soriano, D.; Navarro-Moratalla, E.; Watanabe, K.; et al. Probing magnetism in 2D van der Waals crystalline insulators via electron tunneling. *Science* **2018**, *360*, 1218−1222.

(3) Huang, B.; Clark, G.; Klein, D. R.; MacNeill, D.; Navarro-Moratalla, E.; Seyler, K. L.; et al. Electrical control of 2D magnetism in bilayer CrI$_3$. *Nat. Nanotechnol.* **2018**, *13*, 544−548.

(4) Jiang, S.; Li, L.; Wang, Z.; Mak, K. F.; Shan, J. Controlling magnetism in 2D CrI$_3$ by electrostatic doping. *Nat. Nanotechnol.* **2018**, *13*, 549−553.

(5) McGuire, M. A.; Clark, G.; KC, S.; Chance, W. M.; Jellison, G. E.; Cooper, V. R.; Xu, X.; Sales, B. C. Magnetic behavior and spin-lattice coupling in cleavable van der Waals layered CrCl$_3$ crystals. *Phys. Rev. Materials* **2017**, *1*, 014001.

(6) Djurdjic-Mijin, S. D.; Šolajić, A.; Pešić, J.; Šćepanović, M.; Liu, Y.; Baum, A.; et al. Lattice dynamics and phase transition in CrI$_3$ single crystals. *Phys. Rev. B: Condens. Matter Mater. Phys.* **2018**, *98*, 104307.

(7) Thiel, L.; Wang, Z.; Tschudin, M.; Rohner, D.; Gutierrez-Lezama, I. G.; Ubrig, N.; et al. Probing magnetism in 2D materials at the nanoscale with single-spin microscopy. *Science* **2019**, *364*, 973−976.

(8) Lin, G. T.; Luo, X.; Chen, F. C.; Yan, J.; Gao, J. J.; Sun, Y.; et al. Critical behavior of two-dimensional intrinsically ferromagnetic semiconductor CrI$_3$. *Appl. Phys. Lett.* **2018**, *112*, 072405.

(9) Son, S.; Coak, M. J.; Lee, N.; Kim, J.; Kim, T. Y.; Hamidov, H.; et al. Bulk properties of the van der Waals hard ferromagnet VI$_3$. *Phys. Rev. B: Condens. Matter Mater. Phys.* **2019**, *99*, 041402.

(10) Liu, Y.; Abeykoon, M.; Petrovic, C. Critical behavior and magnetocaloric effect in VI$_3$. *Phys. Rev. Research* **2020**, *2*, 013013.

(11) Huang, B.; Clark, G.; Navarro-Moratalla, E.; Klein, D. R.; Cheng, R.; Seyler, K. L.; et al. Layer-dependent ferromagnetism in a van der Waals crystal down to the monolayer limit. *Nature* **2017**, *546*, 270−273.

(12) Kong, T.; Stolze, K.; Timmons, E. I.; Tao, J.; Ni, D.; Guo, S.; et al. VI$_3$ − a New Layered Ferromagnetic Semiconductor. *Adv. Mater.* **2019**, *31*, 1808074.

(13) Doležal, P.; Kratochvílová, M.; Holý, V.; Čermak, P.; Sechovský, V.; Dušek, M.; et al. Crystal structures and phase transitions of the van der Waals ferromagnet VI$_3$. *Phys. Rev. Materials* **2019**, *3*, 121401.

(14) Tian, S.; Zhang, J.-F.; Li, C.; Ying, T.; Li, S.; Zhang, X.; et al. Ferromagnetic van der Waals Crystal VI$_3$. *J. Am. Chem. Soc.* **2019**, *141*, 5326−5333.

(15) Wang, Y.-M.; Tian, S.-J.; Li, C.-H.; Jin, F.; Ji, J.-T.; Lei, H.-C.; Zhang, Q.-M. Raman scattering study of two-dimensional magnetic van der Waals compound VI$_3$. *Chin. Phys. B* **2020**, *29*, 056301.

(16) Lee, I.; Utermohlen, F. G.; Weber, D.; Hwang, K.; Zhang, C.; van Tol, J.; Goldberger, J. E.; Trivedi, N.; Hammel, P. C. Fundamental Spin Interactions Underlying the Magnetic Anisotropy in the Kitaev Ferromagnet CrI$_3$. *Phys. Rev. Lett.* **2020**, *124*, 017201.

(17) Xu, C.; Feng, J.; Xiang, H.; Bellaiche, L. Interplay between Kitaev interaction and single ion anisotropy in ferromagnetic CrI$_3$ and CrGeTe$_3$ monolayers. *npj Comput. Mater.* **2018**, *4*, 57.

(18) Mermin, N. D.; Wagner, H. Absence of Ferromagnetism or Antiferromagnetism in One- or Two-Dimensional Isotropic Heisenberg Models. *Phys. Rev. Lett.* **1966**, *17*, 1133−1136.

(19) Pershoguba, S. S.; Banerjee, S.; Lashley, J. C.; Park, J.; Ågren, H.; Aeppli, G.; Balatsky, A. V. Dirac Magnons in Honeycomb Ferromagnets. *Phys. Rev. X* **2018**, *8*, 011010.

(20) Liu, J.; Shi, M.; Mo, P.; Lu, J. Electrical-field-induced magnetic Skyrmion ground state in a two-dimensional chromium tri-iodide ferromagnetic monolayer. *AIP Adv.* **2018**, *8*, 055316.

(21) Jiang, S.; Li, L.; Wang, Z.; Shan, J.; Mak, K. Spin tunnel field-effect transistors based on two-dimensional van der Waals heterostructures. *Nature Electronics* **2019**, *2*, 159.

(22) Klein, D. R.; MacNeill, D.; Song, Q.; Larson, D. T.; Fang, S.; Xu, M.; Ribeiro, R. A.; Canfield, P. C.; Kaxiras, E.; Comin, R.; Jarillo-Herrero, P. Enhancement of interlayer exchange in an ultrathin two-dimensional magnet. *Nat. Phys.* **2019**, *15*, 1255−1260.

(23) Wang, Z.; Gibertini, M.; Dumcenco, D.; Taniguchi, T.; Watanabe, K.; Giannini, E.; Morpurgo, A. Determining the phase diagram of atomically thin layered antiferromagnet CrCl$_3$. *Nat. Nanotechnol.* **2019**, *14*, 1116.

(24) Ubrig, N.; Wang, Z.; Teyssier, J.; Taniguchi, T.; Watanabe, K.; Giannini, E.; Morpurgo, A. F.; Gibertini, M. Low-temperature monoclinic layer stacking in atomically thin CrI$_3$ crystals. *2D Mater.* **2020**, *7*, 015007.

(25) Sun, Z.; et al. Giant nonreciprocal second-harmonic generation from antiferromagnetic bilayer CrI$_3$. *Nature* **2019**, *572*, 497−501.

(26) McGuire, M. A.; Clark, G.; KC, S.; Chance, W. M.; Jellison, G. E.; Cooper, V. R.; Xu, X.; Sales, B. C. Magnetic behavior and spin-lattice coupling in cleavable van der Waals layered CrCl$_3$ crystals. *Phys. Rev. Materials* **2017**, *1*, 014001.

(27) Kuhlow, B. Magnetic Ordering in CrCl$_3$ at the Phase Transition. *physica status solidi (a)* **1982**, *72*, 161−168.

(28) Hammersley, A. P.; Svensson, S. O.; Hanfland, M.; Fitch, A. N.; Hausermann, D. Two-dimensional detector software: From real detector to idealised image or two-theta scan. *High Pressure Res.* **1996**, *14*, 235−248.

(29) Yang, X.; Juhas, P.; Farrow, C. L.; Billinge, S. J. L. xPDFsuite: an end-to-end software solution for high throughput pair distribution function transformation, visualization and analysis; 2014.

(30) Toby, B. H.; Von Dreele, R. B. GSAS-II: the genesis of a modern open-source all purpose crystallography software package. *J. Appl. Crystallogr.* **2013**, *46*, 544−549.

(31) Farrow, C. L.; Juhas, P.; Liu, J. W.; Bryndin, D.; Božin, E. S.; Bloch, J.; Proffen, T.; Billinge, S. J. L. PDFfit2 and PDFgui: computer programs for studying nanostructure in crystals. *J. Phys.: Condens. Matter* **2007**, *19*, 335219.

(32) Giannozzi, P.; et al. QUANTUM ESPRESSO: a modular and open-source software project for quantum simulations of materials. *J. Phys.: Condens. Matter* **2009**, *21*, 395502.

(33) Perdew, J. P.; Burke, K.; Ernzerhof, M. Generalized Gradient Approximation Made Simple. *Phys. Rev. Lett.* **1996**, *77*, 3865−3868.

(34) Blöchl, P. E. Projector augmented-wave method. *Phys. Rev. B: Condens. Matter Mater. Phys.* **1994**, *50*, 17953−17979.

(35) Kresse, G.; Joubert, D. From ultrasoft pseudopotentials to the projector augmented-wave method. *Phys. Rev. B: Condens. Matter Mater. Phys.* **1999**, *59*, 1758−1775.

(36) Cococcioni, M.; de Gironcoli, S. Linear response approach to the calculation of the effective interaction parameters in the LDA + U method. *Phys. Rev. B: Condens. Matter Mater. Phys.* **2005**, *71*, 035105.

(37) Juza, D.; Giegling, D.; Schäfer, H. Über die Vanadinjodide $VJ_2$ und $VJ_3$. *Z. Anorg. Allg. Chem.* **1969**, *366*, 121−129.

(38) Berry, K. O.; Smardzewski, R. R.; McCarley, R. E. Vaporization reactions of vanadium iodides and evidence for gaseous vanadium-(IV) iodide. *Inorg. Chem.* **1969**, *8*, 1994−1997.

(39) Klemm, W.; Krose, E. Die Kristallstrukturen von $ScCl_3$, $TiCl_3$ und $VCl_3$. *Z. Anorg. Chem.* **1947**, *253*, 218−225.

(40) Liu, Y.; Petrovic, C. Three-dimensional magnetic critical behavior in $CrI_3$. *Phys. Rev. B: Condens. Matter Mater. Phys.* **2018**, *97*, 014420.

(41) He, J.; Ma, S.; Lyu, P.; Nachtigall, P. Unusual Dirac half-metallicity with intrinsic ferromagnetism in vanadium trihalide monolayers. *J. Mater. Chem. C* **2016**, *4*, 2518−2526.

(42) Wang, Y.-P.; Long, M.-Q. Electronic and magnetic properties of van der Waals ferromagnetic semiconductor $VI_3$. *Phys. Rev. B: Condens. Matter Mater. Phys.* **2020**, *101*, 024411.

(43) Li, Y.; Liu, Y.; Wang, C.; Wang, J.; Xu, Y.; Duan, W. Electrically tunable valleytronics in quantum anomalous Hall insulating transition metal trihalides. *Phys. Rev. B: Condens. Matter Mater. Phys.* **2018**, *98*, 201407.

(44) Lazarević, N.; Popović, Z. V.; Hu, R.; Petrovic, C. Evidence for electron-phonon interaction in $Fe_{1−x}M_xSb_2$ (M = Co and Cr $0 \leq x \leq 0.5$) single crystals. *Phys. Rev. B: Condens. Matter Mater. Phys.* **2010**, *81*, 144302.

(45) Baum, A.; Milosavljević, A.; Lazarević, N.; Radonjić, M. M.; Nikolić, B.; Mitschek, M.; Maranloo, Z. I.; Šćepanović, M.; Grujić-Brojčin, M.; Stojilović, N.; Opel, M.; Wang, A.; Petrovic, C.; Popović, Z. V.; Hackl, R. Phonon anomalies in FeS. *Phys. Rev. B: Condens. Matter Mater. Phys.* **2018**, *97*, 054306.

(46) Milosavljević, A.; Šolajic, A.; Pešić, J.; Liu, Y.; Petrovic, C.; Lazarević, N.; Popović, Z. V. Evidence of spin-phonon coupling in $CrSiTe_3$. *Phys. Rev. B: Condens. Matter Mater. Phys.* **2018**, *98*, 104306.

(47) McCarty, K. F.; Radousky, H. B.; Hinks, D. G.; Zheng, Y.; Mitchell, A. W.; Folkerts, T. J.; Shelton, R. N. Electron-phonon coupling in superconducting $Ba_{0.6}K_{0.4}BiO_3$: A Raman scattering study. *Phys. Rev. B: Condens. Matter Mater. Phys.* **1989**, *40*, 2662−2665.

(48) Proffen, T.; Page, K. L.; McLain, S. E.; Clausen, B.; Darling, T. W.; TenCate, J. A.; Lee, S.-Y.; Ustundag, E. Atomic pair distribution function analysis of materials containing crystalline and amorphous phases. *Z. Kristallogr.* **2005**, *220*, 1002−1008.

(49) Bordet, P. Application of the pair distribution function analysis for the study of cultural heritage materials. *C. R. Phys.* **2018**, *19*, 561−574.

(50) Bozin, E. S.; Yin, W. G.; Koch, R. J.; Abeykoon, M.; Hor, Y. S.; Zheng, H.; Lei, H. C.; Petrovic, C.; Mitchell, J. F.; Billinge, S. J. L. Local orbital degeneracy lifting as a precursor to an orbital-selective Peierls transition. *Nat. Commun.* **2019**, *10*, 3638.

(51) Egami, T.; Billinge, S. J. L. *Underneath the Bragg Peaks: Structural Analysis of Complex Materials*; 2003; p 16.

(52) Jin, F.; Lazarević, N.; Liu, C.; Ji, J.; Wang, Y.; He, S.; Lei, H.; Petrovic, C.; Yu, R.; Popović, Z. V.; Zhang, Q. Phonon anomalies and magnetic excitations in $BaFe_2Se_2O$. *Phys. Rev. B: Condens. Matter Mater. Phys.* **2019**, *99*, 144419.

(53) Moskovits, M.; Dilella, D. Surface-enhanced Raman spectroscopy of benzene and benzene-d6 adsorbed on silver. *J. Chem. Phys.* **1980**, *73*, 6068−6075.

(54) Dubroka, A.; Humlíček, J.; Abrashev, M. V.; Popović, Z. V.; Sapiña, F.; Cantarero, A. Raman and infrared studies of $La_{1−y}Sr_yMn_{1−x}M_xO_3$ (M = Cr,Co,Cu,Zn,Sc or Ga): Oxygen disorder and local vibrational modes. *Phys. Rev. B: Condens. Matter Mater. Phys.* **2006**, *73*, 224401.

(55) Souza Filho, A. G.; Faria, J. L. B.; Guedes, I.; Sasaki, J. M.; Freire, P. T. C.; Freire, V. N.; Mendes Filho, J.; Xavier, M. M.; Cabral, F. A. O.; de Araújo, J. H.; da Costa, J. A. P. Evidence of magnetic polaronic states in $La_{0.70}Sr_{0.30}Mn_{1−x}Fe_xO_3$manganites. *Phys. Rev. B: Condens. Matter Mater. Phys.* **2003**, *67*, 052405.

(56) Lekgoathi, M.; Kock, L. Effect of short and long range order on crystal structure interpretation: Raman and powder X-ray diffraction of $LiPF_6$. *Spectrochim. Acta, Part A* **2016**, *153*, 651−654.

(57) Wolverton, C.; Zunger, A.; Lu, Z.-W. Long-versus short-range order in $Ni_3V$ and $Pd_3V$ alloys. *Phys. Rev. B: Condens. Matter Mater. Phys.* **1994**, *49*, 16058.

(58) Webster, L.; Liang, L.; Yan, J.-A. Distinct spin-lattice and spin-phonon interactions in monolayer magnetic $CrI_3$. *Phys. Chem. Chem. Phys.* **2018**, *20*, 23546−23555.

MATERIALS RESEARCH SOCIETY OF SERBIA
INSTITUTE OF TECHNICAL SCIENCES OF  SASA

Programme and the Book of Abstracts

SIXTEENTH YOUNG RESEARCHERS' CONFERENCE

MATERIALS SCIENCE AND ENGINEERING

Belgrade, December 6–8, 2017
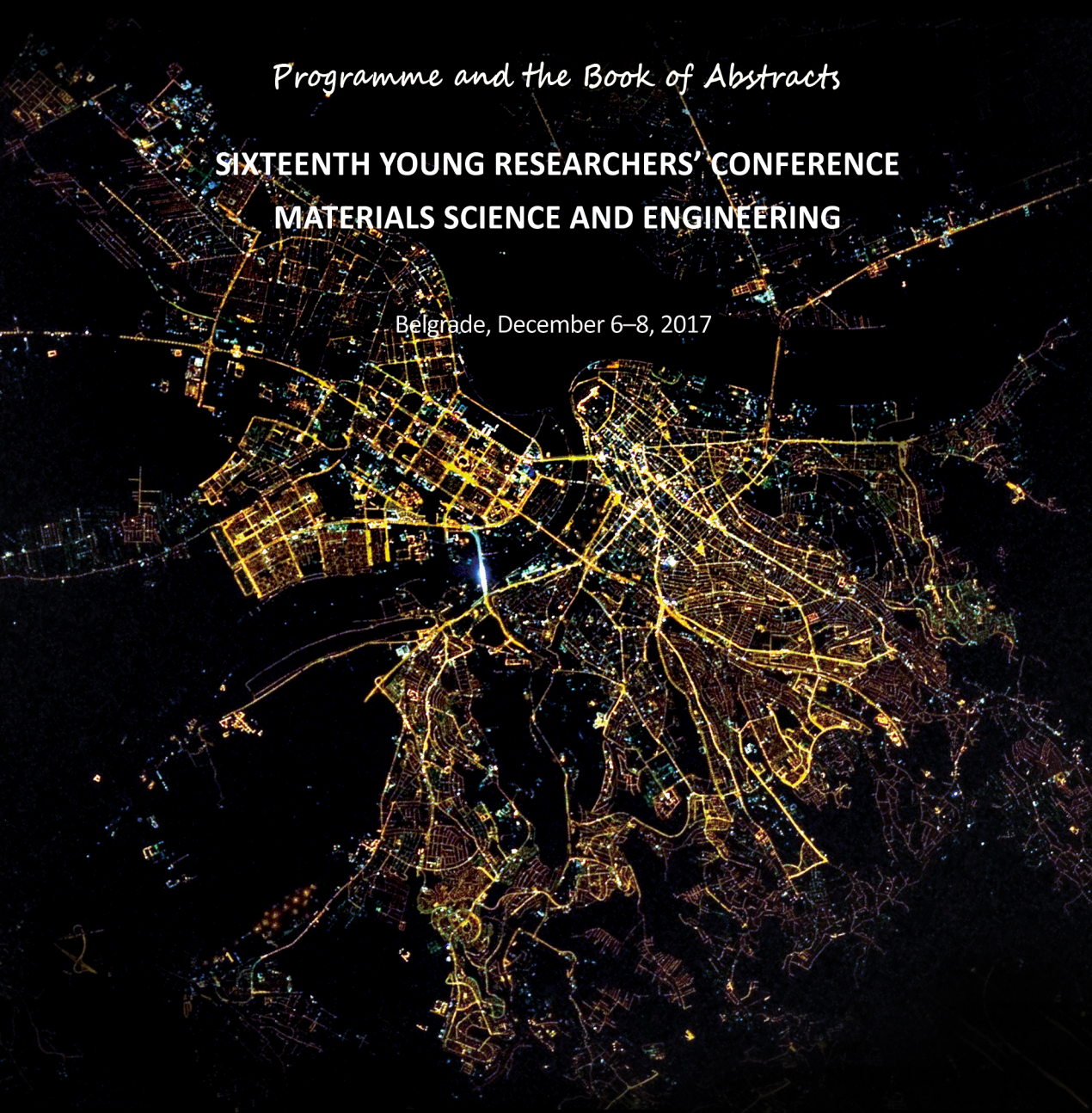
9-5

# Phonon anomalies in FeS

Ana Milosavljević[1], Andreas Baum[2,3], Nenad Lazarević[1], Miloš M. Radonjić[4], Božidar Nikolić[5], Merlin Mitschek[2,3], Zahra Inanloo Maranloo[2], Maja Šćepanović[1], Nenad Stojilović[1], Matthias Opel[2], Aifeng Wang[6], Čedomir Petrović[6], Zoran V. Popović[1], Rudi Kackl[2]

[1]Center for Solid State Physics and New Materials, Institute of Physics Belgrade, University of Belgrade, Pregrevica 118, 11080 Belgrade, Serbia, [2]Walther Meissner Institut, Bayerische Akademie der Wissenschaften, 85748 Garching, Germany, [3]Fakultat fur Physik E23, Technische Universitat Munchen, 85748 Garching, Germany, [4]Scientific Computing Laboratory, Center for the Study of Complex Systems, Institute of Physics Belgrade, University of Belgrade, Pregrevica 118, 11080 Belgrade, Serbia, [5]Faculty of Physics, University of Belgrade, Studentski trg 12, Belgrade, Serbia, [6]Condensed Matter Physics and Materials Science Department, Brookhaven National Laboratory, Upton, NY 11973-5000, USA

In the iron-based superconductors (IBS) magnetic order, structure, nemacity and superconductivity are closely interrelated. Influence of correlation effects seems to increase from 122 systems, such as $BaFe_2As_2$, to the 11 chalcogenides FeTe, FeSe and FeS. Although, isostructural and isoelectronic, 11 class members differ significantly. FeSe undergoes a structural transition at 90 K, shows electronic nemacity, with no long range magnetic ordering down to lowest temperatures, and superconductivity at 9 K. On the other hand, FeTe exhibits magneto-structural transition at 67 K, but no superconductivity. FeS has a superconducting transition at 5 K, but it does not show structural transition. Magnetic ordering in FeS still remains an open question.

Here we present light scattering data on phonons in tetragonal FeS. We identified two out of four Raman-active phonon modes, and a second order scattering process involving two acoustic phonons. Additionally, DFT calculations verify experimentally obtained results. Calculated phonon density of states and selection rules for two-phonon process based on the modified group projector technique confirm second order scattering process within a gap in the projected density of states. Low temperature experiments revealed that temperature dependence of all modes is mainly governed by lattice contraction, except for deviations at 50 K and below 20 K. The anomaly below 20 K coincides with the observation of the possible short range magnetic order.

9-3

## Small influence of magnetic ordering on lattice dynamics in $TaFe_{1.25}Te_3$

Marko Opačić,[1] Nenad Lazarević,[1] Darko Tanasković,[2] Miloš Radonjić,[2]
Ana Milosavljević,[1] Yongchang Ma,[3,4] Čedomir Petrović,[3] Zoran V. Popović[1,5]
[1]*Center for Solid State Physics and New Materials, Institute of Physics Belgrade, University of Belgrade, Pregrevica 118, 11080 Belgrade, Serbia,* [2]*Scientific Computing Laboratory, Center for the Study of Complex Systems, Institute of Physics Belgrade, University of Belgrade, Pregrevica 118, 11080 Belgrade, Serbia,* [3]*Condensed Matter Physics and Materials Science Department, Brookhaven National Laboratory, Upton, New York 11973-5000, USA,* [4]*School of Materials Science and Engineering, Tianjin University of Technology, Tianjin 300384, People's Republic of China,* [5]*Serbian Academy of Sciences and Arts, Knez Mihailova 35, 11000 Belgrade, Serbia*

The $TaFe_{1+y}Te_3$ single crystal is a layered system with monoclinic crystal structure, composed of FeTe chains along the b-axis, separated by a Ta/Te network, with additional Fe ions randomly situated on interstitial sites. It is a correlated bad metal which orders antiferromagnetically at $T\_N \approx 200$ K. The magnetic structure consists of double zigzag spin chains, although the type of intra- and interchain magnetic interactions is still under debate. We present polarized Raman scattering spectra of $TaFe_{1.25}Te_3$ single crystal in a wide temperature range. Nine out of 15 Raman active modes are observed and assigned using measured spectra in different polarization configurations and lattice dynamics calculations. Unlike the case of related FeTe compound, $TaFe_{1.25}Te_3$ do not show significant changes near magnetic transition temperature $T\_N$, which lead us to conclude that the phase transition is continuous. Temperature dependence of energy and linewidth is conventional, with the only exception in the vicinity of $T\_N$, where some of phonon modes broaden. This is probably the consequence of spin fluctuations near the critical temperature. Our results suggest very small changes in the electron-phonon coupling and density of states at the Fermi level in the investigated temperature range.

*Programme and the Book of Abstracts*

# EIGHTEENTH YOUNG RESEARCHERS' CONFERENCE

# MATERIALS SCIENCE AND ENGINEERING

Belgrade, December 4–6, 2019

http://www.mrs-serbia.org.rs/index.php/young-researchers-conference

10-6

## Spin-phonon coupling in CrSiTe$_3$ and CrSi$_{0.8}$Ge$_{0.1}$Te$_3$

Ana Milosavljević[1], A. Šolajić[1], J. Pešić[1], B. Višić[1], M. Opačić[1],
Yu Liu[2], C. Petrovic[2], N. Lazarević[1], Z. V. Popović[1,3]

[1]*Center for Solid State Physics and New Materials, Institute of Physics Belgrade, University of Belgrade, Pregrevica 118, 11080 Belgrade, Serbia, [2]Condensed Matter Physics and Materials Science Department, Brookhaven National Laboratory, Upton, NY 11973-5000, USA, [3]Serbian Academy of Sciences and Arts, Knez Mihailova 35, 11000 Belgrade, Serbia*

Trichalcogenides CrXTe$_3$ (X = Si, Ge) are semiconducting representatives of the van der Waals materials, with ferromagnetic order and band gap of 0.4 eV for Si and 0.7 eV for Ge compound, and Curie temperatures of 32 K and 61 K, respectively. Their layered structure provided exfoliation to mono and few-layer nanosheets, due to the weak van der Waals inter-layer bonding. This possibility togeather with their semiconducting and magnetic properties makes them ideal candidates for applications in optoelectronics and nano-spintronics.

Here we present temperature dependent Raman scattering study on CrSiTe$_3$ and CrSi$_{0.8}$Ge$_{0.1}$Te$_3$. Four and eight out of ten Raman active modes were assigned and observed for pure and slightly doped compound, respectively. The self-energies of $A_g^3$ and $E_g^3$ symmetry modes of CrSiTe$_3$ compound exhibit unconventional temperature evolution around 180 K. In addition, doubly degenerate $E_g^3$ mode shows a clear change of asymmetry in the same temperature region. The observed behavior is consistent with the previously reported presence of short-range magnetic order and strong spin-phonon coupling. Changing the concentrations of elements in parent compounds and doping plays a significant role in semiconducting physics and can lead to surprising physical properties, like considerable change in magnetic transition temperature or structural modifications. SEM measurements performed on our CrSi0.8Ge0.1Te3 single crystals revealed the 10% concentration of Ge atoms and the same amount of vacancies. Inelastic scattering results on CrSi0.8Ge0.1Te3 in addition to symmetry predicted modes, shows the presence of one mode attributed to the inhomogeneous distribution of Ge atoms, and two overtones, all obeying pure $A_g$ selection rules. All analyzed modes display unconventional behavior, but in a difference from the pure compound on a higher temperature of 210 K.

7-11th October 2019
Belgrade, Serbia

**SCMP**

http://www.sfkm.ac.rs/

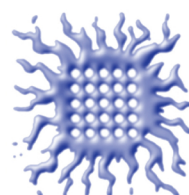# The 20th Symposium on Condensed Matter Physics

# BOOK OF ABSTRACTS

University of Belgrade,
Faculty of Physics

Institute of Physics Belgrade

Vinca Institute
of Nuclear Sciences

Serbian Academy
of Sciences and Arts

Ministry of Education, Science and
Technological Development,
Republic of Serbia

# Lattice dynamics and phonon anomalies in FeS

A. Baum[a,b], A. Milosavljević[c], N. Lazarević[c], M.M. Radonjić[d], B. Nikolić[e], M. Mitschek[a,b], Z. Inanloo Maranloo[a], M. Šćepanović[c], M. Grujić – Brojčin[c], N. Stojilović[f], M. Opel[a], Aifeng Wang[g], C. Petrovic[g], Z.V. Popović[c,h]  and R. Hackl[a]

[a]*Walther Meissner Institut, Bayerische Akademie der Wissenschaften, 85748 Garching, Germany*
[b]*Fakultät für Physik E23, Technische Universität München, 85748 Garching, Germany*
[c]*Center for Solid State Physics and New Materials, Institute of Physics Belgrade, University of Belgrade, Pregrevica 118, 11080 Belgrade, Serbia*
[d]*Scientific Computing Laboratory, Center for the Study of Complex Systems, Institute of Physics Belgrade, University of Belgrade,Pregrevica 118, 11080 Belgrade, Serbia*
[e]*Faculty of Physics, University of Belgrade, Studentski trg 12, Belgrade, Serbia*
[f]*Department of Physics and Astronomy, University of Wisconsin Oshkosh, Oshkosh, Wisconsin 54901, USA*
[g]*Condensed Matter Physics and Materials Science Department, Brookhaven National Laboratory, Upton, New York 11973-5000, USA*
[h]*Serbian Academy of Sciences and Arts, Knez Mihailova 35, 11000 Belgrade, Serbia*

**Abstract.** Crystal structure, magnetic ordering and nematic phase are closely interrelated in the iron-based superconductors.  Although isostructural and isoelectronic, properties of 11 chacogenides, FeSe, FeTe and FeS, differ significantly. Whereas FeSe  undergoes a nematic and structural phase transition at 90 K, togeather with superconductivity below 9 K, and no traces of long-range magnetic ordering, FeTe is not superconducting but exhibits magnetostructural phase transition at temperature  of 67 K. The last member of the familly, FeS, have a superconducting transition at 5 K,  and remains tetragonal down to lowest temperatures.

Here, we present results of Raman scattering experiment on tetragonal FeS, and analysis of vibrational properties close to potential instabilities [1]. Besides $A_{1g}$ and $B_{1g}$ modes assignation,  which is in a good agreement with DFT calculations, third peak whitin a gap  of  calculated phonon density of states can be indentified as a result of   second order scattering process. Both, selection rules for two-phonon processes, based on modified group projector technique and energy are in a good agreement with the experiment. A fourth mode, close to $A_{1g}$ could originate from either deffect-induced scattering or second order scattering as well.  The temperature dependence of all four modes is governed by the contraction of the lattice, with anomalies at 50 K and below 20 K. The anomaly observed at 20 K has a correspondence with previously reported results of short-range magnetic ordering. The presence of two-phonon scattering indicates strong phonon-phonon scattering, which is likely to originate from an electron-phonon interaction being enhanced in comparison to other pnictides and chalcogenides.

## REFERENCES

1.  A. Baum, A. Milosavljević, N. Lazarević, M. M. Radonjić, B. Nikolić, M. Mitschek, Z. I. Maranloo, M. Šćepanović, M. Grujić-Brojčin, N. Stojilović, M. Opel, A. Wang, C.Petrovic, Z.V.Popović, and R. Hackl, Phonon anomaliesin FeS, *Phys.Rev.B* **97**, 054306 (2018).

# Lattice dynamics and phase transitions in $Fe_{3-x}GeTe_2$

A. Milosavljević[a], A. Šolajić[a], S. Djurdjić Mijin[a], J. Pešić[a], B. Višić[a], Y. Liu[b], C. Petrovic[b], N. Lazarević[a] and Z. V. Popović[c]

*[a]Center for Solid State Physics and New Materials, Institute of Physics Belgrade, University of Belgrade, Pregrevica 118, 11080 Belgrade, Serbia*
*[b]Condensed Matter Physics and Materials Science Department, Brookhaven National Laboratory, Upton, New York 11973-5000, USA*
*[c]Center for Solid State Physics and New Materials, Institute of Physics Belgrade, University of Belgrade, Pregrevica 118, 11080 Belgrade, Serbia and Serbian Academy of Sciences and Arts, Knez Mihailova 35, 11000 Belgrade, Serbia*

**Abstract.** A new class of magnetic van der Waals bonded materials has recently become of great interest, as a suitable candidates for various applications. Whereas $CrXTe_3$ (X = Si, Ge, Sn) and $CrX_3$ (X = Cl, Br, I) classes maintain low phase transition temperatures even in a monolayer regime, $Fe_{3-x}GeTe_2$ has a high bulk transition temperature, between 220 and 230 K, making it a promising applicant.

Here we present DFT calculations of lattice dynamics and Raman spectroscopy measurements of the van der Waals bonded ferromagnet $Fe_{3-x}GeTe_2$ [1]. Four out of eight Raman active modes are observed and assigned, in agreement with numerical calculations. The energies and linewidths of the observed modes display an unconventional temperature dependence at about 150 and 220 K, followed by the nonmonotonic evolution of the Raman continuum. Whereas the former can be related to the magnetic phase transition, the origin of the latter anomaly remains an open question.

## REFERENCES

1. A. Milosavljević, A. Šolajić, S. Djurdjić-Mijin, J. Pešić, B. Višić, Yu Liu, C. Petrovic, N. Lazarević, and Z. V. Popović. "Lattice dynamics and phase transitions in $Fe_{3-x}GeTe_2$." Physical Review B 99, no. 21 (2019): 214304.

MATERIALS RESEARCH SOCIETY OF SERBIA
INSTITUTE OF TECHNICAL SCIENCES OF SASA

*Programme and the Book of Abstracts*

# NINETEENTH YOUNG RESEARCHERS' CONFERENCE
# MATERIALS SCIENCE AND ENGINEERING

Belgrade, December 1-3, 2021

12-1

## Raman Spectroscopy of Quasi-two-dimensional transition metal trihalides

S. Djurdjić Mijin[1], AM Milinda Abeykoon[2], A. Solajić[1], A. Milosavljević[1], J. Pešić[1], M. Šćepanović[1], Y. Liu[3], A. Baum[4,5], C. Petrovic[3], N. Lazarević[1], Z. V Popović[1,6]

[1]Center for Solid State Physics and New Materials, Institute of Physics Belgrade, University of Belgrade, Pregrevica 118, 11080 Belgrade, Serbia, [2]National Synchrotron Light Source II, Brookhaven National Laboratory, Upton, New York 11973, [3]Condensed Matter Physics and Materials Science Department, Brookhaven National Laboratory, Upton, New York 11973-5000, United States, [4]Walther Meissner Institut, Bayerische Akademie der Wissenschaften, 85748 Garching, Germany, [5]Fakultat fur Physik E23, Technische Universiẗat Munchen, 85748 Garching, Germany, [6]Serbian Academy of Sciences and Arts, Knez Mihailova 35, 11000 Belgrade, Serbia

Theoretically speaking, the restriction of only one dimension in a three-dimensional material could result in its layered quasi-two-dimensional (2D) analog which has completely unpredictable properties and therefore hosts various unexpected physical phenomena. Successful exfoliation of quasi-2D grapheme by A. Geim's group in 2004 did not only confirm these expectations and create a platform for experimental investigation of low-dimensional phenomena, but also paved the way for the next-generation nanoelectronic devices. All of the above mentioned strongly contributed to the extensive research on the fundamental properties of quasi-2D materials. Great effort has been put towards realization of a magnetic atomically thin crystals which would open up the opportunities of exploring, or even exploiting, of different 2D magnetic states, expand the scope of their possible applications, and point to the possible emergence of a new quantum state of matter. That being said, it is not surprising that the experimental confirmation of 2D magnetism in transition-metal-trihalides (TMTs) caused a stir in scientific community. In an effort to better understand fundamental properties of these materials we have performed the Raman Spectroscopy Study of the two TMT members – CrI3 and VI3, both of which have been confirmed to host low-dimensional magnetism. This experimental technique was used to probe a reported phase transition in CrI3 and crystal structure of VI3. The phase transition, which transforms the low-temperature $R\bar{3}$ structure into the high-temperature C2/m structure, with potential co-existence, has been observed at 220 K. Our findings confirm the mentioned phase transition but at much lower temperature of 180 K, and no co-existence has been tracked. Our investigation into the crystal structure of VI3 tried to give an answer to the long unsolved mystery whether at room temperatures VI3 crystallizes into a $P\bar{3}1c$, $R\bar{3}$ or C2/m crystal structure. Interestingly, what we have observed points to the coexistence of short-range ordered $P\bar{3}1c$ and long-range ordered $R\bar{3}$ phases.

12-5

# Lattice dynamics and magnetism in $Fe_{3-x}GeTe_2$

<u>Ana Milosavljević</u>[1], Andrijana Šolajić[1], Sanja Đurđić Mijin[1], Jelena Pešić[1],
Bojana Višić[1], Yu Liu[2], Cedomir Petrovic[2], Zoran V. Popović[1,3], Nenad Lazarević[1]

[1]Institute of Physics Belgrade, University of Belgrade, Pregrevica 118, 11080 Belgrade,
Serbia, [2]Condensed Matter Physics and Materials Science Department, Brookhaven
National Laboratory, Upton, New York 11973-5000, USA, [3]Serbian Academy of Sciences
and Arts, Knez Mihailova 35, 11000 Belgrade, Serbia

$Fe_{3-x}GeTe_2$ belongs to a highly experimentally and theoretically studied class of van der Waals ferromagnetic materials. Due to the weak interaction between the layers, the exfoliation of the bulk crystals to mono and a few layers is relatively easy. The magnetic properties of these materials are kept even in a low-dimensional regime which makes this class suitable for possible applications in new device engineering.

$Fe_{3-x}GeTe_2$ has a relatively high magnetic transition temperature (220-230 K). This temperature, as well as lattice parameters, strongly depends on vacancies concentration in the sample. Samples with a higher concentration of vacancies grown by flux method have lower $T_C$ (150 K).

In Raman spectra of flux-grown $Fe_{3-x}GeTe_2$ single crystal four out of eight modes predicted by symmetry are detected ($2A_{1g} + 2E_{2g}$). The experimentally obtained phonon energies are in a good agreement with theoretically calculated values. Temperature dependence of phonon self-energies displays deviation from the conventional model at temperatures around 150 K and 220 K. In addition, at the same temperatures nonmonotonic behavior of electronic continuum is present. While the temperature of the first anomaly coincides with the magnetic phase transition temperature, the anomaly at 220 K remains an open question although can be related to a persistence of short-range magnetic ordering in this compound.

UNIVERZITET U BEOGRADU

FIZIČKI FAKULTET

Ana N. Milosavljević

# Elektron-fonon i spin-fonon interakcija u superprovodnicima na bazi gvožđa i kvazi-2D materijalima izučavana metodom Ramanove spektroskopije

doktorska disertacija

Beograd, 2021

UNIVERSITY OF BELGRADE

FACULTY OF PHYSICS

Ana N. Milosavljević

# Electron-phonon and spin-phonon interaction in iron-based superconductors and quasi-2D materials studied by Raman spectroscopy

doctoral dissertation

Belgrade, 2021

**Članovi komisije:**


Mentor:
Dr Nenad Lazarević
Viši naučni saradnik
Institut za fiziku Beograd
Univerzitet u Beogradu


Akademik Zoran V. Popović
Naučni savetnik
Institut za fiziku Beograd
Univerzitet u Beogradu


Prof. dr Đorđe Spasojević
Redovni profesor
Fizički fakultet
Univerzitet u Beogradu


Dr Božidar Nikolić
Vanredni profesor
Fizički fakultet
Univerzitet u Beogradu


Dr Zorica Popović
Docent
Fizički fakultet
Univerzitet u Beogradu

*Mojim roditeljima*

# Zahvalnica

*Na prvom mestu, želim da se zahvalim svom mentoru dr Nenadu Lazareviću na pruženoj podršci i pomoći, podjednako kao studentu i kao prijatelju. Zahvalila bih se na prenesenom znanju, strpljenju, uloženom trudu i optimizmu.*

*Akademiku Zoranu V. Popoviću se zahvaljujem najpre na ukazanoj prilici za rad u Centru za fiziku čvrstog stanja i nove materijale, i na savetima, sugestijama i pruženoj pomoći.*

*Kolegama iz Centra, dr Maji Šćepanović, dr Mirjani Grujić-Brojčin, dr Marku Opačiću i dr Bojani Višić se zahvaljujem na podršci i pomoći tokom mog rada u Centru i tokom izvođenja eksperimenta i na korisnim savetima i sugestijama .*

*Prof. dr Čedomiru Petroviću i njegovim saradnicima, dr Aifeng Wang-u i dr Yu Liu-u, se zahvaljujem na sintezi proučavanih uzoraka u okviru ove disertacije, eksperimentima, diskusijama i savetima.*

*Posebnu zahvalnost želim da izrazim prof. dr Rudi Hackl-u i dr Andreas Baum-u iz Valter Majsner instituta u Minhenu na izuzetnoj saradnji, eksperimentima, diskusijama, savetima i prenesenom znanju.*

*dr Milošu Radonjiću se zahvaljujem na teorijskim proračunima dinamike rešetke FeS sistema; dr Jeleni Pešić i Andrijani Šolajic na izvršenim proračunima za kvazi-dvodimenzione magnetne materijale; dr Božidaru Nikoliću na određivanju selekcionih pravila za dvo-fononske procese.*

*Zahvalila bih se i svom mentoru na master studijama dr Edibu Dobardžiću na pomoći i podrši tokom svih ovih godina.*

*dr Jasmini Lazarević zahvaljujem se na stalnoj podršci i drugarstvu tokom lepih i onih manje lepih trenutaka.*

*Koleginici Sanji Đurđić Mijin se zahvaljujem na više nego korektnoj saradnji i izdvojenom vremenu da ovu disertaciju pročita i da svoje sugestije.*

*Svom najboljem drugu Ivanu Despiću zahvaljujem se na svakoj vrsti podrške tokom izrade ove disertacije. Slavici Mastilović, Nataliji Resimić, Duši Vuković i Marjani Majsotorović, mojim najdivnijim drugaricama, zahvalna sam na strpljenju, ljubavi, podršci i ohrabrenju tokom svih ovih godina. Svojoj drugarici iz pandemijom izazvanog karantina, Dubravki Bunčić bih se zahvalila na uvek lepim i punim podrške rečima, i pozitivnom stavu.*

*Na kraju želim da se zahvalim svojoj porodici na beskonačnoj podršci i ljubavi.*

# Rezime

U okviru ove disetacije predstavljeni su rezultati proučavanja dinamike rešetke dva tipa materijala sa jakim elektronskim korelacijama metodom Ramanove spektroskopije. Prvoj grupi materijala pripada klasa 11-halkogenida superprovodnika na bazi gvožđa, odnosno FeS i $FeSe_{1-x}S_x$ ($0 \leq x \leq 1$), dok drugu čine kvazi-dvodimenzioni materijali magnetnih karakteristika, $Cr(Si:Ge)Te_3$ i $Fe_{3-x}GeTe_2$. Predstavljeni rezultati daju uvid i u složenu međupovezanost različitih stepeni slobode; vibracionih, elektronskih i spinskih.

Superprovodnike na bazi gvožđa karakteriše veliki broj različitih ali međusobno bliskih faza; narušenje kristalne simetrije, superprovodno stanje, nematična faza i magnetno uređenje. Zagonetnost sprege ovih faza i njihove koegzistencije već decenijama podstiče brojna istraživanja u ovoj oblasti. Kompleksnost faznih dijagrama izostrkturnih i izoelektronskih gvožđe halkogenida (FeSe, FeTe i FeS) izazvala je poslednjih godina veliko interesovanje naučne zajednice i dovela do intenzivnog proučavanja kako čistih uzoraka tako i materijala dobijenih mešanjem različitih vrsta atoma halkogena.

U prvom delu ove disertacije najpre su predstavljeni rezultati Ramanove spektroskopije na čistom FeS uzorku, a zatim je ispitivan uticaj dopiranja FeSe uzorka atomima sumpora na vibracione karakteristike ovog materijala. Dva od četiri simetrijom predviđena Raman aktivna moda $A_{1g}$ i $B_{1g}$, su označena u polarizovanim ramanskim spektrima tetragonalnog FeS. Pored simetrijom predviđenih modova, u spektrima su identifikovana dva dodatna moda, od kojih prvi $A_{1g}$ simetrije, dok se drugi mod javlja i u $A_{1g}$ i u $B_{1g}$ kanalu rasejanja. Na osnovu teorijski izračunatih fononskih disperzionih relacija i fononske gustine stanja, zaključeno je da se dodatni mod $A_{1g}$ simetrije nalazi u procepu fononske gustine stanja i da je posledica dvofononskog procesa rasejanja. Za razliku od prethodnog, mod koji se javlja i u $A_{1g}$ i u $B_{1g}$ kanalu rasejanja ne nalazi se u procepu fononske gustine stanja, pa se može objasniti i kao rezultat procesa defektom indukovanog rasejanja. Temperaturska zavisnost ($20 \leq T \leq 300\,\mathrm{K}$) fononskih energija uglavnom je određena kontrakcijama rešetke. Dodatno, skokovite promene ispod $20\,\mathrm{K}$ mogu biti posledica kratkodometnog magnetnog uređenja. DFT proračuni i simetrijska analiza dvofononskih procesa u saglasnosti su sa eksperimentom. Dvofononska ekscitacija prisutna u spektrima ovog materijala koja se nalazi u procepu fononske gustine stanja posledica je pojačane elektron-fonon interakcije u ovom materijalu. U spektrima serije uzoraka $FeSe_{1-x}S_x$ ($0 \leq x \leq 1$) merenim u $A_{1g}$ kanalu rasejanja već pri najmanjim koncentracijama atoma sumpora ($x = 0.05$) dolazi do pojave dodatnih modova. Ovi rezultati ukazuju da prisustvo atoma sumpora utiče na elektron-fonon interakciju posredstvom koje se odvijaju dvofononski procesi koji rezultuju pojavom dodatnih pikova $A_{1g}$ simetrije. S druge strane, prisutno je širenje modova shodno koncentraciji defekata, a recipročna vrednost poluširine $B_{1g}$ moda prati trend kritične temperature merenih uzoraka u zavisnosti od $x$.

Drugi deo istraživanja posvećen je izučavanju dinamike rešetke kvazi-dvodimenzionih magnetnih materijala, tritelurida Cr(Si:Ge)Te$_3$ i ditelurida Fe$_{3-x}$GeTe$_2$. Iako različite prirode provodnosti, pomenuti materijali predstavnici su nove klase feromagnetnih materijala slojevite strukture. Slabe van der Valsove sile među slojevima omogućavaju jednostavnu eksfolijaciju zapreminskih kristala na mono- i poli-slojeve. U Ramanovim spektrima poluprovodnika CrSiTe$_3$ identifikovana su četiri moda, $A_g$ i tri $E_g$, čije su energije u veoma dobrom slaganju sa teorijskim proračunima. Temperaturska zavisnost analiziranih fononskih linija ukazuje na nekonvencionalno ponašanje na temperaturama ispod 180 K, znatno iznad temperature magnetnog prelaza. Pored toga, na istim temperaturama jedan od $E_g$ modova pokazuje asimetriju ka nižim energijama. Ovakvo ponašanje konzistentno je sa prethodno predloženim kratkodometnim magnetnim uređenjem i pojačanom spin-fonon interakcijom. Uticaj dopiranja i vakancija na dinamiku rešetke ispitivan je na uzorku sastava CrSi$_{0.8}$Ge$_{0.1}$Te$_3$. Usled prisustva vakancija, primećen je pad temperature magnetnog prelaza u odnosu na CrSiTe$_3$. U ovom slučaju, u ramanskim spektrima identifikovano je ukupno sedam simetrijom predviđenih modova i dodatni mod $A_g$ simetrije. Ovaj mod javlja se usled „cepanja" jednog od simetrijom predviđenih $A_g$ modova. Cepanje ovog moda posledica je prisustva vakancija u uzorku na pozicijama Si/Ge atoma i njihove nehomogene raspodele na nano-skali. Nekonvencionalno ponašanje energija i polуširina svih analiziranih modova do temperature 210 K ukazuje na prisustvo pojačane spin-fonon interakcije u prisustvu vakancija i atoma germanijuma.

Fe$_{3-x}$GeTe$_2$ je metal sa relativno visokom temperaturom magnetnog faznog prelaza, koja pak zavisi od koncentracije vakancija u uzorku, $x$ i može iznositi od 150 do 230 K. Četiri od osam simetrijom predviđenih Raman aktivnih modova je označeno i analizirano. Eksperimentalni rezultati u saglasnosti su sa teorijskim proračunima. Energije i poluširine analiziranih modova odstupaju od konvencionalnog modela na temperaturama 150 i 220 K. Ovo ponašanje fononskih linija praćeno je nemonotonom evolucijom elektronskog kontinuuma na istim temperaturama. Dok anomalija na temperaturi od 150 K odgovara magnetnom faznom prelazu, ona na oko 220 K za sada ostaje nerazjašnjena i eventualno se može dovesti u vezu sa kratkodometnim magnetnim uređenjem ili formiranjem Kondo rešetke.

**Ključne reči**: Ramanova spetrkoskopija, superprovodnici na bazi gvožđa, van der Valsovi materijali

**Naučna oblast**: Fizika

**Oblast istraživanja**: Fizika kondenzovanog stanja materije

**UDK broj**: 538.9

# Abstract

In this thesis the Raman scattering study results of two types of strongly correlated materials are presented. First, the 11-chalcogenides from iron-based superconductors, FeS and $FeSe_{1-x}S_x$ ($0 \leq x \leq 1$), whereas the second type refers to the quasi-two dimensional magnetic materials Cr(Si:Ge)Te$_3$ and Fe$_{3-x}$GeTe$_2$. In addition, the presented results give insight into the complex correlation of different degrees of freedom; vibrational, electronic, and magnetic.

Iron-based superconductors are materials characterized by a large number of different closely interrelated phases; crystal symmetry breaking, superconducting state, nematic phase, and magnetic order. The correlation and coexistence of these phases have been studied for decades in order to clarify the physical mechanisms in these compounds. The complexity of phase diagrams of isostructural and isoelectronic iron-chalcogenides (FeSe, FeTe, and FeS), brought a lot of attention in the past few years. The pure compounds as well as those obtained by mixing the different types of chalcogen atoms are intensively theoretically and experimentally studied.

In the first part of this thesis, the results of Raman spectroscopy study on pure tetragonal FeS compound are presented, as well as the influence of sulfur atoms doping on the vibrational properties of FeSe. Two out of four modes predicted by symmetry, $A_{1g}$ and $B_{1g}$, are assigned in polarized Raman spectra of tetragonal FeS. In addition to the symmetry predicted modes, two more are also detected. First one is the mode of $A_{1g}$ symmetry, while the second one is observed in $A_{1g}$ as well as in $B_{1g}$ scattering channel. Based on calculated phonon dispersion relations and phonon density of states, the mode of pure $A_{1g}$ symmetry is located in the gap of phonon density of states and represents a result of two-phonon scattering process. Unlike former, the additional mode detected in $A_{1g}$ and $B_{1g}$ scattering channels is not located in the gap of phonon density of states and could be explained as a consequence of defect-induced scattering process. Temperature dependence ($20 \leq T \leq 300\,\mathrm{K}$) of observed modes' energy is mostly governed by lattice contraction, while anomalies below $20\,\mathrm{K}$ indicate the presence of short-range magnetic order. DFT calculations and symmetry analysis for two-phonon processes are in a good agreement with experiment. Presence of two-phonon excitation in the gap of phonon density of states is most likely a consequence of enhanced electron-phonon interaction in this material in comparison to the other members of a class. In polarized Raman spectra of $FeSe_{1-x}S_x$ ($0 \leq x \leq 1$), the additional $A_{1g}$ symmetry modes are detected, even for the very law concentrations of sulfur atoms ($x = 0.05$). This result indicate that the presence of sulfur atoms in the sample affects the electron-phonon interaction responsible for two-phonon processes and the presence of two-phonon modes in $A_{1g}$ scattering channel. In addition, broadening of phonon lines is present due to disorder, as $x$ is increased, while the inverse of the $B_{1g}$ mode line width follows the trend of $T_c(x)$.

In the second part of the research the lattice dynamics of quasi-two-dimensional magnetic

materials, tritellurides Cr(Si:Ge)Te$_3$ and ditelluride Fe$_{3-x}$GeTe$_2$ was studied. Although of a different conducting nature, these materials represent the new class of ferromagnetic layered compounds. Weak van der Waals forces between the layers enable simple exfoliation of bulk crystals to mono and few-layers. In Raman spectra of a semiconductor CrSiTe$_3$ four modes are identified, $A_g$ and three $E_g$, with energies in a very good agreement with theoretical calculations. Temperature dependence of all analyzed modes exhibit unconventional behaviour at temperatures below 180 K, well above magnetic transition temperature. In addition, at the same temperatures one of $E_g$ modes shows clear asymmetry in the lower energy part. These results can be explained by the presence of short-range magnetic order and the strong spin-phonon coupling previously reported in this material. Influence of vacancies and doping on a lattice dynamics was studied using the CrSi$_{0.8}$Ge$_{0.1}$Te$_3$ sample. Due to the presence of vacancies, the shifting of magnetic transition temperature to the lower values in comparison to CrSiTe$_3$ was found. In this case, seven symmetry predicted modes are detected in Raman spectra, and additional mode of $A_g$ symmetry. This additional mode appears due to "splitting" of one of the symmetry predicted $A_g$ modes. The cause of mode splitting could be found in the presence of vacancies in the sample and their inhomogeneous distribution on Si/Ge atomic site at nano-scale. Strong spin-phonon coupling in the presence of vacancies and Ge atoms up to temperature of 210 K is indicated by deviations from conventional temperature dependence of phonon energies and line widths of all analyzed modes.

Fe$_{3-x}$GeTe$_2$ is a metal with a relatively high magnetic transition temperature, which strongly depends on vacancies concentration $x$ in the sample, and takes values between 150 and 230 K. Four out of eight symmetry predicted Raman active modes are assigned and analyzed. The experimental results are in agreement with numerical calculations. At temperatures around 150 and 220 K, energies and line widths of the observed modes deviate from conventional model. The nonmonotonic evolution of the Raman continuum follows the modes' behaviour at the same temperatures. Whereas the anomaly at 150 K corresponds to the magnetic transition, the latter one, at 220 K, could be related to the localization or Kondo lattice behaviour, but still remains an open question.

# Akronimi

DFT - Density Functional Theory

DFPT - Density Functional Perturbation Theory

SEM - Scanning Electron Microscopy

EDS - Electron Dispersive Spectroscopy

ARPES - Angle Resolved Photo Emission Spectroscopy

CVT - Chemical Vapor Transport

NCP - Nematic Critical Point

SDW - Spin Density Wave

ZFC - Zero Field Cooling

FC - Field Cooling

MGPT - Modified Group Projector Technique

# Sadržaj

  *

# Glava 1    Uvod

Ramanova spektroskopija predstavlja optičku metodu za karakterizaciju materijala. Ova metoda zasnovana je na efektu neelastičnog rasejanja svetlosti vidljivog dela spektra na materijalu (Ramanov efekat). Fotoni upadnog snopa svetlosti mogu se rasejati neelastično na različitim vrstama (kvazi)čestica, fononima, magnonima, elektronima, zbog čega je ova tehnika veoma pogodna za ispitivanje različitih vrsta ekscitacija i njihovih interakcija u materijalima sa jakim elektronskim korelacijama [1, 2, 3]. Svakoj vrsti ekscitacije odgovara određen oblik linije u Ramanovom spektru; fononi se javljaju kao uži pikovi na tačno određenim energijama, dvo-magnonske ekscitacije kao široke strukture na višim energijama, dok su obe vrste ekscitacije superponirane na elektronski kontinuum [2].

U ovoj disertaciji predstavljeni su rezultati Ramanove spektroskopije na dvema različitim klasama materijala - superprovodnicima na bazi gvožđa (FeSe$_{1-x}$S$_x$, $0 \leq x \leq 1$) i kvazi-dvodimenzionim magnetnim materijalima (Cr(Si:Ge)Te$_3$ i Fe$_{3-x}$GeTe$_2$).

Iako otkrivena pre više od jednog veka, superprovodnost i dalje uživa veliku naučnu pažnju i nastavlja da bude jedna je od najistraživanijih oblasti fizike kondenzovanog stanja materije. Sve do otkrića visokotemperaturske superprovodnosti u kupratima ovaj efekat uspešno je objašnja-vala BSC (Bardin - Kuper - Šifer) teorija. Prema ovoj teoriji do formiranja Kuperovih parova, odnosno privlačne interakcije među elektronima, dolazi posredstvom fonona. Kako na višim temperaturama dolazi do termalnih ekscitacija elektrona i raskidanja Kuperovih parova, efekat visokotemperaturske superprovodnosti se nije mogao obijasniti postojećim teorijama. Ovime je otvorena potpuno nova oblast fizike kondenzovanog stanja materije - fizika nekonvencionalnih superprovodnika.

Nakon otkrića superprovodnosti u LaOFeP [4], odnosno LaFeAsO$_{1-x}$F$_x$ [5], pored kuprata otkrivena je još čitava jedna klasa superprovodnika na bazi gvožđa, specifična po veoma boga-tim i kompleksim faznim dijagramima. Čisti uzorci ove klase materijala obično se karakterišu normalnim (nesuperprovodnim) stanjem. Narušenje kristalne simetrije koje se javlja usled snižavanja temperature, praćeno je formiranjem dugodometnog magnetnog uređenja. Situacija postaje značajno zanimljivija pri supstituciji atoma matičnih jedinjenja. Pri određenoj koncen-traciji magnetno uređenje biva potisnuto i javlja se superprovodna faza [6]. Takođe, kod nekih superprovodnika na bazi gvožđa dolazi do tzv. nematične faze, stanja koje karatketriše elek-tronska anizotropija i narušenje rotacione simetrije [7, 8, 9, 10]. Proučavanje ovih faza i njihovog međusobnog uticaja ključno je u razjašnjavanju fenomena nekonvencionalne superprovodnosti.

S tim ciljem se poslednjih godina proučavaju članovi klase 11-halkogenida (FeSe, FeTe i

FeS). Ova izostrukturna i izoelektronska jedinjenja pogodna su za proučavanje međusobnog uticaja kristalne strukture, magnetnog uređenja, nematične i superprovodne faze. Zavisno od tipa atoma halkogena svaki predstavnik ove klase odlikuje se različitim fizičkim osobinama. Kod prvog sintetisanog superpovodnika ove klase, FeSe, na temperaturi od oko 90 K dolazi do narušenja simetrije, iz tetragonalne u ortorombičnu [11, 12], odnosno do nematičnog uređenja [13]. Ispod temperature strukturnog faznog prelaza javljaju se spinske fluktuacije i frustrirano magnetno uređenje [14] dok se superprovodna faza javlja na 9 K [15]. Za razliku od FeSe, FeTe nije superprovodan [16] ali ga karakteriše antiferomagnetno uređenje i narušenje simetrije iz tetragonalne u monoklitičnu na temperaturi od 67 K [16, 17, 18]. Do strukturnog faznog prelaza u FeS sistemu ne dolazi ni na najnižim temperaturama, ali ispod 5 K ulazi u superprovodnu fazu [19, 20]. Iako nematično uređenje nije uočeno u ovom materijalu, ispostavilo se da dopiranjem FeSe atomima sumpora, $FeSe_{1-x}S_x$ ($0 \leq x \leq 1$), nematična faza opstaje do nematične kritične tačke $x \approx 0.2$ [21, 22]. U okolini ove tačke kritična temperatura dostiže svoj maksimum. Ovakav rezultat ukazuje na uticaj nematičnih fluktuacija pri formiranju superprovodnog stanja [22]. Iako je kritična temperatura FeS i FeSe superprovodnika niska, očigledno je da su fizičke osobine kao i mehanizmi koji se odvijaju u ovim materijalima različiti. Kako bi se došlo do saznanja zašto i na koji način se ovi procesi odvijaju, i kako jedni na druge utiču, neophodno je doći do novih rzlutata koji bi upotpunili postojeću sliku.

U svemu gore navedenom pronađena je motivacija za predstavljeno istrživanje u okviru kog su primenom Ramanove spektroskopije ispitivani monokristalni uzorci FeS i $FeSe_{1-x}S_x$ ($0 \leq x \leq 1$). Ramanski sprektri čistog FeS uzorka pored modova predviđenih simetrijskom analizom, $A_{1g}$ i $B_{1g}$ simetrije, otkrivaju i dva dodatna moda, od kojih jedan $A_{1g}$ simetrije, i drugi koji se javlja i u $A_{1g}$ i u $B_{1g}$ kanalu rasejanja. Ovakav rezultat stvorio je potrebu za dodatnim analizama. DFT proračunima utvrđeno je da se dodatni mod $A_{1g}$ simetrije nalazi u procepu fononske gustine stanja. Na osnovu selekcionih pravila za dvofononske procese izraču- natih MGPT metodom za prostornu grupu simetrije ovog sistema ($P4/nmm$), određeni su pravci visoke simetrije u blizini kojih se nalaze stanja koja ovom procesu doprinose. Mod koji se javlja u $A_{1g}$ i $B_{1g}$ kanalima rasejanja ne nalazi se u procepu fononske gustine stanja pa može biti rezultat dvofononskog procesa ali i defektom indukovanog rasejanja. Temperaturska zavisnost energija i poluširina ispod 20 K indikacija je kratkodomentnog magnetnog uređenja u ovom materijalu. U polarizovanim ramanskim spektrima serije uzoraka $FeSe_{1-x}S_x$ ($0 \leq x \leq 1$), pored simetrijom predviđenih modova (nedopiranih uzoraka) u $A_{1g}$ kanalu rasejanja čak i mi- nimalno dopiranih uzoraka, javljaju se dodatni modovi. Vodeći se analogijom dodatnog $A_{1g}$ moda detektovanog u spektrima FeS uzorka, vrlo je moguće da su dodatni modovi u $A_{1g}$ kanalu rasejanja rezultat dvofononskih procesa. Ovi dvofononski procesi nejverovatnije su posledica promena u elektron-fonon interakciji u prisustvu atoma sumpora. S druge strane, temperatur- ska zavisnost poluširine $B_{1g}$ moda obrnuto je srazmerna trendu kritične temperature merenih uzoraka. Doprinos predstavljenog istraživanja dosadašnjim saznanjima o ovoj relativno novoj klasi superprovodnih materijala je dvojak. Prikazani su posredni dokazi o elektron-fonon in-

terakciji kako u FeS tako moguće i u dopiranom FeSe počevši od malih koncentracija atoma sumpora.

Poslednjih godina u fokusu istraživanja je i klasa van der Valsovih magnetnih materijala. Ova klasa uključuje metale $(Fe_{3-x}GeTe_2)$[23] i poluprovodnike $CrXTe_3$ (X = Si, Ge, Sn) i $CrX_3$ (X = Cl, I) [24, 25, 26, 27, 28]. Karakteristična je po tome što smanjivanjem dimenzionalnosti zapreminskih kristala materijali zadržavaju svoja magnetna svojstva. Ova osobina omogućuje njihovu tehnološku primenu, ali ujedno stvara i potrebu za njihovim intenzivnim istraživanjem.

$CrSiTe_3$ i $CrGeTe_3$ su poluprovodnici čija je veličina energijskog procepa 0.4 eV i 0.7 eV, a Kirijeva temperatura 32 K, odnosno 61 K [29, 30]. U Ramanovim spektrima $CrSiTe_3$ ($CrGeTe_3$) detektovano je četiri (pet) modova, $A_g + 3E_g$ ($2A_g + 3E_g$). Pored nekonvencionalnog ponaša- nja energija i poluširina modova najvećeg intenziteta $CrSiTe_3$ uzorka ispod temperature od 180 K, jedan od modova $E_g$ simetrije pokazuje asimetriju ka nižim energijama. S obzirom na utvrđeno prisustvo magnetnih korelacija do 150 K, ovakvo ponašanje modova može se pripisati pojačanoj spin-fonon interakciji. S druge strane, menjanje koncentracije nosilaca u poluprovod- nicima može da dovede do promena u određenim fizičkim osobinama, od strukturnih promena do značajnog skoka temperature faznog prelaza. SEM analizom ustanovljeno je da se u uzorku dopiranom atomima Ge nalazi 10% vakanicija i isto toliko atoma Ge, odnosno da je sastava $CrSi_{0.8}Ge_{0.1}Te_3$. Usled prisustva vakancija, merenjem magnetne susceptibilnosti utvrđen je pad Kirijeve temperature u ovom uzorku. U Ramanovim spektrima identifikovana su tri moda $A_g$ i četiri moda $E_g$ simetrije. Pored simetrijom predviđenih modova u spektrima je detektovan dodatni mod $A_g$ simetrije. Ovaj mod se najverovatnije javlja kao posledica vakancija i njihove nehomogene raspodele na pozicijama Si/Ge atoma. Temperaturska zavisnost energija i poluši- rina analiziranih modova odstupa od anharmonijskog modela ispod 210 K, i time ukazuje na prisustvo pojačane spin-fonon interakcije.

Za razliku od $CrXTe_3$ (X = Si, Ge), $Fe_{3-x}GeTe_2$ ima višu temperaturu magnetnog prelaza (220 - 230 K). Parametri rešetke kao i temperatura magnetnog prelaza značajno variraju od kon- centracije vakancija u uzorku, koja pak zavisi i od načina sinteze [31, 32, 33]. Uzorci sintetisani CVT metodom imaju manju koncentraciju vakancija i višu Kirijevu temperaturu (220-230 K) [31], dok obratno važi za one sintetisane fluks metodom i njihova temperatura prelaza je oko 150 K [34]. Četiri od ukupno osam Raman aktivnih modova detektovano je u Ramanovim spektrima, dva $A_{1g}$ i dva $E_{2g}$ simetrije. Vrednosti eksperimentalno dobijenih fononskih energija konzistentne su sa teorijski izračunatim vrednostima. Na temperaturi od oko 150 K primećena je nemonotona temperaturska zavisnost energija i poluširina analiziranih modova. Ovakva temperaturska zavisnost može se dovesti u vezu sa feromagnetnim faznim prelazom [34]. Do- datno, na oko 220 K, ponovo dolazi do nekonvencionalnog ponašanja fononskih karakteristika. U oba slučaja, anomalno ponašanje energija i poluširina praćeno je skokovitim promenama u elektronskom kontinuumu.

Ova doktorska disertacija podeljena je u šest poglavlja. Nakon uvoda u prvom, u dru- gom poglavlju opisane su teorijske osnove Ramanovog rasejanja i eksperimentalne postavke za

merenje neelastičnog rasejanja svetlosti. U trećem poglavlju opisane su fizičke osobine prouča-
vanih materijala. Četvrto poglavlje posvećeno je dinamici rešetke FeS superprovodnika i uticaju
atoma sumpora na fonone u FeSe$_{1-x}$S$_x$ ($0 \leq x \leq 1$). U petom poglavlju prikazani su rezul-
tati Ramanove spektroskopije na kvazi-dvodimenzionim magnetnim materijalima, i analiziran
je uticaj magnetnih fluktuacija i faznih prelaza na njihove vibracione karakteristike. Glavni
zaključci istraživanja sumirani su u šestom poglavlju. Nakon ovog poglavlja nalazi se dodatak
u kome je opisan MGPT metod. Disertacija se završava pregledom korišćene literature.

# Glava 2   Ramanovo rasejanje

Efekat neelastičnog rasejanja svetlosti eskperimentalno je proučavan istovremeno na različitim stranama sveta. Zvaničnu potvrdu dobio je 1928. godine od strane Indijskih naučnika Ramana i Krišnana koji su pokušavali da uoče Komptonov efekat primenom svetlosti vidljivog dela spektra, očekujući vrlo slične rezultate. U eksperimentu je kao izvor korišćena sunčeva svetlost, a monohromatičnost je postignuta primenom filtera [35]. Eksperiment je dao nepredviđene rezultate u vidu pomeraja u odnosu na talasnu dužinu upadnog snopa, što je dovelo do otkrića potpuno novog efekata [36, 37, 38]. Predikciju ovog efekta prvobitno je dao Austrijski teoretičar Smekal pet godina ranije [39].

Istovremeno, u nekadašnjem Sovjetskom Savezu, Mandeljštam i Landsberg ciljano su ispitivali rasejanje svetlosti živine lampe na kristalu kvarca. Nerasejanu svetlost koja je onemogućavala detektovanje rasejane eliminisali su propuštanjem snopa kroz živinu paru [35, 40]. Rezultati Mandeljštama i Landsberga publikovani su samo tri meseca nakon rezultata indijskih naučnika, zbog čega je ovaj efekat nazvan - *Ramanov efekat*. Raman je za ovo otkriće dobio Nobelovu nagradu, 1930. godine. Treba pomenuti da postoje indicije nastale uvidom u beleške indijske i sovjetske grupe načnika da su Mandeljštam i Landsberg, svega nekoliko dana pre Ramana dobili prve rezultate. Iz tog razloga, u Rusiji se i dan danas ovaj efekat naziva *kombinacionim* rasejanjem [35].

## 2.1   Teorija Ramanovog rasejanja

Do Ramanovog rasejanja dolazi usled promene polarizabilnosti molekula $\alpha$, odnosno suscepti-bilnosti kristala $\chi$ [1]. Prilikom ekscitacije uzorka snopom monohromatske svetlosti učestanosti $\omega_L$ može doći do elastičnog (*Rejlijevog*) rasejanja, pri čemu je učestanost rasejane svetlosti jednaka učestanosti upadne, $\omega_L = \omega_S$. Sa manjom verovatnoćom dolazi do neelastičnog (*Ramanovog*) rasejanja jer se samo mali deo, oko $10^{-8}$ - $10^{-12}$, fotona neelastično raseje. Ukoliko je učestanost rasejanog fotona veća od učestanosti upadnog, $\omega_S = \omega_L + \omega_j$, govorimo o *anti-Stoksovom* procesu odnosno anhilaciji fonona. U suprotnom, kada je $\omega_S = \omega_L - \omega_j$ u pitanju je *Stoksov* proces, u kome dolazi do kreacije fonona [1, 41]. Šematski prikaz procesa rasejanja dat je na Slici 2.1.

Za Ramanovo rasejanje odgovorne su elektronske ekscitacije. Upadni foton kreira par elektron-šupljina, pri čemu se fonon rasejava na ekscitovanom elektronu (ili šupljini). Proces rekombinacije elektrona i šupljine, praćen je emisijom rasejanog fonona. U ovom procesu
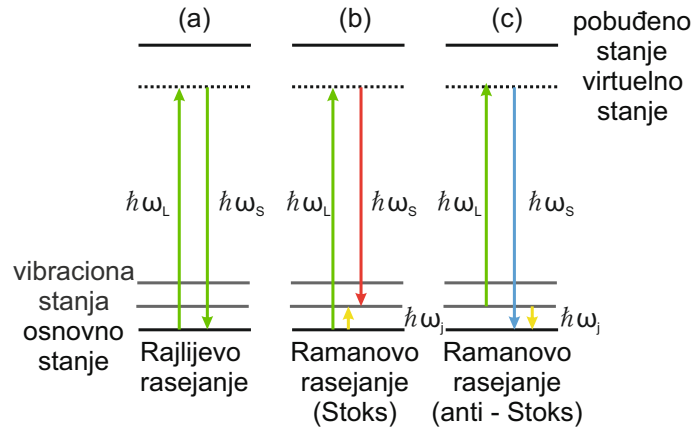
Slika 2.1: Šematski prikaz (a) Rejlijevog i Ramanovog rasejanja u slučaju (b) Stoksovog i (c) anti-Stoksovog procesa.

zakoni održanja energije i kristalnog impulsa moraju važiti, pri čemu se zakon održanja energije odnosi samo na inicijalna i finalna stanja. Na osnovu zakona održanja kristalnog impulsa, zbog velikog intenziteta talasnog vektora fonona na ivici Briluenove zone ($\pi/a$, gde je $a$ parametar rešetke) u odnosu na fotone vidljivog dela spektra ($k_L \approx k_S$), samo su ekscitacije iz centra Briluenove zone, odnosno $\Gamma$ tačke ($q \approx 0$) opservabilne u Ramanovom eksperimentu [1, 41]. Ovo naravno važi u slučaju translaciono invarijantnih sistema kao što su kristali.

## 2.1.1 Klasična teorija Ramanovog rasejanja

Klasična teorija Ramanovog rasejanja zasnovana je na ideji da elektromagnetno polje upadnog snopa sveltosti, indukuje vremeski zavistan dipolni moment sistema $\mathbf{M}(t) = \sum e_i \mathbf{r}_i(t)$ [41]. Neka je $\mathbf{E} = \mathbf{E}_0 \cos \omega_L t$ vektor električnog polja upadnog elektromagnetnog talasa. Zadržavajući se na linearnom članu, izraz za indukovani električni dipolni moment je

$$\mathbf{M} = \alpha \mathbf{E} \tag{2.1}$$

gde je $\alpha$ polarizabilnost molekula. U opštem slučaju pravac vektora $\mathbf{M}$ ne poklapa se sa pravcem vektora električnog polja $\mathbf{E}$, i $\alpha$ predstavlja tenzor drugog ranga. Jednostavnosti radi, pretpostavimo da se pravac vektora $\mathbf{E}$ poklapa sa nekim od pravaca visoke simetrije sistema, odnosno da je paralelan vektoru $\mathbf{M}$.

Kako polarizabilnost $\alpha$, zavisi od raspodele gustine naelektrisanja $\rho$, $\alpha = \alpha(\rho)$, vibracijom molekula dolazi do promene $\rho$, a time i polarizabilnosti $\alpha$. Za dovoljno male pomeraje atoma u odnosu na njihove ravnotežne položaje, $\alpha$ će imati linearnu zavisnost od normalne koordinate $Q = \sqrt{\mu}(u_2 - u_1)$, gde je $\mu$ redukovana masa. Ako je $\alpha_0$ polarizabilnost molekula u ravnotežnom

položaju, razvojem $\alpha$ u Tejlorov red za male pomeraje oko ravnotežnih položaja dobija se:

$$\alpha = \alpha_0 + \left(\frac{\partial \alpha}{\partial Q}\right)_0 Q + \frac{1}{2}\left(\frac{\partial^2 \alpha}{\partial Q^2}\right)_0 Q^2 + \ldots \tag{2.2}$$

Red procesa rasejanja određen je članom uz odgovarajući stepen po normalnoj koordinati $Q$, pa je tako proces rasejanja u prvom redu određen članom linearnim po $Q$, u drugom redu kvadratnim, itd [41].

Ako molekul vibrira učestanošću $\omega_j$ i $Q = Q_0 \cos \omega_j t$, polarizabilnost je:

$$\alpha(t) = \alpha_0 + \left(\frac{\partial \alpha}{\partial Q}\right)_0 Q_0 \cos \omega_j t \tag{2.3}$$

Zamenom izraza za polarizabilnost (2.3) u izraz za dipolni moment (2.1) a zatim i trigonometrijskom transformacijom dobijenog izraza dipolni moment postaje:

$$\mathbf{M}(t) = \alpha_0 \mathbf{E}_0 \cos \omega_L t + \left(\frac{\partial \alpha}{\partial Q}\right)_0 Q_0 \mathbf{E}_0 \cos \omega_j t \cos \omega_L \tag{2.4}$$

$$\mathbf{M}(t) = \alpha_0 \mathbf{E}_0 \cos \omega_L t + \frac{1}{2}\left(\frac{\partial \alpha}{\partial Q}\right)_0 Q_0 \mathbf{E}_0 \left[\cos(\omega_L - \omega_j)t + \cos(\omega_L + \omega_j)t\right] \tag{2.5}$$

Na osnovu izraza (2.5) može se zaključiti da pored toga što indukovani dipolni moment vibrira učestanošću $\omega_L$, vibrira i učestanošću $\omega_L \pm \omega_j$, usled toga što vibracije atoma modulišu polarizabilnost $\alpha$ [41].

Prema klasičnoj teoriji, intenzitet zračenja koje emituje dipolni moment $\mathbf{M}(t)$ u prostorni ugao $d\Omega = \sin\theta d\theta d\phi$

$$dI(t) = \frac{d\Omega}{4\pi c^3}\sin^2\theta |\ddot{\mathbf{M}}(t)|^2 \tag{2.6}$$

po jediničnom prostornom uglu $d\Omega$ je:

$$I(t) = \frac{1}{4\pi c^3}\sin^2\theta |\ddot{\mathbf{M}}(t)|^2 = A|\ddot{\mathbf{M}}(t)|^2 \tag{2.7}$$

Integracijom izraza (2.7) po $\theta$ i $\phi$, intenzitet zračenja koje se emituje u prostorni ugao $4\pi$ je:

$$\hat{I}(t) = \frac{2}{3c^3}|\ddot{\mathbf{M}}(t)|^2. \tag{2.8}$$

Dalje je, koristeći (2.5), (2.6) i (2.8), intenzitet rasejane svetlosti po jediničnom prostornom uglu:

$$I(t) = AE_0^2\left[k_0^2\cos^2\omega_L t + k_1^2\cos^2(\omega_L - \omega_j)t + k_2^2\cos^2(\omega_L + \omega_j)t\right] \tag{2.9}$$

gde je:

$$k_0^2 = \alpha_0^2\omega_L^4 \tag{2.10a}$$

$$k_1^2 = \frac{1}{4}\left(\frac{\partial \alpha}{\partial Q}\right)_0^2 Q_0^2 (\omega_L - \omega_j)^4 \qquad (2.10\text{b})$$

$$k_1^2 = \frac{1}{4}\left(\frac{\partial \alpha}{\partial Q}\right)_0^2 Q_0^2 (\omega_L + \omega_j)^4 \qquad (2.10\text{c})$$

Mešoviti članovi u izrazu (2.9) su izostavljeni s obzirom na to da se snaga zračenja u srednjem anulira u dovoljno dugim vremenskim intervalima, odnosno:

$$I = \lim_{\tau \to \infty} \frac{1}{\tau} \int_0^\tau I(t)dt = \frac{1}{2} A E_0^2 (k_0^2 + k_1^2 + k_2^2) \qquad (2.11)$$

Na osnovu izraza za intenzitet rasejane svetlosti (2.9) vidi se da će rasejana svetlost oscilovati učestanošću $\omega_L$ i $\omega_L \pm \omega_S$ [41]. Furije transformacijom dipolnog momenta $\mathbf{M}(t)$, uz korišćenje izraza (2.7), definisana je snaga zračenja:

$$P(\omega) = A \lim_{\tau \to \infty} \frac{2}{\tau} \int_{-\tau/2}^{\tau/2} |\ddot{\mathbf{M}}(t)e^{-i\omega t}dt|^2 \qquad (2.12\text{a})$$

$$P(\omega) = \pi A E_0^2 (k_0^2 \delta(\omega - \omega_L) + k_1^2 \delta(\omega - (\omega_L - \omega_j)) + k_2^2 \delta(\omega - (\omega_L + \omega_j))) \qquad (2.12\text{b})$$

Na osnovu ovog izraza, intenzitet rasejanja (2.11) postaje:

$$I = \frac{1}{2\pi} \int_0^\infty P(\omega)d\omega \qquad (2.13)$$

Prvi član u izrazu (2.12b) predstavlja izraz za elastično odnosno *Rejlijevo* rasejanje, dok drugi i treći člana odgovaraju neelastičnom *Ramanovom* procesu, *Stoksovom* i *anti-Stoksovom*, respektivno [41].

Klasična teorija na dobar način predviđa pojavu Stoksove i anti-Stoksove linije u Ramanovim spektrima, ali ne i njihov odnos intenziteta [41]. Naime, eksperimentalno je utvrđeno da Stoksova linija ima jači intenzitet od anti-Stoksove, dok se na osnovu izraza (2.10) i (2.11) dobija da je taj odnos manji od jedinice, odnosno, da je anti-Stoksova linija jačeg intenziteta:

$$\frac{I_{Stoks}}{I_{anti-Stoks}} = \frac{(\omega_L - \omega_j)^4}{(\omega_L + \omega_j)^4} \qquad (2.14)$$

Ova nekonzistentnost klasične teorije i eksperimentalnih rezultata razjašnjena je kvantnim pristupom teoriji Ramanovog rasejanja.

U kristalima atomi neprekidno vibriraju oko svojih ravnotežnih položaja, a u zavisnosti od broja i vrste atoma u elementarnoj ćeliji i simetrije njihovih položaja, javljaju se različite kombinacije pomeraja u kristalnoj rešetki koje se nazivaju normalne koordinate vibracija ili normalni modovi [1]. U kristalima postoji $3N - 3$ normalnih koordinata u zavisnosti od broja atoma $N$ u elementarnoj ćeliji. Ukoliko dolazi do promene dielektrične propustljivosti ma-

terijala, normalni mod je infracrveno aktivan, dok se usled promene susceptibilnosti kristala javljaju Raman aktivni modovi. Zavisno od simetrije elementarne ćelije kristala, normalni modovi mogu biti i istovremeno infracrveno i Raman aktivni, u slučaju sistema koji nemaju centar inverzije, a mogu biti i optički neaktivni [1]. Dakle, umesto polarizabilnosti, kod kristala se razmatra tenzor susceptibilnosti $\chi$. Razvoj ovog tenzora po normalnim koordinatama $Q_k$ je oblika [1, 41]:

$$\chi_{ij} = \chi_{ij}^{(0)} + \sum_k \chi_{ij,k} Q_k + \frac{1}{2} \sum_{k',k''} \chi_{ij,k',k''} Q_{k'} Q_{k''} + \ldots \tag{2.15}$$

Promena komponente tenzora susceptibilnosti za normalnu koordinatu $Q_k$ definiše se kao:

$$\Delta\chi_{ij,k} = \chi_{ij,k} Q_k = \left(\frac{\partial\chi_{ij}}{\partial Q_k}\right)_0 Q_k \tag{2.16}$$

a u matričnom obliku:

$$R = \delta\chi^{(k)} = \begin{pmatrix} \chi_{xx,k} & \chi_{xy,k} & \chi_{xz,k} \\ \chi_{yx,k} & \chi_{yy,k} & \chi_{yz,k} \\ \chi_{zx,k} & \chi_{zy,k} & \chi_{zz,k} \end{pmatrix} \tag{2.17}$$

gde je $R$ Ramanov tenzor drugog reda. Intenzitet rasejane svetlosti $I$ proporcionalan je:

$$I \propto |\mathbf{e}_S \cdot R \cdot \mathbf{e}_L|^2, \tag{2.18}$$

gde su $\mathbf{e}_S$ i $\mathbf{e}_L$ jedinični vektori polarizacije rasejane i upadne svetlosti. Relacija

$$|\mathbf{e}_S \cdot R \cdot \mathbf{e}_L|^2 \neq 0 \tag{2.19}$$

predstavlja selekciona pravila za Ramanovo rasejanje [1]. Dakle u zavisnosti od geometrije rasejanja i od toga da li je neka od komponenti Ramanovog tenzora različita od nule, normalni mod je Raman aktivan.

## 2.1.2 Kvantna teorija Ramanovog rasejanja

U terminima teorije čestica, Rejlijevo rasejanje odgovara elastičnom sudaru fotona i kristala, dok Ramanovo rasejanje odogovara neelastičnom, pri čemu foton ili gubi (Stoksov proces) ili dobija (anti-Stoksov proces) jedan ili više kvanata vibracione energije. Proces rasejanja prvog reda uključuje samo jedan fonon i opisan je linearnim članom po normalnim koordinatama $Q_k$ u izrazu (2.15). U procesu rasejanja drugog reda učestvuju dva fonona, i opisan je članom uz $Q_{k'}Q_{k''}$ u relacijii (2.15) [41].

Neka $(\omega_L, \mathbf{k}_L)$ određuje upadni foton, učestanosti $\omega_L$ i talasnog vektora $\mathbf{k}_L$, $(\omega_S, \mathbf{k}_S)$ rasejani foton i $(\omega_j, \mathbf{q})$ fonon u procesu prvog reda. Na osnovu zakona održanja energije i kristalnog

impulsa u inicijalnom i finalnom stanju za Rejlijevo rasejanje važi:
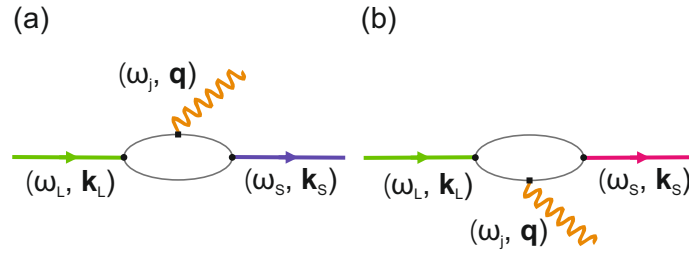
$$\omega_L = \omega_S \tag{2.20a}$$

$$k_L = k_S, \tag{2.20b}$$

dok za Ramanovo rasejanje važi:

$$\omega_L = \omega_S \pm \omega_j(\mathbf{q}) \tag{2.21a}$$

$$\mathbf{k}_L = \mathbf{k}_S \pm \mathbf{q} \tag{2.21b}$$

gde znak "+" odgovara Stoksovom procesu prilikom kog dolazi do kreacije fonona, dok znak "-" odgovara anti-Stoksovom procesu, odnosno procesu anhilacije fonona [41]. Fajnmanovi dijagrami ovih procesa prikazani su na Slici 2.2.



Slika 2.2: Fajnmanov diagram (a) Stoksovog i (b) anti-Stoksovog procesa.

Kako je $\omega_L \gg \omega_j(\mathbf{q})$, na osnovu zakona održanja energije (2.21a) $\omega_L \approx \omega_S$. Na osnovu talasnih dužina upadne i rasejane svetlosti $\lambda_{L,S} = \lambda_0/n(\omega_{L,S})$, gde je $\lambda_0 = c/\nu$ talasna dužina u vakuumu a $n$ indeks prelamanja, za talasne vektore upadne i rasejane svetlosti u kristalu $k_{L,S} = 2\pi/\lambda_{L,S}$ dobijamo $k_{L,S} = n(\omega_{L,S})\omega_{L,S}/c$. Uzevši u obzir da je $\omega_L \approx \omega_S$, za talasne vektore upadne i rasejane svetlosti važi $k_L \approx k_S$ [1].

Dalje je $\lambda_{L,S} \gg a$, gde je $a$ parametar rešetke, pa je intenzitet talasnih vektora upadne i rasejane svetlosti mnogo manji od onog sa ivice zone, tj. $k_{L,S} \ll \pi/a$. Sada se na osnovu zakona održanja kristalnog impulsa može zaključiti da je $q_j \ll \pi/a$, tj. da su u Ramanovom procesu prvog reda opservabilni samo fononi za koje je $q \approx 0$, odnosno iz $\Gamma$ tačke Briluenove zone [1, 41].

Kvantna teorija Ramanovog rasejanje objašnjava nekonzistentnosti eksperimenta i teorijske predikcije odnosa intenziteta Stoksove i anti-Stoksove linije. Naime, u Stoksovom procesu sistem apsorbuje energiju, i nakon prelaska na virtuelni nivo prelazi u prvo pobuđeno vibraciono stanje. Energija rasejanog fotona je u ovom procesu manja od energije upadnog. Obratno važi za anti-Stoksov proces, sistem gubi energiju i energija rasejanog fotona veća je od energije upadnog.

Na osnovu Boze-Ajnštajnove statistike za popunjenost nivoa, odnos intenziteta Stoksove i anti-Stoksove linije proporcionalan je izrazu (2.22) koji je znatno veći od jedinice:

$$\frac{I_{Stoks}}{I_{anti-Stoks}} \propto \left(\frac{\omega_L - \omega_j}{\omega_L + \omega_j}\right)^4 exp\left(\frac{\hbar\omega_j}{k_B T}\right) \tag{2.22}$$

U procesu rasejanja drugog reda upadni foton $(\omega_L, \mathbf{k}_L)$ ekscituje sistem iz inicijalnog vibracionog i elektronskog stanja u virtuelno. Sistem tada emituje foton $(\omega_S, \mathbf{k}_S)$ pri čemu dolazi do prelaza iz virtuelnog u finalno elektronsko i vibraciono stanje koje se od inicijalnog razlikuje za dva kvanta vibracione energije. Ukoliko su u pitanju optički fononi govorimo o Ramanovom rasejanju drugog reda. U ovom procesu mogu učestvovati fononi u različitim kvantnim stanjima, i tada govorimo o *kombinaciji*, ili fononi u istom kvantnom stanju, odnosno *overtonovi*. U slučaju kombinacije, učestanosti $\omega_{j'} \pm \omega_{j''}$ između inicijalnog i finalnog stanja vibracioni kvantni brojevi menjaju se kao $n_{j'} \to n_{j'} \pm 1$ i $n_{j''} \to n_{j''} \pm 1$, a u slučaju overtona učestanosti $2\omega_j$ kao $n_j \to n_j \pm 2$. Šematski prikaz prelaza Stoksovog procesa prikazan je na Slici 2.3. Zakon održanja energije i kristalnog impulsa sada su oblika [41]:

$$\omega_L = \omega_S \pm \omega_{j'}(\mathbf{q}') \pm \omega_{j''}(\mathbf{q}'') \tag{2.23a}$$

$$\mathbf{k}_L = \mathbf{k}_S \pm \mathbf{q}_{j'} \pm \mathbf{q}_{j''} \tag{2.23b}$$
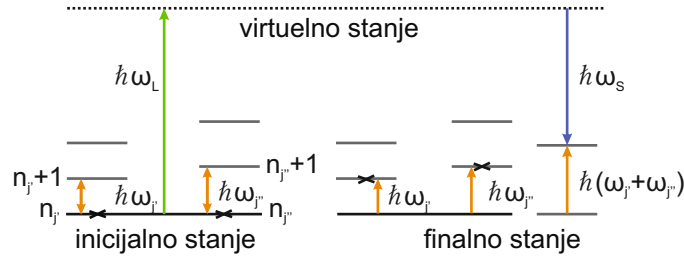


Slika 2.3: Šematski prikaz prelaza u dvofononskom Stoksovom procesu [41].
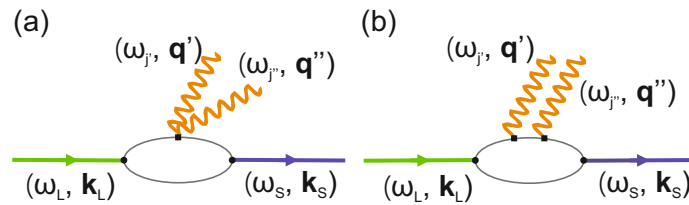


Slika 2.4: Fejnmanovi diagrami (a) direktnog i (b) indirektnog procesa rasejanja drugog reda.

Kao i u slučaju rasejanja prvog reda je $k_L \approx k_S \ll \pi/a$. U Stoksovom procesu drugog reda $(\omega_S < \omega_L)$ dolazi do kreacije dva fonona, $(\omega_{j'}, \mathbf{q}')$ i $(\omega_{j''}, \mathbf{q}'')$, ili kreacije jednog fonona

i anhilacije fonona niže energije. U anti-Stoksovom procesu drugog reda ($\omega_S > \omega_L$), može doći do anhilacije dva fonona ili anhilacije jednog fonona i kreacije fonona niže energije. Na osnovu (2.23b) zaključuje se da u Ramanovom procesu drugog reda učestvuju samo fononi iz prve Briluenove zone. Do rasejanja drugog reda može doći na direktan ili indirektan način. U prvom slučaju, svetlost se direktno rasejava na $Q_{k'}$ i $Q_{k''}$, pri čemu dolazi do promene u polarizabilnosti drugog reda, opisane trećim članom u izrazu (2.15). Kada je u pitanju indirektan proces, dolazi do anharmonijskog sprezanja u prvom redu Raman aktivnih fonona koji u stvari predstavljaju međustanja u ovakvoj vrsti procesa. Fajnmanovi diagrami obe vrste procesa drugog reda prikazani su na Slici 2.4 [41].

### 2.1.3   Uticaj temperature na Raman aktivne fonone

U realnom kristalu, za razliku od izotropnih harmonijskih sistema, u kojima fononi međusobno ne interaguju i mogu dugo živeti, optički fononi razmenjuju energiju među sobom i sa drugim ekscitacijama. Usled fonon-fonon interakcija dolazi do neravnotežne populacije i raspada fonona na fonone niže energije ili rasejanja na termalnim fononima pri čemu se javljaju modovi na različitim energijama [1]. Ove interakcije opisuju se svojstvenom energijom fonona, kompleksnom veličinom koja se može zapisati u obliku [1]:

$$\Sigma = \Delta(\omega) - i\Gamma(\omega), \tag{2.24}$$

gde je $\Delta(\omega)$ promena fononske učestanosti a $\Gamma$ širina, obrnuto proporcionalna vremenu života fonona ($\Gamma \sim 1/\tau$) [1, 42]. Temperaturska zavisnost učestanosti Raman aktivnog moda može se predstaviti kao:

$$\omega(T) = \omega_0 + \Delta(T), \tag{2.25}$$

gde $\omega_0$ predstavlja učestanost moda na apsolutnoj nuli, dok promena učestanosti $\Delta$ potiče od dva doprinosa čisto zapreminskog, koji se manifestuje kroz termalno širenje i čisto temperaturskog, koji potiče od anharmonijskog efekta. Doprinos ovih mehanizama promeni učestanosti dat je izrazom:

$$\Delta(T) = \Delta^V + \Delta^A, \tag{2.26}$$

Prvi član u jednačini (2.26) dat je izrazom (2.27a), u kom $\gamma$ i $\alpha$ označavaju Grunajzenov parametar moda i koeficijent toplotnog širenja. Grunajzenov parametar $\gamma$ opisuje promenu učestanosti ramanskog moda prilikom izotropnog naprezanja u kristalu, $\gamma = -(\partial \ln \nu / \partial \ln V)_T$, gde je $\nu$ učestanost a $V$ zapremina kristala. Efekat termalnog širenja dovodi samo do promene učestanosti datog moda, ne i njegove širine. S tim razlogom se član (2.27a) naziva i kvazi-harmonijski doprinos, odnosno čisto zapreminski doprinos. Kod većine materijala ovaj član je negativan jer efekat termalnog širenja dovodi do širenja kristalne rešetke i omekšavanja modova,

odnosno pomeraja ka nižim energijama [1].

Anharmonijski član $\Delta^A$ potiče od fonon-fonon interakcija, odnosno trofononskih i četvoro-fononskih procesa. U trofononskim procesima dolazi do raspada fonona ili sudara termalnih fonona pri čemu nastaju novi fononi. Analogno, četvorofononski procesi dovode do raspada fonona na tri fonona niže energije ili opet, sudara termalnih fonona i nastanka novih. Zadržava-jući se na trofononskim procesima, ovaj član dat je izrazom (2.27b) koji je uvek negativan jer ovi procesi dovode do negativnog pomeraja učestanosti. $\omega_0$, $\Gamma_0$ i $\lambda_{ph-ph}$ u izrazima (2.27b) i (2.27a) oznaka su za učestanost, konstantu anharmoničnosti, tj. širinu datog moda na $T = 0\,\text{K}$ i parametar fonon-fonon interakcije [1].

$$\Delta^V = \omega_0 \left[ e^{\left(-3\gamma \int_0^T \alpha(T')dT'\right)} - 1 \right] \tag{2.27a}$$

$$\Delta^A = -\frac{\Gamma_0^2}{2\omega_0} \left( 1 + \frac{4\lambda_{ph-ph}}{e^{\hbar\omega_0/2k_BT} - 1} \right) \tag{2.27b}$$

Temperaturska zavisnost širine datog moda zavisi samo od anharmoničnosti i data je izra-zom:

$$\Gamma = \Gamma_0 \left( 1 + \frac{2\lambda_{ph-ph}}{e^{\hbar\omega_0/2k_BT} - 1} \right) \tag{2.28}$$

## 2.2 Oblici spektralnih linija

Rekombinacijom pri prelasku elektrona iz pobuđenog u osnovno stanje dolazi do zračenja, pri čemu ekscitacija ima određeno vreme života i događa se sa određenom verovatnoćom. For-malno, spektralna svetlost može se smatrati zračenjem prigušenog harmonijskog oscilatora. U klasičnoj teoriji prigušeni harmonijski oscilator emituje električno polje dato vremenski zavi-snom difernecijalnom jednačinom:

$$\ddot{E} + \Gamma\dot{E} + \omega_0^2 E = 0, \tag{2.29}$$

čije su svojstvene vrednosti:

$$\alpha_{1,2} = -\frac{\Gamma}{2} \pm i\sqrt{\omega_0^2 - \frac{\Gamma^2}{4}}, \tag{2.30}$$

tako da je njeno opšte kompleksno rešenje linearna kombinacija $e^{\alpha_1 t}$ i $e^{\alpha_2 t}$, sa kompleksnim koeficijentima [43]. Kako se polje opisuje realnim delom ove funkcije, imamo da je:

$$E = C_1 e^{-\Gamma t/2} \cos\omega t + C_2 e^{-\Gamma t/2} \sin\omega t, \tag{2.31}$$

gde je $\omega = \sqrt{\omega_0^2 - \Gamma^2/4}$. Da bi oscilovanje bilo prigušeno, mora važiti $\Gamma/2 < \omega_0$, pri čemu se koeficijenti $C_{1,2}$ iz jednačine (2.31) određuju na osnovu graničnih uslova. U slučaju električnog

polja koje dostiže svoj maksimum i čiji je izvod jednak nuli u početnom trenutku, $t = 0$, rešenje je oblika [43]:

$$E = E_0 e^{-\Gamma t/2} \left[ \cos \omega t + \frac{\Gamma}{2\omega} \sin \omega t \right]. \tag{2.32}$$

Restrikcijom uslova na $E = 0$, za $t < 0$, ova jednačina postaje:

$$E = E_0 e^{-\Gamma t/2} \cos \omega t. \tag{2.33}$$

Treba napomenuti da funkcija (2.33) nije rešenje (2.29) ali je matematički pogodnija za opisivanje energetskog spektra prigušenih oscilacija. Spektar bilo koje vremenski zavisne funkcije dobija se njenom Furije transformacijom. S obzirom na to da funkcija (2.33) trpi skok u tački $t = 0$, njen spektar je dosta komplikovan pa se za opis prigušenih oscilacija koristi kompleksan oblik (i dalje uz restrikciju $E = 0$ za $t < 0$)[43]:

$$E = E_0 e^{-\Gamma t/2} e^{i\omega t}. \tag{2.34}$$

Označavanjem učestanosti prigušenih oscilacija $\omega$ sa $\omega_0$ jednostavnosti radi, Furije transformacijom (2.34), spektar je oblika [43]:

$$E(f) = \int_0^\infty E_0 e^{-\Gamma t/2} e^{i\omega_0 t} e^{-i2\pi f t} dt = \frac{E_0}{\Gamma/2 + i2\pi(f - f_0)}. \tag{2.35}$$

Eksperimentalno, raspodela učestanosti dobija se na osnovu intenziteta zračenja $S(f)$, koji se definiše kao kvadrat opsega učestanosti. U terminima ugaonih učestanosti, intenzitet zračenja koje emituje prigušeni oscilator je:

$$S(\omega) = E(\omega) E^*(\omega) = \frac{E_0^2}{(\Gamma/2)^2 + (\omega - \omega_0)^2} \tag{2.36}$$

Ovaj profil spektralne linije naziva se Lorencov ili još i prirodni (Slika 2.5 (a)) [43]. Širina Lorencove linije određena je parametrom $\Gamma = 2\pi/\tau$, koji predstavlja meru neodređenosti učestanosti $\omega$, gde je $\tau$ vreme života oscilacije. Normiran na jedinicu intenzitet zračenja može se zapisati kao [43]:

$$I_L(\omega - \omega_0) = \frac{\Gamma/2\pi}{(\Gamma/2)^2 + (\omega - \omega_0)^2} \tag{2.37}$$

Pored Lorencovog profila, u spektroskopskim tehnikama koriste se i drugi oblici spektralnih linija. Kada je raspodela energija koju emituje oscilator statistički raspodeljena dolazi do širenja spektralne linije i u tom slučaju koristi se Gausova raspodela [43]. Gausov profil spektralne linije je oblika:

$$I_G(\omega - \omega_0) = \frac{1}{\sigma\sqrt{2\pi}} e^{-\frac{(\omega - \omega_0)^2}{2\sigma^2}}, \text{gde je } \sigma = \frac{\Gamma_G^2}{8\ln 2} \tag{2.38}$$

U izrazu (2.38), $\Gamma_G$ ponovo predstavlja poluširinu, dok je $\sigma^2$ varijansa, odnosno disperzija Gausove raspodele (Slika 2.5 (b)). Pored ovih oblika spektralnih linija koristi se još i Voitov profil [43]. Voitov profil linije (Slika 2.5 (c)) predstavlja konvoluciju linija Gausovog i Lorencovog profila. U eksperimentima rasejanja, često linija izvora koji se koristi za pobudu sistema ima sopstvenu širinu, koja doprinosi širini linije koja potiče od rasejanja na sistemu, odnosno javlja se instrumentalno širenje. Instrumentalnom širenju odgovara Gausov profil linije. Dekonvolucijom Voitove linije dobija se prava poluširina linije koja potiče od sistema.
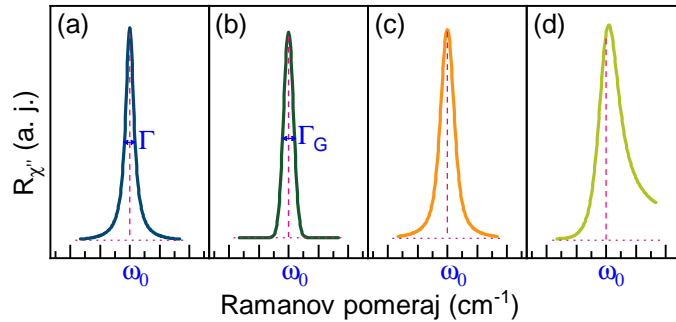


Slika 2.5: (a) Lorencov, (b) Gausov, (c) Voitov i (d) Fano profil spektralne linije.

Fano profil (Slika 2.5 (d)) koristi se kada se u ramanskim spektrima javljaju linije asimetričnog oblika. Da bi se primenila u analizi neophodna je interakcija između kontinualnih (elektronskih) i diskretnih (fononskih) ekscitacija [43, 44, 45]. Najjednostavniji oblik ove linije je:

$$I_F(\omega - \omega_0) = C\frac{(q + \varepsilon)^2}{1 + \varepsilon}, \text{ gde je } \varepsilon = \frac{\omega - \omega_0}{\Gamma} \tag{2.39}$$

U ovom izrazu $\omega_0$ predstavlja čistu fononsku učestanost, $\Gamma$ poluširinu, dok je $q$ parametar asimetrije.

## 2.3   Eksperiment

U ovom poglavlju ukratko će biti opisane komponente i ramanski spektrometri korišćeni u eksperimentima na osnovu kojih su dobijeni rezulatati predstavljeni u narednim poglavljima. Kao ekscitacioni izvori korišćeni su čvrstotelni laseri Coherent Verdi G i Coherent GENESIS, koji emituju zelenu liniju talasne dužine 532 nm i žutu liniju talasne dužine 575 nm.

Emitovana svetlost se optičkim putem usmerava na uzorak. Optički put se može sastojati iz velikog broja komponenti, sa ciljem da se iz emitovanog laserskog snopa eliminišu divergentne komponente i potisnu plazma linije. Primer optičkog puta prikazan je na Slici 2.6. Emitovana svetlost filtrira se najpre kroz filter PH1. Monohromator sa prizmom (PMC) otklanja ostatak plazma linija i razlaže svetlost. Razložena svetlost se zatim projektuje na otvor kroz koji prolazi samo svetlost određene talasne dužine. Filter PH2 oblikuje snop i uklanja divergentne komponente snopa. Prepolarisani snop kontroliše se pomoću $\lambda/2$ pločice u odnosu na polarizaciju određenu Glen-Tompson polarizatorom (P). Polarizacija upadne svetlosti ima
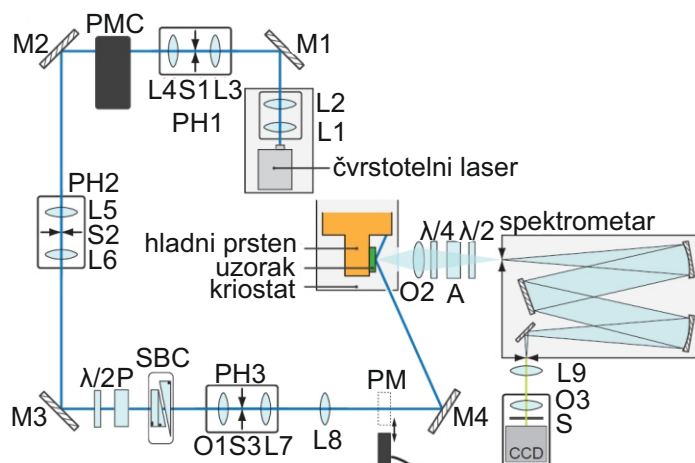
Slika 2.6: Šematski prikaz optičkog puta u eksperimentalnoj postavci za Ramanovo rasejanje koja se nalazi na Valter Majsner institutu u Minhenu. Korišćenjem ove eksperimentalne postavke ispitivan je tetragonalni FeS. Preuzeto iz [46].

veliku ulogu u ovom tipu eksperimenta i određuje se kombinovanjem Glen-Tompson polarizatora i Soleil-Babinet kompenzatora (SBC). Prostorni filter PH3 obezbeđuje otklanjanje efekata interferencije polarizatora i Gausov profil laserske linije. Polarizovana "pročišćena" svetlost usmerena je na uzorak pod uglom od 66°, odakle se neelastično rasjena svelost pomoću sočiva sakuplja i odvodi u spektrometar [46].

Laserski snop se može usmeravati na uzorak i uz pomoć konfokalnog mikroskopa, čime se omogućava fokusiranje laserskog snopa na uzorku od nekoliko $\mu$m a time i rad sa veoma malim uzorcima. Neelastično rasejana svetlost se istim mikroskopom sakuplja i odvodi u spektrometar. Ovakva eksperimentalna konfiguracija naziva se konfiguracija rasejanja unazad (backscattering) i takođe je korišćena tokom izrade ove disertacije. Eksperimentalna konfiguracija, uključujući polarizaciju upadnog i rasejanog snopa, kao i orijentaciju samog uzorka igra veliku ulogu u eksperimentima Ramanovog rasejanja i utiče na selekciona pravila. S obzirom na prirodu uzoraka, eksperimenti su rađeni u kriogenoj sredini sa helijumskim sistemom hlađenja, čime su omogućena merenja na temperaturama od 2 do 300 K, i u visokom vakuumu od $10^{-5}$ do $10^{-6}$ mbar.

Pri izradi ove disertacije, korišćeni su Jobin Yvon T64000, Tri Vista 557 trostepeni ramanski sistemi i dvostepeni monohromator Jobin Yvon U1000. Trostepeni sistemi sastoje se iz dvostepenog pre-monohromatora i spektrometra (Slika 2.7) i mogu da rade u oduzimajućem i sabirajućem režimu. U oduzimajućem režimu (Slika 2.8 (a)), polihromatska svetlost ulazi u prvi stepen monohromatora kroz otvor S1, i razlaže se po talasnim dužinama na rešetki G1, odakle se sistemom ogledala usmerava na otvor $S_{1/2}$ i ulazi u drugi stepen pre-monohromatora. Uloga otvora $S_{1/2}$ je da selektuje određeni opseg talasnih dužina koji će propustiti u drugi stepen premonohrtomatora, i time eliminiše elastično rasejanu svetlost. Rešetka G2 rekombinuje neelastično rasjanu svetlost ponovo u polihromatsku, koja kroz $S_{2/3}$ prolazi u spektrometar gde se uz pomoć rešetke G3 razlaže i sistemom ogledala usmerava na lateralni izlaz. Ovde se nee-
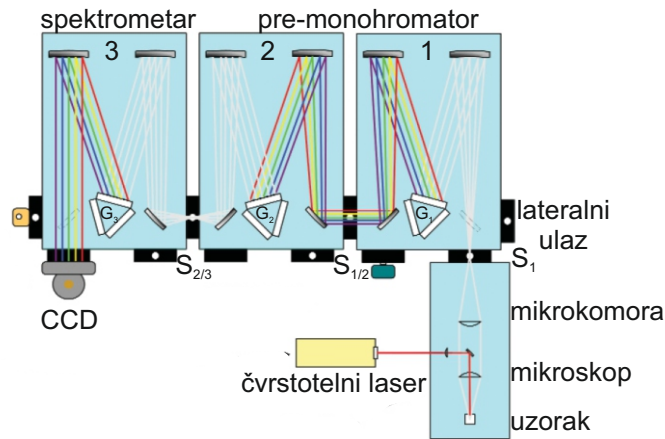
Slika 2.7: Šematski prikaz trostepenog Raman sistema TriVista 557 koji se nalazi u Centru za fiziku čvrstog stanja i nove materijale, Instituta za fiziku u Beogradu. Na ovom sistemu dobijen je deo rezultata vezan za FeS, seriju uzoraka $FeSe_{1-x}S_x$ ($0 \leq x \leq 1$), kao i rezultati Ramanovog rasejanja na van der Valsovim magnetnim materijalima. Preuzeto iz [47].
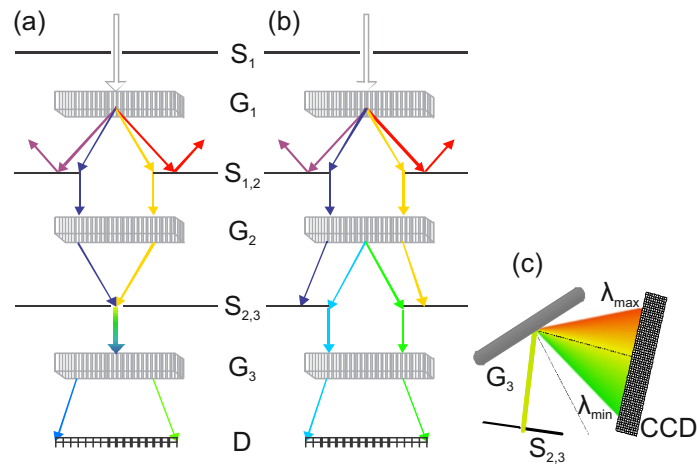


Slika 2.8: Šematski prikaz (a) oduzimajućeg i (b) sabirajućeg režima rada spektrometra. (c) Razlaganje svetlosti rešetkom G3. Preuzeto iz [47].

lastično rasejana svetlost detektuje uz pomoć CCD detektora (Slika 2.8 (c)), koji optički signal pretvara u električni. Kod TriVista 557 sistema, oduzimajući režim postiže se tako što rešetka G2 rotira za isti ugao ali u suprotnom smeru u odnosu na rešetku G1, dok se kod sistema Jobin Yvon T64000 propušteni snop sistemom ogledala invertuje pre nego što padne na rešetku G2.

U sabirajućem režimu (Slika 2.8 (b)) rešetka G2 razlaže već razloženu svetlost propuštenu kroz prvi stepen pre-monohromatora. Glavna karakteristika sabirajućeg režima je visoka spektralna rezolucija. S druge strane oduzimajući režim omogućava detekciju niskoenergetskih ekscitacija i potiskivanje „zalutale svetlosti" zbog čega se i više koristi.

Dvostepeni sistem Jobin Yvon U1000 funkcioniše u sabirajućem režimu na analogan način kao i pre-monohromator trostepenih sistema.

## 2.4   Simetrijska analiza

Kao što je već rečeno u Poglavlju 2.1.1 i 2.3, opservabilnost Raman aktivnih modova u visokosimetričnim sistemima kao što su kristali jako zavisi od geometrije rasejanja. Detekcija i ponašanje modova zavisno od orijentacije kristala u odnosu na laboratorijski koordinatni sistem, kao i ugla između vektora polarizacije upadne i rasejane svetlosti jednoznačno definiše simetriju vibracije i njenu asignaciju.
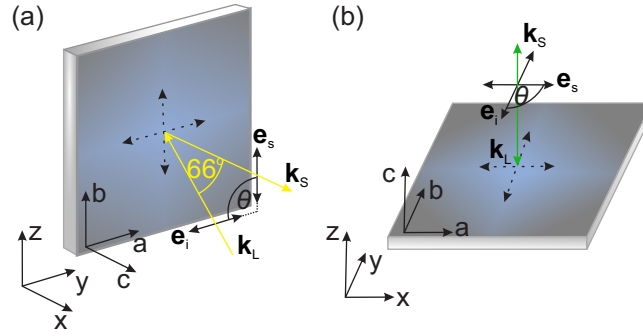


Slika 2.9: Šematski prikaz geometrije rasejanje (a) pod pseudo-Brusterovim uglom i (b) unazad ($\phi = 0$). Ugao između vektora polarizacije upadne i rasejane svetlosti označen je sa $\theta = \angle(\mathbf{e}_L, \mathbf{e}_S)$.

Na osnovu prostorne grupe simetrije kristala i pozicione simetrije atoma u elementarnoj ćeliji moguće je utvrditi Raman aktivne modove i njima odgovarajuće tenzore. Relaciju (2.18) moguće je veoma jednostavno proširiti u terminima ugla rotacije kristala u odnosu na laboratorijski koordinatni sistem. Ako sa $R_\phi$ označimo matricu rotacije oko glavne kristalografske $c$ ose, relacija (2.18) postaje:

$$I \propto |\mathbf{e}_S \cdot \left( R_\phi^T \cdot R \cdot R_\phi \right) \cdot \mathbf{e}_L|^2 \tag{2.40}$$

Analogno izrazu (2.18), da bi mod bio opservabilan, desna strana relacije (2.40) mora biti različita od nule.

Na Slici 2.9 prikazane su geometrije rasejanja (a) pod pseudo-Brusterovim uglom i (b) unazad, u ukštenoj polarizaciji ($\theta = \angle(\mathbf{e}_L, \mathbf{e}_S) = 90°$) kada se ose kristala i laboratorijskog sistema poklapaju ($\phi = 0$). U prvom slučaju generalno je moguće detektovati više fonona nego u geometriji rasejanja u nazad. Naime, kada je ravan na koju se usmeravaju fotoni $ab$ kristalografska ravan, fononi čiji Ramanov tenzor sadrži samo $z$ komponente u geometriji rasejanja unazad ne mogu biti detektovani. Takođe, ukoliko Ramanov tenzor sadrži samo dijagonalne komponente, opservabilan je isključivo u paralelnoj polarizačiji ($\theta = 0°$). Naravno, detekcija fonona čak i u slučaju kada su selekcionih pravila ispunjena, značajno zavisi od samog uzorka, svetlosnog izvora, kalibracije i rezolucije instrumenta.

# Glava 3  Materijali

## 3.1  Superprovodnici na bazi gvožđa

Otkriće superprovodnosti u prvom superprovodniku na bazi gvožđa LaFePO na kritičnoj temperaturi $T_c = 5\,\mathrm{K}$ [4] iznenadilo je naučnu javnost i dovelo do ekspanzije u sintezi i karakterizaciji ovih materijala. Sinteza izostrukturnog materijala LaFeAsO imala je veliki uticaj na razvoj ove oblasti fizike kondenzovanog stanja materije. Naime, dopiranjem ovog materijala atomima fluora kritična temperatura na kojoj dolazi do superprovodne faze bila je znatno viša u odnosu na LaFePO (26 K) [5]. Ovo je bio začetak klase „1111" superprovodnika na bazi gvožđa koji je podstakao dalja istraživanja i sintezu superprovodnika sve viših kritičnih temperatura. Nakon toga slede klase pniktida (FePn), „122" ($Ba_{0.6}K_{0.4}Fe_2As_2$) [48] i „111" [49], zatim halkogenida (FeCh) „11" [50], „21311" klasa ($Sr_2MO_3FePn$) [51] i „122*" ($A_xFe_{2-y}Se_2$ gde je A = K, Rb, Cs, Ti) [6].

### 3.1.1  Kristalna strutura i fazni prelazi
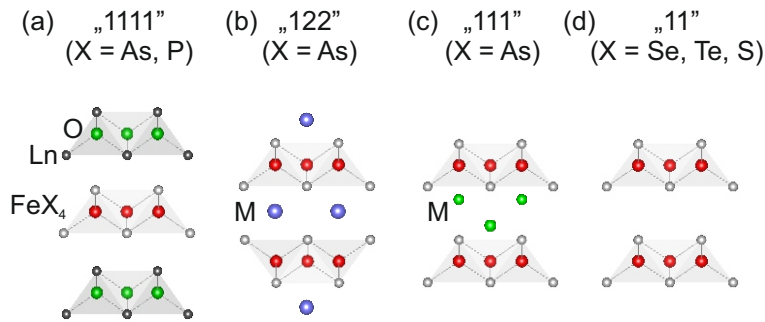


Slika 3.1: Kristalna struktura klase (a) „1111" (Ln = La, Pr, Ce, Nd, Sm, Gd, Sr, Ca), (b) „122" (M = Ba, Sr, Ca, Eu), (c) „111" (M = Li, Na) i (d) „11" superprovodnika na bazi gvožđa.

Generalno, svaku klasu superprovodnika na bazi gvožđa karakteriše tetragonalna kristalna struktura u normalnoj fazi. Kristalna rešetka sastoji se od FeX$_4$ (X = Pn, Ch) tetraedarskih ravni između odgovarajućih slojeva metala i/ili oksida zavisno od klase. Kristalna struktura prve četiri klase prikazana je na Slici 3.1. Klase „1111", „111", „11" i „21311" opisuju se istom prostornom grupom simetrije $P4/nmm$, dok klasama „122" i „122*" odgovaraju $I4/nmm$, odnosno $I4/m$ [6]. Kod velikog broja superprovodnika na bazi gvožđa obično na tempera-

turama višim od $T_c$ dolazi do narušenja simetrije koje, u nekim slučajevima, koegzisitira sa dugodometnim magnetnim uređenjem. Ispostavilo se i da dopiranje ovih materijala elektronima ili šupljinama ima velikog uticaja na porast kritične temperature $T_c$.

Kod nedopiranih članova klase „1111" najpre dolazi do narušenja tetragonalne simetrije u ortorombičnu. Na temperaturama nižim od temperature strukturnog faznog prelaza javlja se magnetno uređenje (spinske gustine talasa - SDW) ($T_S > T_{SDW}$). Izuzetak je GdFeAsO kod kog se ne javlja SDW stanje [6]. Dopiranjem elektronima najčešće dolazi do porasta kritične temperature, za šta je primer pomenut na početku ovog poglavlja LaFeAsO$_{0.88}$F$_{0.12}$ ($T_c = 26$ K).

Za razliku od „1111" klase, strukturni i magnetni fazni prelaz se javljaju na istim temperaturama u nedopiranim MFe$_2$As$_2$ (M = Ba, Sr, Ca, Eu) iz „122" klase. Dopiranjem na mestu metala ili pniktogena ovi prelazi se razdvajaju. Dopiranjem elektronima (Fe), šupljinama (M), ili izoelektronskim dopiranjem (As) dolazi do drastičnog porasta kritične temperature [6].

Prisustvo vakancija u Li$_{1-y}$FeAs („111" klasa) uzrokuje opadanje kritične temperature, kao i dopiranje elektronima polikristala LiFe$_{1-x}$(Co, Ni)$_x$As za oko 10 K za $x = 0.1$ [52]. Ovo je potvrđeno i eksperimentima na monokristalu LiFe$_{0.95}$C$_{0.05}$As sa izmerenom $T_c = 11$ K [6, 53].

Materijali „11" klase, proučavani su u okviru ove distertacije, pa će njihovim karakteristikama biti posebno posvećeno sledeće poglavlje.

Kod velikog broja superprovodnika na bazi gvožđa dolazi do pojave tzv. nematične faze [7, 8, 9, 10]. Ovo stanje karakteriše velika anizotropija u elektronskim osobinama dok je anizotropija rešetke skoro zanemarljiva [46]. Postavlja se pitanje kakvu i koliku ulogu pri narušenju kristalne simetrije imaju elektronski stepeni slobode. Kako do narušenja simetrije u elektronskoj strukturi može doći na temperaturama znatno višim u odnosu na temperauru regularnog strukturnog faznog prelaza [54, 55] ispostavlja se da strukturni fazni prelaz može biti posledica promena u elektronskoj strukturi [46]. S druge strane, ako je nematična faza posledica elektronske anizotropije još uvek nije u potpunosti jasno da li do nje dolazi posredstvom spinskih [55, 56] ili orbitalnih [57] stepeni slobode [46].

Kompleksni fazni dijagrami svake od klasa superprovodnika na bazi gvožđa, od strukturnog prelaza, preko magnetnog, nematičnog i superprovodnog stanja, njihove koegzistencije, i uticaj supstitucije atoma na svako od ovih svojstava u potpunosti opravdava njihovo višedecenijsko proučavanje. S druge strane, mehanizmi usled kojih se ove faze javljaju još uvek nisu u potpunosti jasni.

### 3.1.2    11 - halkogenidi

Na osnovu prethodnog poglavlja može se reći da su u superprovodnicima na bazi gvožđa, kristalna struktura, magnetno uređenje, nematična i superprovodna faza međusobno spregnute osobine. 11 - halkogenidi (FeCh) predstavljaju klasu superprovodnika na bazi gvožđa najjednostavnije kristalne strukture, čije predstavnike karakterišu neka od ovih svojstava. Članovi ove klase (FeSe, FeS i FeTe) kristališu u tetragonalnu kristalnu strukturu, opisanu prostornom

grupom simetrije $P4/nmm$. Kristalna struktura se sastoji od FeCh$_4$ tetraedara, transliranih duž glavne kristalografske ose (Slika 3.2). Interesantno je da su ovi materijali, pored toga što su izostrukturni i izoelektronski, veoma različiti po gore navedenim osobinama.
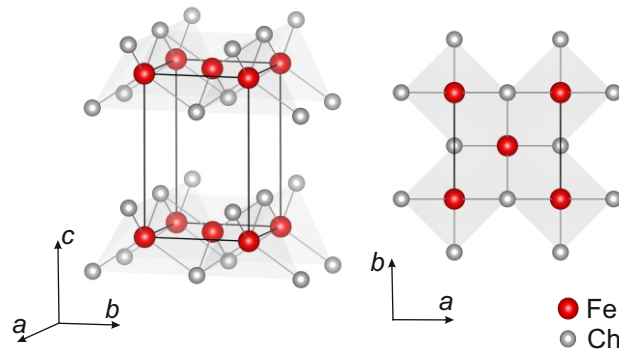


Slika 3.2: Kristalna struktura gvožđe halkogenida. Sivom linijom predstavljena je jedinična ćelija.

Prvi otkriveni superprovodnik iz ove klase je FeSe. U ovom materijalu na temperaturi od oko 90 K dolazi do narušenja simetrije iz tetragonalne u ortorombičnu pri čemu materijal ulazi u nematičnu fazu [11, 12, 13]. Još jedno otvoreno pitanje je i magnetno uređenje u prvom iz klase 11 - halkogenida. Skorija studija elektronskog Ramanovog rasejanja FeSe ukazuje na postojanje spinskih fluktuacija i frustriranog magnetnog uređenja [14]. Sniživanjem temperature ispod 9 K, FeSe ulazi u superprovodnu fazu [15]. Ono što je pokrenulo sve veće interesovanje za ovaj materijal jeste visokotemperaturska superprovodna faza FeSe monoslojeva. Naime, monosloj FeSe na SrTiO$_3$ supstratu dostiže kritičnu temperaturu od oko 77 K [58, 59].

S druge strane, dopiranjem ovog materijala atomima telura ($x = 0.5$), dolazi do porasta kritične temperature na 14 K pri atmosferskom pritisku [16]. Najviša kritična temperatura od 23 K izmerena je na uzorku sastava Fe$_{1.03}$Se$_{0.57}$Te$_{0.43}$ pri pritisku od 3.1 GPa [60].

Potpuna supstitucija atoma selena atomima telura rezultuje nesuperprovodnim FeTe [16, 61]. U ovom materijalu istovremeno na temperaturi od 67 K dolazi do strukturnog faznog prelaza (narušenja simetrije iz tetragonalne u monokliničnu) i antiferomagnetnog uređenja [16, 17, 18].

Fazni dijagram FeSe$_{1-x}$Te$_x$ ($0 \leq x \leq 1$) sistema prikazan je na Slici 3.3 (a). Ovaj fazni dijagram može se podeliti u nekoliko oblasti. Prvu u kojoj dominira dugodometno antiferomagnetno uređenje (AFM) praćeno narušenjem simetrije iz tetragonalne u monokliničnu (Mono). U drugoj oblasti se sa opadanjem koncentracije atoma telura gubi AFM uređenje i javlja se superprovodna faza. Superprovodna faza je prisutna do kraja serije, odnosno čistog FeSe. Paralelno sa superprovodnom fazom za $x \leq 0.5$ (treća oblast) dolazi do narušenje simetrije iz tetragonalne u ortorombičnu.

Poslednji u nizu materijala iz ove klase, FeS, za razliku od svojih prethodnika ne ispoljava strukturni fazni prelaz, čak ni na najnižim temperaturama [19]. U superprovodno stanje prelazi na temperaturama ispod 5 K [20]. Do sada nema konkretnih informacija o magnetnom uređenju
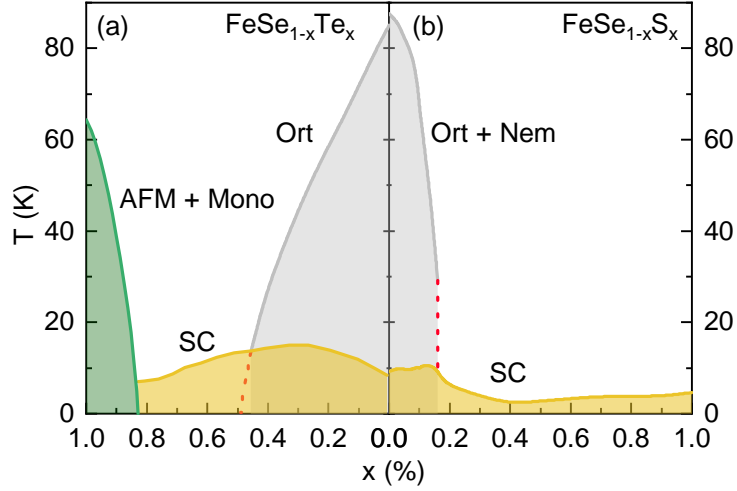
Slika 3.3: Fazni dijagram u funkciji koncentracije atoma (a) Te i (b) S u FeSe sistemu . Superprovodno, antiferomagnetno, i nematično stanje označeni su sa SC, AFM, odnosno Nem. Monoklinična, odnosno ortorombična faza označene su sa Mono i Orto. Podaci za $FeSe_{1-x}Te_x$ i $FeSe_{1-x}S_x$ preuzeti su iz Ref. [62], odnosno Ref. [22]

u ovom materijalu, mada određene studije ukazuju na kratkodometno magnetno uređenje koje potiče od magnetnih momenata atoma gvožđa [63].

Kako atom sumpora ima manji jonski radijus od atoma selena, njegovom supstitucijom u FeSe, dolazi do pozitivnog hemijskog pritiska i promena u FeSe elektronskoj strukturi kao i suzbijanja nematične faze. Naime, što je koncentracija atoma sumpora veća, to je temperatura na kojoj dolazi do nematičnog uređenja niža (Slika 3.3 (b)) [22]. Ova faza javlja se do koncentracije od oko $x \approx 0.2$, pa se iz tog razloga ova tačka naziva nematičnom kritičnom tačkom (NCP). Kritična temperatura FeSe uzorka od $9.3\,\mathrm{K}$ supstitucijom atoma sumpora raste i dostiže maksimum u sistemu $FeSe_{0.89}S_{0.11}$ ($T_c = 10.6\,\mathrm{K}$). Nakon ove koncentracije naglo opada i za $x = 0.4$ njena minimalna vrednost iznosi $2.1\,\mathrm{K}$. Daljim povećavanjem koncentracije atoma sumpora $T_c$ raste i za FeS sistem uzima vrednost $4.6\,\mathrm{K}$ (Slika 3.3). Takođe, zanimljivo je da se blag porast u kritičnoj temperaturi dešava istovremeno sa opadanjem temperature nematične faze, i da je maksimalna vrednost $T_c$ u blizini tačke skoka $T_S$ [22].

## 3.2 Kvazi-2D magnetni materijali

Poslednjih godina intenzivno se teorijski i eksperimentalno pručava klasa materijala koja, pored dugodomentnog magnetnog uređenja, ima za osobinu da su strukturne komponente u 2D ravni vezane jakim kovalentnim vezama, dok je interakcija između samih ravni slaba van der Valsova. Slaba interakcija omogućava jednostavnu eksfolijaciju ovih materijala na monoslojeve, koji zadržavaju magnetne karakteristike i time otvaraju mogućnost primene ove vrste materijala u dizajniranju uređaja nove generacije. Ova klasa materijala je veoma široka, i može se podeliti na nekoliko podklasa [64], poluprovodnike (Cr(Si, Ge)Te$_3$, MSe$_2$ (M = V, Mn), CrX$_3$ (X = Cl, Br, I)) [24, 25, 26, 27, 28] i metale (Fe$_3$GeTe$_2$)[23] feromagnetnog uređenja i antiferomag-

netne izolatore $(MP(S, Se)_3$, M = prelazi metal) [65]. U okviru ove disertacije proučavani su poluprovodnici Cr(Si:Ge)Te$_3$ i metal Fe$_{3-x}$GeTe$_2$.

### 3.2.1   Feromagnetni poluprovodnici Cr(Si:Ge)Te$_3$

Triteluridi CrSiTe$_3$ i CrGeTe$_3$ su poluprovodni materijali sa feromagnetnim uređenjem. Na osnovu apsorpcionog spektra CrSiTe$_3$ dobijen je energetski procep od 0.4 eV [29]. U istoj studiji, temperaturska zavisnost odnosa magnetne susceptibilnosti ($\chi = M(T)/H$, $H = 1$ kOe), u $ab$ ravni i duž $c$-ose ukazuje da do feromagnetnog prelaza dolazi na temperaturi $T_{Curie} = 33$ K i uređenja magnetnih momenata duž $c$-ose. S druge strane, odnos $H/M(T)$ na temperaturama nižim od 150 K odstupa od linearnog modela, što ukazuje na postojanje kratkodometnih magnetnih korelacija, drastično iznad temperature magnetnog prelaza (Slika 3.4).
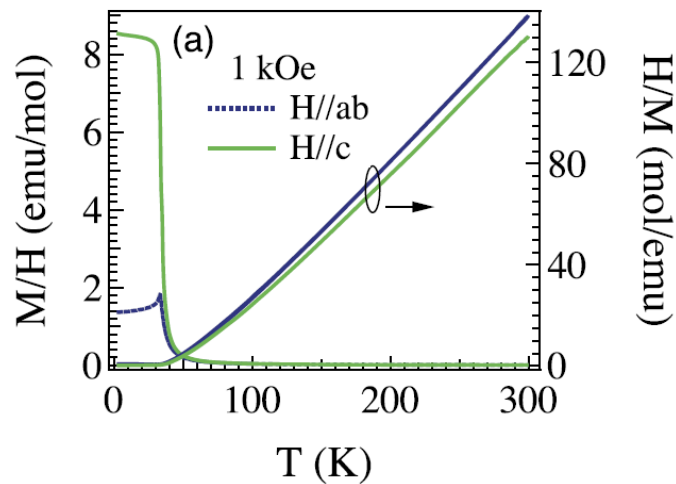


Slika 3.4: Temperaturska zavisnost magnetizacije CrSiTe$_3$ u polju jačine 1 kOe i $H/M(T)$. Preuzeto iz [29].

S druge strane, na osnovu transmisionog spektra CrGeTe$_3$ na sobnoj temperaturi određen je procep između provodne i valentne zone od 0.7 eV [30]. Slično, CrSiTe$_3$, na osnovu magnetnih merenja određena je temperatura magnetnog prelaza $T_{Curie} = 61$ K i uređenje magnetnih momenata duž $c$-ose [30].

Prisustvo spinskih talasa u CrSiTe$_3$, do temperature čak deset puta iznad $T_{Curie}$ u $ab$ ravni i odsustvo trodimenzionih magnetnih korelacija iznad $T_{Curie}$ proučavano je metodom (ne)elastičnog rasejanja na neutronima [24]. Metodom eksfolijacije izolovani su mono i polislojevi CrSiTe$_3$ na Si/SiO$_2$ supstratu. Zavisno od broja slojeva, dolazi do promene otpornosti u opsegu temperatura od 80 K do 120 K, konzistentno teorijskim predikcijama o značajnom porastu Kirijeve temperature sa opadanjem dimenzionalnosti [66].

Ugaono razloženom fotoemisionom spektroskopijom visoke rezolucije (ARPES) određena je elektronska struktura CrSiTe$_3$ u blizini Fermi nivoa. Zbog spin-orbit interakcije, ovaj materijal klasifikovan je kao Motov feromagnetni izolator [67]. Istom metodom analizirana je i elektronska struktura CrGeTe$_3$, u kojoj su niske valentne zone centrirane oko $\Gamma$ tačke [68].

### 3.2.2 Metalični feromagnet Fe$_{3-x}$GeTe$_2$

Za razliku od poluprovodnih CrXTe$_3$ (X = I, Ge, Sn) i CrX$_3$ (X = Cl, Br, I) sa relativno niskim temperaturama magnetnog prelaza, čak i u slučaju monoslojeva [66], Fe$_{3-x}$GeTe$_2$ u feromagnetno stanje prelazi na višim temperaturama. Kirijeva temperatura Fe$_{3-x}$GeTe$_2$, $T_{Curie}$, može dostizati 220 - 230 K čak i u formi zapreminskog kristala [31, 32].

Zavisno od metode rasta kristala u ovom materijalu se javljaju vakancije na poziciji Fe2 atoma. Pokazano je da fizičke osobine kao što su parametri rešetke, Kirijeva temperatura i magnetizacija zavise od koncentracije vakancija u uzorku [33]. Naime, uzorci u kojima je prisutna veća koncentracija vakancija imaju veći parametar rešetke $c$ i manji parametar $a$ u odnosu na uzorke sa manjom koncentracijom vakancija.
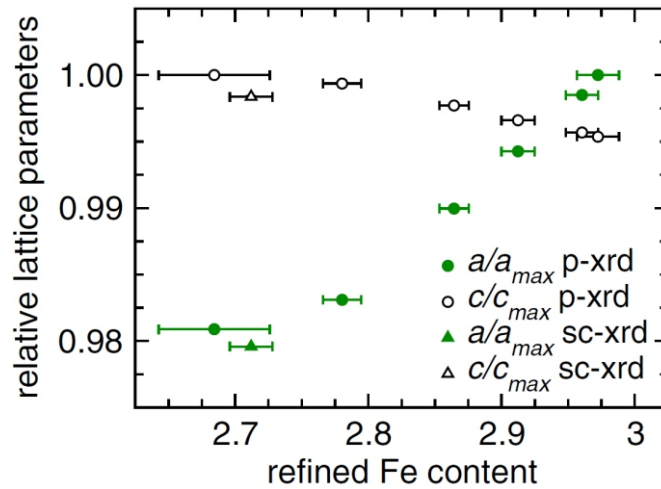


Slika 3.5: Normirani parametri rešetke u funkciji koncetracije Fe atoma u Fe$_{3-x}$GeTe$_2$ po-likristalnim uzoracima (p-xrd) na sobnoj temperaturi. Prikazana se i vrednosti dobijene za monokristalni uzorak (sc-xrd) na 173 K; $a_{\max} = 4.0244(1)$Å i $c_{\max} = 16.405(1)$Å. Preuzeto iz [33].

Na Slici 3.5 prikazane su vrednosti normiranih parametara rešetke u zavisnosti od kon-centracije atoma gvožđa u uzorcima sintetisanim metodom rasta iz fluksa. Parametri rešetke monokristala (sc-xrd) takođe su prikazani na ovom grafiku i potvrđuju širenje rešetke duž $a$ pravca i skupljanje duž $c$, sa porastom koncentracije Fe atoma. Takođe je primećeno da je širenje rešetke u $ab$ ravni znatno veće u odnosu na promene duž $c$ pravca [33]. Nehomogena promena u vrednostima parametara rešetke fizički znači da se usled širenja rešetke u $ab$ ravni popunjavanjem vakancija atomima na Fe2 poziciji, rastojanje između ravni atoma telura i Fe$_3$Ge ravni smanjuje. Kada se atomi telura pomere ka Fe$_3$Ge ravni, dolazi do skupljanja rešetke duž $c$ pravca, kako bi se održala van der Valsova struktura [33].

Temperaturska zavisnost magnetne susceptibilnosti ispitivana je pri različitim koncentraci-jama vakancija u Fe$_{3-x}$GeTe$_2$ polikristalima ($0.03 \leq x \leq 0.31$) i u monokristalu Fe$_{0.76}$GeTe$_2$ [33]. Primećeno je da povećavanje koncentracije vakancija utiče na opadanje $T_{Curie}$ (Slika 3.6).

Naime, nedostatak atoma na pojedinim Fe2 pozicijama, odnosno neuređenost sistema, remeti magnetne korelacije i dovodi do opadanja temperature magnetnog faznog prelaza. Prisustvo vakancija utiče na strukturne parametre i širenje rešetke duž $c$ pravca. To znači da se među-atomsko rastojanje Fe1 - Fe1 povećava i Fe1 - Fe2 smanjuje. Kako su feromagnetne interakcije uspostavljene između atoma gvožđa strukturne promene utiču na magnetne karakteristike sistema [33].
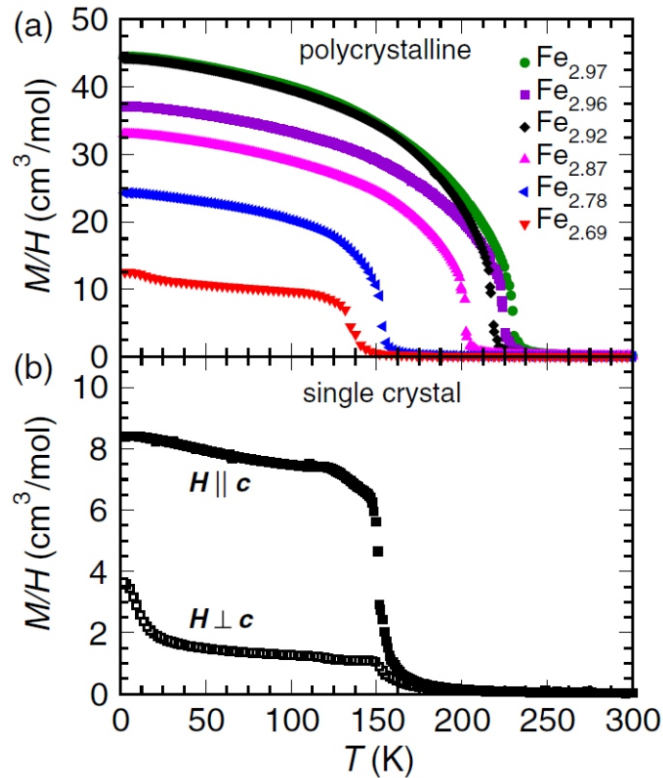


Slika 3.6: Temperaturska zavisnost magnetne susceptibilnosti $\chi = M/H$ ($H = 100\,\mathrm{Oe}$) polikristala $Fe_{3-x}GeTe_2$ u zavisnosti od koncetracije vakancija i monokristala ($x = 0.24$). Preuzeto iz [33].

Uzorci stehiometrijskog sastava uglavnom su sintetisani CVT metodom i imaju visoku temperaturu feromagnetnog prelaza [31, 32]. Pored ovog tipa magnetnog prelaza na $T_{Curie} = 214\,\mathrm{K}$ u dvodimenzionim slojevima ispod $152\,\mathrm{K}$ uočeno je prisustvo antiferomagnetnog uređenja [69]. Imaginarni deo ac susceptibilnosti $Fe_3GeTe_2$ prikazan je na Slici 3.7. Prema ovim rezultatima prisutna je konkurentnost 3D - feromagnetne i 2D - antiferomagnetne faze u temperaturskom opsegu od 152 do $214\,\mathrm{K}$ [69].

Prema jednom od istraživanja, u blizini temperature feromagnetnog faznog prelaza u $Fe_3GeTe_2$ ($230\,\mathrm{K}$) postoji indikacija formiranja Kondo rešetke. Naime na $T_K = 190\,\mathrm{K} \pm 20\,\mathrm{K}$, koja je u saglasnosti sa teorijskom predikcijom od $222\,\mathrm{K}$, dolazi do interakcije provodnih elektrona i periodično lokalizovanih spinova [70]. Teorijski proračuni predviđaju dinamičku stabilnost $Fe_{3-x}GeTe_2$ slojeva i magnetnu anizotropiju koja potiče od jake spin-orbit interakcije [71]. Na osnovu anomalnog Holovog efekta $Fe_{3-x}GeTe_2$ nanoljuspica ustanovljena je jaka ortogonalna
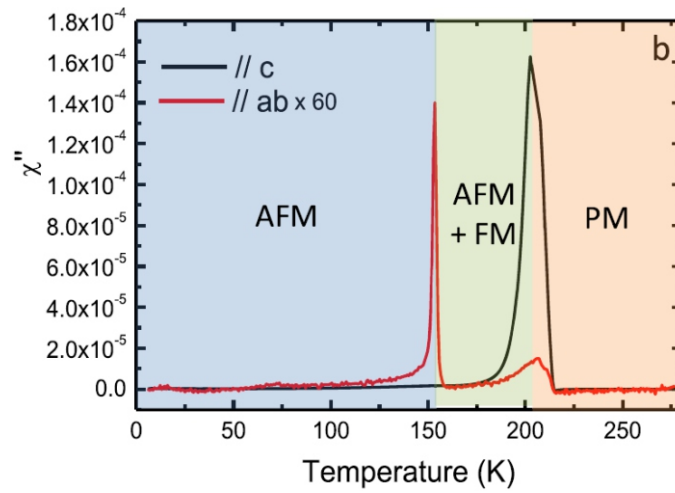
Slika 3.7: Imaginarni deo ac susceptibilnosti $Fe_{3-x}GeTe_2$. Kriva $H//ab$ uvećana je 60 puta. Preuzeto iz [69].

magnetna anizotropija, uz $T_{Curie}$ od oko 200 K [72].

# Glava 4 Ramanova spektroskopija superprovodnika na bazi gvožđa

Ramanova spektroskopija pokazala se kao veoma korisna, neinvanzivna i neizostavna eksperimentalna metoda za ispitivanje ekscitacija i njihovih interakcija u materijalima sa jakim elektronskim korelacijama. Ovom tehnikom su uspešno proučavane sve do sada poznate klase superprovodnika na bazi gvožđa [73, 74, 75, 76, 77]. Primarna uloga Ramanove spektroskopije bila je pročavanje fononskih ekscitacija. Usavršavanjem metoda za sintezu kvalitet kristala značajno je poboljšan, te se za ispitivanje superprovodnika na bazi gvožđa godinama intenzivno koristi elektronsko Ramanovo rasejanje [3]. Ovom metodom uspešno su ispitivane dvomagnonske ekscitacije, spinske i nematične fluktuacije, SDW stanje, superprovodni procep [3].

U ovom poglavlju prikazani su rezultati Ramanove spektroskopije FeS i $\text{FeSe}_{1-x}\text{S}_x$ ($0 \leq x \leq 1$). Najpre je detaljno analizirana dinamika rešetke čistog FeS. Nakon toga ispitivan je uticaj defekata na vibracioni spektar dopiranih uzoraka.

## 4.1 Ekseprimentalni detalji i teorija

U zavisnosti od koncentracije atoma sumpora uzorci monokristala $\text{FeSe}_{1-x}\text{S}_x$ ispitivani u ovom istraživanju sintetisani su CVT metodom za vrednosti $0 \leq x \leq 0.24$, odnosno hidrotermalno za vrednosti $0.4 \leq x \leq 1$ [22, 78]. Za eksperiment neelastičnog rasejanja svetlosti korišćene su eksperimentalne postavke opisane u Poglavlju 2.3. Konkretno, vibracioni spektri tetragonalnog FeS mereni su upotrebom eksperimentalne postavke za Ramanovo rasejanje Valter Majsner instituta u Minhenu (Poglavlje 2.3, Slika 2.6). Fononske ekscitacije FeS i $\text{FeSe}_{1-x}\text{S}_x$ ($0 \leq x \leq 1$) ispitivane su primenom eksperimentalne postavke u Centru za fiziku čvrstog stanja i nove materijale, Instituta za fiziku u Beogradu (Poglavlje 2.3, Slika 2.7).

Za uzorke koji sadrže atom halkogena karakterištično je vezivanje kiseonika iz vazduha. Da bi neelastično rasejana svetlost sa sigurnošću poticala od sistema koji se analizira potrebno je obezbediti čistu površinu na koju će laserski snop biti usmeren. Eliminisanje nečistoća postiže se cepanjem kristala neposredno pre stavljanja u vakuum ($\sim 10^{-6}$ mbar).

Za potrebe magnetnih merenja korišćen je Quantum Design MPMS XL-7 SQUID magnetometar. Temperatura na FeS uzorku snižavana je do 2 K sa korakom 0.1 K/min. Snižavanjem temperature, bez prisustva spoljašnjeg polja (Slika 4.1, ZFC), superprovodno stanje analiziranog uzorka javlja se na $T_c = 4.5$ K. Primećeno je da u prisustvu spoljašnjeg polja (FC) prilikom
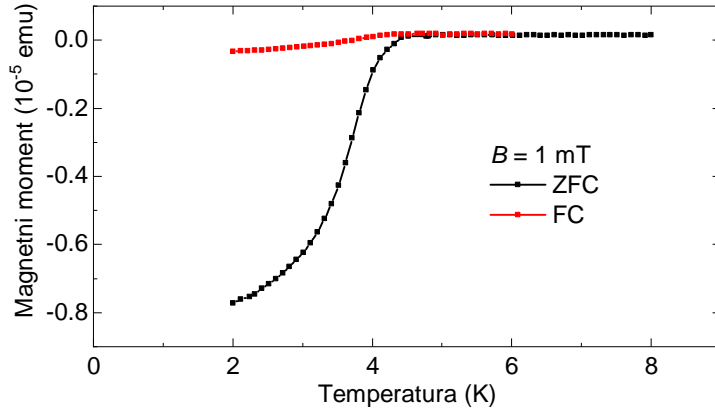
Slika 4.1: Temperaturska zavisnost magnetnog momenta FeS sistema u spoljašnjem polju $B = 1\,mT$.

sniživanje temperature magnetizacija u superprovodnom stanju sporije opada.

Elektronska struktura i fononske disperzije tetragonalnog FeS određene su korišćenjem teorije gustine funkcionala (DFT), odnosno perturbacione teorije gustine funkcionala (DFPT) [79] u okviru QUANTUM ESPRESSO paketa [80].

Prilikom izračunavanja elektronske strukture i fononskih disperzija korišćeni su eksperimentalni parametri elementarne ćelije, $a = 3.6735$ Å, $c = 5.0328$ Å, i $z = 0.2602$, gde je $z$ visina na kojoj se nalaze atomi sumpora u odnosu na Fe ravan [81]. U proračunima su primenjeni Vanderbilt ultra-mekani pseudopotencijali sa Becke-Lee-Yang-Parr (BLYP) izmensko-korelacionim funkcionalom i $s$ i $p$ stanjima uključenim u valencu gvožđa. Elektronska talasna funkcija i gustina energije ograničene su na 70, odnosno $500\,Ry$, sa ciljem stabilne konvergencije fononskih modova. Briluenova zona uzorkovana je pomoću $16 \times 16 \times 16$ Monkhorst-Pack mreže u impulsnom prostoru sa Gausovim širenjem od $0.01\,Ry$. Dobijeni rezultati elektronske i fononske strukture konzistentni su sa prethodno objavljenim [82, 83].

Fononske disperzije i gustina stanja računate su na $6 \times 6 \times 6$ Monkhorst-Pack mreži, uz interpolaciju disperzija duž određenog pravca. Rezultujuće fononske disperzije dobijene pomoću optimizovanih i eksperimentalnih parametara se kvalitativno poklapaju, sličnog su oblika i sadrže procep.

Selekciona pravila za dvofononske procese određena su metodom modifikovanih grupnih projektora (MGPT) [84] koji je opisan u Dodatku A.1.

## 4.2 Dinamika rešetke FeS

FeS kristališe u tetragonalnu kristalnu strukturu opisanu prostornom grupom simetrije $P4/nmm$ ($D_{4h}^7$). Poziciona simetrija atoma, ireducibilne reprezentacije i odgovarajući Ramanovi tenzori prikazani su u Tabeli 4.1. Na osnovu simetrijske analize u Ramanovim spektrima mogu se očekivati četiri moda; $A_{1g}$, $B_{1g}$ i dva $E_g$ moda. Na osnovu oblika Ramanovog tenzora moguće je jednoznačno odrediti u kojim geometrijama rasejanja će određeni mod biti

Tabela 4.1: Za prostornu grupu simetrije FeS, $P4/nmm$ ($D_{4h}^7$), date su pozicione simetrije atoma, ireducibilne reprezentacije Raman aktivnih modova i odgovarajući Ramanov tenzor.

| FeS | Prostorna grupa $P4/nmm$ ($D_{4h}^7$) |
|---|---|
| Fe (2a) | $B_{1g} + E_g$ |
| S (2c) | $A_{1g} + E_g$ |

| Ramanovi tenzori |
|---|

$$A_{1g} = \begin{pmatrix} A & 0 & 0 \\ 0 & A & 0 \\ 0 & 0 & B \end{pmatrix} \quad B_{1g} = \begin{pmatrix} C & 0 & 0 \\ 0 & -C & 0 \\ 0 & 0 & 0 \end{pmatrix} \quad {}^1E_g = \begin{pmatrix} 0 & 0 & 0 \\ 0 & 0 & E \\ 0 & E & 0 \end{pmatrix} \quad {}^2E_g = \begin{pmatrix} 0 & 0 & -E \\ 0 & 0 & 0 \\ -E & 0 & 0 \end{pmatrix}$$

opservabilan.

U zavisnosti od orijentacije uzorka i odnosa vektora polarizacije upadne i rasejane svetlosti moguće je uočiti ekscitacije koje se javljaju u svim kanalima rasejanja $D_{4h}$ prostorne grupe, $A_{1g}$, $A_{2g}$, $B_{1g}$ i $B_{2g}$. Ako su fotoni polarizovani duž $b$ - ose usmereni na uzorak pod dovoljno velikim uglom, projekcija na $c$ - osu će biti konačna. Ovo znači da je u ovakvoj polarizacionoj konfiguraciji moguće detektovati ekscitacije $E_g$ simetrije.

Četiri glavne geometrije rasejanja u kojima su izvršena merenja FeS monokristala prikazane su na umetku Slike 4.2. Sa $a$, $b$ ($|a| = |b|$) i $c$ označene glavne kristalografske ose tetragonalnog FeS, pri čemu je $c$ - osa paralelna optičkoj osi. Rotacijom uzorka oko $c$ - ose za ugao od 45°, ose $a$ i $b$ preslikavaju se u $a'$ i $b'$. Ugao pod kojim je upadni snop svetlosti usmeravan na $bc$ ravan u ovom eksperimentu je 66° (Poglavlje 2.4, Slika 2.9 (a)). Na osnovu oblika Ramanovog tenzora utvrđeno je da se $A_{1g}$ mod se može uočiti samo u paralelnim polarizacionim konfiguracijama dok $B_{1g}$ mod nije opservabilan u $ba$ konfiguraciji. Kao što je već rečeno, da bi se uočili modovi $E_g$ simetrije potrebna je konačna projekcija fotona polarizovanih duž $b$ - ose na $c$ - osu.
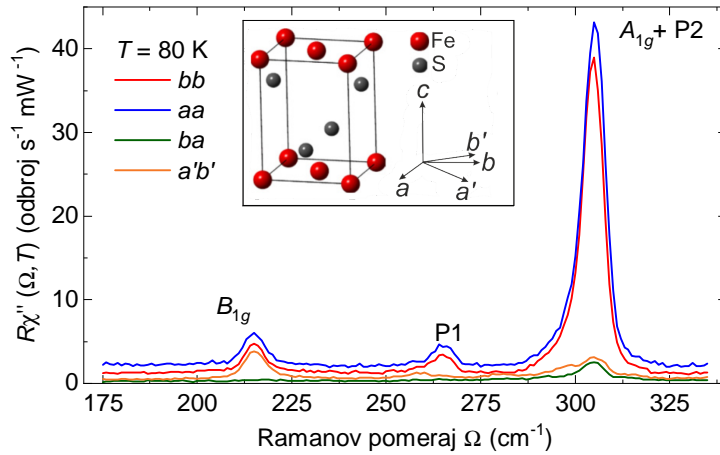


Slika 4.2: Ramanov spektar FeS na $T = 80\,\mathrm{K}$ u četiri polarizacione konfiguracije. Umetak: FeS kristalna struktura i pravci polarizacije u odnosu na orijentaciju kristala.

Na Slici 4.2 prikazani su Ramanovi spektri na 80 K mereni u četiri glavne linearne polariza-

Tabela 4.2: Raman aktivni modovi u tetragonalnom FeS. Prikazane su simetrije, izračunate vrednosti energije na $T = 0\,\mathrm{K}$, i atomi koji doprinose svakoj od vibracija. Eksperimentalne vrednosti energija u trećoj koloni dobijene su ekstrapolacijom do $T = 0\,\mathrm{K}$ na osnovu eksperimentalnih vrednosti između $20\,\mathrm{K}$ i $50\,\mathrm{K}$.

| Simetrija | Energija fonona $(\mathrm{cm}^{-1})$ | | Tip atoma |
|---|---|---|---|
| | Teorija | Eksperiment | |
| $A_{1g}$ | 316.1 | 305.3 | S |
| $B_{1g}$ | 220.4 | 215.8 | Fe |
| $E_g$ | 231.6 | | Fe, S |
| $E_g$ | 324.8 | | Fe, S |

cione konfiguracije. Uočena su tri pika na energijama 215, 265 i 305 $\mathrm{cm}^{-1}$. Pik uočen na najnižoj energiji (215 $\mathrm{cm}^{-1}$) prisutan je u spektrima $aa$, $bb$ i $a'b'$ ali iščezava u spektrima $ab$ polarizacione konfiguracije. Na osnovu simetrijske analize i selekcionih pravila zaključeno je da je njegova simetrija $B_{1g}$. Ovaj mod opisuje vibracije atoma gvožđa duž $c$ - ose. Mod najvećeg intenziteta javlja se na energiji od oko 305 $\mathrm{cm}^{-1}$. Iako na ovoj energiji postoje doprinosi u $ba$ i $a'b'$ konfiguracijama rasejanja, njegov dominantan doprinos prisutan je u $A_{1g}$ kanalu rasejanja. Doprinos ovog moda u $ba$ i $a'b'$ konfiguracijama može biti posledica curenja ili defektom-indukovanog rasejanja. Dodatno, $A_{1g}$ mod pokazuje asimetriju ramanske linije ka nižim energijama. Asimetrija ramanske linije obično se javlja kao posledica interakcije fonona i elektronskih stepeni slobode. U tom slučaju pik se modeluje Fano oblikom spektralne linije (Poglavlje 2.2). Na Slici 4.3 prikazan je rezultat modelovanja ovog pika konvolucijom linija Gausovog i Fano profila. Zbog odstupanja od eksperimentalnih tačaka upravo na asimetričnoj strani, pik je modelovan dvema simetričnim spektralnim linijama. Ovaj metod dao je mnogo bolje slaganje sa eksperimentalnim rezultatima. Zaključeno je da je na prvi pogled pik najvećeg intenziteta u stvari sastavljen od dva moda; jednog $A_{1g}$ simetrije koji odgovara vibracijama atoma sumpora duž $c$ ose i drugog označenog sa P2. Dodatni pik P2 javlja se u spektrima paralelne polarizacije, nestaje u $ab$, ali njegov doprinos postoji u $a'b'$ konfiguraciji. Ovo sugeriše da je P2 pik niže simetrije koji se javlja u $A_{1g}$ i $B_{1g}$ kanalima rasejanja. Pik označen sa P1 na energiji od 265 $\mathrm{cm}^{-1}$ uočen je isključivo u spektrima paralelne polarizacione konfiguracije, na osnovu čega je zaključeno da je ova ekscitacija $A_{1g}$ simetrije.

Imajući u vidu da se u eksperimentalnim rezultatima pored simetrijom predviđenih modova nalaze dva dodatna pika, s ciljem verifikacije eksperimentalnih rezultata, izvršeni su DFT proračuni tetragonalnog FeS. Dobijene vrednosti energija sumirane su zajedno sa eksperimentalnim u Tabeli 4.2. Poređenjem ovih vrednosti dobija se odstupanje manje od 4%, odnosno modovi $A_{1g}$ i $B_{1g}$ su korektno označeni.
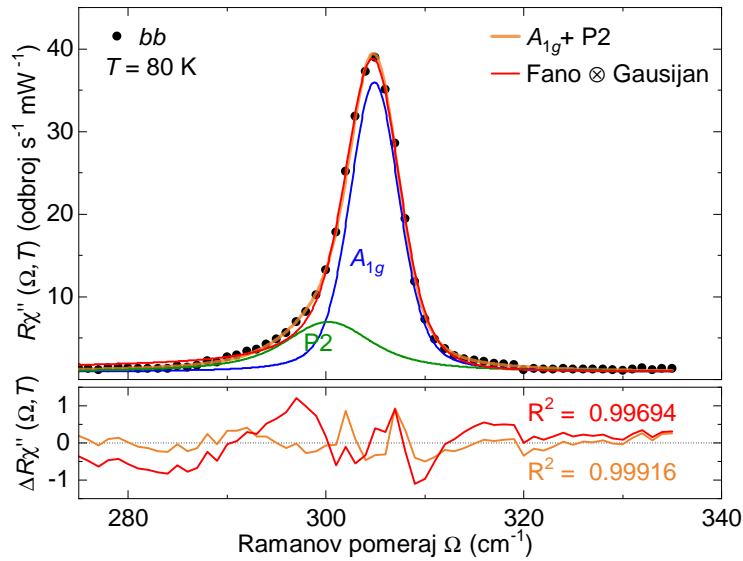
Slika 4.3: Dekompozicija asimetričnog pika na energiji $305\,\mathrm{cm}^{-1}$. Crnom bojom označeni su eksperimentalni rezultati , narandžastom suma dve linije Voitovog profila (zelena i plava linija). Crvenom linijom označena je konvolucija Gausijana i Fano profila. Ova linija odstupa od ekseprimentalnih vrednosti na asimetričnoj strani pika.

## 4.2.1 Temperaturska zavisnost

Nakon adekvatne simetrijske analize i označavanja modova kvantitativno su analizirane detektovane ekscitacije. S obzirom na to da je oblik ramanske linije svih modova simetričan i $\Gamma_L \ll \omega(T)$, gde je $\Gamma_L$ Lorencova poluširina i $\omega(T)$ energija moda, odgovara im Lorencov profil spektralne linije. Međutim, u obzir treba uzeti i instrumentalno širenje koje se opisuje Gausovim profilom (Poglavlje 2.2). Za poluširinu Gausijana ($\Gamma_G$) i spektralnu rezoluciju ($\sigma$) važi $\Gamma_G \equiv \sigma$. S tim u vezi, da bi se izvršila analiza uočenih modova potrebno je koristiti Voitov profil linije odnosno, konvoluciju Gausijana i Lorencovog profila.
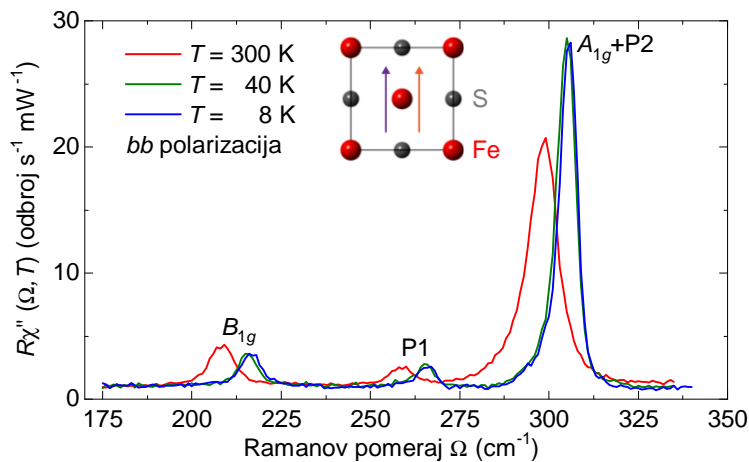


Slika 4.4: Ramanov spektar FeS u $bb$ polariacionoj konfiguraciji koja projektuje $A_{1g}$, $B_{1g}$ i $E_g$ simetriju. Prikazani spektri mereni su na temperaturama 8, 40 i $300\,\mathrm{K}$. Umetak: polarizacija svetlosti u odnosu na orijentaciju kristala.

31

Tabela 4.3: Simetrija, Grunajzenov parametar $\gamma$, i parametar fonon-fonon interakcije $\lambda_{\mathrm{ph-ph}}$ sva četiri moda.

| Mod | Simetrija | $\gamma$ | $\lambda_{\mathrm{ph-ph}}$ |
|-----|-----------|----------|-----------------------------|
| S | $A_{1g}$ | 2.2 | 1.68 |
| Fe | $B_{1g}$ | 3.4 | 0.31 |
| P1 | $A_{1g}$ | 2.4 | 0.25 |
| P2 | $A_{1g} + B_{1g}$ | 2.2 | 0.31 |

Temperaturska merenja izvršena su u opsegu temperatura između 300 i 4 K. Na Slici 4.4 prikazani su Ramanovi spektri u *bb* polarizacionoj konfiguraciji na temperaturama 300, 40 i 8 K. Jasno se može se uočiti da pri sniženju temperature energije svih modova monotono rastu a poluširine opadaju. Na Slici 4.6 prikazana je temperaturska zavisnost energija i poluširina u merenom temperaturskom opsegu. Na temperaturama ispod 20 K prisutan je blagi skok u energiji svih modova. Dodatno, skokovite promene u fononskim energijama prisutne su i na oko 50 K. Zanemarujući tačke u kojima se javljaju devijacije u energijama i poluširinama analizirano je ponašanje ovih fononskih osobina u terminima zapreminskog i anharmonijskog doprinosa (Poglavlje 2.1.3) u temperaturskom opsegu $20 \leq T < 50$ K. Temperaturska zavisnost Lorencove poluširine, $\Gamma_L$, data je izrazom (2.28). Na osnovu ovog izraza dobijene su vrednosti parametra fonon-fonon interakcije, $\lambda_{ph-ph}$, koji u njemu figuriše. Za svaki mod vrednosti $\lambda_{ph-ph}$ su prikazane u poslednjoj koloni Tabele 4.3. Interesantno je da je vrednost ovog parametra $A_{1g}$ moda skoro šest puta veća u odnosu na ostale analizirane modove. Uz modifikaciju zapreminskog dela (2.27a) u jednačini (2.26) izraz za energiju datog moda može se zapisati kao

$$\omega(T) = \omega_0 \left[ 1 - \gamma \frac{V(T) - V_0}{V_0} - \left( \frac{\Gamma_{L,0}}{\sqrt{2}\omega_0} \right)^2 \left( 1 + \frac{4\lambda_{ph_ph}}{\exp(\frac{\hbar\omega_0}{k_B T}) - 1} \right) \right], \tag{4.1}$$

gde su $V(T)$ i $V_0$ zapremina elementarne ćelije na temperaturi $T$ i $T \to 0$. Na Slici 4.5 prikazane su vrednosti parametara rešetke i zapremine elementarne ćelije tetragonalnog FeS u zavisnosti od temperature koje su korišćene u ovoj analizi [19]. Koristeći izvedene vrednosti parametra fonon-fonon interakcije iz izraza (2.28), jedini preostali slobodni parametar u izrazu (4.1) je Grunajzenov parametar, $\gamma$. Vrednosti ovog parametra prikazane su u pretposlednjoj koloni Tabele 4.3. Iz ovih rezultata se može videti da parametar $\gamma$ za $A_{1g}$, P1 i P2 uzima svoju standardnu vrednost $\sim 2$, za razliku od njegove vrednosti za $B_{1g}$ mod ($\gamma(B_{1g}) = 3.4$). Krive temperaturske zavisnosti energija $\omega$ i poluširina $\Gamma_L$, prikazane su na Slici 4.6 punom i isprekidanom crvenom linijom.

Vratimo se sada devijacijama u fononskim energijama na temperaturama ispod 20 K i oko 50 K. Na temperaturi $T \approx 50$ K energije svih modova odstupaju od inače monotone temperaturske zavisnosti. Ovo ponašanje je izraženije kod $A_{1g}$ moda i P2, u odnosu na $B_{1g}$ mod i P1. Za razliku od energija, nije uočeno nemonotnono ponašanje fononskih poluširina. Na ovoj
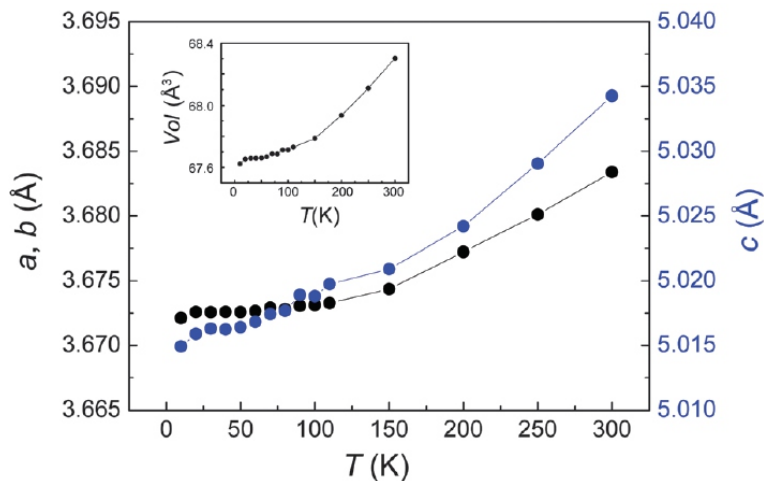
Slika 4.5: Temperaturska zavisnost parametara rešetke i zapremine elementarne ćelije (umetak) FeS [19].

temperaturi ne dolazi do skokovitih promena parametara rešetke (Slika 4.5) [19], kao ni do faznih prelaza, pa uzrok ovakvog ponašanja za sada ostaje nerazjašnjen.

Pri sniжavanju temperature između 20 i 4 K javlja se skokovita promena u energiji sva četiri moda (Slika 4.6). Dok promene u poluširini nisu najuočljivije kod modova P1 i P2, poluširina $A_{1g}$ moda opada, dok poluširina $B_{1g}$ moda raste. Skokovite promene u fononskim energijama i poluširinama tipično su indikator faznih prelaza. Međutim, na ovim temperaturama za sada nije potvrđeno prisustvo faznog prelaza. S druge strane, devijacije ispod 20 K mogu se dovesti u vezu sa rezultatima dve $\mu$SR studije [63, 85] u kojima je uočeno kratkodometno magnetno uređenje. Dodatno, zapremina elementarne ćelije smanjuje se nešto značajnije između 20 i 10 K u odnosu na zapreminu na višim temperaturama (Slika 4.5 [19]). Redukovanje zapremine elementarne ćelije moglo bi uticati na skokovite promene fononskih energija.

Kada je u pitanju dugodometno magnetno uređenje u FeS, rezultati neutronske difrakcije ukazuju da se ono javlja na temperaturi $T_N = 116$ K [86]. Imajući ovo na umu, ispitivana je detaljna temperaturska zavisnost $A_{1g}$ i $B_{1g}$ modova između 100 i 300 K sa korakom 10 K. U Ramanovim spektrima nije uočeno nikakvo odstupanje od monotonog trenda fononskih energija i poluširina na temperaturama oko 120 K (Slika 4.7). U XRD rezultatima [19] je na oko 100 K (Slika 4.5) primećena mala skokovita promena u $c$ parametru rešetke koja bi se mogla dovesti u vezu sa rezultatima neutronske difrakcije, ali koja nema značajnog uticaja na fononske ekscitacije.

## 4.2.2 Analiza modova P1 i P2

Neočekivani eksperimentalni rezultati u kojima su jasno uočeni dodatni pikovi zahtevali su detaljniju analizu. Trebalo je utvrditi da li možda P1 i P2 odgovaraju očekivanim $E_g$ modovima; da li su ove ekscitacije fononskog porekla; i koji je njihov uzrok.

Ekscitacije označene sa P1 i P2 uočene su u spektrima $aa$ polarizacije u kojima električno
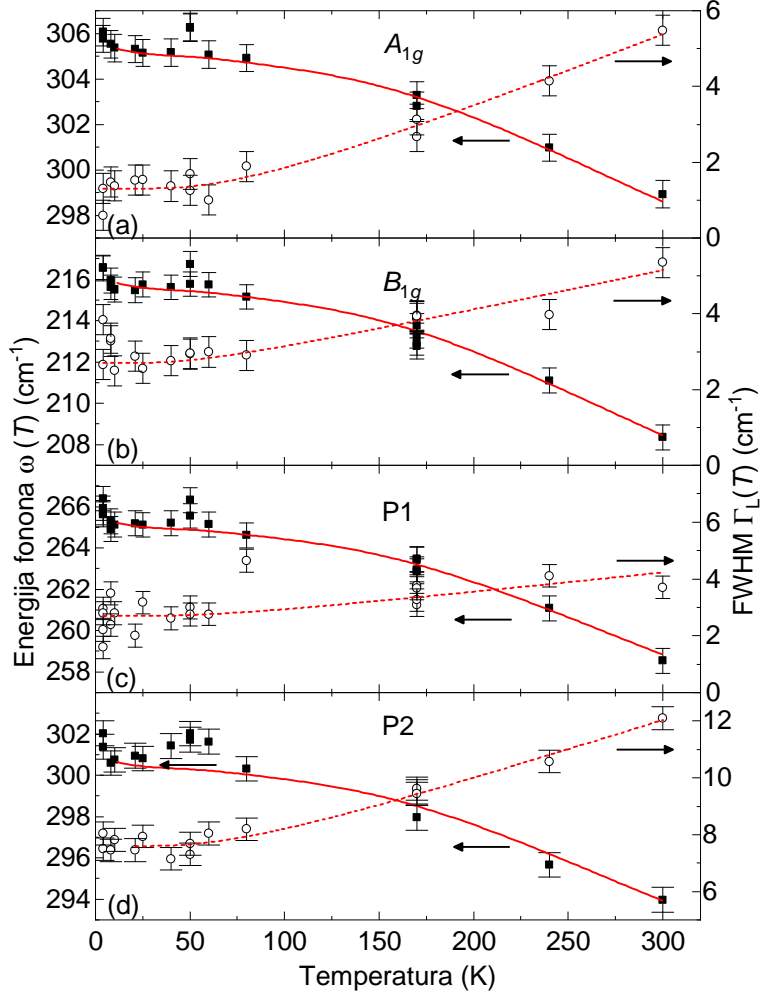
Slika 4.6: Temperaturska zavisnost energija i poluširina sva četiri moda. Kvadratima su označene energije $\omega$, krugovima poluširine $\Gamma_L$. Crvenom isprekidanom i punom linijom označena je temperaturska zavisnost poluširina i energija na osnovu (2.28) i (4.1).

polje nema projekciju na $c$-osu. Kako se modovi $E_g$ simetrije mogu javiti samo u $ca$ i $cb$ polarizacionim konfiguracijama (Tabela 4.1), zaključeno je da P1 i P2 ne odgovaraju $E_g$ modovima. Dodatno, teorijske vrednosti energija $E_g$ modova (Tabela 4.2) značajno odstupaju od eksperimentalnih vrednosti energija pikova P1 i P2, što se ne može reći za $A_{1g}$ i $B_{1g}$ mod. Ovime je eliminisana moguća veza između P1 i P2, i fonona $E_g$ simetrije.

Prilikom analize temperaturske zavisnosti energije i poluširine P1 i P2 dobijene su njima odgovarajuće vrednosti Grunajzenovog parametra i parametra fonon-fonon interakcije. Grunajzenov parametar uzima svoju standardnu vrednost $\gamma \sim 2$ [87]; parametar fonon-fonon interakcije $\lambda_{ph-ph} \sim 0.3$ - uporedivu sa vrednošću ovog parametra za $B_{1g}$ mod. Dodatno, $(\Gamma_{L,0}/\sqrt{2}\omega_0)^2 = \mathcal{O}(10^{-3})$ pa je dorinos fonon-fonon interakcije temperaturskoj zavisnosti $\omega(T)$ zanemarljiv. Na osnovu ovih razmatranja izveden je zaključak da su fononske energije suštinski određene kontrakcijama rešetke i da su ekscitacije P1 i P2 fononske prirode.

Definisanjem prirode ekscitacija P1 i P2 pojavila se potreba za određivanjem mehanizma koji stoji iza njihove pojave. Upotrebom DFT i DFPT metoda izračunate su fononske disperzione
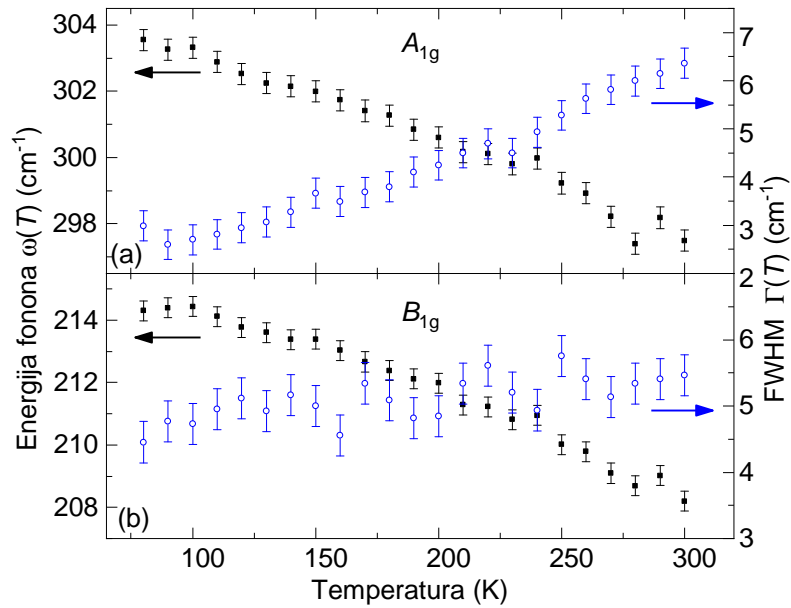
Slika 4.7: Temperaturska zavisnost $A_{1g}$ i $B_{1g}$ modova u opsegu temperatura od $80\,\mathrm{K}$ do $300\,\mathrm{K}$. Crnom bojom označene su fononske energije; plavom bojom poluširine.
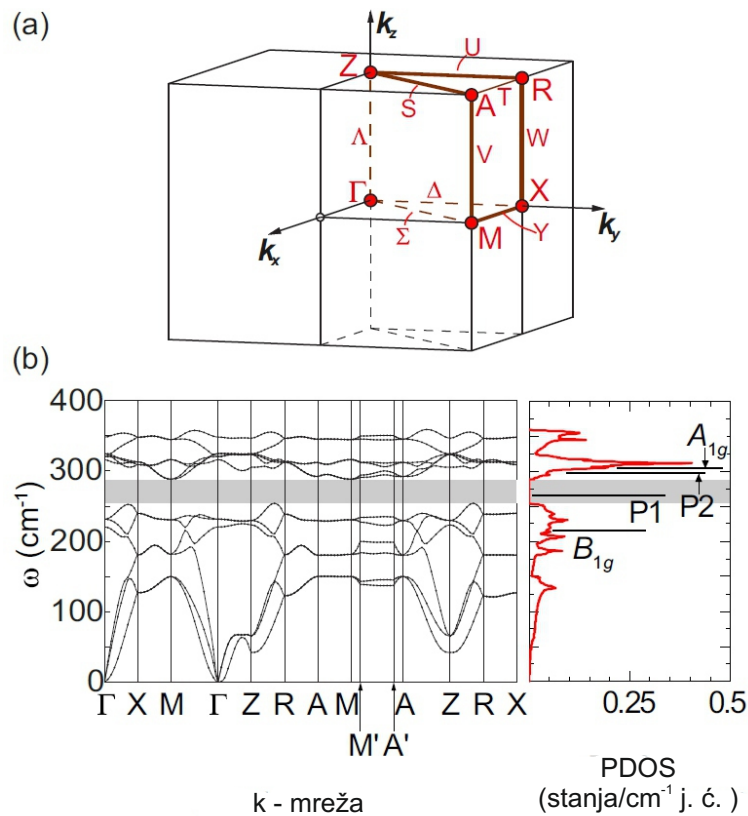


Slika 4.8: (a) Briluenova zona tetragonalnog FeS sistema. (b) Fononske disperzije duž obeleženih pravaca i fononska gustina stanja (PDOS). Sivom bojom označen je procep u fononskim disperzionim relacijama i PDOS-u.

relacije i fononska gustina stanja (PDOS) (Slika 4.8). Nezavisno od toga da li su u proračunima korišćeni optimizovani ili eksperimentalni parametri, pik P1 se nalazi u procepu fononske gustine

stanja. Ovo znači da P1 ne može biti rezultat defektom indukovanog rasejanja prvog reda. Na osnovu zakona održanja kristalnog impulsa ($q \approx 0$) pik P1, odnosno njegova energija $\omega_{P1} = 265 \mathrm{cm}^{-1}$ i talasni vektor moraju odgovarati zbiru fononskih energija $\omega_{P1'}(\mathbf{k}) + \omega_{P1''}(-\mathbf{k})$ i talasnih vektora $\pm\mathbf{k}$.

Generalno, do rasejanja drugog reda može doći usled prisustva defekata [88]. U tom slučaju rasejanje prvog reda proporcionalno je fononskoj gustini stanja. Direktnim poređenjem eksperimentalnih rezultata (Slika 4.2) i fononske gustine stanja (Slika 4.8 (b)), može se utvrditi da P1 nije rezultat defektom indukovanog rasejanja drugog reda. S duge strane, do rasejanja drugog reda može doći i usled pojačane elektron-fonon interakcije [89]. Iako se u opštem slučaju dvofononske ekscitacije mogu videti u svim kanalima rasejanja [90], činjenica da je P1 uočen u $A_{1g}$ kanalu ukazuje da se može povezati sa fononima van $\Gamma$ tačke čiji talasni vektori odgovaraju pravcima visoke simetrije odnosno njihove neposredne okoline.

Selekciona pravila za procese rasejanja drugog reda za prostornu grupu $P4/nmm$ određena su metodom modifikovanih grupnih projektora (Dodatak A.1). Ova selekciona pravila prikazana su u Tabeli 4.4. Piku P1 odgovaraju $A_{1g}$ selekciona pravila pa se iz razmatranja mogu isključiti sve nesimetrične kombinacije (desna kolona u Tabeli 4.4). U levoj koloni Tabele 4.4 prikazane su sve simetrične kombinacije. Među njima je potrebno naći one sa isključivo $A_{1g}$ selekcionim pravilima. Zatim treba odrediti tačke i pravce visoke simetrije Briluenove zone za koje oko energije $\omega_{P1}/2$ postoji nenulta fononska gustina stanja.

Postoji samo nekoliko tačaka, odnosno pravaca visoke simetrije sa isključivo $A_{1g}$ selekcionim pravilima. Doprinos stanja iz tačaka visoke simetrije $\Gamma$, $M$ i/ili $A$ dolazi sa veoma malom verovatnoćom. Favorizovani su pravci visoke simetrije $S = A - Z$, $\Sigma = \Gamma - M$ i $V = A - M$ sa ravnim fononskim disperzijama. Disperzije duž pravaca $S$ i $\Sigma$ daju mali doprinos fononskoj gustini stanja. Duž pravca $V$ dvostruko degenerisana grana sa ravnom disperzijom značajno doprinosi gustini stanja, ali se njena energija ($150 \mathrm{~cm}^{-1}$) za oko 13% razlikuje od očekivane vrednosti ($132.5 \mathrm{~cm}^{-1}$). Međutim, u neposrednoj okolini pravca $V$ na energijama između 130 i $140 \mathrm{~cm}^{-1}$, duž pravca $M' - A'$, nalazi se najveća fononska gustina stanja (Slika 4.8).

Ekvivalentno piku P1, P2 se ne može dovesti u vezu sa $E_g$ modovima, ali se za razliku od njega ne nalazi u procepu fononske gustine stanja. Stoga P2 može biti posledica defektom indukovanog rasejanja prvog reda ili, slično P1 rasejanja drugog reda. Ukoliko govorimo o procesu rasejanja drugog reda, analognim razmatranjem moguće je odrediti pravce visoke simetrije kojima odgovaraju $A_{1g}$ i $B_{1g}$, isključujući $E_g$ selekciona pravila. U ovom slučaju doprios može doći iz pravaca $\Delta = \Gamma - X$ i $U = Z - R$. Duž ovih pravaca je prisutna mala fononska gustina stanja, pa se mogućnost defektom indukovanog rasejanja prvog reda ne može u potpunosti isključiti. Maksimum fononske gustine stanja se prema teorijskim proračunima nalazi na oko $300 \mathrm{~cm}^{-1}$. Ova vrednost odgovara eksperimentalno određenoj energiji pika P2. Dodatno, velika gustina stanja u opsegu energija od 300 - 325 $\mathrm{cm}^{-1}$ mogla bi biti uzrok doprinosa $A_{1g}$ moda u spektrima ukrštene polarizacije.

Analizom temperaturske zavisnosti energija i poluširina (Poglavlje 4.2.1) dobijena je skoro

Tabela 4.4: Selekciona pravila za dvofononske procese u FeS sistemu opisanom prostornom grupom $P4/nmm$. Za proizvode ireducibilnih reprezentacija (IR) u levoj koloni, dekompozicija na Raman aktivne modove (RM) nalazi se u desnoj. Raman aktivni modovi FeS sistema su $\Gamma_1^+$ ($A_{1g}$), $\Gamma_2^+$ ($B_{1g}$) i dva dvostruko degenerisana $\Gamma_5^+$ ($E_g$) moda. $\Gamma_1^+$ potiče od vibracija S atoma, $\Gamma_2^+$ od Fe, dok oba tipa atoma doprinose svakom paru $\Gamma_5^+$ modova. Za kompleksne reprezentacije ($V_{1,2,3,4}$ i sve $W$) dvostruki indeks označava korišćenje realne reprezentacije, na primer: $V_{13} = V_1 \oplus V_1^* = V_1 \oplus V_3$. Korišćene su ireducibilne reprezentacije iz Ref. [91]

| Overtonovi | | Kombinacije | |
|---|---|---|---|
| IR | RM | IR | RM |
| $[(\Gamma_i^\pm)^2]$, $(i=1,2,3,4)$ | $A_{1g}$ | $\Gamma_1^h \otimes \Gamma_2^h$, $\Gamma_3^h \otimes \Gamma_4^h$, $(h=\pm)$ | $B_{1g}$ |
| $[(\Gamma_5^\pm)^2]$ | $A_{1g},B_{1g}$ | $\Gamma_i^h \otimes \Gamma_5^h$, $(i=1,2,3,4,\ h=\pm)$ | $E_g$ |
| $[(X_i)^2]$, $(i=1,2)$ | $A_{1g},B_{1g},E_g$ | $X_1 \otimes X_2$ | $E_g$ |
| $[(M_i)^2]$, $(i=1,2,3,4)$ | $A_{1g}$ | $M_1 \otimes M_2$, $M_3 \otimes M_4$ | $B_{1g}$ |
| $[(\Sigma_i)^2]$, $(i=1,2,3,4)$ | $A_{1g}$ | $M_1 \otimes M_3$, $M_1 \otimes M_4$, $M_2 \otimes M_3$, $M_2 \otimes M_4$ | $E_g$ |
| $[(\Delta_i)^2]$, $(i=1,2,3,4)$ | $A_{1g},B_{1g}$ | $\Sigma_1 \otimes \Sigma_2$, $\Sigma_3 \otimes \Sigma_4$ | $B_{1g}$ |
| $[(V_{13})^2]$, $[(V_{24})^2]$, $[(V_5)^2]$ | $A_{1g}$ | $\Sigma_1 \otimes \Sigma_3$, $\Sigma_1 \otimes \Sigma_4$, $\Sigma_2 \otimes \Sigma_3$, $\Sigma_2 \otimes \Sigma_4$ | $E_g$ |
| $[(W_{13})^2]$, $[(W_{24})^2]$, | $A_{1g},B_{1g},\ E_g$ | $\Delta_1 \otimes \Delta_2$, $\Delta_1 \otimes \Delta_3$, $\Delta_2 \otimes \Delta_4$, $\Delta_3 \otimes \Delta_4$ | $E_g$ |
| $[(Y_1)^2]$ | $A_{1g},B_{1g},E_g$ | $V_{13} \otimes V_{24}$ | $B_{1g}$ |
| $[(Z_i^\pm)^2]$, $(i=1,2,3,4)$ | $A_{1g}$ | $V_{13} \otimes V_5$, $V_{24} \otimes V_5$ | $E_g$ |
| $[(Z_5^\pm)^2]$ | $A_{1g},B_{1g}$ | $W_{13} \otimes W_{24}$ | $E_g$ |
| $[(A_i)^2]$, $(i=1,2,3,4)$ | $A_{1g}$ | $Z_1^h \otimes Z_2^h$, $Z_3^h \otimes Z_4^h$, $(h=\pm)$ | $B_{1g}$ |
| $[(R_i)^2]$, $(i=1,2)$ | $A_{1g},B_{1g},E_g$ | $Z_i^h \otimes Z_5^h$, $(i=1,2,3,4,\ h=\pm)$ | $E_g$ |
| $[(S_i)^2]$, $(i=1,2,3,4)$ | $A_{1g}$ | $A_1 \otimes A_2$, $A_3 \otimes A_4$ | $B_{1g}$ |
| $[(U_i)^2]$, $(i=1,2,3,4)$ | $A_{1g},B_{1g}$ | $A_1 \otimes A_3$, $A_1 \otimes A_4$, $A_2 \otimes A_3$, $A_2 \otimes A_4$ | $E_g$ |
| $[(\Lambda_i)^2]$, $(i=1,2,3,4)$ | $A_{1g}$ | $R_1 \otimes R_2$ | $E_g$ |
| $[(\Lambda_5)^2]$ | $A_{1g},B_{1g}$ | $S_1 \otimes S_2$, $S_3 \otimes S_4$ | $B_{1g}$ |
| $[(T_1)^2]$ | $A_{1g},B_{1g},E_g$ | $S_1 \otimes S_3$, $S_1 \otimes S_4$, $S_2 \otimes S_3$, $S_2 \otimes S_4$ | $E_g$ |
| | | $U_1 \otimes U_2$, $U_1 \otimes U_3$, $U_2 \otimes U_4$, $U_3 \otimes U_4$ | $E_g$ |
| | | $\Lambda_1 \otimes \Lambda_2$, $\Lambda_3 \otimes \Lambda_4$ | $B_{1g}$ |
| | | $\Lambda_i \otimes \Lambda_5$, $(i=1,2,3,4)$ | $E_g$ |

šest puta veća vrednost parametra fonon-fonon interakcije $A_{1g}$ moda u odnosu na ostale uočene i analizirane modove (Tabela 4.3). Vrednosti energija ukazuju na raspad $A_{1g}$ fonona na fonone čije su energije bliske onima koji učestvuju u procesu rasejanja drugog reda koji rezultuje pikom P1. U ovim procesima fonon-fonon interakcija je od suštinskog značaja. Fonon-fonon interakcija meri se parametrom $\lambda_{ph-ph}$ i njegova vrednost za $A_{1g}$ mod je jako velika ($\sim 1.7$). Do fonon-fonon interakcije dolazi u svim materijalima i javlja se kao posledica anharmoničnosti.

U prisustvu defekata ovaj efekat je pojačan [88]. Uzimajući u obzir činjenicu da je FeS metal, fonon-fonon interakcija se mora barem delimično odvijati posredstvom elektronskih stanja. Parametar $\lambda_{ph-ph}$ proporcionalan je kvadratu parametra elektron-fonon interakcije ($\lambda_{el-ph}^2$), pa velika vrednost $\lambda_{ph-ph}^{A_{1g}}$ takođe može biti indikator pojačane elektron-fonon interakcije u ovom materijalu.

## 4.3 Uticaj supstitucije na dinamiku rešetke FeSe$_{1-x}$S$_x$ $(0 \leq x \leq 1)$

Dosadašnja istraživanja superprovodnika FeSe i FeS ukazuju na različite faze i interakcije koje utiču na formiranje superprovodnog stanja. Narušenje kristalne simetrije, nematična faza i frustrirano magnetno uređenje u FeSe prisutni su iznad $T_c$. Ovi efekti nisu uočeni u izostrukturnom i izoelektronskom FeS, u kom do formiranja superprovodnog stanja dolazi iz tetragonalne kristalne faze. Očigledno, mehanizmi koji utiču na supeprovodnost su u ovim materijalima različiti. Zbog toga je važno ispitati na koji način evoluiraju određene osobine između FeS i FeSe.

U ovom poglavlju predstavljeni su eksperimentalni rezultati neelastičnog rasejanja svetlosti na seriji uzoraka FeSe$_{1-x}$S$_x$ $(0 \leq x \leq 1)$. Ovi rezultati deo su trenutno aktuelnog istraživanja, pa iako preliminarni, prikazani rezultati daju uvid u evoluciju vibracione strukture.
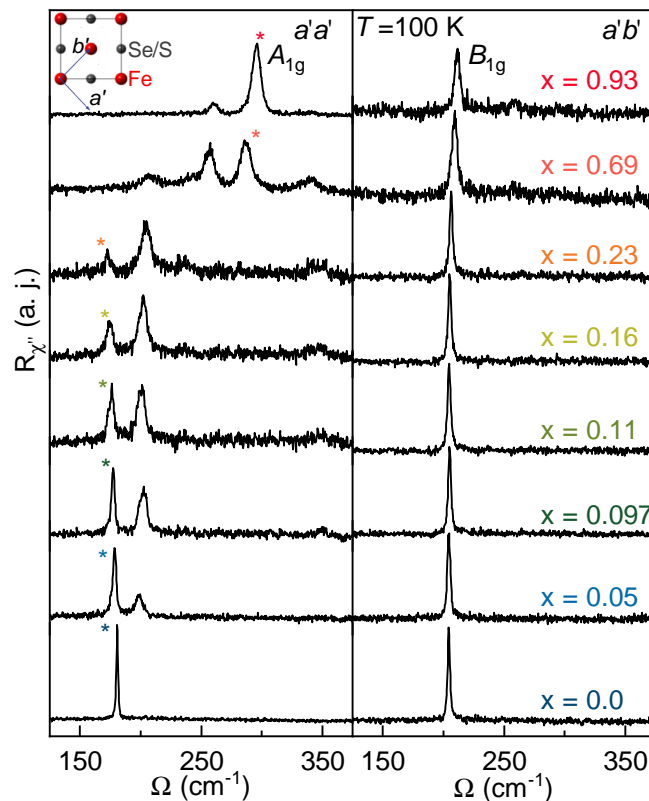


Slika 4.9: Ramanovi spektri FeSe$_{1-x}$S$_x$ $(0 \leq x \leq 0.93)$ na $T = 100\,\mathrm{K}$ u $a'a'$ i $a'b'$ polarizacionoj konfiguraciji. Zvezdicom je oznčena evolucija $A_{1g}$ moda sa $x$. Umetak: pravci polarizacije u odnosu na orijentaciju kristala.

Na Slici 4.9 prikazani su Ramanovi spektri $FeSe_{1-x}S_x$, $(0 \leq x \leq 0.93)$ u $a'a'$ i $a'b'$ polarizacionim konfiguracijama. Generalno, u translaciono invarijantnim sistemima u $a'a'$ i $a'b'$ konfiguracijama moguće je detektovati isključivo ekscitacije $A_{1g}$, odnosno $B_{1g}$ simetrije. Uzevši u obzir koncentraciju defekata merenih uzoraka narušenje selekcionih pravila i projekcija fononske gustine stanja potpuno su očekivani u ramanskim spektrima. Međutim, pored simetrijom predviđenih modova u spektrima dopiranih uzoraka u $A_{1g}$ kanalu rasejanja uočeni su dodatni modovi. U Poglavlju 4.2.2 je bilo reči o posledicama defektom indukovanog rasejanja prvog reda i rasejanja drugog reda. Kada bi dodatni modovi bili posledica defektom indukovanog rasejanja prvog reda, došlo bi do narušenja selekcionih pravila i ovi modovi bi bili prisutni u svim kanalima rasejanja, uključujući i $B_{1g}$. Poređenjem spektara na Slici 4.9 to definitivno nije slučaj. U $a'b'$ polarizacionoj konfiguraciji prisutan je samo mod $B_{1g}$ simetrije.

Evolucija ramanskih spektara u $A_{1g}$ kanalu rasejanja u zavisnosti od koncentracije atoma sumpora u uzorku $(x)$ pokazuje da se prvi dodatni mod javlja već pri malim koncentracijama $(x = 0.05)$. U čistom FeSe uzorku nisu uočeni dodatni modovi. Ovaj rezultat konzistentan je sa rezultatima Ramanovog rasejanja na $FeSe_{1-x}S_x$, $(0 \leq x \leq 0.2)$, u kojima je dodatni mod $A_{1g}$ simetrije uočen pri koncentraciji atoma sumpora $x = 0.04$ [92]. Na Slici 4.9 se može videti da kako koncentracija atoma sumpora raste, intenzitet simetrijom predviđenog $A_{1g}$ moda opada dostižući svoj minimum za $x = 0.23$. Suprotno, intenzitet dodatnog moda raste sa porastom $x$.
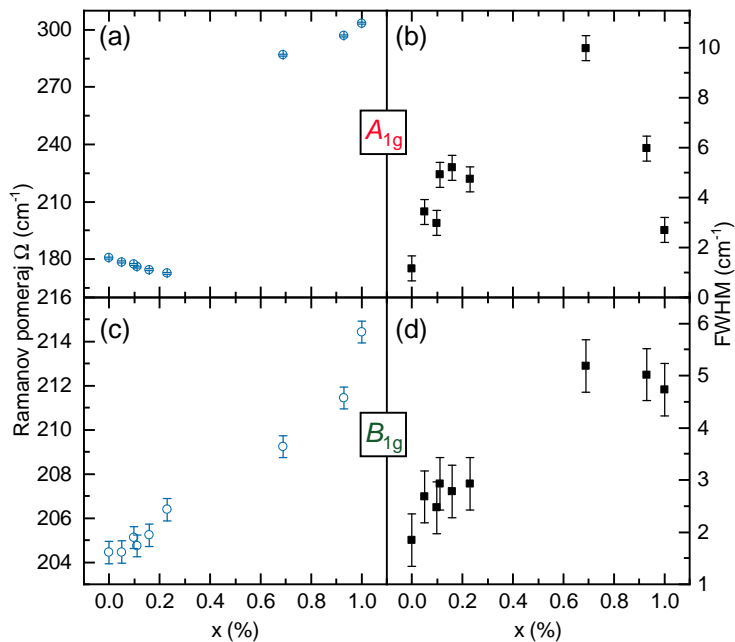


Slika 4.10: Zavisnost energije i poluširine ((a) i (b)) $A_{1g}$ i ((c) i (d)) $B_{1g}$ modova od koncentracije atoma sumpora u $FeSe_{1-x}S_x$ $(0 \leq x \leq 1)$.

Dodatni pik u $A_{1g}$ kanalu rasejanja u prisustvu atoma sumpora sugeriše sličan scenario kao u FeS. Prethodno je utvrđeno da ovaj mod ne može poticati od defektom indukovanog rasejanja prvog reda. Analogno FeS, na osnovu selekcionih pravila i promene u elektronskoj strukturi u prisustvu atoma sumpora u dopiranim uzorcima dolazi do pojačane elektron-fonon

interakcije. Kao posledica pojačane elektron-fonon interakcije javljaju se dvofononski procesi koji rezultuju pojavom dodatnih pikova u $A_{1g}$ kanalu rasejanja. Dodatno, pri koncentraciji $x \approx 0.2$ (NCP) odnos intetnziteta $A_{1g}$ i dodatnog moda se drastično menja u odnosu na $\mathrm{FeSe_{0.95}S_{0.05}}$ i $\mathrm{FeSe_{0.07}S_{0.93}}$ (odnosno FeS). U okolini ove tačke nematična faza iščezava (Slika 3.3, Poglavlje 3.1.2) i najverovatnije elektron-fonon interakcija postaje dominantna.

Zavisnost energije i poluširine $A_{1g}$ i $B_{1g}$ modova od koncentracije atoma sumpora u $\mathrm{FeSe_{1-x}S_x}$ prikazana je na Slici 4.10. Uzevši u obziru simetričnost ekscitacija, prikazani rezultati dobijeni su korišćenjem Voitovog profila spektralne linije. Energija $A_{1g}$ moda (Slika 4.10 (a)) do NCP tačke monotono opada, da bi pri većim koncentracijama ($x \geq 0.69$) nastavila monotoni rast. Poluširina ovog moda (Slika 4.10 (b)) ponaša se u skladu sa koncentracijom defekata u uzorku. U krajnjim tačkama (ili u njihovoj blizini) poluširina fononske linije manja je u odnosu na ostatak serije, zbog manje koncentracije defekata. S druge strane energija $B_{1g}$ moda monotono raste (Slika 4.10 (c)) duž čitave $\mathrm{FeSe_{1-x}S_x}$ ($0 \leq x \leq 1$) serije. Poluširina (Slika 4.10 (d)) raste sa povećanjem koncentracije defekata, analogno $A_{1g}$ modu.
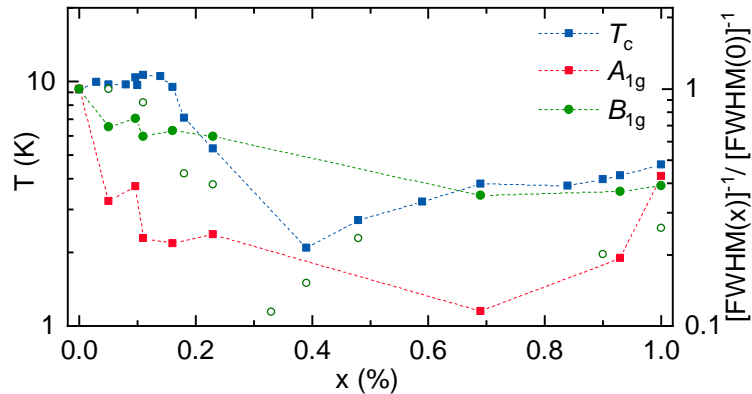


Slika 4.11: Kritična temperatura ($T_c$) [22] i invertovane normirane poluširine $A_{1g}$ i $B_{1g}$ fononskih modova u $\mathrm{FeSe_{1-x}S_x}$ ($0 \leq x \leq 1$). Punim slimbolima predstavljene su poluširine modova dobijene na Institutu za fiziku u Beogradu, a otvorenim simbolima poluširine dobijene na Valter Majsner Institutu u Minhenu.

Nematične fluktuacije u FeSe javljaju se u $B_{1g}$ kanalu rasejanja [14, 93] pa bi se njihov uticaj na $B_{1g}$ mod mogao očekivati. Na Slici 4.11 prikazane su poluširine Raman aktivnih modova $A_{1g}$ i $B_{1g}$ simetrije u zavisnosti od $x$. Poluširine normirane su na odgovarajuće poluširine modova FeSe uzorka ($x = 0$) ([FWHM($x$)]$^{-1}$/[FWHM($0$)]$^{-1}$). Na grafiku je ujedno prikazana i kritična temperatura ispitivanih uzoraka [22]. Može se uočiti da invertovana normirana poluširina $B_{1g}$ moda prati trend kritične temperature za razliku od moda $A_{1g}$ simetrije. Ovo bi značilo da se prisustvo nematičnih fluktuacija reflektuje na vibracioni spektar ovih materijala kroz $B_{1g}$ mod.

# Glava 5    Ramanova spektroskopija kvazi-2D materijala

## 5.1    Ramanova spektroskopija Cr(Si:Ge)Te$_3$

### 5.1.1    Eksperimentalni detalji i teorija

Monokristali Cr(Si:Ge)Te$_3$ ispitivani u ovoj disertaciji sintetisani su metodom rasta iz fluksa [94, 95]. Za eksperimente Ramanovog rasejanja korišćena je eksperimentalna postavka rasejanja unazad koja se nalazi u Centru za fiziku čvrstog stanja i nove materijale, Instituta za fiziku u Beogradu. Ova eksperimentalna postavka je detaljno opisana u Poglavlju 2.3 i prikazana na Slici 2.7. S ciljem postizanja visoke spektralne rezolucije, u trostepenom TriVista 557 sistemu podešena je kombinacija rešetki 1800/2400/2400 zareza/mm. Kako bi se obezbedila čista površina na uzorku, neposredno pre stavljanja u visok vakuum ($10^{-6}$ mbar) uzorci su cepani. Pravac upadne, odnosno rasejane svetlosti u ovoj eksperimentalnoj konfiguraciji poklapa se sa pravcem kristalografske $c$ - ose.

Energije fonona u $\Gamma$ tački dobijene su korišćenjem teorije gustine funkcionala u okviru QUANTUM ESPRESSO paketa [80], uz PBE izmensko-korelacioni funkcional i PAW pseudo-potencijale. Energije talasne funkcije i gustina naelektrisanja ograničene su na 85, odnosno 425 Ry. Briluenova zona uzorkovana je $8 \times 8 \times 8$ Monkhorst-Pack mrežom. Parametri rešetke i položaji atoma optimizovani su do minimizacije međuatomskih sila od $10^{-6}$ Ry/Å. Da bi se dobile što preciznije vrednosti parametara uključena je van der Valsova interakcija korišćenjem Grimme-D2 popravke. Fononske energije u $\Gamma$ tački izračunate su metodom linearnog odziva.

Magnetna svojstva merena su pomoću Quantum Design MPMS-XL5 sistema. SEM i EDS merenja izvršena su na FEI Helios Nanolab 650 sistemu.

### 5.1.2    Dinamika rešetke CrXTe$_3$ (X = Si, Ge)

Monokristali CrXTe$_3$ (X = Si, Ge) kristališu u romboedarsku kristalnu strukturu opisanu prostornom grupom simetrije $R\overline{3}$ ($C_{3i}^2$) [96]. Kristalna struktura prikazana je na Slici 5.1. U Tabeli 5.1 su date teorijske i eksperimentalne vrednosti parametara rešetke ($|a| = |b|$, $\measuredangle(a, b) = 120°$), kao i dužine veza među atomima, rastojanje između slojeva ($d$) i van der Valsov procep (vdW gap) za oba jedinjenja.

Poziciona simetrija atoma, ireducibilne reprezentacije i odgovarajući Ramanovi tenzori prikazani su u Tabeli 5.2. Broj molekulsih jedinica po elementarnoj ćeliji u ovim jedinjenjima
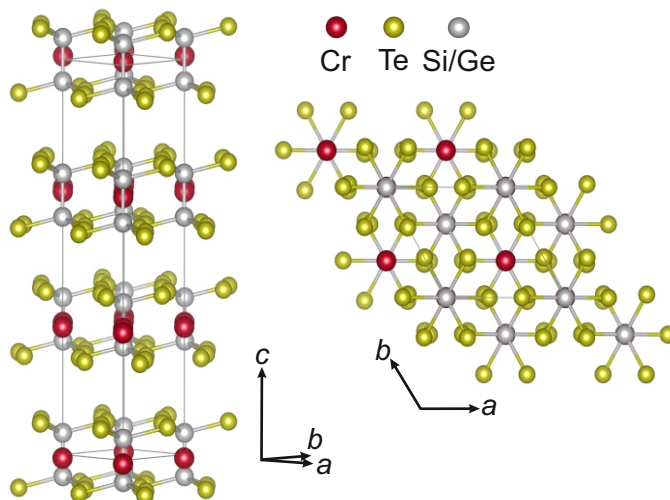
Slika 5.1: Kristalna rešetka CrXTe₃ (X = Si, Ge) sistema. Sivom linijom predstavljena je jedinična ćelija CrXTe₃ (X = Si, Ge) kristalne strukture.

Tabela 5.1: Teorijske i eksperimentalne vrednosti parametara rešetke CrXTe₃ (X = Si, Ge) ($|a| = |b|$), dužina veze, rastojanje između slojeva ($d$) i van der Valsov procep (vdW gap). Sve vrednosti date su u Å.

|  | X = Si | | X = Ge | |
| --- | --- | --- | --- | --- |
|  | Teorija | Eksperiment [97] | Teorija | Eksperiment [97] |
| $a$ | 6.87 | 6.76 | 6.91 | 6.83 |
| $c$ | 19.81 | 20.67 | 21.82 | 20.56 |
| X − X | 2.27 | 2.27 | 2.40 | 2.43 |
| X − Te | 2.52 | 2.51 | 2.61 | 2.55 |
| Cr − Te | 2.77 | 2.78 | 2.79 | 2.77 |
| $d$ | 6.86 | 6.91 | 7.27 | 6.85 |
| vdW gap | 3.42 | 3.42 | 3.81 | 3.35 |

je $Z = 2$ pa se na osnovu faktor-grupa analize dobija raspodela fononskih modova za sistem opisan prostornom grupom simetrije $R\bar{3}$:

$$\begin{aligned} \Gamma_{\text{Raman}} &= 5A_g + 5E_g, \\ \Gamma_{\text{IR}} &= 4A_u + 4E_u, \\ \Gamma_{\text{Acoustic}} &= A_u + E_u. \end{aligned} \qquad (5.1)$$

Imajući u vidu da je ravan cepanja $ab$ (001) kristalografska ravan, na osnovu selekcionih pravila, odnosno oblika Ramanovih tenzora (Tabela 5.2), u ovoj eksperimentalnoj konfiguraciji moguće je uočiti svih deset Raman aktivnih modova. Nezavisno od orijentacije kristala, modovi $A_g$ simetrije mogu se javiti samo u spektrima paralelne polarizacione konfiguracije, dok se dvostruko degenerisani $E_g$ modovi mogu uočiti i u spektrima paralelne i u spektrima ukrštene

Tabela 5.2: Atom i poziciona simetrija atoma, ireducibilne reprezentacije i odgovarajući Ramanov tenzor za prostornu grupu $R\overline{3}$.

| Prostorna grupa $R\overline{3}$ ($C_{3i}^2$) | |
|---|---|
| Atomi (Poziciona simetrija) | Ireducibilne reprezentacije |
| Cr, X (6$c$) | $A_g + E_g + A_u + E_u$ |
| Te (18$f$) | $3A_g + 3E_g + 3A_u + 3E_u$ |

Ramanovi tenzori

$$A_g = \begin{pmatrix} A & 0 & 0 \\ 0 & B & 0 \\ 0 & 0 & C \end{pmatrix} \quad {}^1E_g = \begin{pmatrix} C & D & E \\ D & -C & F \\ E & F & 0 \end{pmatrix} \quad {}^2E_g = \begin{pmatrix} D & -C & -F \\ -C & -D & E \\ -F & E & 0 \end{pmatrix}$$

polarizacione konfiguracije.

Ramanovi spektri CrSiTe$_3$ u paralelnoj i ukrštenoj polarizacionoj konfiguraciji prikazani su na Slici 5.2. U spektrima su uočena četiri pika na energijama 88.9, 118.2, 147.4 i 217.2 cm$^{-1}$. U spektru merenom u ukrštenoj polarizacionoj konfiguraciji (Slika 5.2 (b)) nije uočen jedino pik na energiji 147.4 cm$^{-1}$. Na osnovu selekcionih pravila zaključeno je da je ovaj pik $A_g$ simetrije. Ostali uočeni modovi javljaju se u obe polarizacione konfiguracije, te s toga ispunjavaju $E_g$ selekciona pravila.
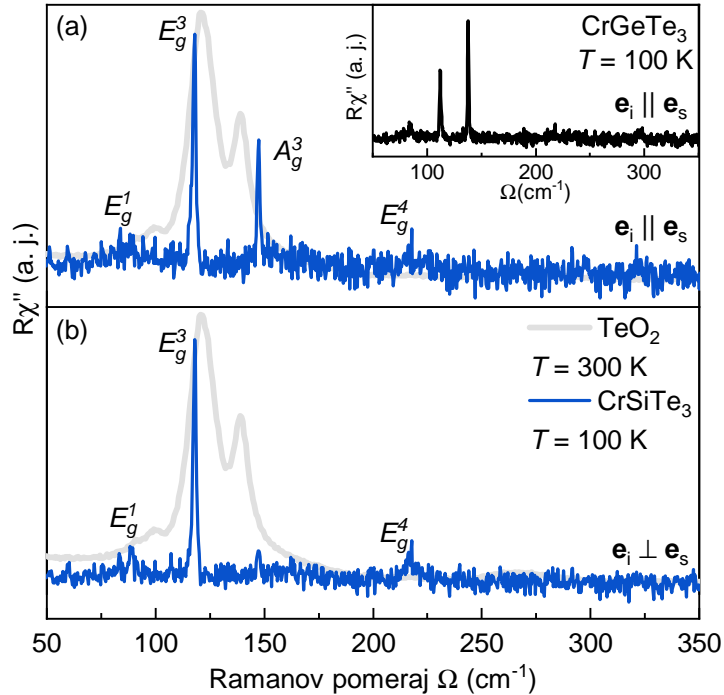


Slika 5.2: Ramanov spektar CrSiTe$_3$ kristala na $T = 100$ K u (a) paralelnoj i (b) ukrštenoj polarizacionoj konfiguraciji. Spektar TeO$_2$ na $T = 300$ K prikazan je sivom linijom. Umetak: Ramanov spektar CrGeTe$_3$ u paralelnoj polarizacionoj konfiguraciji na temperaturi $T = 100$ K.

S obzirom na to da su atomi telura skloni građenju oksidnih jedinjenja sa kiseonikom iz

vazduha, da bi se sa sigurnošću utvrdilo da uočeni modovi ne potiču od vibracija $TeO_2$ [25, 98],
njegov spektar takođe je prikazan na Slici 5.2. Na osnovu ovih rezultata može se zaključiti da
u spektrima $CrSiTe_3$ nema doprinosa $TeO_2$.

U Ramanovom spektru izostrukturnog jedinjenja $CrGeTe_3$ u paralelnoj polarizacionoj kon-
figuraciji (umetak na Slici 5.2) uočeno je pet modova, dva $A_g$ simetrije na energijama 137.9 i
296.6 $cm^{-1}$ i tri $E_g$ moda na energijama 83.5, 112.2 i 217.5 $cm^{-1}$. Ovi rezultati u saglasnosti
su sa prethodno objavljenom Ramanovom studijom na ovom materijalu [25, 99]. Razlika u
energijama uočenih modova $CrSiTe_3$ i $CrGeTe_3$ jedinjenja javlja se kao posledica efekta mase i
razlike u parametrima rešetke.

Kako bi eksperimentalni rezultati bili potvrđeni izvršeni su DFT prorčuni i dobijene su
energije fonona ($T = 0$). Ove vrednosti su zajedno sa eksperimentalnim objedinjene u Tabeli
5.3 i pokazuju veoma dobro slaganje. Dodatno, atomski pomeraji $A_g$ i $E_g$ vibracionih modova,
prikazani su na Slici 5.3.

Tabela 5.3: Simetrija fonona, izračunate ($T = 0\,K$) i eksperimentalne ($T = 100\,K$) fononske
energije Raman aktivnih modova $CrXTe_3$ (X = Si, Ge). Eksperimentalne vrednosti za Raman
aktivne fonone $CrSi_{0.8}Ge_{0.1}Te_3$ prikazane su u poslednjoj koloni. Sve vrednosti date su u $cm^{-1}$.

| | Raman aktivni modovi | | | | |
|---|---|---|---|---|---|
| | Teorija | | Eksperiment | | |
| Simetrija | X = Si | X = Ge | X = Si | X = Ge | $CrSi_{0.8}Ge_{0.1}Te_3$ |
| $A_g^1$ | 88.2 | 84.2 | - | - | 80.2 |
| $E_g^1$ | 93.5 | 82.0 | 88.9 | 83.5 | 84.5 |
| $E_g^2$ | 96.9 | 90.8 | - | - | 88.3 |
| $E_g^3$ | 118.3 | 114.2 | 118.2 | 112.2 | 117.2 |
| $A_g^2$ | 122.0 | 105.9 | - | - | 116.4 |
| $A_g^3$ | 148.0 | 134.8 | 147.4 | 137.9 | 146.7 |
| $A_g^4$ | 208.7 | 200.3 | - | - | - |
| $E_g^4$ | 219.5 | 209.6 | 217.2 | 217.5 | 215.0 |
| $E_g^5$ | 357.4 | 229.8 | - | - | - |
| $A_g^5$ | 508.9 | 290.7 | - | 296.6 | - |

### 5.1.2.1 Temperaturska zavisnost: spin-fonon interakcija

Nakon simetrijske analize i označavanja modova, izvršena je temperaturska analiza fononskih
energija i poluširina. Uzorci $CrSiTe_3$ monokristala mereni su u temperaturskom opsegu od 300
do 100 K. Detaljno su analizirani modovi najvećeg intenziteta, $E_g^3$ i $A_g^3$. Na Slici 5.4 (a) prikazan
je Ramanov spektar u opsegu energija dvostruko degenerisanog $E_g^3$ moda (118.2 $cm^{-1}$) meren
na različitim temperaturama. Na temperaturi $T = 100\,K$ ramanska linija $E_g^3$ moda pokazuje
asimetriju ka nižim energijama. Prisustvo defekata može biti uzrok asimetričnog oblika fononske
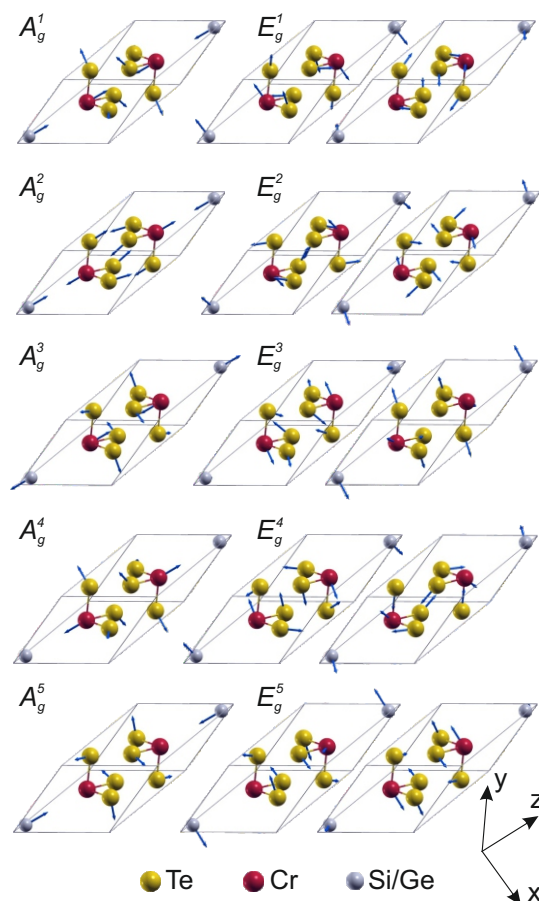
Slika 5.3: Elementarna ćelija CrXTe$_3$ (X = Si, Ge) (siva linija) i atomski pomeraji $A_g$ i $E_g$ modova. Dužine strelica proporcionalne su kvadratnom korenu međuatomskih sila.

linije. U slučaju rasejanja na defektima narušena je translaciona simetrija sistema i u spektrima se mogu javiti ekscitacije sa ivica Briluenove zone [100]. Dodatno, prisustvo defekata utiče na širenje ramanskih linija. Međutim, osim simetrijom predviđenih modova u ramanskim spektrima nisu prisutne dodatne strukture. Takođe, relativno mala poluširina fononskih linija indikacija je visoke kristaličnosti uzoraka. Asimetrija ramanske linije može se javiti kao posledica interakcije fononskih i elektronskih/spinskih ekscitacija [101]. Zbog feromagnetne prirode ovog materijala spin-fonon interakcija mogla bi biti uzrok ovakvog ponašanja $E_g^3$ moda. Uzimajući u obzir instrumentalno širenje, ovaj pik modelovan je konvolucijom spektralne linije Fano profila i Gausijana (Poglavlje 2.2). Rezultat je prikazan na Slici 5.5. Takođe, na Slici 5.5 prikazan je i rezultat modelovanja $E_g^3$ pika simetričnim (Voitovim) profilom spektralne linije. U ovom slučaju javlja se odstupanje od eksperimentalnih vrednosti upravo na asimetričnoj strani pika.

Snižavanjem temperature od 300 do 180 K energija $E_g^3$ moda raste. Na temperaturi oko 180 K dolazi do malog skoka u energiji ovog moda i daljim hlađenjem uzorka energija nastavlja monotono da raste(Slika 5.4 (b)). Poluširina $E_g^3$ do 180 K monotono opada saglasno anharmonijskom modelu (Poglavlje 2.1.3). Između 300 i 180 K temperaturska zavisnost data je izrazom (2.28) i prikazana je crvenom linijom na Slici 5.4 (c). Daljim snižavanjam temperature poluši-
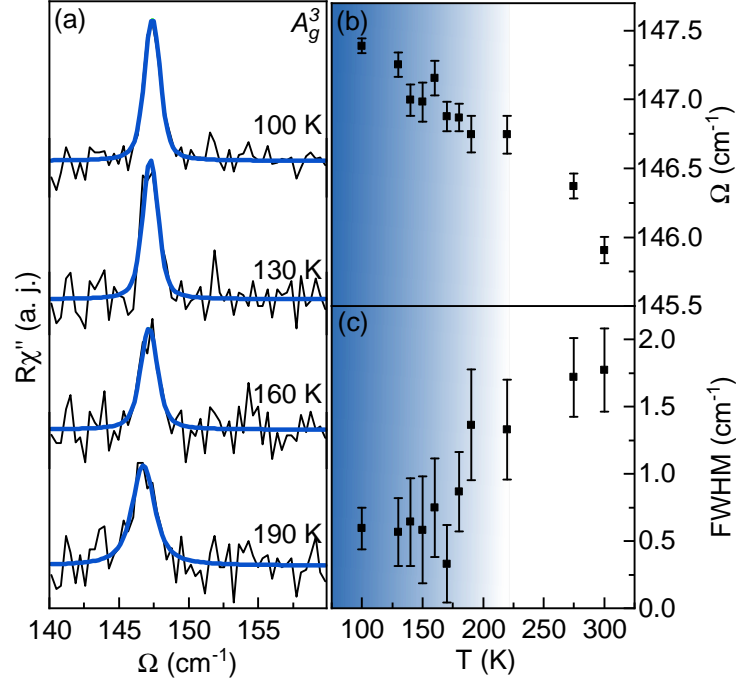
45
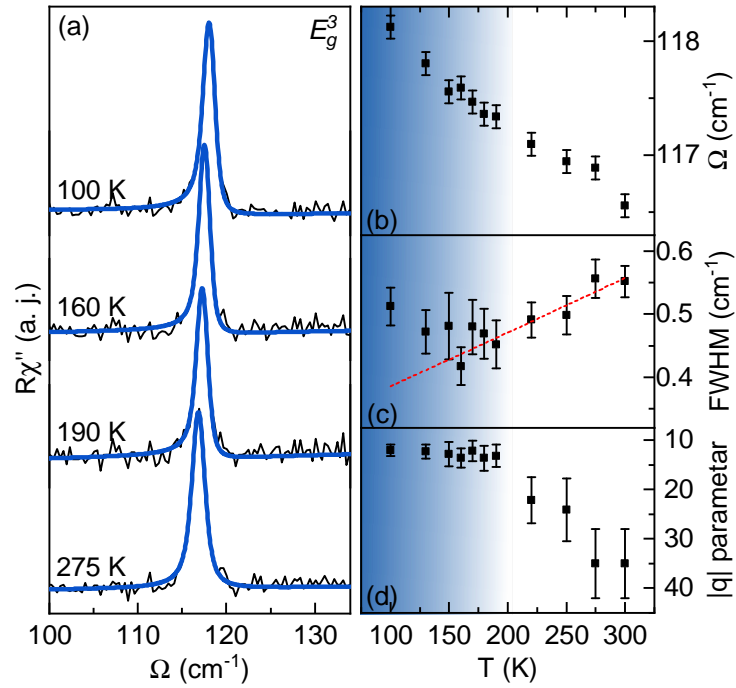
Slika 5.4: (a) Ramanov spektar u opsegu energija $E_g^3$ moda na različitim temperaturama u ukrštenoj polarizacionoj konfiguraciji. Plava linija predstavlja konvoluciju linije Fano profila i Gausijana. Temperaturska zavisnost (b) energije, (c) poluširine i (d) parametra asimetrije $q$, $E_g^3$ moda. Isprekidanom crvenom linijom predstavljen je anharmonijski model.
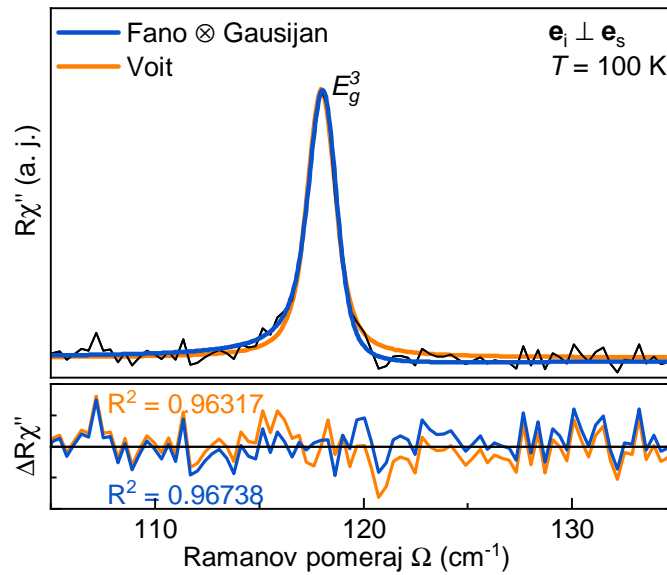


Slika 5.5: Analiza simetričnosti $E_g^3$ moda. Crnom linijom predstavljeni su eksperimentalni podaci, plavom - konvolucija Fano profila i Gausijana, narandžastom - Voitov profil.

rina $E_g^3$ moda raste, odstupajući od ovog modela. Ovakovo ponašanje indikacija je prisustva dodatnih mehanizama rasejanja, odnosno, spin-fonon interakcije. Na Slici 5.4 (d) prikazana je temperaturska evolucija Fano parametra asimetrije, $|q|$. Ispod 180 K ovaj parametar neznatno kontinualno raste, dok na višim temperaturama dolazi do naglog pada, i mod dobija simetrični oblik. Ovakvo ponašanje $E_g^3$ moda indikacija je kratkodometnog magnetnog uređenja u ovom

materijalu, koje je u literaturi [29] potvrđeno do oko 150 K, i pojačanom spin-fonon interakcijom. Slično ponašanje energija i poluširina, koje odstupa od standardnog anharmonijskog modela, kao i asimetrija $E_g$ moda u $\alpha$-RuCl$_3$, takođe je pripisano spin-fonon interakciji [102].



Slika 5.6: (a) Ramanov spektar u opsegu energija $A_g^3$ moda na različitim temperaturama u paralelnoj polarizacionoj konfiguraciji. Plava linija predstavlja Voitov profil spektralne linije kojom su modelovani eksperimentalni podaci. Temperaturska zavisnost (b) energije i (c) poluširine $A_g^3$ moda.

Za razliku od $E_g^3$, ramanska linija $A_g^3$ moda ne pokazuje asimetriju ni na najnižim temperaturama (Slika 5.6 (a)). Na Slici (Slika 5.6 (b) i (c)) prikazana je temperaturska zavisnost energije i poluširina $A_g^3$ moda. Može se uočiti sličan trend ovih fononskih osobina u okolini tačke 180 K kao kod $E_g^3$ moda.

Asimetrija ramanske linije dvostruko degenerisanog $E_g$ moda, nemonotono ponašanje analiziranih fononskih energija i poluširina na temperaturi od oko 180 K indikacija su pojačane spin-fonon interakcije u ovom materijalu. Dodatno, ovi rezultati ukazuju na prisustvo kratkodometnog magnetnog uređenja na temperaturama znatno iznad temperature magnetnog faznog prelaza ($T_{Curie} = 33$ K [29]).

### 5.1.3 Dinamika rešetke CrSi$_{0.8}$Ge$_{0.1}$Te$_3$

O eksperimentalnoj postavci Ramanovog rasejanja korišćenoj za proučavanje ovih materijala i selekcionim pravilima nedopiranih uzoraka CrXTe$_3$ (X = Si, Ge) bilo je reči u Poglavlju 5.1.1, odnosno Poglavlju 5.1.2. Od ukupno deset Raman aktivnih modova CrXTe$_3$ (X = Si, Ge) pet je $A_g$, i isto toliko $E_g$ simetrije.
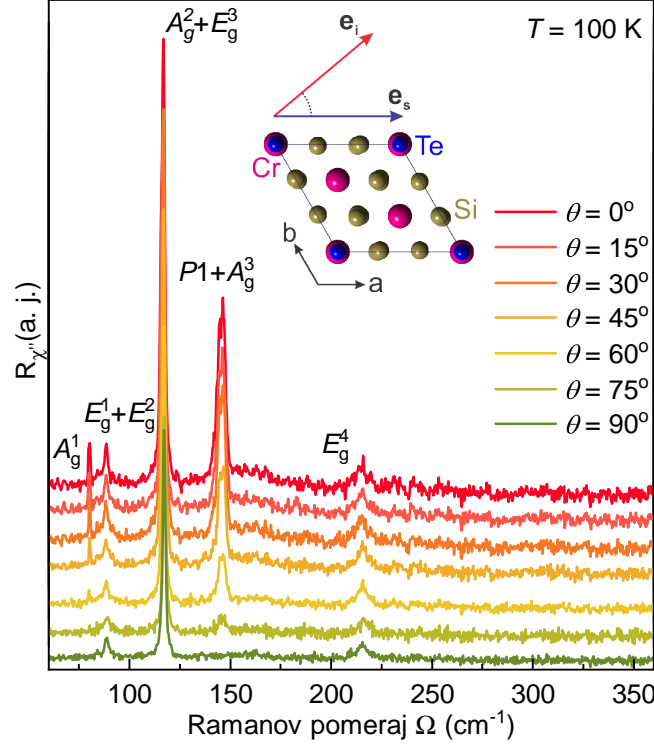
Slika 5.7: Ramanovi spektri CrSi$_{0.8}$Ge$_{0.1}$Te$_3$ monokristala, na temperaturi $100$ K u funkciji ugla $\theta$, između vektora polarizacije upadne i rasejane svetlosti. Umetak: Vektori polarizacije upadne i rasejane svetlosti u odnosu na orijentaciju kristala.

Ramanovi spektri CrSi$_{0.8}$Ge$_{0.1}$Te$_3$ monokristala mereni na temperaturi $T =$100 K prikazani su na Slici 5.7. Detaljnijim uvidom u spektre paralelne ($\theta = 0°$) i ukrštene ($\theta = 90°$) polarizacione konfiguracije, može se uočiti da niskoenergetski deo ekscitacije na oko 117 cm$^{-1}$ iščezava u ukrštenoj polarizacionoj konfiguraciji, dok deo na višoj energiji opstaje. Uvećan prikaz Ramanovog spektra u opsegu energija oko 117 cm$^{-1}$ u ove dve polarizacije dat je na Slici 5.8 (a). Dodatno, detaljnijim uvidom u ramanske spektre paralelne polarizacione konfiguracije u spektralnom opsegu oko 145.5 cm$^{-1}$ mogu se uočiti dva moda na veoma bliskim energijama (Slika 5.8 (b)). Imajući u vidu da modovi $A_g$ simetrije nisu opservabilni u ukrštenoj polarizacionoj konfiguraciji, i da sa kontinualnom promenom ugla $\theta$ ka paralelnoj polarizacionoj konfiguracijji intenzitet $A_g$ modova raste dostižući svoj maksimum za $\theta = 0°$, izvršena su merenja u funkciji ugla $\theta$. Intenzitet modova $E_g$ simetrije ne zavisi od ugla između vektora polarizacije upadne i rasejane svetlosti, te na njih promena ugla $\theta$ nema uticaja. Dodatno, inteniztet $A_g$ i $E_g$ modova ne zavisi od orijentacije kristala. Zbog toga nije bilo potrebno ispitivati zavisnost od ovog parametra. Ovakvim postupkom moguće je tačno odrediti simetrije svih modova koji se u spektru javljaju. Stoga je ispitivana samo zavisnost fononskih ekscitacija u zavisnosti od ugla $\theta = \angle(\mathbf{e}_i, \mathbf{e}_s)$ ($0° \leq \theta \leq 90°$) (Slika 5.7).

Povećavajući ugao, počevši od $\theta = 0°$, intenzitet pikova na energijama 80.2 i 145.5 cm$^{-1}$ kontinualno opada. Za vrednost $\theta = 90°$ ovi modovi potpuno nestaju, pa im na osnovu selekcionih pravila (Tabela 5.2) odgovara $A_g$ simetrija. S druge strane, promena ugla polarizacije

ne utiče na intenzitet modova na energijama 84.5, 88.3, i 215.0 cm$^{-1}$. Na osnovu selekcionih pravila može se zaključiti da su ovi modovi $E_g$ simetrije. Dodatno je potrebno izanalizirati modove na oko 117 i 145.5 cm$^{-1}$. Kontinualnom promenom ugla $\theta$ deo strukture na oko 117 cm$^{-1}$ na nižim energijama gubi intenzitet i potpuno nestaje u ukrštenoj polarizaciji, dok na deo na višim energijama promena ugla nema uticaja. Simultanim modelovanjem spektara u paralelnoj i ukrštenoj polarizaciji dobija se dekompozicija ove ramanske linije na fonone enrgija 116.4 cm$^{-1}$ i 117.2 cm$^{-1}$. Prema selekcionim pravilima, na nižoj energiji nalazi se mod $A_g^2$ a na višoj mod $E_g^3$. Ovo je detaljnije prikazano na Slici 5.8 (a). Osim toga, detaljnijom analizom pika $A_g$ simetrije na energiji oko 145.5 cm$^{-1}$ ispostavlja se da je i ovaj pik u stvari superpozicija dve ramanske linije. Modelovanjem ove strukture pomoću dve linije Voitovog profila dobijaju se fononske energije 144.6 cm$^{-1}$ ($P1$) i 146.7 cm$^{-1}$ ($A_g^3$) (Slika 5.8 (b)). Kako bi se proverila verodostojnost ovog rezultata, struktura na oko 117 cm$^{-1}$ modelovana je i pomoću jedne Voitove linije. Rezultat ovog postupka davao je drastično lošije slaganje sa eksperimentalnim rezultatima (Slika 5.8 (b)).
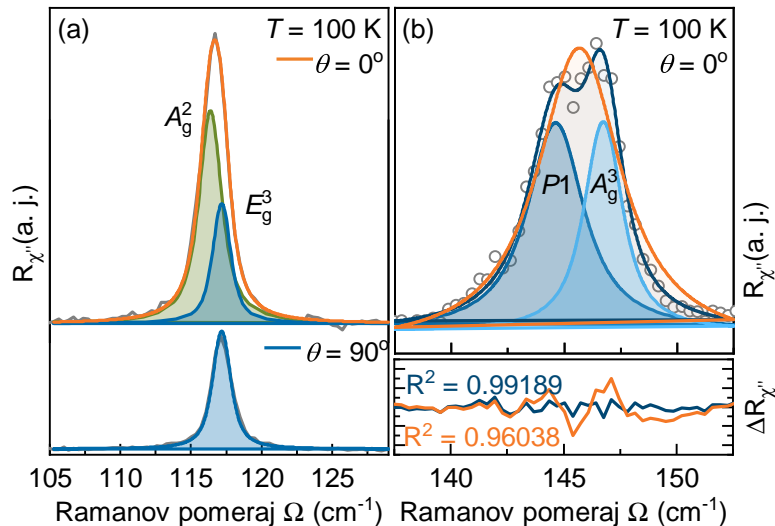


Slika 5.8: (a) Dekompozicija $A_g^2$ i $E_g^3$ modova. Prikazani su istovremeno modelovani spektri u paralelnoj i ukrštenoj polarizacionoj konfiguraciji. Sivom bojom označeni su eksperimentalni rezultati, zelenom Voitov profil $A_g^2$ moda, plavom $E_g^3$ mod u obe polarizacione konfiguracije i narandžastom superpozicija pikova. (b) Dekompozicija modova $A_g^3$ i $P1$. Sivom bojom označeni su eksperimentalni rezultati, plavom superpozicija dve linije Voitovog profila, narandžastom modelovanje rezultata jednom linijom Voitovog profila.

Vrednosti energija Raman aktivnih modova nedopiranih uzoraka CrXTe$_3$ (X = Si, Ge) izračunate DFT metodom i njihove eksperimentalne vrednosti date su u Tabeli 5.3 u Poglavlju 5.1.2. U poslednjoj koloni ove tabele prikazane su eksperimentalne vrednosti Raman aktivnih modova CrSi$_{0.8}$Ge$_{0.8}$Te$_3$ uzorka. Očekivano, energije modova dopiranog uzorka nalaze se između njihovih vrednosti CrSiTe$_3$ i CrGeTe$_3$ uzoraka. Na Slici 5.9 (a) prikazana je evolucija modova najvećeg intenziteta, $E_g^3$ i $A_g^3$, u sva tri jedinjenja. Energija $E_g^3$ moda ima gotovo linearnu zavisnost od koncentracije atoma silicijuma (Slika 5.9 (b)), usled promena u parametrima rešetke i

efekta mase, dok neuređenost u kirstalu dovodi do udvostručavanja poluširine. Slično ponašanje sa nešto većim porastom u poluširini uočeno je i kod $A_g^3$ moda.
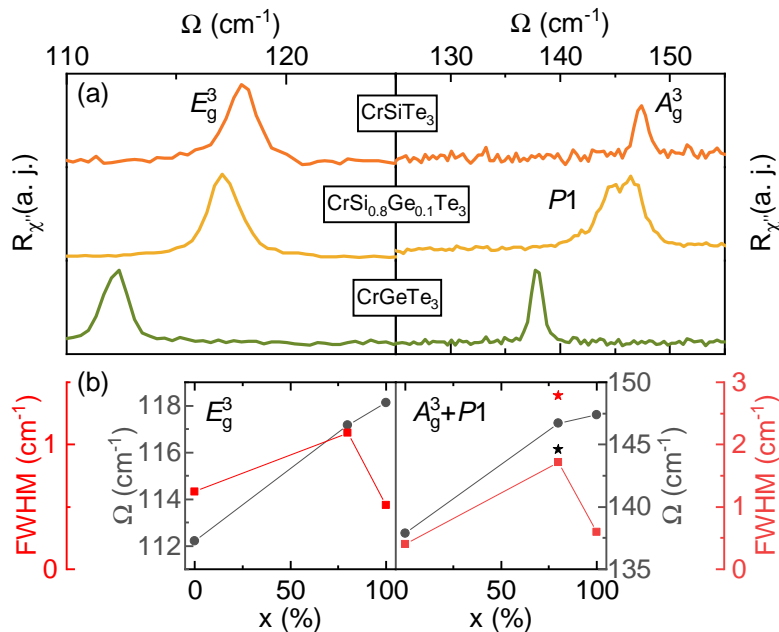


Slika 5.9: (a) Ramanovi spektri $E_g^3$ i $A_g^3$ moda CrSiTe$_3$ (narandžasto), CrSi$_{0.8}$Ge$_{0.8}$Te$_3$ (žuto) i CrGeTe$_3$ (zeleno) na $T = 100$ K mereni u ukrštenoj, odnosno paralelnoj polarizacionoj konfiguraciji. (b) Energija (sivo) i poluširina (crveno) ovih modova u funkciji koncentracije atoma silicijuma. Energija i poluširina pika $P1$ oznčene su crnom, odnosno crvenom zvezdicom.

Kao što je već rečeno, u dopiranom uzorku je pored očekivanih modova uočen dodatni pik $A_g$ simetrije, označen sa $P1$ (Slika 5.8 (b)). Kako bi se objasnilo odakle potiče ovaj mod bilo je neophodno izvršiti dodatne analize. Prilikom supstitucije atoma matičnih jedinjenja može doći do pojave vakancija i nehomogenosti u uzorku. Zbog toga je na ovom uzorku izvržena SEM i EDS analiza (Slika 5.10). Uzorci su cepani i položeni na grafitnu pločicu. Dobijeno je da usrednjen odnos elemenata, Cr:Si:Ge:Te, iznosi 1:0.8:0.1:3. Na osnovu ovog rezultata ustanovljeno je prisustvo 10% vakanicija i isto toliko atoma germanijuma u uzorku.

Generalno, defekti izazvani supstitucijom atoma i vakancije mogu izazvati promene u energiji i poluširini Raman aktivnih modova (Slika 5.9 (b)). Dodatno, ovim defektima se može obijasniti i prisustvo pika $P1$. Prisustvo vakancija na Si/Ge atomskim pozicijama i njihova nehomogena raspodela na nano-skali može da dovede do pojave dodatnih pikova u ramanskim spektrima, usled narušenja translacione simetrije. Ako je ovo uzrok „cepanja" simetrijom predviđenog $A_g$ moda, postavlja se pitanje zbog čega ovaj efekat nije uočen kod ostalih modova. Prvo, priroda ovih vibracija je raličita, pa su različiti i pomeraji u njihovim energijama. Drugo, spektralna rezolucija instrumenta je $\sim 1.8$ cm$^{-1}$ što znači da se ekscitacije čija je razlika u energiji manja od ove vrednosti ne mogu uočiti. Na osnovu ove analize može se zaključiti da je najverovatnije efekat „cepanja" ostalih modova prisutan, ali neopservabilan u ovoj eksperimentalnoj konfiguraciji.
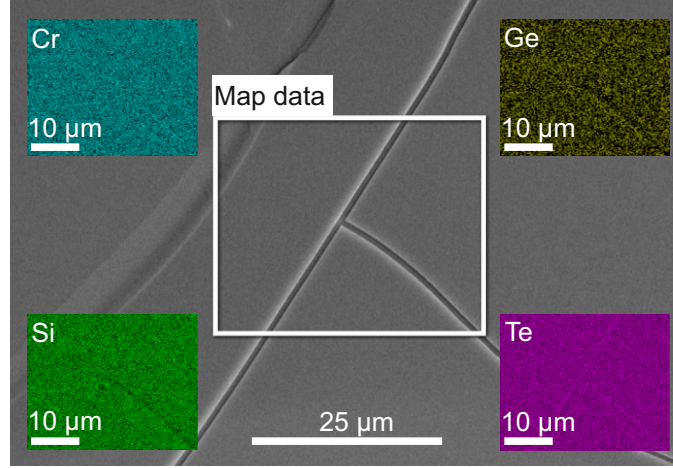
Slika 5.10: EDS mapiranje $CrSi_{0.8}Ge_{0.1}Te_3$ monokristala.

### 5.1.3.1 Magnetna susceptibilnost

U feromagnetnim van der Valsovim materijalima koncentracija vakancija u uzorku ima značajnog uticaja na temepraturu feromagnetnog faznog prelaza [33]. Uzevši u obzir rezultate predstavljene u prethodnom poglavlju ispitivan je uticaj supstitucije atoma i vakancija na magnetne karakteristike $CrSi_{0.1}Gr_{0.8}Te_3$.

Na Slici 5.11((a), (b)) prikazana je temperaturska zavisnost magnetne susceptibilnosti $\chi(T) = M(T)/H$ u polju jačine $1\,kOe$ usmerenom duž $a$, odnosno $c$ kristalografske ose. Modelovanjem Kiri-Vajsovim (*Curie-Weiss*) zakonom:

$$\chi = \frac{C}{T - \theta} \tag{5.2}$$

dobijene su Vajsove temperature $\theta_a = 61(2)\,K$ i $\theta_c = 70(2)\,K$ i paramagnetni momenti na višim temperaturama $\mu_{eff,a} = 4.14(2)\mu_B$ i $\mu_{eff,c} = 3.91(2)\mu_B$. Ovi rezultati u saglasnosti su sa feromagnetnim prelazom uočenom u matičnim jedinjenjima $CrXTe_3$ (X = Si, Ge) i odgovarajućim histerezisnim petljama [95, 97]. Temperatura magnetnog prelaza, $T_{Curie}$, se može odrediti na osnovu minimuma krive $d\chi/dT$ (umetak na Slici 5.11 (a) i (b)). U poređenju sa $CrSiTe_3$ dolazi do blagog pada $T_{Curie}$. Pokazano je da u ovoj klasi materijala povećanje koncentracije vakancija prati snižavanje temperature na kojoj dolazi do feromagnetnog uređenja [33]. Stoga se blagi pad $T_{Curie}$ u $CrSi_{0.1}Gr_{0.8}Te_3$ može obijasniti rezultatima SEM analize.

### 5.1.3.2 Temperaturska zavisnost: spin-fonon interakcija

U matičnom jedinjenju $CrSiTe_3$ u temperaturskoj zavisnosti Raman aktivnih fonona uočeno je prisustvo pojačane spin-fonon interakcije i kratkodometnog magnetnog uređenja na temperaturi koja je značajno viša od $T_{Curie}$ (Poglavlje 5.1.2). S obzirom da je uticaj supstitucije atoma i vakancija na magnetne i vibracione karakteristike $CrSi_{0.8}Gr_{0.1}Te_3$ prisutan, dalja karakterizacija ovog jedinjenja zahtevala je analizu temperaturske evolucije ramanskih spektara. Na ovom
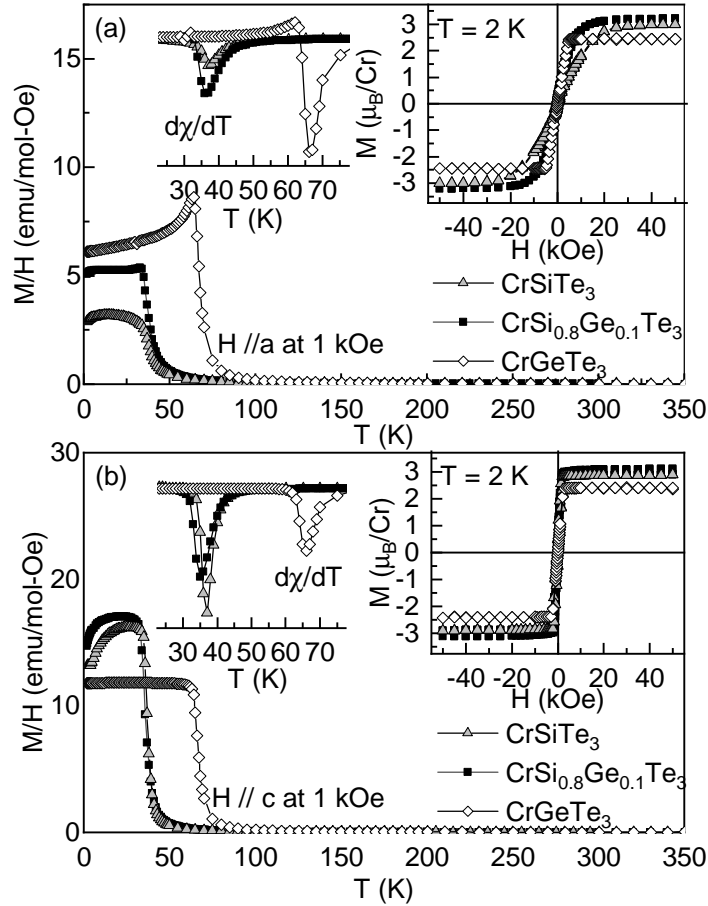
Slika 5.11: Temperaturska zavisnost magnetne susceptibilnosti $\chi = M/H$ CrSiTe$_3$, CrSi$_{0.8}$Ge$_{0.1}$Te$_3$ i CrSiGeTe$_3$ monokristala u polju jačine $1\,$kOe duž (a) $a$ i (b) $c$-ose. Umetak: Temperatura feromagnetnog prelaza $d\chi/dT$ i histerezisna petlja na $T = 2\,$K.

uzorku izvršena su merenja u opsegu temperatura između 300 i 100 K.

Na Slici 5.12 prikazani su Ramanovi spektri ovog jedinjenja na nekoliko različitih temperatura. Kako modovi $A_g^2$ i $E_g^3$ nisu odvojivi u paralelnoj polarizacionoj konfiguraciji (puna linija), preglednosti radi, u ovom energetskom opsegu prikazani su i spektri mereni u ukrštenoj konfiguraciji (isprekidana linija). Delovi spektra u nižem i višem spektralnom opsegu pomnoženi su faktorom pet. Spektri su analizirani upotrebom Voitovog profila spektralne linije za fononske eksitacije, dok je kontinuum modelovan prigušenim Lorencijanom koji sadrži i linearni član:

$$\chi''_{cont} = \frac{a\Gamma\omega}{\Gamma^2 + \omega^2} + b\omega, \tag{5.3}$$

gde su $a$, $b$ i $\Gamma$ temperaturski zavisni parametri [2].

Ovim pristupom dobijene su energije i poluširine svih modova $A_g$ i $E_g$ simetrije. Temperaturska evolucija energija i poluširina modova $A_g$ simetrije (uključujući $P1$) prikazana je na Slici 5.13. Sa porastom temperature od 100 do 210 K, kao posledica termalnog širenja [42], energije ovih modova monotono opadaju. Na temperaturi oko 210 K dolazi do skoka ka višim vrednostima, da bi sa daljim porastom temperature energije ponovo pratile monotono opadajući
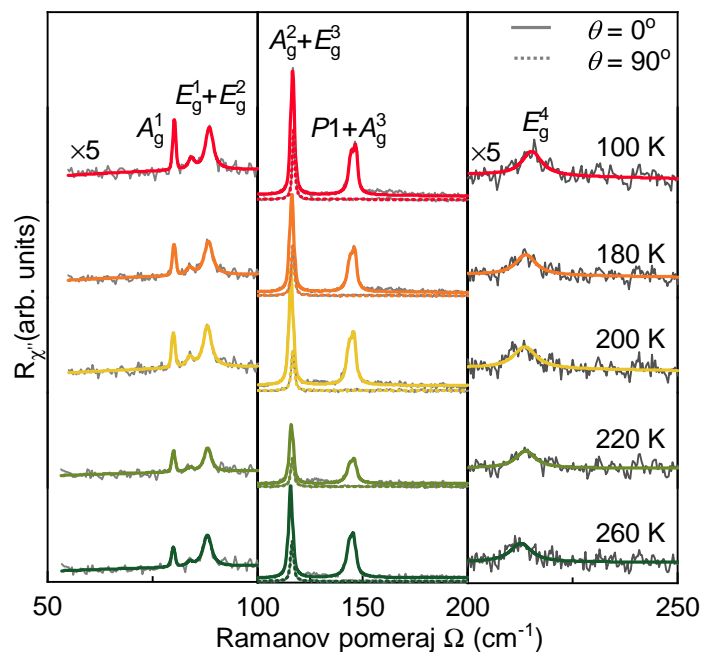
Slika 5.12: Ramanovi spektri $CrSi_{0.8}Ge_{0.1}Te_3$ monokristala na različitim temperaturama. Fononske ekscitacije u spektrima modelovane su Voitovim profilom linije. Simultano je analiziran i elektronski kontinuum koji je modelovan funkcijom (5.3). Spektri paralelne polarizacione konfiguracije ($\theta = 0°$) označeni su punom, ukrštene ($\theta = 90°$) isprekidanom linijom.
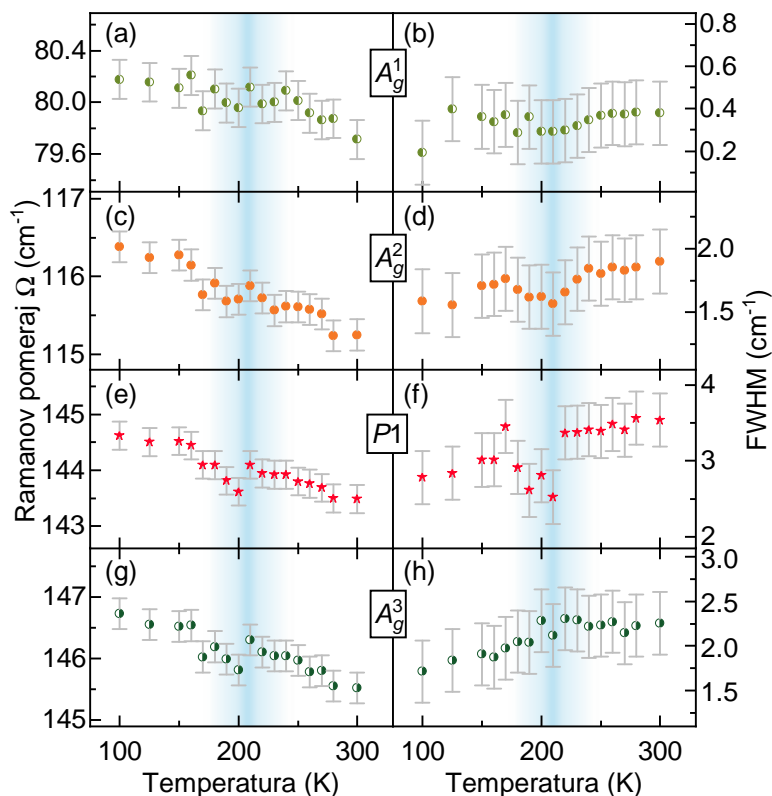


Slika 5.13: Temperaturska zavisnost energije i poluširine $A_g^1$ ((a) i (b)), $A_g^2$ ((c) i (d)), $P1$ ((e) i (f)) i $A_g^3$ ((g) i (h)) modova.

trend. U okolini 210 K poluširine analiziranih modova odstupaju od standardnog anharmon-ijskog modela (Poglavlje 2.1.3). Ovaj efekat je dominantniji kod modova na višim energijama gde je anharmoničnost inače izraženija.
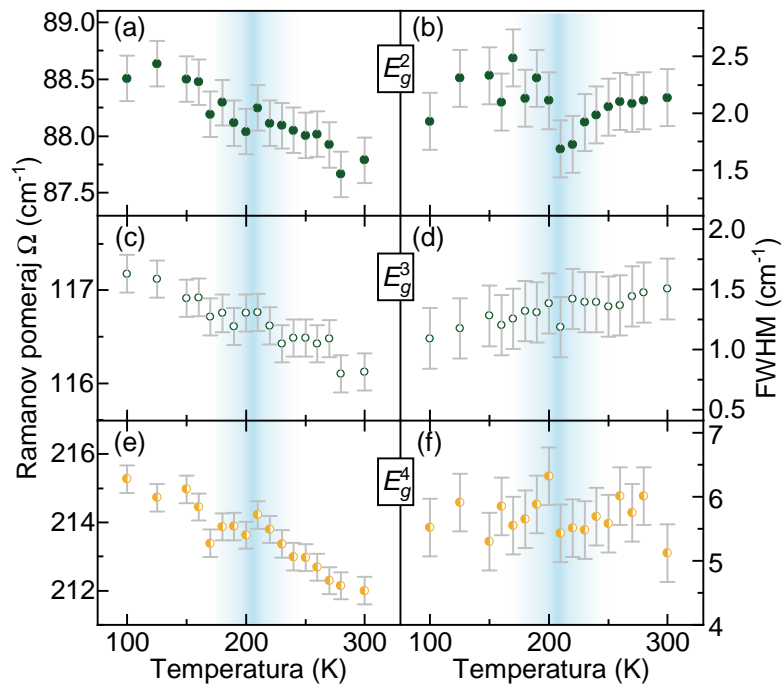


Slika 5.14: Temperaturska zavisnost energije i poluširine $E_g^2$ ((a) i (b)), $E_g^3$ ((c) i (d)) i $E_g^4$ ((e) i (f)) modova.

Prilikom analize dvostruko degenerisanih $E_g$ modova uočena je vrlo slična temperaturska evolucija energija i poluširina (Slika 5.14). Diskontinuiteti u energijama i poluširinama prisutni su na temperaturi oko 210 K.

Rezultati Ramanove spektroskopije matičnog jedinjenja CrSiTe$_3$ (Poglavlje 5.1.2) ukazuju na prisustvo spin-fonon interakcije do temperature od 180 K. Spin-fonon interakcija se u ovom jedinjenju reflektuje kroz nekonvencionalno ponašanje energija i poluširina Raman aktivnih modova, i asimetriju dvostruko degenerisanog $E_g$ moda. Asimetrija ramanske linije nije uočena ni kod jednog od modova prisutnih u spektrima CrSi$_{0.8}$Ge$_{0.8}$Te$_3$. U ovom jedinjenju spin-fonon interakcija se uočava kroz diskontinuitete fononskih energija i poluširina. Pored „cepanja" modova i pada temperature feromagnetnog prelaza, supstitucija atoma i prisustvo vakancija za posledicu ima i prisustvo magnetnih korelacija do 210 K. Ova temperatura je značajno viša u odnosu na temperaturu na kojoj je detektovan ovaj tip interakcije u CrSiTe$_3$. Stoga, prikazani rezultati ukazuju na značaj supstitucije atoma i vakancija na strukturne i magnetne osobine u ovoj klasi materijala.

## 5.2 Ramanova spektroskopija $Fe_{3-x}GeTe_2$

### 5.2.1 Eksperimentalni detalji i teorija

Monokristalni uzorci $Fe_{3-x}GeTe_2$ sintetisani su metodom rasta iz fluksa. Strukturnom analizom utvrđeno je prisustvo vakancija $x \approx 0.3$ i određeni su parametri rešetke $a = 3.954(2)$ i $c = 16.372(2)$ [34]. Za eksperiment neelastičnog rasejanja svetlosti korišćen je trostepeni Ramanov spektrometar TriVista 557 u konfiguraciji rasejanja unazad (Poglavlje 2.3, Slika 2.7). Sva merenja izvršena su u visokom vakumu ($10^{-6}$ mbar). Neposredno pre stavljanja u vakuum uzorci su cepani. U ovoj eksperimentalnoj konfiguraciji pravac upadne (rasejane) svetlosti poklapa se sa $c$ kristalografskom osom. Ravan na koju je usmeravan laserski snop je $ab$ kristalografska ravan ($|a| = |b|$, $\angle(a, b) = 120°$). Za potrebe SEM analize korišćenjen je FEI Helios nanoLab 650 sistem.

Teorijski proračuni izvršeni su upotrebom DFT metoda u okviru QUANTUM ESPRESSO paketa [80], uz PBE izmensko-korelacioni funkcional i PAW pseudo-potencijale. Energije talasne funkcije i gustina naelektrisanja ograničene su na 64, odnosno 782 Ry. Briluenova zona uzorkovana je $8 \times 8 \times 8$ Monkhorst-Pack mrežom. Energije fonona u $\Gamma$ tački u magnetnoj (M) i nemagnetnoj (NM) fazi dobijene su korišćenjem eksperimentalnih parametara rešetke i relaksiranih teorijskih parametara za predloženu strukturu. Da bi se dobile što preciznije vrednosti parametara uključena je van der Valsova interakcija korišćenjem Grimme-D2 popravke. Fononske energije u $\Gamma$ tački izračunate su metodom linearnog odziva.

### 5.2.2 Dinamika rešetke $Fe_{3-x}GeTe_2$

$Fe_3GeTe_2$ kristališe u heksagonalnu kristalnu strukturu opisanu prostornom grupom simetrije $P6_3/mmc$ ($D_{6h}^4$). Kristalna rešetka ovog sistema sastoji se od $Fe_3Ge$ ravni u kojima se javljaju neekvivalentne pozicije atoma gvožđa (Fe1 i Fe2), umetnutih između slojeva atoma telura. Susedni slojevi atoma telura razdvojeni su van der Valsovim procepom (Slika 5.15).
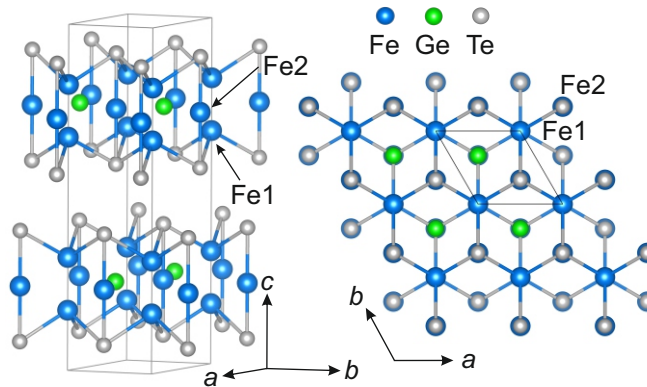


Slika 5.15: Kristalna struktura $Fe_{3-x}GeTe_2$. Sivom bojom označena je jedinična ćelija. Fe1 i Fe2 označavaju dve neekvivalentne pozicije atoma gvožđa.

Na osnovu prostorne grupe simetrije i pozicione simetrije atoma u elementarnoj ćeliji faktor-grupa analizom se dobija da je osam modova Raman aktivno od ukupno šesnaest optičkih modova (Izraz (5.4)). Atomi i njihove pozicione simetrije, ireducibilne reprezentacije i Ramanovi tenzori dati su u Tabeli 5.4.

$$\Gamma_{\text{Raman}} = 2A_{1g} + 2E_{1g} + 4E_{2g},$$
$$\Gamma_{\text{IR}} = 4A_{2u} + 4E_{1u}, \tag{5.4}$$
$$\Gamma_{\text{Acoustic}} = A_{2u} + E_{1u}.$$

Ramanov tenzor moda $E_{1g}$ simetrije sadrži samo $z$ komponentu pa ih nije moguće uočiti u eksperimentalnoj konfiguraciji rasejanja unazad. U ovoj geometriji rasejanja moguće je uočiti samo fonone $A_{1g}$ i $E_{2g}$ simetrije. Atomski pomeraji kojima odgovaraju ove dve simetrije prikazani su na Slici 5.16 (a). U vibracijama $A_{1g}$ simetrije duž $c$ ose učestvuju Fe i Te atomi, dok u vibracijama $E_{2g}$ simetrije učestvuju sva četri tipa atoma.

Tabela 5.4: Atom i poziciona simetrija atoma, ireducibilne reprezentacije i Ramanovi tenzori za prostornu grupu $P6_3/mmc$ ($D_{6h}^4$).

| Prostorna grupa $P6_3/mmc$ ($D_{6h}^4$) | |
|---|---|
| Atom (Poziciona simetrija) | Ireducibilne reprezentacije |
| Fe1 (4e) | $A_{1g} + E_{1g} + E_{2g} + A_{2u} + E_{1u}$ |
| Fe2 (2c) | $E_{2g} + A_{2u} + E_{1u}$ |
| Ge (2d) | $E_{2g} + A_{2u} + E_{1u}$ |
| Te (4f) | $A_{1g} + E_{1g} + E_{2g} + A_{2u} + E_{1u}$ |
| Ramanovi tenzori | |

$$A_{1g} = \begin{pmatrix} A & 0 & 0 \\ 0 & A & 0 \\ 0 & 0 & B \end{pmatrix} \quad E_{1g} = \begin{pmatrix} 0 & 0 & -C \\ 0 & 0 & C \\ -C & C & 0 \end{pmatrix} \quad E_{2g} = \begin{pmatrix} D & -D & 0 \\ -D & -D & 0 \\ 0 & 0 & 0 \end{pmatrix}$$

Ramanovi spektri u magnetnoj (80 K) i nemagnetnoj fazi $\text{Fe}_{3-x}\text{GeTe}_2$ (280 K) u paralelnoj polarizacionoj konfiguraciji prikazani su na Slici 5.16 (b). Uočena su četiri pika na energiji 89.2, 121.1, 214.8 i 239.6 cm$^{-1}$ na $T = 80$ K. Primenom DFT metoda fononske energije su računate upotrebom relaksiranih (R) i eksperimentalnih (NR) parametara rešetke. U oba slučaja određena su rešenja u feromagnetnoj (M) i paramagnetnoj (NM) fazi. Ovi rezultati prikazani su u Tabeli 5.5 zajedno sa eksperimentalnim vrednostima energija. Pri poređenju teorijskih i eksperimentalnih vrednosti treba imati na umu dve stvari. Prvo, teorijske vrednosti određene su za stehiometrijski uzorak, a uzorak koji je analiziran Ramanovom spektroskopijom sadrži vakancije. Drugo, na $T = 80$ K uzorak se nalazi u feromagnetnom stanju. Prema tome, najadekvatnije slaganje sa eksperimentom trebalo bi da daje magnetno rešenje dobijeno korišćenjem eksperimentalnih parametara rešetke. Poređenjem vrednosti u Tabeli 5.5 zaključeno je da to i jeste slučaj. Pikovima na energiji 89.2 i 239.6 cm$^{-1}$ odgovaraju modovi $E_{2g}^2$ i $E_{2g}^3$. Modovi $A_{1g}^1$

i $A_{1g}^2$ u spektru se nalaze na energijama 121.1 i 214.8 cm$^{-1}$.
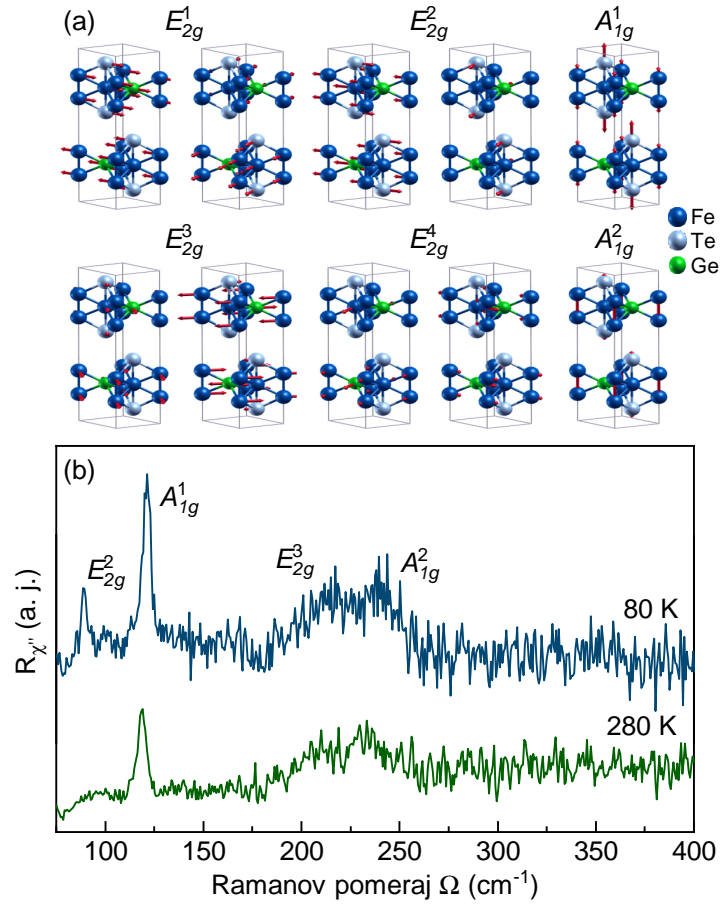


Slika 5.16: (a) Atomski pomeraji optičkih modova $A_{1g}$ i $E_{2g}$ simetrije. (b) Ramanovi spektri Fe$_{3-x}$GeTe$_2$ monokristala u paralelnoj polarizacionoj konfiguraciji u feromagnetnoj ($T = 80$ K) i paramagnetnoj ($T = 280$ K) fazi.

### 5.2.2.1 Temperaturska zavisnost: fazni prelazi

Imajući na umu zavisnost temperature magnetnog faznog prelaza od koncentracije vakancija u uzorku (Poglavlje 3.2.2) trebalo je ispitati da li magnetne korelacije utiču na fononske linije, na kojoj temperaturi i u kojoj meri. S tim ciljem ispitivana je temperaturska evolucija fonon-skih energija i poluširina u temperaturskom opsegu od 100 do 300 K. S obzirom na to da je Fe$_{3-x}$GeTe$_2$ metal, očekivan je doprinos elektronskih ekscitacija Ramanovoj susceptibilnosti.

U Ramanovim spektrima Fe$_{3-x}$GeTe$_2$ u funkciji od temperature (Slika 5.17 (a)) primećen je nelinearni odziv elektronskog kontinuuma. Iz tog razloga bilo je potrebno najpre izvršiti nje-govu analizu modelom prigušenog Lorencijana i linearnog člana (Izraz (5.3), Poglavlje 5.1.3.2) Temperaturska evolucija elektronskog kontinuuma analizirana ovim modelom prikazana je na Slici 5.17 (b). Integracijom ovih krivih može se dobiti poziciona vrednost njihovog maksimuma (Umetak na Slici 5.17 (b)). Ove vrednosti ukazuju na devijacije u inače monotonoj tempera-turskoj evoluciji kontinuuma na temperaturama od 150 K i 220 K.

Tabela 5.5: Teorijske vrednosti energija Raman aktivnih modova $Fe_{3-x}GeTe_2$ izračunate upotrebom relaksiranih (R) i eksperimentalnih (NR) parametara rešetke u magnetnoj (M) i nemagnetnoj (NM) fazi. Sve vrednosti date su u $cm^{-1}$. Eksperimentalne vrednosti u magnetnoj fazi ($T = 80\,K$) date su u poslednjoj koloni.

| | Raman aktivni modovi | | | | |
|---|---|---|---|---|---|
| | Teorija | | | | Eksperiment (M) |
| Simetrija | NM-R | M-R | NM-NR | M-NR | |
| $E_{2g}^1$ | 28.4 | 49.6 | 33.9 | 50.2 | - |
| $E_{1g}^1$ | 79.2 | 70.2 | 71.7 | 70.3 | - |
| $E_{2g}^2$ | 115.5 | 121.0 | 100.0 | 122.2 | 89.2 |
| $A_{1g}^1$ | 151.7 | 139.2 | 131.7 | 137.2 | 121.1 |
| $E_{1g}^2$ | 225.5 | 206.0 | 194.3 | 209.5 | - |
| $E_{2g}^3$ | 238.0 | 232.6 | 204.9 | 228.6 | 214.8 |
| $A_{1g}^2$ | 272.0 | 262.6 | 235.7 | 233.4 | 239.6 |
| $E_{2g}^4$ | 362.0 | 337.6 | 315.4 | 334.7 | - |
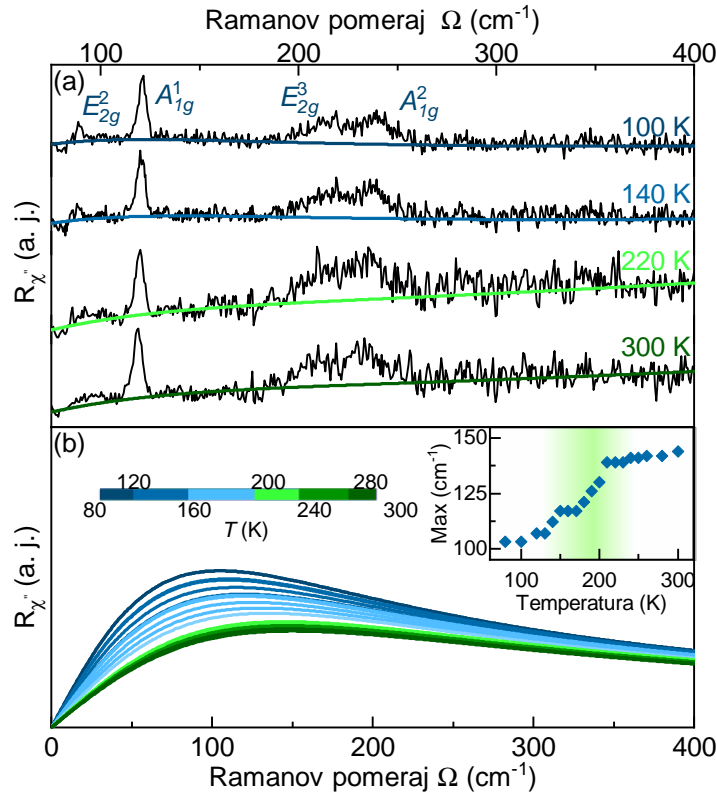


Slika 5.17: (a) Ramanovi spektri $Fe_{3-x}GeTe_2$ monokristala na označenim temperaturama mereni u paralelnoj polarizacionoj konfiguraciji. Rezultati modelovanja elektronskog kontinuuma prikazani su linijama u boji. (b) Temperaturska evolucija elektronskog kontinuuma. Umetak: Promena maksimuma krive modelovanja.
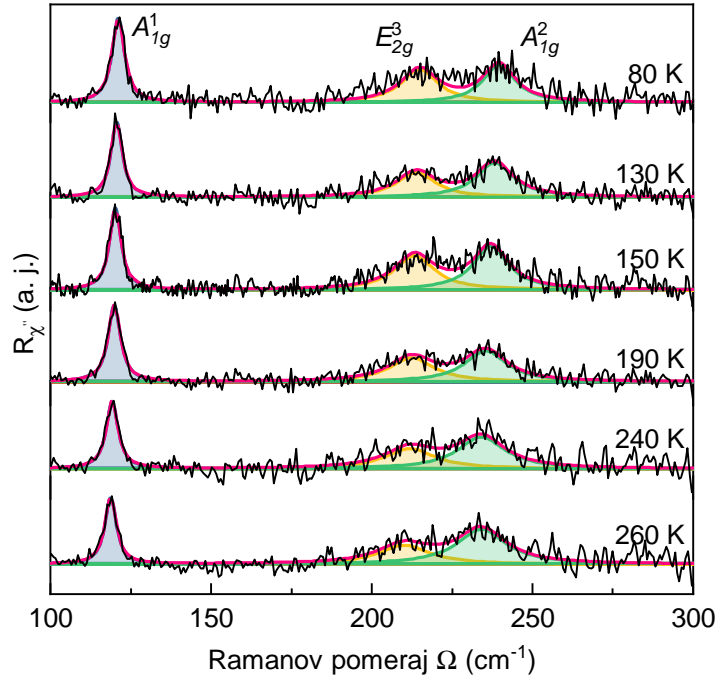
Slika 5.18: Analiza fononskih ekscitacija u Fe$_{3-x}$GeTe$_2$ momokristalu upotrebom Voitovog profila spektralne linije nakon oduzimanja doprinosa elektronskog kontinuuma na označenim temperaturama.

Fononske ekscitacije superponirane su na elektronski kontinuum. Da bi se pristupilo njihovim karakteristikama bilo je potrebno iz spektara oduzeti doprinos koji potiče od elektronskih ekscitacija. Ovim postupkom dobijaju se spektri prikazani na Slici 5.18 (crna linija). Uzevši u obzir instrumentalno širenje ($\Gamma_G = 0.8$ cm$^{-1}$) i simetričnost ramanske linije, fononske ekscitacije modelovane su Voitovim profilom spektralne linije. Rezultat ove analize prikazan je na Slici 5.18. Plavom, žutom i zelenom linijom prikazane su spektralne linije $A_{1g}^1$, $E_{2g}^3$, odnosno $A_{1g}^2$ moda. Sveukupan fit eksperimentalnih podataka prikazan je crvenom. Nedovoljno veliki intenzitet $E_{2g}^2$ moda onemogućava korektno modelovanje, te je ovaj mod izuzet iz analize.

Na ovaj način dobijena je temperaturska evolucija energije i poluširine $A_{1g}^1$, $E_{2g}^3$ i $A_{1g}^2$ fononskih modova između 80 K i 300 K, prikazana na Slici 5.19. Može se uočiti da sa porastom temperature energije modova $A_{1g}$ simetrije pokazuju mali skok na $T \sim 150$ K (Slika 5.19 (a) i (e)). Daljim zagrevanjem uzorka, na oko 220 K dolazi ponovo do odstupanja od monotono opadajućeg trenda energije svih analiziranih modova. Temperaturska zavisnost poluširine modova može se podeliti u tri oblasti, između 80 i 150 K, 150 i 220 K i između 220 K i 300K. U svakoj od pojedinčnih oblasti sa porastom temperature raste i poluširina fononskih linija. Međutim, u okolini graničnih tačaka ovih oblasti ($\approx 150$ K i $\approx 220$ K) dolazi do odstupanja vrednosti od standardnog anharmonijskog modela opisanog u Poglavlju 2.1.3.

Analiza temperaturske evolucije elektronskog kontinuuma i fononskih ekscitacija ukazuje na prisustvo faznih prelaza u Fe$_{3-x}$GeTe$_2$. Uzorci ispitivani u ovom istraživanju sintetisani su metodom rasta iz fluksa. Strukturna analiza ovih uzoraka ukazuje na koncentraciju vakancija
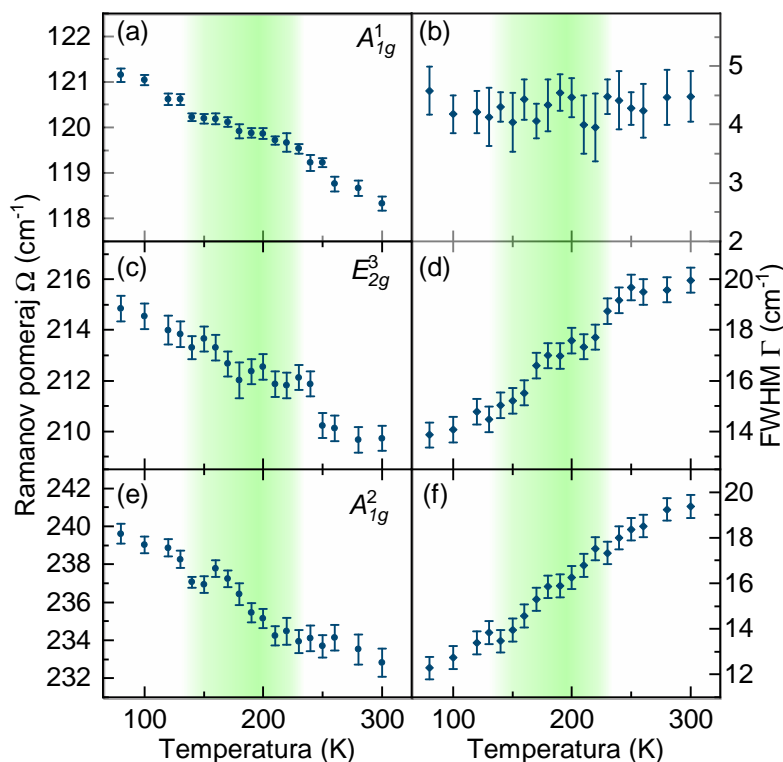
Slika 5.19: Temperaturska zavisnost energije i polušírine $A_{1g}^1$ ((a) i (b)), $E_{2g}^3$ ((c) i (d)) i $A_{1g}$ ((e) i (f)) modova Fe$_{3-x}$GeTe$_2$ monokristala.
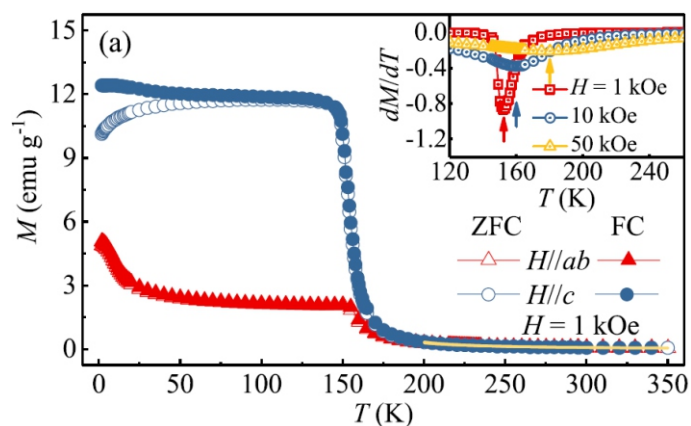


Slika 5.20: Temperaturska zavisnost magnetizacije Fe$_{3-x}$GeTe$_2$ monokristala korišćenih u ovoj disertaciji u spoljašnjem polju $H = 1$ kOe duž $ab$ i $c$ pravca. Umetak: temperaturska zavisnost $dM/dT$ u poljima različite jačine usmerenih duž $c$ ose. Preuzeto iz [34]

od oko 30% [34]. Temperaturska zavisnost magnetizacije, $M(T)$, ispitivanog uzorka prikazana je na Slici 5.20 [34]. Na nižim temperaturama dolazi do razdvajanja ZFC i FC krivih ($H||c$) što ukazuje na jaku magnetnu anizotropiju. Zavisnost $dM(T)/dT$ od jačine spoljašnjeg polja prikazana je na umetku Slike 5.20. Na osnovu minimuma ove krive određena je $T_{Curie} = 152$ K ($H = 1$ kOe), i uočen je njen porast pri jačim poljima [34]. Na osnovu ovoga zaključeno je da su skokovite promene u elektronskim i fononskim karakteristikama na oko 150 K posledica feromagnetnog faznog prelaza.
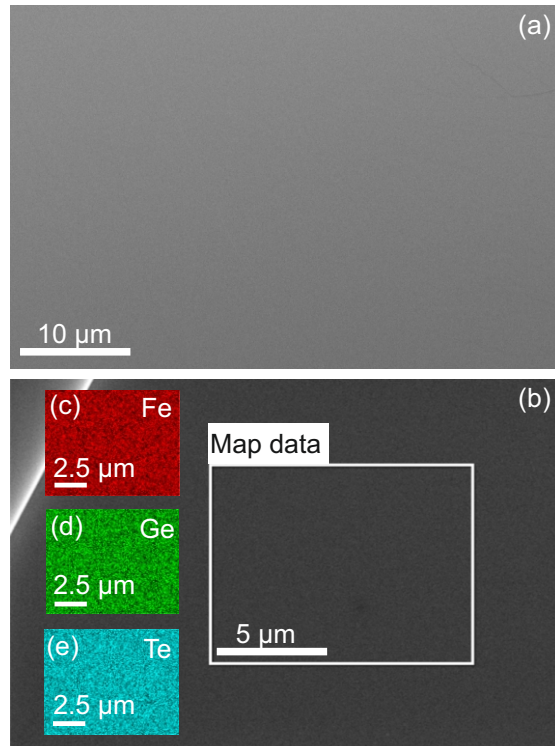
Slika 5.21: (a)SEM (b)EDS mapiranje $Fe_{3-x}GeTe_2$, sekundarna elektronska slika kristala. Mapiranje je izvršeno u granicama pravougaonika. (c) - (e) Pridružene EDS mape za Fe, Ge i Te.

Devijacije na temperaturi oko 220 K zahtevale su dodatna istraživanja. Imajući u vidu da Kirijeva temperatura stehiometrijskih uzoraka sintetisanih CVT metodom dostiže 220, čak i 230 K [31, 32, 103], ideja je bila ispitati homogenost i sastav uzorka. Naime, ukoliko bi raspodela vakancija na uzorku bila nehomogena, u rezultatima neelastičnog rasejanja bi se mogao detektovati signal iz oblasti u kojima je prisutna različita koncentracija vakancija. Time bi se mogle objasniti dve temperature magnetnog faznog prelaza. SEM i EDS analizom (Slika 5.21) ispitivan je hemijski sastav cepanog uzorka i ustanovljena je homogenost površine monokristala duž oba pravca od po nekoliko desetina mikrona. Usrednjen odonos atoma Fe:Ge:Te dobijen EDS mapiranjem izražen u procentima iznosi 47 : 17 : 36 ($\pm$2%). Prisustvo vakancija u uzorku, $x = 0.4 \pm 0.1$, u saglasnosti je sa prethodno izvršenom strukturnom analizom merenih uzoraka [34]. Imajući u vidu SEM rezultate mogućnost postojanja oblasti sa različitom koncentracijom vakancija u uzorku je isključena.

Skokovite promene u elektronskim i fononskim svojstvima na 220 K eventualno bi mogle biti posledica kratkodometnog magnetnog uređenja. Naime, slično ponašanje već je uočeno kod van der Valsovih materijala Cr(Si:Ge)Te$_3$. U ovim materijalima jake magnetne korelacije prisutne su na mnogo višim temperaturama od $T_{Curie}$ (Poglavlje 5.1). Takođe, na temperaturi $190 \pm 20$ K postoje indikacije formiranja Kondo rešetke, odnosno dolazi do interakcije provodnih elektrona i periodično lokalizovanih spinova. Iako trenutno ne raspolažemo podacima kojima bi mogli potvrditi ovaj scenario, ipak ga ne možemo u potpunosti odbaciti.

Feromagnetni fazni prelaz na temperaturi od oko 150 K ostavlja jasan trag ne samo na

fononske energije i poluširine već i na elektronski kontinuum $Fe_{3-x}GeTe_2$ monokristala. Do-datno, analiza temperaturske zavisnosti fononskih i elektronskih ekscitacija ukazuje na nemono-tonu evoluciju njihovih osobina i na temperaturi oko 220 K. Homogenost uzorka isključuje mogućnost feromagnetnih prelaza na različitim temperaturama usled grupisanja vakancija u oblasti sa različitim vrednostima $x$. Promene na 220 K se za sada mogu dovesti u vezu sa kratkodometnim magnetnim uređenjem ili Kondo efektom u $Fe_{3-x}GeTe_2$.

# Glava 6    Zaključak

U ovoj disertaciji prikazani su rezultati ispitivanja dinamike rešetke, i analizirani su efekti elektron-fonon i spin-fonon interakcije u superprovodnicima na bazi gvožđa odnosno, 11-halkogenidima FeS i FeSe$_{1-x}$S$_x$ ($0 \leq x \leq 1$) i kvazi-dvodimenzionim magnetnim materijalima Cr(Si:Ge)Te$_3$ i Fe$_{3-x}$GeTe$_2$.

U polarizovanim Ramanovim spektrima prvog proučavanog materijala iz klase superprovodnika na bazi gvožđa, FeS, pored očekivanih modova $A_{1g}$ i $B_{1g}$ simetrije prisutna su dva dodatna pika, $P1$ i $P2$. DFT i DFPT proračunima dobijene su fononske energije, fononske disperzione relacije i gustina stanja. Rezultati ovih proračuna potvrđuju korektno označavanje $A_{1g}$ i $B_{1g}$ modova koji opisuju vibracije S i Fe atoma duž $c$ - ose. Simetrijskom analizom, na osnovu selekcionih pravila je utvrđeno da je pik $P1$ visoke $A_{1g}$ simetrije. Pik $P2$ je niže simetrije jer se javlja i u $A_{1g}$ i u $B_{1g}$ kanalu rasejanja. Dodatno, pik $P1$ se nalazi u procepu izračunate fononske gustine stanja. S obzirom na visoku simetriju ovog moda i njegov položaj u fononskoj gustini stanja zaključeno je da $P1$ ne može biti rezultat defektom indukovanog rasejanja i da se javlja kao posledica procesa rasejanja drugog reda. MGPT metodom određena su selekciona pravila za dvofononske procese u tačakama i duž pravaca visoke simetrije Briluenove zone tetragonalnog FeS. Ovaj rezultat i fononske disperzione relacije omogućili su da se definišu fononske grane duž pravaca visoke simetrije kojima pripadaju stanja koja ovom procesu doprinose. Mod niže simetrije, $P2$, se ne nelazi u procepu fononske gustine stanja. Zbog toga ovaj mod može biti posledica procesa rasejanja drugog reda ali i defektom indukovanog rasejanja prvog reda. Ispitivana je i temperaturska evolucija fononskih energija i poluširina u opsegu temperatura od 300 do 4 K. Utvrđeno je da su fononske energije između 300 i 20 K suštinski određene kontrakcijama rešetke. Ispod 20 K dolazi do odstupanja od monotone temperaturske zavisnosti fononskih energija i poluširina, što je dovedeno u vezu sa kratkodometnim magnetnim uređenjem u ovom materijalu. Analizom temperaturske zavisnostni poluširine $A_{1g}$ moda anharmonijskim modelom određena je vrednost parametra fonon-fonon interakcije za ovaj mod. Dobijena je vrednost skoro šest puta veća u poređenju sa ostalim modovima. Kako se fonon-fonon interakcija u metalima odvija preko elektronskih stanja a imajući u vidu dvofononsku ekscitaciju u procepu fononske gustine stanja, u ovom materijalu elektron - fonon interakcija je najverovatnije pojačana u odnosu na FeSe. U fononskim spektrima FeSe$_{1-x}$S$_x$ ($0 \leq x \leq 1$) u $A_{1g}$ kanalu rasejanja javljaju se dodatni modovi već pri jako malim koncentracijama atoma sumpora ($x = 0.05$). Slično FeS, ovakvo ponašanje najverovatnije ukazuje na pojačavanje elektron-fonon interakcije u prisustvu atoma sumpora. Ispitivanjem zavisnosti poluširine $A_{1g}$ i

$B_{1g}$ moda u zavisnosti od $x$, uočeno je da invertovana poluširina $B_{1g}$ moda prati trend kritične temperature ispitivanih uzoraka.

Sledeći deo istrživanja je bio usmeren na van der Valsove magnetne materijale Cr(Si:Ge)Te$_3$ i Fe$_{3-x}$GeTe$_2$. Pored dinamike rešetke ispitivan je i uticaj spinskih stepeni slobode na fononske ekscitacije u Cr(Si:Ge)Te$_3$. U polarizovanim Ramanovim spektrima CrSiTe$_3$ sistema detektovan je jedan mod $A_g$ simetrije i tri $E_g$ moda. Eksperimentalne vrednosti energija ovih modova konzistentne su sa vrednostima dobijenim DFT proračunima. Ispitivanjem fononskih osobina u zavisnosti od temperature uočeno je njihovo odstupanje od anharonijskog modela na temperaturama ispod 180 K. Na istim temperaturama jedan od modova $E_g$ simetrije pokazuje asimetriju ramanske linije ka nižim energijama. Na osnovu ovih rezultata zaključeno je da je spin-fonon interakcija u ovom materijalu prisutna na temperaturi značajno višoj od $T_{Curie}$.

Na uzorku sastava CrSi$_{0.8}$Ge$_{0.1}$Te$_3$ ispitivan je uticaj supstitucije atoma i vakancija na dinamiku rešetke i spin-fonon interakciju ove klase materijala. Neodvojivost modova u spektrima paralelne polarizacione konfiguracije zahtevala je ispitivanje fononskih ekscitacija u funkciji ugla između vektora polarizacije upadne i rasejane svetlosti. Na osnovu ovih rezultata označeno je sedam modova predviđenih simetrijom $(3A_g + 4E_g)$ i dodatni mod $A_g$ simetrije. Položaj energije dodatnog $A_g$ moda u neposrednoj blizini jednog od simetrijom predviđenih $A_g$ modova sugerisao je njihovo „cepanje" čiji je uzrok trebalo dodatno ispitati. S tim ciljem izvršena je SEM analiza i utvrđeno je prisustvo 10% vakancija i isto toliko atoma germanijuma u uzorku. Zaključeno je da su defekti i njihova nehomogena raspodela na nano-skali najverovatnije uzrok ovog „cepanja". U temperaturskoj zavisnosti energija i poluširina svih analiziranih modova javljaju se skokovite promene na temperaturi oko 210 K. Imajući u vidu jake magnetne korelacije u matičnom jedinjenju (CrSiTe$_3$) do 180 K, ovakvo ponašanje fononskih enerija i poluširina pripisano je spin-fonon interakciji. Ovakvi rezultati ukazuju na značaj supstitucije atoma i prisustva vakancija na vibracione i magnetne osobine ove klase materijala.

Pored fonoskih ekscitacija u van der Valsovom feromagnetu Fe$_{3-x}$GeTe$_2$ sintetisanom metodom rasta iz fluksa analizirana je i nemonotona evolucija elektronskog kontinuuma. U fononskom delu spektra detektovana su četiri moda dva $A_{1g}$ i dva $E_{2g}$ simetrije. Analizom njihove temperaturske zavisnosti uočeno je nemonotono ponašanje modova i to na temperaturama u okolini 150 i 220 K. Temperaturska evolucija elektronskog kontinuuma u istim tačkama pokazuje skokovite promene. Imajući u vidu da je temperatura feromagnetnog prelaza u ovom uzorku 152 K, prva devijacija odgovara ovom faznom prelazu. SEM analizom utvrđena je homogenost uzorka. Ovaj rezultat isključivao je mogućnost feromagnetnih prelaza na različitim temperaturama usled varijacije koncentracije vakancija u različitim segmentima uzorka. Prisustvo spin-fonon interakcije na temperaturama iznad $T_{Curie}$ prethodno je potvrđeno u klasi van der Valsovih magnetnih materijala. Shodno tome, eksperimentalni rezultati se najverovatnije mogu objasniti jakim magnetnim korelacijama u ovom materijalu do temperatureod 220 K.

# Dodatak

## A.1 MGPT metod - Selekciona pravila u dvofononskim procesima

U procesu rasejanja višeg reda sistem iz inicijalnog (osnovnog) vibracionog stanja $|0, 0, \ldots\rangle$ prelazi u finalno višefononsko stanje $|n_\mu, n_{\mu'}, \ldots\rangle$, gde je $n_\mu$ broj fonona u istom stanju $\mu$ i označava čitav skup kvantnih brojeva (kvazi-impuls $k$, kvantni broj ugaonog momenta $m$, itd.). U dvofononskom procesu finalno vibraciono stanje je stanje u kome učestvuju dva fonona u istom kvantnom stanju (overton stanja) ili dva fonona u različitim stanjima (kombinacija stanja). Odgovarajući matrični element dvofononskog Ramanovog procesa je:

$$\langle 0, \ldots, n_\mu, 0, \ldots | \mathcal{R} | 0, 0, \ldots \rangle, n_\mu = 2, \text{overton},$$
$$\langle 0, \ldots, n_\mu, 0, \ldots, n_{\mu'}, \ldots | \mathcal{R} | 0, 0, \ldots \rangle, n_\mu = n_{\mu'} = 1, \text{kombinacija}, \tag{1}$$

gde je $\mathcal{R}$ Ramanov tenzor. Ovaj matrični element je ili skalar ili se transformimše po jediničnoj reprezentaciji prostorne grupe sistema $\mathcal{S}$. U standardnoj aproksimaciji (u aproksimaciji svetlosti beskonačne talasne dužine) Ramanov tenzor je u nerezonantnom slučaju tenzor polarizabilnosti, koji se transformiše kao (simetrizovani) kvadrat vektorske reprezentacije, $D^{\mathcal{R}}(\mathcal{S})$. Razlaganje $D^{\mathcal{R}}(\mathcal{S})$ daje ireducibilne reprezentacije Raman aktivnih modova. Osnovno stanje transformiše se po jediničnoj reprezentaciji, dok se finalno dvofononsko stanje transformiše kao simetrizovani kvadrat, $[(D^\mu(\mathcal{S}))^2]$, odgovarajuće ireducibilne reprezentacije $D^\mu(\mathcal{S})$ (overton) ili direktan proizvod dve ireducibilne reprezentacije $D^\mu(\mathcal{S}) \otimes D^{\mu'}(\mathcal{S})$ (kombinacija). Simetrizacija u slučaju overtonova dolazi od boznoske prirode fonona. Matrični element u jednačini (1) transformiše se kao reducibilna reprezentacija

$$[(D^\mu(\mathcal{S}))^2] \otimes D^{\mathcal{R}}(\mathcal{S}), \text{ za overtonove, ili}$$
$$D^\mu(\mathcal{S}) \otimes D^{\mu'}(\mathcal{S}) \otimes D^{\mathcal{R}}(\mathcal{S}), \text{ za kombinacije.} \tag{2}$$

Ako dekompozicija reprezentacija sadrži jediničnu, ovaj matrični element je skalar, ili ekvivalentno, ako je presek dekompozicija $[(D^\mu(\mathcal{S}))^2]$ ili $D^\mu(\mathcal{S}) \otimes D^{\mu'}(\mathcal{S})$ i $D^{\mathcal{R}}(\mathcal{S})$ neprazan skup. Da bi se dobila selekciona pravila za dvofononske procese Birmanovim metodom [104] dovoljno je naći dekompoziciju $[(D^\mu(\mathcal{S}))^2]$ (za overtonove) i $D^\mu(\mathcal{S}) \otimes D^{\mu'}(\mathcal{S})$ (za kombinacije) svih ireducibilnih reprezentacija. Ukoliko u dekompoziciji postoji reprezentacija Raman aktivnog moda, tada je taj overton ili kombinacija simetrijski dozvoljena u procesu Ramanovog rasejanja. Dekompozi-

cija (simetrizovanog) kvadrata vektorske reprezentacije je direktna i predstavlja problem konačnodimenzionalne tačkaste grupe. Sa druge strane, dekompozicija $[(D^\mu(\mathcal{S}))^2]$ ili $D^\mu(\mathcal{S}) \otimes D^{\mu'}(\mathcal{S})$ za svaku ireducibilnu reprezentaciju može biti nerešiv problem, jer su prostorne grupe beskonačne. Zato se standardni metod zasnovan na teoriji karaktera, u kom se sumiraju svi elementi grupe, ne može primeniti. Potrebno je primeniti metod koji zaobilazi sumiranje elemenata grupe. Metod modifikovanih grupnih projektora (MGPT) koristi samo generatore grupe i konačnodimenzione matrice [84]. Dekompozicija $D(\mathcal{S}) = \oplus_\mu f_D^\mu D^{(\mu)}(\mathcal{S})$ proizvoljne reducibilne reprezentacije $D(\mathcal{S})$ na ireducibilne je suštinski određivanje $f_D^\mu$. Izraz MGPT na osnovu kog se određuju $f_D^\mu$, uključuje samo generatore $s_i$:

$$f_D^\mu = \mathrm{Tr} F \left( \prod_{i=1}^{S} F \left( D(s_i) \otimes D^{(\mu)^*}(s_i) \right) \right) \tag{3}$$

Ovde je $S$ broj generatora grupe, $F(X)$ projektor na podprostor fiksirane tačkaste grupe operatora $X$, i Tr trag matrice. Problem se sada svodi na određivanje $S+1$ projektora. Tehnički to znači da se za svaku svojstvenu vrednost 1 operatora $D(s_i) \otimes D^{(\mu)^*}(s_i)$ traže njegovi svojstveni prostori, a zatim i njihovi projektori. Odgovarajući projektori se tada pomnože i procedura se ponavlja za čitav proizvod iz jednačine (3). Trag krajnjeg projektora daje odgovarajući $f_D^\mu$.

# Literatura

[1] Zorana D. Dohčević-Mitrović, Maja J. Šćepanović, Mirjana Grujić-Brojčin, and Zoran V. Popović. *Optička svojstva nanomaterijala*. Institut za fiziku i Akademska misao, Beograd, str. 254, ISBN: 978-86-7466-414-8, 2011. 1, 5, 6, 8, 9, 10, 12, 13

[2] Thomas P. Devereaux and Rudi Hackl. Inelastic light scattering from correlated electrons. *Rev. Mod. Phys.*, 79:175–233, Jan 2007. 1, 52

[3] N Lazarević and R Hackl. Fluctuations and pairing in Fe-based superconductors: light scattering experiments. *Journal of Physics: Condensed Matter*, 32(41):413001, jul 2020. 1, 27

[4] Yoichi Kamihara, Hidenori Hiramatsu, Masahiro Hirano, Ryuto Kawamura, Hiroshi Yanagi, Toshio Kamiya, and Hideo Hosono. Iron-Based Layered Superconductor: LaOFeP. *Journal of the American Chemical Society*, 128(31):10012–10013, Aug 2006. 1, 19

[5] Yoichi Kamihara, Takumi Watanabe, Masahiro Hirano, and Hideo Hosono. Iron-Based Layered Superconductor La[$O_{1-x}F_x$]FeAs (x = 0.05-0.12) with Tc = 26 K. *Journal of the American Chemical Society*, 130(11):3296–3297, Mar 2008. 1, 19

[6] G. R. Stewart. Superconductivity in iron compounds. *Rev. Mod. Phys.*, 83:1589–1652, Dec 2011. 1, 19, 20

[7] Rafael M Fernandes and Jörg Schmalian. Manifestations of nematic degrees of freedom in the magnetic, elastic, and superconducting properties of the iron pnictides. *Superconductor Science and Technology*, 25(8):084005, jul 2012. 1, 20

[8] K. Kothapalli, A. E. Böhmer, W. T. Jayasekara, B. G. Ueland, P. Das, A. Sapkota, V. Taufour, Y. Xiao, E. Alp, S. L. Bud'ko, P. C. Canfield, A. Kreyssig, and A. I. Goldman. Strong cooperative coupling of pressure-induced magnetic order and nematicity in FeSe. *Nature Communications*, 7(1):12728, 2016. 1, 20

[9] F. Kretzschmar, T. Böhm, U. Karahasanovic, B. Muschler, A. Baum, D. Jost, J. Schmalian, S. Caprara, M. Grilli, C. Di Castro, J. G. Analytis, J.-H. Chu, I. R. Fisher, and R. Hackl. Critical spin fluctuations and the origin of nematic order in Ba(Fe$_{1-x}$Co$_x$)$_2$As$_2$. *Nature Physics*, 12(6):560–563, 2016. 1, 20

[10] U. F. Kaneko, P. F. Gomes, A. F. García-Flores, J.-Q. Yan, T. A. Lograsso, G. E. Barberis, D. Vaknin, and E. Granado. Nematic fluctuations and phase transitions in LaFeAsO: A Raman scattering study. *Phys. Rev. B*, 96:014506, Jul 2017. 1, 20

[11] A. E. Böhmer, T. Arai, F. Hardy, T. Hattori, T. Iye, T. Wolf, H. v. Löhneysen, K. Ishida, and C. Meingast. Origin of the Tetragonal-to-Orthorhombic Phase Transition in FeSe: A Combined Thermodynamic and NMR Study of Nematicity. *Phys. Rev. Lett.*, 114:027001, Jan 2015. 2, 21

[12] T. M. McQueen, A. J. Williams, P. W. Stephens, J. Tao, Y. Zhu, V. Ksenofontov, F. Casper, C. Felser, and R. J. Cava. Tetragonal-to-Orthorhombic Structural Phase Transition at 90 K in the Superconductor $Fe_{1.01}Se$. *Phys. Rev. Lett.*, 103:057002, Jul 2009. 2, 21

[13] M. D. Watson, T. K. Kim, A. A. Haghighirad, N. R. Davies, A. McCollam, A. Narayanan, S. F. Blake, Y. L. Chen, S. Ghannadzadeh, A. J. Schofield, M. Hoesch, C. Meingast, T. Wolf, and A. I. Coldea. Emergence of the nematic electronic state in FeSe. *Phys. Rev. B*, 91:155106, Apr 2015. 2, 21

[14] A. Baum, H. N. Ruiz, N. Lazarevic, Yao Wang, T. Böhm, R. Hosseinian Ahangharne-jhad, P. Adelmann, T. Wolf, Z. V. Popovic, B. Moritz, T. P. Devereaux, and R. Hackl. Frustrated spin order and stripe fluctuations in FeSe. *Communications Physics*, 2(1):14, 2019. 2, 21, 40

[15] Fong-Chi Hsu, Jiu-Yong Luo, Kuo-Wei Yeh, Ta-Kun Chen, Tzu-Wen Huang, Phillip M. Wu, Yong-Chi Lee, Yi-Lin Huang, Yan-Yi Chu, Der-Chung Yan, and Maw-Kuen Wu. Superconductivity in the PbO-type structure $\alpha$-FeSe. *Proceedings of the National Academy of Sciences*, 105(38):14262–14264, 2008. 2, 21

[16] M. H. Fang, H. M. Pham, B. Qian, T. J. Liu, E. K. Vehstedt, Y. Liu, L. Spinu, and Z. Q. Mao. Superconductivity close to magnetic instability in $Fe(Se_{1-x}Te_x)_{0.82}$. *Phys. Rev. B*, 78:224503, Dec 2008. 2, 21

[17] Shiliang Li, Clarina de la Cruz, Q. Huang, Y. Chen, J. W. Lynn, Jiangping Hu, Yi-Lin Huang, Fong-Chi Hsu, Kuo-Wei Yeh, Maw-Kuen Wu, and Pengcheng Dai. First-order magnetic and structural phase transitions in $Fe_{1+y}Se_xTe_{1-x}$. *Phys. Rev. B*, 79:054503, Feb 2009. 2, 21

[18] Wei Bao, Y. Qiu, Q. Huang, M. A. Green, P. Zajdel, M. R. Fitzsimmons, M. Zher-nenkov, S. Chang, Minghu Fang, B. Qian, E. K. Vehstedt, Jinhu Yang, H. M. Pham, L. Spinu, and Z. Q. Mao. Tunable $(\delta\pi, \delta\pi)$-Type Antiferromagnetic Order in $\alpha$-Fe(Te,Se) Superconductors. *Phys. Rev. Lett.*, 102:247001, Jun 2009. 2, 21

[19] U. Pachmayr, N. Fehn, and D. Johrendt. Structural transition and superconductivity in hydrothermally synthesized FeX (X = S, Se)". *Chem. Commun.*, 52:194–197, 2016. 2, 21, 32, 33

[20] Xiaofang Lai, Hui Zhang, Yingqi Wang, Xin Wang, Xian Zhang, Jianhua Lin, and Fuqiang Huang. Observation of Superconductivity in Tetragonal FeS. *Journal of the American Chemical Society*, 137(32):10148–10151, Aug 2015. 2, 21

[21] Yuki Sato, Shigeru Kasahara, Tomoya Taniguchi, Xiangzhuo Xing, Yuichi Kasahara, Yoshifumi Tokiwa, Youichi Yamakawa, Hiroshi Kontani, Takasada Shibauchi, and Yuji Matsuda. Abrupt change of the superconducting gap structure at the nematic critical point in $FeSe_{1-x}S_x$. *Proceedings of the National Academy of Sciences*, 115(6):1227–1231, 2018. 2

[22] Aifeng Wang, E. Stavitski, M. Naamneh, V. N. Ivanovski, M. Abeykoon, A. Milosavljevic, W. H. Brito, A. Baum, J. Jandke, Qianheng Du, N. Lazarevic, Yu Liu, N. C. Plumb, G. Kotliar, R. Hackl, Z. V. Popovic, M. Radovic, K. Attenkofer, and C. Petrovic. Superconducting order from local disorder, 2020. 2, 22, 27, 40

[23] Yujun Deng, Yijun Yu, Yichen Song, Jingzhao Zhang, Nai Zhou Wang, Zeyuan Sun, Yangfan Yi, Yi Zheng Wu, Shiwei Wu, Junyi Zhu, Jing Wang, Xian Hui Chen, and Yuanbo Zhang. Gate-tunable room-temperature ferromagnetism in two-dimensional $Fe_3GeTe_2$. *Nature*, 563(7729):94–99, 2018. 3, 22

[24] T. J. Williams, A. A. Aczel, M. D. Lumsden, S. E. Nagler, M. B. Stone, J.-Q. Yan, and D. Mandrus. Magnetic correlations in the quasi-two-dimensional semiconducting ferromagnet $CrSiTe_3$. *Phys. Rev. B*, 92:144404, Oct 2015. 3, 22, 23

[25] Yao Tian, Mason J Gray, Huiwen Ji, R J Cava, and Kenneth S Burch. Magneto-elastic coupling in a potential ferromagnetic 2D atomic crystal. *2D Materials*, 3(2):025035, jun 2016. 3, 22, 44

[26] Michael A. McGuire, Hemant Dixit, Valentino R. Cooper, and Brian C. Sales. Coupling of Crystal Structure and Magnetism in the Layered, Ferromagnetic Insulator $CrI_3$. *Chemistry of Materials*, 27(2):612–620, Jan 2015. 3, 22

[27] Manuel Bonilla, Sadhu Kolekar, Yujing Ma, Horacio Coy Diaz, Vijaysankar Kalappattil, Raja Das, Tatiana Eggers, Humberto R. Gutierrez, Manh-Huong Phan, and Matthias Batzill. Strong room-temperature ferromagnetism in $VSe_2$ monolayers on van der Waals substrates. *Nature Nanotechnology*, 13(4):289–293, 2018. 3, 22

[28] Dante J. O'Hara, Tiancong Zhu, Amanda H. Trout, Adam S. Ahmed, Yunqiu Kelly Luo, Choong Hee Lee, Mark R. Brenner, Siddharth Rajan, Jay A. Gupta, David W. McComb,

and Roland K. Kawakami. Room Temperature Intrinsic Ferromagnetism in Epitaxial Manganese Selenide Films in the Monolayer Limit. *Nano Letters*, 18(5):3125–3131, May 2018. 3, 22

[29] L. D. Casto, A. J. Clune, M. O. Yokosuk, J. L. Musfeldt, T. J. Williams, H. L. Zhuang, M.-W. Lin, K. Xiao, R. G. Hennig, B. C. Sales, J.-Q. Yan, and D. Mandrus. Strong spin-lattice coupling in CrSiTe$_3$. *APL Materials*, 3(4):041515, 2015. 3, 23, 47

[30] Huiwen Ji, R. A. Stokes, L. D. Alegria, E. C. Blomberg, M. A. Tanatar, Anjan Reijnders, L. M. Schoop, Tian Liang, R. Prozorov, K. S. Burch, N. P. Ong, J. R. Petta, and R. J. Cava. A ferromagnetic insulating substrate for the epitaxial growth of topological insulators. *Journal of Applied Physics*, 114(11):114907, 2013. 3, 23

[31] Jian-Xin Zhu, Marc Janoschek, D. S. Chaves, J. C. Cezar, Tomasz Durakiewicz, Filip Ronning, Yasmine Sassa, Martin Mansson, B. L. Scott, N. Wakeham, Eric D. Bauer, and J. D. Thompson. Electronic correlation and magnetism in the ferromagnetic metal Fe$_3$GeTe$_2$. *Phys. Rev. B*, 93:144404, Apr 2016. 3, 24, 25, 61

[32] Bin Chen, JinHu Yang, HangDong Wang, Masaki Imai, Hiroto Ohta, Chishiro Michioka, Kazuyoshi Yoshimura, and MingHu Fang. Magnetic Properties of Layered Itinerant Electron Ferromagnet Fe$_3$GeTe$_2$. *Journal of the Physical Society of Japan*, 82(12):124711, 2013. 3, 24, 25, 61

[33] Andrew F. May, Stuart Calder, Claudia Cantoni, Huibo Cao, and Michael A. McGuire. Magnetic structure and phase stability of the van der Waals bonded ferromagnet Fe$_{3-x}$GeTe$_2$. *Phys. Rev. B*, 93:014411, Jan 2016. 3, 24, 25, 51

[34] Yu Liu, V. N. Ivanovski, and C. Petrovic. Critical behavior of the van der Waals bonded ferromagnet Fe$_{3-x}$GeTe$_2$. *Phys. Rev. B*, 96:144429, Oct 2017. 3, 55, 60, 61

[35] B Nikolić. *Ramanovo rasejanje na jednoslojnim ugljeničnim nanotubama*. PhD thesis, Univerzitet u Beogradu, Fizički Fakultet, Belgrade, Serbia, June 2012. 5

[36] Chandrasekhara Venkata Raman and Kariamanikkam Srinivasa Krishnan. A new type of secondary radiation. *Nature*, 121(3048):501, 1928. 5

[37] CV Raman and KS Krishnan. The optical analogue of the Compton effect. *Nature*, 121(3053):711–711, 1928. 5

[38] CV Raman and KS Krishnan. The negative absorption of radiation. *Nature*, 122(3062):12–13, 1928. 5

[39] Adolf Smekal. Zur Quantentheorie der Dispersion. *Naturwissenschaften*, 11(43):873–875, Oct 1923. 5

[40] G Landsberg and L Mandelstam. A novel effect of light scattering in crystals. *Naturwissenschaften*, 16(5):5, 1928. 5

[41] P Braiesch. Phonons: Theory and experiments II. *Springer Series in Solid State Sciences*, 65:172, 1986. 5, 6, 7, 8, 9, 10, 11, 12

[42] M Opačić, N Lazarević, M Šćepanović, Hyejin Ryu, Hechang Lei, C Petrovic, and Z V Popović. Evidence of superconductivity-induced phonon spectra renormalization in alkali-doped iron selenides. *Journal of Physics: Condensed Matter*, 27(48):485701, nov 2015. 12, 52

[43] Hans Kuzmany. *Solid-state Spectrosccopy, An Introduction.* Springer, 2009. 13, 14, 15

[44] U. Fano. Effects of configuration interaction on intensities and phase shifts. *Phys. Rev.*, 124:1866–1878, Dec 1961. 15

[45] Feng Jin, Nenad Lazarević, Changle Liu, Jianting Ji, Yimeng Wang, Shuna He, Hechang Lei, Cedomir Petrovic, Rong Yu, Zoran V. Popović, and Qingming Zhang. Phonon anomalies and magnetic excitations in $BaFe_2Se_2O$. *Phys. Rev. B*, 99:144419, Apr 2019. 15

[46] Florian Kretzschmar. *Nematic Fluctuatuins, Fermiology and the Pairing Potential in Iron-Based superconductors.* PhD thesis, Techniche Universität München, Facultät fur Physik, Munchen, Germany, 2015. 16, 20

[47] https://www.princetoninstruments.com/wp-content/uploads/2020/04/TriVista-System-Manual-Issue-1B-4411-0113.pdf. 17

[48] Marianne Rotter, Marcus Tegel, and Dirk Johrendt. Superconductivity at 38 K in the Iron Arsenide $(Ba_{1-x}K_x)Fe_2As_2$. *Phys. Rev. Lett.*, 101:107006, Sep 2008. 19

[49] X.C. Wang, Q.Q. Liu, Y.X. Lv, W.B. Gao, L.X. Yang, R.C. Yu, F.Y. Li, and C.Q. Jin. The superconductivity at 18 K in LiFeAs system. *Solid State Communications*, 148(11):538 – 540, 2008. 19

[50] Fong-Chi Hsu, Jiu-Yong Luo, Kuo-Wei Yeh, Ta-Kun Chen, Tzu-Wen Huang, Phillip M. Wu, Yong-Chi Lee, Yi-Lin Huang, Yan-Yi Chu, Der-Chung Yan, and Maw-Kuen Wu. Superconductivity in the PbO-type structure a-FeSe. *Proceedings of the National Academy of Sciences*, 105(38):14262, Sep 2008. 19

[51] Hiraku Ogino, Yutaka Matsumura, Yukari Katsura, Koichi Ushiyama, Shigeru Horii, Kohji Kishio, and Jun ichi Shimoyama. Superconductivity at 17 K in $(Fe_2P_2)(Sr_4Sc_2O_6)$: a new superconducting layered pnictide oxide with a thick perovskite oxide layer. *Superconductor Science and Technology*, 22(7):075008, jun 2009. 19

[52] Michael J. Pitcher, Tom Lancaster, Jack D. Wright, Isabel Franke, Andrew J. Steele, Peter J. Baker, Francis L. Pratt, William Trevelyan Thomas, Dinah R. Parker, Stephen J. Blundell, and Simon J. Clarke. Compositional Control of the Superconducting Properties of LiFeAs. *Journal of the American Chemical Society*, 132(30):10467–10476, Aug 2010. 20

[53] S. Aswartham, G. Behr, L. Harnagea, D. Bombor, A. Bachmann, I. V. Morozov, V. B. Zabolotnyy, A. A. Kordyuk, T. K. Kim, D. V. Evtushinsky, S. V. Borisenko, A. U. B. Wolter, C. Hess, S. Wurmehl, and B. Büchner. Suppressed superconductivity in charge-doped Li(Fe$_{1-x}$Co$_x$)As single crystals. *Phys. Rev. B*, 84:054534, Aug 2011. 20

[54] Ming Yi, Donghui Lu, Jiun-Haw Chu, James G. Analytis, Adam P. Sorini, Alexander F. Kemper, Brian Moritz, Sung-Kwan Mo, Rob G. Moore, Makoto Hashimoto, Wei-Sheng Lee, Zahid Hussain, Thomas P. Devereaux, Ian R. Fisher, and Zhi-Xun Shen. Symmetry-breaking orbital anisotropy observed for detwinned Ba(Fe$_{1-x}$Co$_x$)$_2$As$_2$ above the spin density wave transition. *Proceedings of the National Academy of Sciences*, 108(17):6878–6883, 2011. 20

[55] E. P. Rosenthal, E. F. Andrade, C. J. Arguello, R. M. Fernandes, L. Y. Xing, X. C. Wang, C. Q. Jin, A. J. Millis, and A. N. Pasupathy. Visualization of electron nematicity and unidirectional antiferroic fluctuations at high temperatures in NaFeAs. *Nature Physics*, 10(3):225–232, Mar 2014. 20

[56] R. M. Fernandes, L. H. VanBebber, S. Bhattacharya, P. Chandra, V. Keppens, D. Mandrus, M. A. McGuire, B. C. Sales, A. S. Sefat, and J. Schmalian. Effects of Nematic Fluctuations on the Elastic Properties of Iron Arsenide Superconductors. *Phys. Rev. Lett.*, 105:157003, Oct 2010. 20

[57] Masahito Yoshizawa, Daichi Kimura, Taiji Chiba, Shalamujiang Simayi, Yoshiki Nakanishi, Kunihiro Kihou, Chul-Ho Lee, Akira Iyo, Hiroshi Eisaki, Masamichi Nakajima, and Shin-ichi Uchida. Structural Quantum Criticality and Superconductivity in Iron-Based Superconductor Ba(Fe$_{1-x}$Co$_x$)$_2$As$_2$. *Journal of the Physical Society of Japan*, 81(2):024604, 2012. 20

[58] Shaolong He, Junfeng He, Wenhao Zhang, Lin Zhao, Defa Liu, Xu Liu, Daixiang Mou, Yun-Bo Ou, Qing-Yan Wang, Zhi Li, Lili Wang, Yingying Peng, Yan Liu, Chaoyu Chen, Li Yu, Guodong Liu, Xiaoli Dong, Jun Zhang, Chuangtian Chen, Zuyan Xu, Xi Chen, Xucun Ma, Qikun Xue, and X. J. Zhou. Phase diagram and electronic indication of high-temperature superconductivity at 65 K in single-layer FeSe films. *Nature Materials*, 12(7):605–610, 2013. 21

[59] Qing-Yan Wang, Zhi Li, Wen-Hao Zhang, Zuo-Cheng Zhang, Jin-Song Zhang, Wei Li, Hao Ding, Yun-Bo Ou, Peng Deng, Kai Chang, Jing Wen, Can-Li Song, Ke He, Jin-Feng

Jia, Shuai-Hua Ji, Ya-Yu Wang, Li-Li Wang, Xi Chen, Xu-Cun Ma, and Qi-Kun Xue. Interface-Induced High-Temperature Superconductivity in Single Unit-Cell FeSe Films on SrTiO$_3$. *Chinese Physics Letters*, 29(3):037402, mar 2012. 21

[60] Nathalie C. Gresty, Yasuhiro Takabayashi, Alexey Y. Ganin, Martin T. McDonald, John B. Claridge, Duong Giap, Yoshikazu Mizuguchi, Yoshihiko Takano, Tomoko Kagayama, Yasuo Ohishi, Masaki Takata, Matthew J. Rosseinsky, Serena Margadonna, and Kosmas Prassides. Structural Phase Transitions and Superconductivity in Fe$_{1+d}$Se$_{0.57}$Te$_{0.43}$ at Ambient and Elevated Pressures. *Journal of the American Chemical Society*, 131(46):16944–16952, Nov 2009. 21

[61] Kuo-Wei Yeh, Tzu-Wen Huang, Yi lin Huang, Ta-Kun Chen, Fong-Chi Hsu, Phillip M. Wu, Yong-Chi Lee, Yan-Yi Chu, Chi-Lian Chen, Jiu-Yong Luo, Der-Chung Yan, and Maw-Kuen Wu. Tellurium substitution effect on superconductivity of the $\alpha$-phase iron selenide. *EPL (Europhysics Letters)*, 84(3):37002, oct 2008. 21

[62] Athena Safa-Sefat and David J. Singh. Chemistry and electronic structure of iron-based superconductors. Jan 2011. Research Org.: Oak Ridge National Lab. (ORNL), Oak Ridge, TN (United States). 22

[63] S. Holenstein, U. Pachmayr, Z. Guguchia, S. Kamusella, R. Khasanov, A. Amato, C. Baines, H.-H. Klauss, E. Morenzoni, D. Johrendt, and H. Luetkens. Coexistence of low-moment magnetism and superconductivity in tetragonal FeS and suppression of $T_c$ under pressure. *Phys. Rev. B*, 93:140506, Apr 2016. 22, 33

[64] Kenneth S. Burch, David Mandrus, and Je-Geun Park. Magnetism in two-dimensional van der Waals materials. *Nature*, 563(7729):47–52, 2018. 22

[65] Cheng-Tai Kuo, Michael Neumann, Karuppannan Balamurugan, Hyun Ju Park, Soonmin Kang, Hung Wei Shiu, Jin Hyoun Kang, Byung Hee Hong, Moonsup Han, Tae Won Noh, and Je-Geun Park. Exfoliation and Raman Spectroscopic Fingerprint of Few-Layer NiPS$_3$ Van der Waals Crystals. *Scientific Reports*, 6(1):20904, 2016. 23

[66] Ming-Wei Lin, Houlong L. Zhuang, Jiaqiang Yan, Thomas Zac Ward, Alexander A. Puretzky, Christopher M. Rouleau, Zheng Gai, Liangbo Liang, Vincent Meunier, Bobby G. Sumpter, Panchapakesan Ganesh, Paul R. C. Kent, David B. Geohegan, David G. Mandrus, and Kai Xiao. Ultrathin nanosheets of CrSiTe$_3$: a semiconducting two-dimensional ferromagnetic material. *J. Mater. Chem. C*, 4:315–322, 2016. 23, 24

[67] Jiaxin Zhang, Xiaochan Cai, Wei Xia, Aiji Liang, Junwei Huang, Chengwei Wang, Lexian Yang, Hongtao Yuan, Yulin Chen, Shilei Zhang, Yanfeng Guo, Zhongkai Liu, and Gang Li. Unveiling Electronic Correlation and the Ferromagnetic Superexchange Mechanism in the van der Waals Crystal CrSiTe$_3$. *Phys. Rev. Lett.*, 123:047203, Jul 2019. 23

[68] Y. F. Li, W. Wang, W. Guo, C. Y. Gu, H. Y. Sun, L. He, J. Zhou, Z. B. Gu, Y. F. Nie, and X. Q. Pan. Electronic structure of ferromagnetic semiconductor $CrGeTe_3$ by angle-resolved photoemission spectroscopy. *Phys. Rev. B*, 98:125127, Sep 2018. 23

[69] Jieyu Yi, Houlong Zhuang, Qiang Zou, Zhiming Wu, Guixin Cao, Siwei Tang, S A Calder, P R C Kent, David Mandrus, and Zheng Gai. Competing antiferromagnetism in a quasi-2D itinerant ferromagnet: $Fe_3GeTe_2$. *2D Materials*, 4(1):011005, nov 2016. 25, 26

[70] Yun Zhang, Haiyan Lu, Xiegang Zhu, Shiyong Tan, Wei Feng, Qin Liu, Wen Zhang, Qiuyun Chen, Yi Liu, Xuebing Luo, Donghua Xie, Lizhu Luo, Zhengjun Zhang, and Xinchun Lai. Emergence of Kondo lattice behavior in a van der Waals itinerant ferromagnet, $Fe_3GeTe_2$. *Science Advances*, 4(1), 2018. 25

[71] Houlong L. Zhuang, P. R. C. Kent, and Richard G. Hennig. Strong anisotropy and magnetostriction in the two-dimensional Stoner ferromagnet $Fe_3GeTe_2$. *Phys. Rev. B*, 93:134407, Apr 2016. 25

[72] Cheng Tan, Jinhwan Lee, Soon-Gil Jung, Tuson Park, Sultan Albarakati, James Partridge, Matthew R. Field, Dougal G. McCulloch, Lan Wang, and Changgu Lee. Hard magnetic properties in nanoflake van der Waals $Fe_3GeTe_2$. *Nature Communications*, 9(1):1554, 2018. 26

[73] V. G. Hadjiev, M. N. Iliev, K. Sasmal, Y.-Y. Sun, and C. W. Chu. Raman spectroscopy of $R$FeAsO ($R$=Sm, La). *Phys. Rev. B*, 77:220505, Jun 2008. 27

[74] A. P. Litvinchuk, V. G. Hadjiev, M. N. Iliev, Bing Lv, A. M. Guloy, and C. W. Chu. Raman-scattering study of $K_xSr_{1-x}Fe_2As_2$ ($x = 0.0, 0.4$). *Phys. Rev. B*, 78:060503, Aug 2008. 27

[75] N. Lazarević, M. Abeykoon, P. W. Stephens, Hechang Lei, E. S. Bozin, C. Petrovic, and Z. V. Popović. Vacancy-induced nanoscale phase separation in $K_xFe_{2-y}Se_2$ single crystals evidenced by Raman scattering and powder x-ray diffraction. *Phys. Rev. B*, 86:054503, Aug 2012. 27

[76] M. Rahlenbeck, G. L. Sun, D. L. Sun, C. T. Lin, B. Keimer, and C. Ulrich. Phonon anomalies in pure and underdoped $R_{1-x}K_xFe_2As_2$ ($R$ = Ba, Sr) investigated by Raman light scattering. *Phys. Rev. B*, 80:064509, Aug 2009. 27

[77] Y. J. Um, J. T. Park, B. H. Min, Y. J. Song, Y. S. Kwon, B. Keimer, and M. Le Tacon. Raman scattering study of the lattice dynamics of superconducting LiFeAs. *Phys. Rev. B*, 85:012501, Jan 2012. 27

[78] Aifeng Wang, Lijun Wu, V. N. Ivanovski, J. B. Warren, Jianjun Tian, Yimei Zhu, and C. Petrovic. Critical current density and vortex pinning in tetragonal $FeS_{1-x}Se_x$ ($x = 0, 0.06$). *Phys. Rev. B*, 94:094506, Sep 2016. 27

[79] Stefano Baroni, Stefano de Gironcoli, Andrea Dal Corso, and Paolo Giannozzi. Phonons and related crystal properties from density-functional perturbation theory. *Rev. Mod. Phys.*, 73:515–562, Jul 2001. 28

[80] Paolo Giannozzi, Stefano Baroni, Nicola Bonini, Matteo Calandra, Roberto Car, Carlo Cavazzoni, Davide Ceresoli, Guido L Chiarotti, Matteo Cococcioni, Ismaila Dabo, Andrea Dal Corso, Stefano de Gironcoli, Stefano Fabris, Guido Fratesi, Ralph Gebauer, Uwe Gerstmann, Christos Gougoussis, Anton Kokalj, Michele Lazzeri, Layla Martin-Samos, Nicola Marzari, Francesco Mauri, Riccardo Mazzarello, Stefano Paolini, Alfredo Pasquarello, Lorenzo Paulatto, Carlo Sbraccia, Sandro Scandolo, Gabriele Sclauzero, Ari P Seitsonen, Alexander Smogunov, Paolo Umari, and Renata M Wentzcovitch. QUANTUM ESPRESSO: a modular and open-source software project for quantum simulations of materials. *Journal of Physics: Condensed Matter*, 21(39):395502, sep 2009. 28, 41, 55

[81] A. R. Lennie, S. A. T. Redfern, P. F. Schofield, and D. J. Vaughan. Synthesis and rietveld crystal structure refinement of mackinawite, tetragonal FeS. *Mineralogical Magazine*, 59(397):677–683, dec 1995. 28

[82] Alaska Subedi, Lijun Zhang, D. J. Singh, and M. H. Du. Density functional study of FeS, FeSe, and FeTe: Electronic structure, magnetism, phonons, and superconductivity. *Phys. Rev. B*, 78:134514, Oct 2008. 28

[83] Y. El Mendili, B. Minisini, A. Abdelouas, and J.-F. Bardeau. Assignment of Raman-active vibrational modes of tetragonal mackinawite: Raman investigations and ab initio calculations. *RSC Adv.*, 4:25827–25834, 2014. 28

[84] M. Damnjanovic and I. Milosevic. Modified group-projector technique: subgroups and generators. *Journal of Physics A: Mathematical and General*, 27(14):4859–4866, jul 1994. 28, 66

[85] Franziska K. K. Kirschner, Franz Lang, Craig V. Topping, Peter J. Baker, Francis L. Pratt, Sophie E. Wright, Daniel N. Woodruff, Simon J. Clarke, and Stephen J. Blundell. Robustness of superconductivity to competing magnetic phases in tetragonal FeS. *Phys. Rev. B*, 94:134509, Oct 2016. 33

[86] S.J. Kuhn, M.K. Kidder, D.S. Parker, C. dela Cruz, M.A. McGuire, W.M. Chance, Li Li, L. Debeer-Schmitt, J. Ermentrout, K.C. Littrell, M.R. Eskildsen, and A.S. Sefat. Struc-

ture and property correlations in FeS. *Physica C: Superconductivity and its Applications*, 534:29 – 36, 2017. 33

[87] Rosemary A. MacDonald and William M. MacDonald. Thermodynamic properties of fcc metals at high temperatures. *Phys. Rev. B*, 24:1715–1724, Aug 1981. 34

[88] W. Spengler and R. Kaiser. First and second order Raman scattering in transition metal compounds. *Solid State Communications*, 18(7):881 – 884, 1976. 36, 38

[89] W. Spengler, R. Kaiser, A. N. Christensen, and G. Müller-Vogt. Raman scattering, superconductivity, and phonon density of states of stoichiometric and nonstoichiometric TiN. *Phys. Rev. B*, 17:1095–1101, Feb 1978. 36

[90] W. Hayes and R. Loudon. *Scattering of Light by Crystals*. John Wiley ans Sons, New York, 1978. 36

[91] Mois I. Aroyo, Asen Kirov, Cesar Capillas, J. M. Perez-Mato, and Hans Wondratschek. Bilbao Crystallographic Server. II. Representations of crystallographic point groups and space groups. *Acta Crystallographica Section A*, 62(2):115–128, Mar 2006. 37

[92] W. L. Zhang, S. F. Wu, S. Kasahara, T. Shibauchi, Y. Matsuda, and G. Blumberg. Stripe quadrupole order in the nematic phase of $FeSe_{1-x}S_x$, 2018. 39

[93] Pierre Massat, Donato Farina, Indranil Paul, Sandra Karlsson, Pierre Strobel, Pierre Toulemonde, Marie-Aude Méasson, Maximilien Cazayous, Alain Sacuto, Shigeru Kasahara, Takasada Shibauchi, Yuji Matsuda, and Yann Gallais. Charge-induced nematicity in FeSe. *Proceedings of the National Academy of Sciences*, 113(33):9177–9181, 2016. 40

[94] Yu Liu and C. Petrovic. Critical behavior of quasi-two-dimensional semiconducting ferromagnet $Cr_2Ge_2Te_6$. *Phys. Rev. B*, 96:054406, Aug 2017. 41

[95] Yu Liu and C. Petrovic. Anisotropic magnetic entropy change in $Cr_2X_2Te_6$ (X = Si and Ge). *Phys. Rev. Materials*, 3:014001, Jan 2019. 41, 51

[96] Richard E. Marsh. The crystal structure of $Cr_2Si_2Te_6$: Corrigendum. *Journal of Solid State Chemistry*, 77(1):190 – 191, 1988. 41

[97] G. T. Lin, H. L. Zhuang, X. Luo, B. J. Liu, F. C. Chen, J. Yan, Y. Sun, J. Zhou, W. J. Lu, P. Tong, Z. G. Sheng, Z. Qu, W. H. Song, X. B. Zhu, and Y. P. Sun. Tricritical behavior of the two-dimensional intrinsically ferromagnetic semiconductor $CrGeTe_3$. *Phys. Rev. B*, 95:245212, Jun 2017. 42, 51

[98] N. Lazarević, E. S. Bozin, M. Šćepanović, M. Opačić, Hechang Lei, C. Petrovic, and Z. V. Popović. Probing $IrTe_2$ crystal symmetry by polarized Raman scattering. *Phys. Rev. B*, 89:224301, Jun 2014. 44

[99] Y. Sun, R. C. Xiao, G. T. Lin, R. R. Zhang, L. S. Ling, Z. W. Ma, X. Luo, W. J. Lu, Y. P. Sun, and Z. G. Sheng. Effects of hydrostatic pressure on spin-lattice coupling in two-dimensional ferromagnetic $Cr_2Ge_2Te_6$. *Applied Physics Letters*, 112(7):072409, 2018. 44

[100] N. Lazarević, M. Radonjić, M. Šćepanović, Hechang Lei, D. Tanasković, C. Petrovic, and Z. V. Popović. Lattice dynamics of $KNi_2Se_2$. *Phys. Rev. B*, 87:144305, Apr 2013. 45

[101] N. Lazarević, Z. V. Popović, Rongwei Hu, and C. Petrovic. Evidence for electron-phonon interaction in $Fe_{1-x}M_xSb_2$ ($M =$ Co and Cr; $0 \leq x \leq 0.5$) single crystals. *Phys. Rev. B*, 81:144302, Apr 2010. 45

[102] Luke J. Sandilands, Yao Tian, Kemp W. Plumb, Young-June Kim, and Kenneth S. Burch. Scattering Continuum and Possible Fractionalized Excitations in $\alpha-RuCl_3$. *Phys. Rev. Lett.*, 114:147201, Apr 2015. 47

[103] Deiseroth, Hans - Jorg and Aleksandrov, Krasimir and Reiner, Christof and Kienle, Lorenz and Kremer, Reinhard K. $Fe_3GeTe_2$ and $Ni_3GeTe_2$ - Two New Layered Transition-Metal Compounds: Crystal Structures, HRTEM Investigations, and Magnetic and Electrical Properties. *European Journal of Inorganic Chemistry*, 2006(8):1561–1567, 2006. 61

[104] Joseph L. Birman. Space group selection rules: Diamond and zinc blende. *Phys. Rev.*, 127:1093–1106, Aug 1962. 65

# Spisak objavljenih naučnih radova kandidata korišćenih u disertaciji

[1] A. Baum, A. Milosavljević, N. Lazarević, M.M. Radonjić, B. Nikolić, M. Mitschek, Z. Inanloo Maranloo, M. Šćepanović, M. Grujić-Brojčin, N. Stojilović, M. Opel, Aifeng Wang, C. Petrovic, Z.V. Popović, R Hackl, "Phonon anomalies in FeS", *Phys. Rev. B* **97**, 054306, 2018.

[2] A. Milosavljević, A. Šolajić, J. Pešić, Yu Liu, C. Petrovic, N. Lazarević, Z.V. Popović, "Evidence of spin-phonon coupling in $CrSiTe_3$", *Phys. Rev. B* **98**, 104306, 2018.

[3] A. Milosavljević, A. Šolajić, S. Djurdjić Mijin, J. Pešić, B. Višić, Yu Liu, C. Petrovic, N. Lazarević, Z.V. Popović, "Lattice dynamics and phase transitions in $Fe_{3-x}GeTe_2$", *Phys. Rev. B* **99**, 214304, 2019.

[4] A. Milosavljević, A. Šolajić, B. Višić, M. Opačić, J. Pešić, Yu Liu, C. Petrovic, Z.V. Popović, N. Lazarević, "Vacancies and spin-phonon coupling in $CrSi_{0.8}Ge_{0.1}Te_3$", *J. Raman Spectrosc.* **51**, 2153-2160, 2020.

# Biografija

Ana Milosavljević rođena je 30.06.1986. godine u Smederevu, gde je završila osnovnu školu i gimnaziju. Osnovne studije završila je na Matematičkom fakultetu Univerziteta u Beogradu, smer Profesor matematike i računarstva. Nakon završenih osnovnih studija 2010. godine upisuje master studije na Fizičkom fakultetu Univerziteta u Beogradu, smer Teorijska i eksperimentalna fizika. Master rad pod nazivom *Vibracione osobine ZnO nanotuba* brani 2013. godine. Iste godine upisuje doktorske studije na Fizičkom fakultetu Univerziteta u Beogradu, uža naučna oblast - Fizika kondenzovane materije i statistička fizika. Od 10.03.2015. godine zaposlena je u Centru za fiziku čvrstog stanja i nove materijale Instituta za fiziku u Beogradu, gde se pod mentorstvom dr Nenada Lazarevića bavila ispitivanjem vibracionih osobina materijala sa jakim elektronskim korelacijama. Do sada je publikovala šest naučnih radova u vrhunskim međunarodnim časopisima od kojih je na četiri vodeći autor. Njeni radovi citirani su 50 puta uz h-indeks 3 (Google Akademik). Od marta 2015. do decembra 2019. godine bila je angažovana na projektu *Nanostrukturni multifunkcionalni nanomaterijali i nanokompoziti* (III450018) Ministarstva prosvete, nauke i tehnološkog razvoja Republike Srbije pod rukovodstvom akademika Zorana V. Popovića. Učesnik je bilateralnih projekata sa Valter Majsner institutom u Minhenu i Centrom za jake korelacije Instituta za fiziku u Augsburgu, a od avgusta 2020. godine angažovana je i na projektu Fonda za nauku Republike Srbije *StrainedFeSC* (broj 6062656) čiji je rukovodilac dr Nenad Lazarević.

# Изјава о ауторству

Име и презиме аутора  Ана  Милосављевић

Број индекса  8010/2013

### Изјављујем

да је докторска дисертација под насловом

Електрон-фонон и спин-фонон интеракција у суперпроводницима на  бази гвожђа
и квази-2Д материјалима изучавана методом Раманове спектроскопије

- резултат сопственог истраживачког рада;
- да дисертација у целини ни у деловима није била предложена за стицање друге дипломе према студијским програмима других високошколских установа;
- да су резултати коректно наведени и
- да нисам кршио/ла ауторска права и користио/ла интелектуалну својину других лица.

**Потпис аутора**

У Београду, _____

_____

# Изјава о истоветности штампане и електронске верзије докторског рада

Име и презиме аутора   Ана  Милосављевић

Број индекса  8010/2013

Студијски програм  Физика

Наслов рада  Електрон-фонон и спин-фонон интеракција у суперпроводницима на бази гвожђа и квази-2Д материјалима изучавана методом Раманове спектроскопије

Ментор        др Ненад Лазаревић

Изјављујем да је штампана верзија мог докторског рада истоветна електронској верзији коју сам предао/ла ради похрањена у **Дигиталном репозиторијуму Универзитета у Београду.**

Дозвољавам да се објаве моји лични подаци везани за добијање академског назива доктора наука, као што су име и презиме, година и место рођења и датум одбране рада.

Ови лични подаци могу се објавити на мрежним страницама дигиталне библиотеке, у електронском каталогу и у публикацијама Универзитета у Београду.

**Потпис аутора**

У Београду, _____

_____

# Изјава о коришћењу

Овлашћујем Универзитетску библиотеку „Светозар Марковић" да у Дигитални репозиторијум Универзитета у Београду унесе моју докторску дисертацију под насловом:

<u>Електрон-фонон и спин-фонон интеракција у суперпроводницима на бази гвожђа и квази-2Д материјалима изучавана методом Раманове спектроскопије</u>

која је моје ауторско дело.

Дисертацију са свим прилозима предао/ла сам у електронском формату погодном за трајно архивирање.

Моју докторску дисертацију похрањену у Дигиталном репозиторијуму Универзитета у Београду и доступну у отвореном приступу могу да користе сви који поштују одредбе садржане у одабраном типу лиценце Креативне заједнице (Creative Commons) за коју сам се одлучио/ла.

1. Ауторство (CC BY)

2. Ауторство – некомерцијално (CC BY-NC)

3. Ауторство – некомерцијално – без прерада (CC BY-NC-ND)

4. Ауторство – некомерцијално – делити под истим условима (CC BY-NC-SA)

5. Ауторство –  без прерада (CC BY-ND)

6. Ауторство –  делити под истим условима (CC BY-SA)

(Молимо да заокружите само једну од шест понуђених лиценци.
 Кратак опис лиценци је саставни део ове изјаве).

**Потпис аутора**

У Београду, _____                                    _____

1. **Ауторство**. Дозвољавате умножавање, дистрибуцију и јавно саопштавање дела, и прераде, ако се наведе име аутора на начин одређен од стране аутора или даваоца лиценце, чак и у комерцијалне сврхе. Ово је најслободнија од свих лиценци.

2. **Ауторство – некомерцијално**. Дозвољавате умножавање, дистрибуцију и јавно саопштавање дела, и прераде, ако се наведе име аутора на начин одређен од стране аутора или даваоца лиценце. Ова лиценца не дозвољава комерцијалну употребу дела.

3. **Ауторство – некомерцијално – без прерада**. Дозвољавате умножавање, дистрибуцију и јавно саопштавање дела, без промена, преобликовања или употребе дела у свом делу, ако се наведе име аутора на начин одређен од стране аутора или даваоца лиценце. Ова лиценца не дозвољава комерцијалну употребу дела. У односу на све остале лиценце, овом лиценцом се ограничава највећи обим права коришћења дела.

 4. **Ауторство – некомерцијално – делити под истим условима**. Дозвољавате умножавање, дистрибуцију и јавно саопштавање дела, и прераде, ако се наведе име аутора на начин одређен од стране аутора или даваоца лиценце и ако се прерада дистрибуира под истом или сличном лиценцом. Ова лиценца не дозвољава комерцијалну употребу дела и прерада.

5. **Ауторство – без прерада**. Дозвољавате умножавање, дистрибуцију и јавно саопштавање дела, без промена, преобликовања или употребе дела у свом делу, ако се наведе име аутора на начин одређен од стране аутора или даваоца лиценце. Ова лиценца дозвољава комерцијалну употребу дела.

6. **Ауторство – делити под истим условима**. Дозвољавате умножавање, дистрибуцију и јавно саопштавање дела, и прераде, ако се наведе име аутора на начин одређен од стране аутора или даваоца лиценце и ако се прерада дистрибуира под истом или сличном лиценцом. Ова лиценца дозвољава комерцијалну употребу дела и прерада. Слична је софтверским лиценцама, односно лиценцама отвореног кода.